OPTIMIZATION OF A REAL-TIME PORTAL IMAGING SYSTEM FOR QUANTITATIVE IMAGING

by

PATHIRAGE RASIKA DEEPAL RAJAPAKSHE

A Thesis
Submitted to the Faculty of Graduate Studies
in Partial Fulfillment of the Requirements
for the Degree of

DOCTOR OF PHILOSOPHY

Department of Physics
University of Manitoba
Winnipeg, Manitoba

ISBN 0-612-16276-1

Name _____

Dissertation Abstracts International is arranged by broad, general subject categories. Please select the one subject which most nearly describes the content of your dissertation. Enter the corresponding four-digit code in the spaces provided.

RADIATION PHYSICS
SUBJECT TERM

0756
SUBJECT CODE

U·M·I

Subject Categories

THE HUMANITIES AND SOCIAL SCIENCES

COMMUNICATIONS AND THE ARTS
Architecture 0729
Art History 0377
Cinema 0900
Dance 0378
Fine Arts 0357
Information Science 0723
Journalism 0391
Library Science 0399
Mass Communications 0708
Music 0413
Speech Communication 0459
Theater 0465

EDUCATION
General 0515
Administration 0514
Adult and Continuing 0516
Agricultural 0517
Art 0273
Bilingual and Multicultural 0282
Business 0688
Community College 0275
Curriculum and Instruction 0727
Early Childhood 0518
Elementary 0524
Finance 0277
Guidance and Counseling 0519
Health 0680
Higher 0745
History of 0520
Home Economics 0278
Industrial 0521
Language and Literature 0279
Mathematics 0280
Music 0522
Philosophy of 0998
Physical 0523
Psychology 0525
Reading 0535
Religious 0527
Sciences 0714
Secondary 0533
Social Sciences 0534
Sociology of 0340
Special 0529
Teacher Training 0530
Technology 0710
Tests and Measurements 0288
Vocational 0747

LANGUAGE, LITERATURE AND LINGUISTICS
Language
- General 0679
- Ancient 0289
- Linguistics 0290
- Modern 0291

Literature
- General 0401
- Classical 0294
- Comparative 0295
- Medieval 0297
- Modern 0298
- African 0316
- American 0591
- Asian 0305
- Canadian (English) 0352
- Canadian (French) 0355
- English 0593
- Germanic 0311
- Latin American 0312
- Middle Eastern 0315
- Romance 0313
- Slavic and East European 0314

PHILOSOPHY, RELIGION AND THEOLOGY
Philosophy 0422
Religion
- General 0318
- Biblical Studies 0321
- Clergy 0319
- History of 0320
- Philosophy of 0322

Theology 0469

SOCIAL SCIENCES
American Studies 0323
Anthropology
- Archaeology 0324
- Cultural 0326
- Physical 0327

Business Administration
- General 0310
- Accounting 0272
- Banking 0770
- Management 0454
- Marketing 0338

Canadian Studies 0385
Economics
- General 0501
- Agricultural 0503
- Commerce-Business 0505
- Finance 0508
- History 0509
- Labor 0510
- Theory 0511

Folklore 0358
Geography 0366
Gerontology 0351
History
- General 0578
- Ancient 0579
- Medieval 0581
- Modern 0582
- Black 0328
- African 0331
- Asia, Australia and Oceania 0332
- Canadian 0334
- European 0335
- Latin American 0336
- Middle Eastern 0333
- United States 0337

History of Science 0585
Law 0398
Political Science
- General 0615
- International Law and Relations 0616
- Public Administration 0617

Recreation 0814
Social Work 0452
Sociology
- General 0626
- Criminology and Penology 0627
- Demography 0938
- Ethnic and Racial Studies 0631
- Individual and Family Studies 0628
- Industrial and Labor Relations 0629
- Public and Social Welfare 0630
- Social Structure and Development 0700
- Theory and Methods 0344

Transportation 0709
Urban and Regional Planning 0999
Women's Studies 0453

THE SCIENCES AND ENGINEERING

BIOLOGICAL SCIENCES
Agriculture
- General 0473
- Agronomy 0285
- Animal Culture and Nutrition 0475
- Animal Pathology 0476
- Food Science and Technology 0359
- Forestry and Wildlife 0478
- Plant Culture 0479
- Plant Pathology 0480
- Plant Physiology 0817
- Range Management 0777
- Wood Technology 0746

Biology
- General 0306
- Anatomy 0287
- Biostatistics 0308
- Botany 0309
- Cell 0379
- Ecology 0329
- Entomology 0353
- Genetics 0369
- Limnology 0793
- Microbiology 0410
- Molecular 0307
- Neuroscience 0317
- Oceanography 0416
- Physiology 0433
- Radiation 0821
- Veterinary Science 0778
- Zoology 0472

Biophysics
- General 0786
- Medical 0760

EARTH SCIENCES
Biogeochemistry 0425
Geochemistry 0996
Geodesy 0370
Geology 0372
Geophysics 0373
Hydrology 0388
Mineralogy 0411
Paleobotany 0345
Paleoecology 0426
Paleontology 0418
Paleozoology 0985
Palynology 0427
Physical Geography 0368
Physical Oceanography 0415

HEALTH AND ENVIRONMENTAL SCIENCES
Environmental Sciences 0768
Health Sciences
- General 0566
- Audiology 0300
- Chemotherapy 0992
- Dentistry 0567
- Education 0350
- Hospital Management 0769
- Human Development 0758
- Immunology 0982
- Medicine and Surgery 0564
- Mental Health 0347
- Nursing 0569
- Nutrition 0570
- Obstetrics and Gynecology 0380
- Occupational Health and Therapy 0354
- Ophthalmology 0381
- Pathology 0571
- Pharmacology 0419
- Pharmacy 0572
- Physical Therapy 0382
- Public Health 0573
- Radiology 0574
- Recreation 0575
- Speech Pathology 0460
- Toxicology 0383

Home Economics 0386

PHYSICAL SCIENCES
Pure Sciences
Chemistry
- General 0485
- Agricultural 0749
- Analytical 0486
- Biochemistry 0487
- Inorganic 0488
- Nuclear 0738
- Organic 0490
- Pharmaceutical 0491
- Physical 0494
- Polymer 0495
- Radiation 0754

Mathematics 0405
Physics
- General 0605
- Acoustics 0986
- Astronomy and Astrophysics 0606
- Atmospheric Science 0608
- Atomic 0748
- Electronics and Electricity 0607
- Elementary Particles and High Energy 0798
- Fluid and Plasma 0759
- Molecular 0609
- Nuclear 0610
- Optics 0752
- Radiation 0756
- Solid State 0611

Statistics 0463

Applied Sciences
Applied Mechanics 0346
Computer Science 0984
Engineering
- General 0537
- Aerospace 0538
- Agricultural 0539
- Automotive 0540
- Biomedical 0541
- Chemical 0542
- Civil 0543
- Electronics and Electrical 0544
- Heat and Thermodynamics 0348
- Hydraulic 0545
- Industrial 0546
- Marine 0547
- Materials Science 0794
- Mechanical 0548
- Metallurgy 0743
- Mining 0551
- Nuclear 0552
- Packaging 0549
- Petroleum 0765
- Sanitary and Municipal 0554
- System Science 0790

Geotechnology 0428
Operations Research 0796
Plastics Technology 0795
Textile Technology 0994

PSYCHOLOGY
General 0621
Behavioral 0384
Clinical 0622
Developmental 0620
Experimental 0623
Industrial 0624
Personality 0625
Physiological 0989
Psychobiology 0349
Psychometrics 0632
Social 0451

OPTIMIZATION OF A REAL-TIME PORTAL IMAGING SYSTEM FOR QUANTITATIVE IMAGING

BY

PATHIRAGE RASIKA DEEPAL RAJAPAKSHE

A Thesis submitted to the Faculty of Graduate Studies of the University of Manitoba in partial fulfillment of the requirements of the degree of

DOCTOR OF PHILOSOPHY

ABSTRACT

The outcome of radiation therapy in treating cancerous tumour relies mainly on the ability to destroy the tumour with minimal damage to the surrounding normal tissues. The accuracy and the reproducibility in the radiation dose delivered to the target volume on a daily basis over a period of several weeks are important factors in improving overall precision of the treatment process. A prototype video-based electronic portal imaging device (VEPID) was developed at the Manitoba Cancer Foundation for verifying the accuracy and reproducibility of radiotherapy treatments in real-time. The performance of the prototype VEPID was far from ideal for both geometric and dosimetric verification of radiation treatments due to the inferior noise properties of the system.

The ideal imaging system is a quantum noise limited system in which contributions from all other sources of noise are smaller than the quantum noise. The major objective of this work was to optimize the noise characteristics of the VEPID so that it can operate in the quantum noise limited regime with high signal-to-noise characteristics. In order to achieve this, all the significant noise sources in the imaging system were identified and the contribution from each source was quantified either by theoretical modeling or experimental measurements. Both hardware and software methods were then utilized to optimize the system noise. In particular, the optimization of the video camera played a major role in this process, and a cooled CCD camera based on a dual field capture CCD was found to be the ideal candidate for real-time quantitative portal imaging. In order to verify the satisfactory performance of the optimized VEPID over time, a quality control test was also implemented. It has been shown that the optimized VEPID can be used to verify electron treatments with linear accelerators, and it is capable of monitoring the stability of linear accelerators during the first few seconds of operation. The VEPID is also shown to be capable of measuring relative exit doses to an accuracy better than 3%.

ACKNOWLEDGEMENTS

I would like to take this opportunity to thank, however inadequately, those individuals who generously gave of their time and talent to make this project possible.

Firstly, I would like to acknowledge my debt to my adviser and mentor, Dr. Shlomo Shalev. His commitment to sound education, scientific integrity and his deep insight into the nature of scientific enquiry will long be an example for me. It is with regret that I terminate a fruitful relationship with Shlomo and I hope we can maintain a warm personal and professional relationship for years to come.

I would also like to thank the members of my advisory committee, Professors Ed Shwedyk and Norm Davison, and Dr. Stephen Pistorius for their invaluable advice. I would particularly like to thank Stephen for the guidance on clinical dosimetry.

I would also like to thank my friends and colleagues Drs. Georgi Gluhchev and Tom Radcliffe, as well as Kurt Luchka, Demeng Chen, Brian Wowk, Gerald Wegner, Mike Hoppansack, Elana Goldberg, and Kiaren McGee for their invaluable guidance and support. Special thanks go to Kurt for his editorial and numerous other help.

Special thanks also go to Drs. Jeff Bews, Yuri Mandelzweig, and David Viggars for their advice and support on the clinical aspects of my work.

I have been very fortunate in having excellent technical support at various stages of my work. Firstly, the Medical Devices staff, including Ian Paul, Bob Miller, and of course Ed Maisey, must be acknowledged for their enormous support on the mechanical aspects of my work. Special thanks also go to the staff of the Nuclear Electronics section including Richard Shabaga, Chris Dyke, Brian Myslicki, Vic Goetzen, and Gerald Stoesz.

I would like thank Randy Roels, John Gatschuff, and Jim Fedorowich for their help on getting the "stupid" computers to work all the time.

I would like to acknowledge the financial support form the Siemens Medical Systems of Concord CA, Manitoba Health Research Council, and Canadian Breast Cancer Foundation. Special thanks go to the Manitoba Cancer Treatment and Research Foundation for keeping my body and soul in close proximity during the course of this work through the continued financial support provided in the form of a studentship.

Last, but not least, I would like to express my deepest gratitude to my wife Nilanthi, for her encouragement, support, and patience during our stay in Winnipeg.

I dedicate this work to my parents, Sirisena and Dulcy Rajapakshe.

TABLE OF CONTENTS

Chapter 1

Rationale for portal imaging

1.1 Introduction

The goal of external beam radiotherapy is to sterilize the malignant tumour with minimal destruction of the surrounding normal, non-cancerous tissue, ultimately resulting in tumour cure with sufficient normal tissue remaining to ensure viability and function. Unfortunately, radiation interacts with and is absorbed by normal tissues in its path en route to the tumour. Not all the radiation is absorbed by the tumour; some continues through the body, eventually exiting at the skin surface, irradiating these normal tissues as well. Furthermore, the tendency for malignant tumours to infiltrate surrounding normal tissue means that a radiation treatment field must encompass a margin of normal tissue around the known extent of the tumour. Consequently, radiation damage is produced in normal tissues in the treatment area as well as in the tumour.

1.2 Dose response and tumour control

Various levels of radiation yield different tumour control probabilities depending upon the size and anatomic extent of the lesion. The total number of surviving cells is proportional to the initial number and biological characteristics of clonogenic cells and the total cell kill achieved with a specified dose of radiation. The relationship between radiation dose and the probability of tumour control of a homogeneous group of tumours is sigmoidal. That is, with increasing radiation doses, more and more neoplastic cells are killed until ultimately, all clonogenic cells are destroyed and a cure is achieved. Dose response relationships for local control of homogeneous tumour groups have been empirically determined[1].

The dose of radiation which can be delivered to a tumour is limited by the probability of serious normal tissue complications[2]. Therefore, the choice of tumour dose is based on the relative probability of tumour control and normal tissue complications. The potential therapeutic gain can be estimated for an average group of patients based on tumour size, histological type and the normal tissues which will be included in the treatment fields. Figure 1-1 shows a theoretical dose response relationship for tumour control and normal tissue complications. These two curves have been drawn parallel to one another for simplicity, although it is likely that in practice, because of the heterogeneity of tumour response to irradiation, the tumour-control curve will be shallower than that for normal tissue response[2]. The therapeutic ratio is often defined as percentage of tumour cures which are obtained at a given level toxicity for normal tissues. Hill[2], however, suggested that the therapeutic ratio is better defined in terms of a ratio of radiation doses required to produce a given percentage of tumour control and complications.

The greater the displacement between the two curves, the higher the probability of tumour control. If the tumour-control curve is shallower than that for normal tissue damage, however, then the therapeutic ratio may only be favourable for low and intermediate tumour-control levels. If the two curves are close together or the curve for tumour control is displaced to the right of that for complications, the therapeutic ratio is unfavourable, where a high level of complications must be accepted to achieve even a minimal level of tumour control.

1.3 Precision required in radiotherapy

Unfortunately, very little quantitative information about these dose response curves is available. The information available, however, does allow us to make some conclusions regarding accuracy of dose delivered to the patient. The slopes of these curves are sufficiently steep that a change in dose of 5% is expected to result in a change

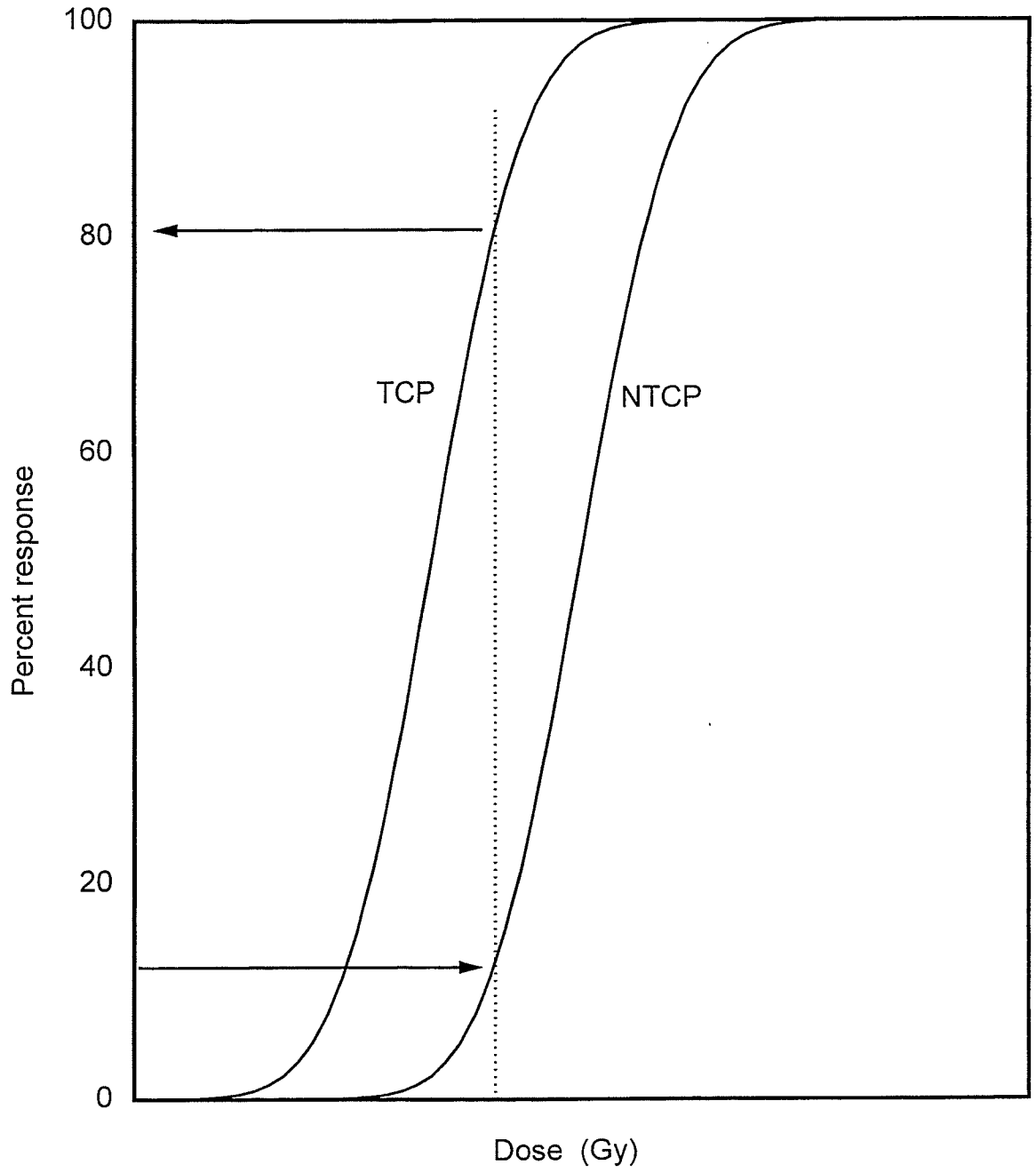

Figure 1-1 Illustration of the concept of therapeutic ratio in terms of dose response relationships for tumour control and normal tissue damage. See Text for details.

of over 10% either in tumour control or complication rate. This is a large change in results and for this reason the ICRU report 24[3] has recommended that an overall accuracy of ±5% be considered as reasonable, in which case even higher accuracy is required for each individual activity in the treatment process. Svensson[4] showed that various contributing factors in the calculation and delivery of dose to a homogeneous phantom combine to give an uncertainty of this magnitude at 95% confidence level. For tumours with high dose gradient, however, a limit of ± 3 % may be required[5].

1.4 Limits to precision

Uncertainty in the delivered dose to the patient can arise from any one of the chain of activities in the treatment process: accurate delineation of the tumour volume; calibration of the treatment unit; treatment planning process; set-up of the patient. The set-up of the patient can be divided into three steps: setting the machine parameters, patient positioning and patient immobilization during treatment.

The accurate delineation of the target volume is essentially a clinical task which requires close collaboration between the radiotherapist and the physicist. Although this task is assumed to be achieved in most cases[6], Leunens et. al.[7] have shown that for brain tumours, the largest contributing factor in the global uncertainty might come from the subjective interpretation of the tumour boundaries from diagnostic CT images. However, future developments in correlation between MRI and CT images which provide complementary patient information, will eventually decrease the uncertainty in tumour and target volume delineations.

Cunningham[8] recently pointed out that the goal recommended by ICRU report 24 of a ±5% accuracy for dose delivery is difficult to achieve with currently available treatment planning systems. However, in an attempt to attain a goal of 3% in accuracy, a new generation of dose calculation methods has been proposed. These are the Δ-volume method[9], differential pencil beam method[10], dose spread array method[11], and Fourier

convolution method[12]. They all employ theoretically calculated absorbed dose arrays as input data. In particular, the latter three methods rely on similar Monte Carlo-generated data, which include electron transport information. These methods are undergoing critical evaluations and have not been implemented into commercial treatment planning systems as yet.

As the uncertainties associated with treatment unit calibration and treatment planning are handled with extensive quality assurance programs and accurate radiation transport algorithms, patient set-up remains the major concern in the overall accuracy of the treatment process. Dutreix[6] claimed that in a good radiotherapy centre, where a quality assurance program is regularly applied, the setting-up of the patient is generally the weakest point of the chain which largely contributes to the overall uncertainty. Portal verification, in which a transmission image of the patient is acquired during therapy, plays a significant role in verifying that the uncertainties associated with patient set-up are within acceptable limits.

1.5 Documented patient set-up errors

A number of studies have documented the frequency and magnitude of patient set-up errors in external beam radiotherapy, in most cases using portal imaging. By systematic use of verification films in their pioneering work, Marks et. al.[13,14] demonstrated a high incidence of localization errors on patients irradiated for head and neck cancer or malignant lymphomas. These errors were corrected with improved immobilization of the patients. For instance, the use of a bite block in patients with head and neck tumours reduced localization incidence of errors from 16% to 1%[14]. Hendrickson[15] reported a 3.5% incidence of error in multiple parameters (setting of field size, timer, gantry and collimator angles, and patient positioning) with one technologist working. The error rate declined to 2.8% when two technologists worked together.

Byhardt et. al.[16] compared the frequency and magnitude of errors for different sites of treatment. They found that 17% of the 434 ear, nose, and throat (ENT) treatments included in the study had errors greater than 5 mm, and errors of similar magnitude were found in 7% of 163 cranial region portals. Furthermore, there was a 13% error rate (field displacements of 5mm or more) reported among the 317 chest region films examined. Of the cases included in the study, the highest error rate was observed for treatments in the pelvic region where discrepancies greater than 5 mm were found in 26% of the 153 cases.

Rabinowitz et. al.[17] reported on the analysis of simulator and portal films of 71 patients, 25 of whom were analyzed retrospectively, 39 prospectively, and seven with daily portal films. Some discrepancies were noted between the simulator and the localization portal films. With an average value of 3 mm standard deviation of the variations, the mean worst case discrepancy averaged 3.5 mm in the head and neck region, 9.2 mm in the thorax, 5.1 in the abdomen, 8.4 in the pelvis and 6.9 in the extremities.

Hulshof et. al.[18] analyzed the incidence and magnitude of localization errors detected by verification films during mantle field irradiation for Hodgkin's disease in 126 treatment set-ups. The first verification film at the beginning of treatment showed localization errors of over 1 cm in 13% of the cases leading to a critical margin between the shielding block and tumour-bearing area in 9% of treatment set-ups. After the first correction, an adequate treatment set-up was obtained in 60% of the cases and after two corrections in 84%, thus demonstrating the verification films in improving the localization of portals and monitoring subsequent corrections. Others have documented similar localization errors on the basis of portal film or EPID image review analysis in treatments of the breast[19-24], head and neck[25-33], mantle/thorax[26,33-40], and pelvis[26,41-54].

1.6 Impact of local control on survival

Some studies have pointed out that set-up errors may also correlate with decreased tumour control. Kinzie et. al.[55] in the Patterns of Care Study, reviewed patients with Hodgkin's disease treated with radiation therapy alone, and found that 33% of patients whose treatment portals were inadequate, subsequently developed in-field or marginal recurrences, in comparison with only 7% of those treated with adequate portals. Marks et. al.[56] also reported a higher incidence of failures in patients with carcinoma of the nasopharynx on whom shielding of the ear inadvertently caused some blocking of tumour volume.

Suit et. al.[57] have reported that experimentally, in animal tumour models, the incidence of distant metastases is usually higher in those animals with local failure than in those with local tumour control. Similar phenomenon is observed in patients with carcinoma of the lung[58], prostate[59], and uterine cervix[60]. Suit et. al.[57] pointed out that in the United States, elimination of locoregional failures in patients without distant metastases at the time of diagnosis would result in a significant increase in survivors. They have also noted that long-term disease free survival after salvage treatment of patients with local failure only should be viewed as proof that improved treatment of the primary lesion results in higher survival rates, provided that the patients do not have and will not develop distant metastases. These authors presented data to indicate that in a variety of tumours, a correlation exists between the incidence of locoregional failures and the development of distant metastases. They have also reported data demonstrating the importance of higher doses of radiation in improving the probability of tumour control.

1.7 The need for real-time portal imaging

Suit et. al.[61] pointed out the benefits of reducing the treatment volume in an effort to deliver higher doses of radiation, which may improve the quality of tumour control without excessively irradiating surrounding normal tissues, thereby decreasing treatment-related morbidity. As early as 1965 Takahashi proposed dynamic conformal therapy, in which blocks, radiation field direction, and patient might be dynamically controlled during treatment in order to achieve a tightly conforming high dose region around the target volume[62]. Dynamic conformal radiation therapy is technically feasible today with the commercial availability of multileaf collimators, and is under study at a number of institutions[63]. The use of a smaller treatment volume in these treatments requires methods to confirm that the target volume has been exactly aligned for each beam path, and the dynamic nature requires that the methods be real-time. Therefore, there is a specific need for real-time portal imaging devices to make dynamic conformal therapy a success. In particular, the NCI workshop on geometric accuracy and reproducibility in radiation therapy held in 1987[64] made specific recommendations to encourage the development of convenient real-time on-line portal imaging systems.

References

[1] G. H. Fletcher, "The scientific basis of the present and future practice of clinical radiotherapy," Int. J. Radiat. Oncol. Biol. Phys. **9,** 1073-1082 (1983).

[2] R. P. Hill, "Experimental radiotherapy," in *The basic science of oncology*, edited by I. F. Tannock and R. P. Hill (McGraw-Hill, Inc., New York, 1992), pp. 276-301.

[3] ICRU Report # 24, *Determination of absorbed dose in a patient irradiated by beams of X or Gamma rays in radiotherapy procedures,* (International Commission on Radiation Units and Measurements, Washington, D.C., 1976).

[4] G. K. Svensson, "Quality assurance in radiation therapy: Physics efforts," Int. J. Radiat. Oncol. Biol. Phys. **10 (Sup. 1),** 23-29 (1984).

[5] A. Brahme, "Dosimetric precision requirements in radiation therapy," Acta Radiol. Oncology **23,** 379-391 (1984).

[6] A. Dutreix, "When and how can we improve precision in radiotherapy," Radiother. Oncol. **2,** 275-292 (1984).

[7] G. Leunens, J. Menten, C. Weltens, J. Verstraete, and E. van der Schueren, "Quality assessment of medical decision making in radiation oncology: variability in target volume deliation for brain tumors," Radiother. Oncol. **29,** 169-175 (1993).

[8] J. R. Cunningham, "Development of computer algorithms for radiation treatment planning," Int. J. Radiat. Oncol. Biol. Phys. **16,** 1367-1376 (1989).

[9] J. W. Wong and R. M. Henkelman, "A new approach to CT pixel-based photon dose calculations in heterogeneous media," Med. Phys. **10,** 199-208 (1983).

[10] R. Mohan, C. S. Chui, and L. Lidofsky, "Differential pencil beam dose computation model for photons," Med. Phys. **13,** 64-73 (1986).

[11] T. R. Mackie, J. W. Scrimger, and J. J. Battista, "A convolution method of calculating dose for 15-MV X-rays," Med. Phys. **12,** 188-196 (1985).

[12] A. L. Boyer and E. Mok, "A photon dose distribution model employing convolution calculations," Med. Phys. **12,** 169-177 (1985).

[13] J. E. Marks, A. G. Haus, H. G. Sutton, and M. L. Griem, "Localization error in the radiotherapy of hodgkin's disease and malignant lymphoma with extended mantle fields," Cancer **34,** 83-90 (1974).

[14] J. E. Marks and A. G. Haus, "The effect of immobilisation on localisation error in the radiotherapy of head and neck cancer," Clin. Radiol. **27,** 175-177 (1976).

[15] F. R. Hendrickson, "The four P's of human error in treatment delivery," Int. J. Radiat. Oncol. Biol. Phys. **4,** 913-914 (1978).

[16] R. W. Byhardt, J. D. Cox, A. Hornburg, and G. Liermann, "Weekly localization films and detection of field placement errors," Int. J. Radiat. Oncol. Biol. Phys. **4,** 881-887 (1978).

[17] I. Rabinowitz, J. Broomberg, M. Goitein, K. McCarthy, and J. Leong, "Accuracy of radiation field alignment in clinical practice," Int. J. Radiat. Oncol. Biol. Phys. **11,** 1857-1867 (1985).

[18] M. Hulshof, L. Vanuytsel, W. Van den Bogaert, and E. van der Schueren, "Localization errors in mantle-field irradiation for hodgkin's disease," Int. J. Radiat. Oncol. Biol. Phys. **17,** 679-683 (1989).

[19] A. Jakobsen, P. Iversen, C. Gadeberg, J. L. Hansen, and M. Hjeim-Hansen, "A new system for patient fixation in radiotherapy," Radiother. Oncol. **8,** 145-151 (1987).

[20] C. Mitine, A. Dutreix, and E. van der Schueren, "Tangential breast irradiation: influence of technique of set-up on transfer errors and reproducibility," Radiother. Oncol. **22,** 308-310 (1991).

[21] R. Valdangi and C. Italia, "Early breast cancer irradiation after conservative surgery: quality control by portal localization films," Radiother. Oncol. **22,** 311-313 (1991).

[22] G. van Tienhoven, J. H. Lanson, D. Crabeels, S. Heukelom, and B. J. Mijnheer, "Accuracy in tangential breast treatment set-up: A portal imaging study," Radiother. Oncol. **22,** 317-322 (1991).

[23] C. Westbrook, J. Gildersleve, and J. Arnold, "Quality assurance in daily treatment procedure: patient movement during tangential fields treatment," Radiother. Oncol. **22,** 299-303 (1991).

[24] C. L. Creutzberg, V. G. M. Althof, H. Huizenga, A. G. Visser, and P. C. Levendag, "Quality assurance using portal imaging: The accuracy of patient positioning in irradiation of breast cancer," Int. J. Radiat. Oncol. Biol. Phys. **25,** 529-539 (1993).

[25] H. Huizenga, P. C. Levendag, P. M. Z. R. De Porre, and A. G. Visser, "Accuracy in radiation field alignment in head and neck cancer: A prospective study," Radiother. Oncol. **11,** 181-187 (1988).

[26] B. Kihlen and B. -I. Ruden, "Reproducibility of field alignment in radiation therapy A large-scale clinical experience," Acta Radiol. **28,** 689-692 (1989).

[27] C. Mitine, G. Leunens, J. Verstraete, N. Blanckaert, J. Van Dam, A. Dutreix, and E. van der Schueren, "Is it necesary to repeat quality control procedures for head and neck patients?," Radiother. Oncol. **21,** 201-210 (1991).

[28] K. J. Halverson, T. C. Leung, J. B. Pellet, R. L. Gerber, M. S. Weinhous, and J. W. Wong, "Study of treatment variation in the radiotherapy of head and neck tumors using a fiber-optic on-line radiotherapy imaging system," Int. J. Radiat. Oncol. Biol. Phys. **21,** 1327-1336 (1991).

[29] S. A. Rosenthal, J. M. Galvin, J. W. Goldwein, A. R. Smith, and P. H. Blitzer, "Improved methods for determination of variability in patient positioning for radiation therapy using simulation and serial portal film measurements," Int. J. Radiat. Oncol. Biol. Phys. **23,** 621-625 (1992).

30 P. B. Dunscombe, K. Fox, S. Loose, and K. Leszczynski, "The investigation and rectification of field placement errors in the delivery of complex head and neck fields," Int. J. Radiat. Oncol. Biol. Phys. **26,** 155-161 (1993).

31 M. . Hunt, G. J. Kutcher, C. Burman, D. Fass, L. Harrison, S. Leibel, and Z. Fuks, "The effect of setup uncertainties on the treatment of nasopharynx cancer," Int. J. Radiat. Oncol. Biol. Phys. **27,** 437-447 (1993).

32 C. Mitine, A. Dutreix, and E. van der Schueren, "Black and white in accuracy assesment of megavoltage images: the medical decision is grey," Radiother. Oncol. **28,** 31-36 (1993).

33 E. J. Holupka, J. L. Humm, N. J. Tarbell, and K. Svensson, "Effect of set-up error on the dose across the junction of matching cranial-spinal fields in the treatment of medulloblastoma," Int. J. Radiat. Oncol. Biol. Phys. **27,** 345-352 (1993).

34 S. E. Griffiths and R. G. Pearcey, "The daily reproducibility of large, complex-shaped radiotherapy fields to the thorax and neck," Clin. Radiol. **37,** 39-41 (1986).

35 W. C. Lam, M. Partowmah, J. D. Lee, M. D. Wharam, and K. S. Lam, "On-line measurement of field placement errors in external beam radiotherapy," Br. J. Radiol. **60,** 361-365 (1987).

36 B. W. Taylor, N. P. Mendenhall, and R. R. Million, "Reproducibility of mantle irradiation with daily imaging films," Int. J. Radiat. Oncol. Biol. Phys. **19,** 149-151 (1990).

[37] C. L. Creutzberg, A. G. Visser, P. M. Z. R. De Porre, J. H. Meerwaldt, V. G. M. Althof, and P. C. Levendag, "Accuracy of patient positioning in mantle field irradiation," Radiother. Oncol. **23,** 257-264 (1992).

[38] D. J. Gladstone, M. van Herk, and L. M. Chin, "Verification of lung attenuator positioning before total body irradiation using an electronic portal imaging device," Int. J. Radiat. Oncol. Biol. Phys. **27,** 449-454 (1993).

[39] C. Weltens, G. Leunens, A. Dutreix, J. M. Cosset, F. Eschwege, and E. van der Schueren, "Accuracy in mantle field irradiations: irradiated volume and daily dose," Radiother. Oncol. **29,** 18-26 (1993).

[40] P. H. Vos, "The accuracy of field shape definition using standard shielding blocks and the consequences for field shape verification," Radiother. Oncol. **31,** 169-175 (1994).

[41] M. J. S. Richards and D. A. Buchler, "Errors in reproducing pelvic radiation portals," Int. J. Radiat. Oncol. Biol. Phys. **2,** 1017-1019 (1977).

[42] R. G. Pearcey and S. E. Griffiths, "The impact of treatment errors on post-operative radiotherapy for testicular tumours," Br. J. Radiol. **58,** 1003-1005 (1985).

[43] S. E. Griffiths, R. G. Pearcey, and J. Thorogood, "Quality control in radiotherapy: The reduction of field placement errors," Int. J. Radiat. Oncol. Biol. Phys. **13,** 1583-1588 (1987).

[44] S. E. Griffiths, G. G. Khoury, and A. Eddy, "Quality control of radiotherapy during pelvic irradiation," Radiother. Oncol. **20,** 203-206 (1991).

[45] E. M. Soffen, G. E. Hanks, C. C. Hwang, and J. C. H. Chu, "Conformal static field therapy for low volume low grade prostate cancer with rigid immobilization," Int. J. Radiat. Oncol. Biol. Phys. **20,** 141-146 (1991).

[46] J. Bijhold, J. V. Lebesque, A. A. M. Hart, and R. E. Vijlbrief, "Maximizing setup accuracy using portal images as applied to a conformal boost technique for prostatic cancer," Radiother. Oncol. **24,** 261-271 (1992).

[47] J. M. Balter, G. T. Y. Chen, C. A. Pelizzari, S. Krishnasamy, S. Rubin, and S. Vijayakumar, "Online repositioning during treatment of the prostate: A study of potential limits and gains," Int. J. Radiat. Oncol. Biol. Phys. **27,** 137-143 (1993).

[48] L. Cionini and M. Bucciolini, "Role of portal imaging in clinical radiotherapy: Florence experience," Radiother. Oncol. **29,** 230-236 (1993).

[49] W. De Neve, F. Van den Heuvel, M. Coghe, D. Verellen, M. De Beukeleer, A. Roelstraete, P. De Roover, L. Thon, and G. Storme, "Interactive use of on-line portal imaging in pelvic radiation," Int. J. Radiat. Oncol. Biol. Phys. **25,** 517-524 (1993).

[50] P. B. Dunscombe, S. Loose, and K. Leszczynski, "Sizes and sources of field placement error in routine irradiation for prostate cancer," Radiother. Oncol. **26,** 174-176 (1993).

[51] A. A. H. El-Gayed, A. Bel, R. E. Vijlbrief, H. Bartelink, and J. V. Lebesque, "Time trend of patient setup deviations during pelvic irradiation using electronic portal imaging," Radiother. Oncol. **26,** 162-171 (1993).

[52] S. A. Rosenthal, M. Roach, B. Goldsmith, E. C. Doggett, B. Pickett, H. You, E. M. Soffen, R. L. Stern, and J. K. Ryu, "Immobilization improves the reproducibility of patient positioning during six-field conformal radiation therapy for prostate carcinoma," Int. J. Radiat. Oncol. Biol. Phys. **27,** 921-926 (1993).

[53] J. Gildersleve, D. P. Dearnaley, P. M. Evans, M. Law, C. Rawlings, and W. Swindell, "A randomised trial of patient repositioning during radiotherapy using a megavoltage imaging system," Radiother. Oncol. **31,** 161-168 (1994).

[54] R. D. Kortmann, C. F. Hess, R. Jani, C. Meisner, and M. Bamberg, "Reproducibility of field alignment in difficult patient positioning," Int. J. Radiat. Oncol. Biol. Phys. **29,** 869-872 (1994).

[55] J. J. Kinzie, G. E. Hanks, C. J. Maclean, and S. Kramer, "Patterns of care study: Hodgkin's disease relapse rates and adequacy of portals," Cancer **52,** 2223-2226 (1983).

[56] J. E. Marks, J. M. Bedwinek, F. Lee, J. A. Purdy, and C. A. Perez, "Dose-response analysis for nasopharyngeal carcinoma," Cancer **50,** 1042-1050 (1982).

[57] H. D. Suit and S. J. Westgate, "Impact of improved local control on survival," Int. J. Radiat. Oncol. Biol. Phys. **12,** 453-458 (1986).

[58] C. A. Perez, M. Bauer, S. Edelstein, B. W. Gillespie, and R. Birch, "Impact of tumor control on survival in carcinoma of the lung treated with irradiation," Int. J. Radiat. Oncol. Biol. Phys. **12,** 539-547 (1986).

[59] C. A. Perez, M. V. Pilepich, and F. Zivnuska, "Tumor control in definitive irradiation of localized carcinoma of the prostate," Int. J. Radiat. Oncol. Biol. Phys. **12,** 523-531 (1986).

[60] C. A. Perez, R. R. Kuske, H. M. Camel, A. E. Galakatos, M. A. Hederman, M. Kao, and B. J. Waltz, "Analysis of pelvic tumor control and impact on survival in carcinoma of the uterine cervix treated with radiation therapy alone," Int. J. Radiat. Oncol. Biol. Phys. **14,** 613-621 (1988).

[61] H. D. Suit, J. Becht, J. Leong, M. Stracher, W. C. Wood, L. Verhey, and M. Goitein, "Potential for improvement in radiation therapy," Int. J. Radiat. Oncol. Biol. Phys. **14,** 777-786 (1988).

[62] S. Takahashi, "Confirmation radiotherapy. Rotation techniques as applied to Radiography and Radiotherapy of cancer," Acta Radiol. **S 242,** (1965).

[63] J. P. Gerard, "High dose-high precision in radiation oncology," Radiother. Oncol. **29,** 167-168 (1993).

[64] L. E. Reinstein and A. G. Meek, "Workshop on geometric accuracy and reproducibility in radiation therapy," Int. J. Radiat. Oncol. Biol. Phys. **13,** 809-810 (1987).

Chapter 2

Introduction to portal imaging systems

2.1 Portal imaging with radiographic film

Portal imaging with radiographic film was the conventional method of verifying the accuracy of radiotherapy. A film is placed on the exit side of the patient, and records a projection of the patient's anatomy within the radiation field boundary. The report of the AAPM task group 28[1] defined three types of portal radiographs: *localization*, *verification*, and *double exposure* radiographs. *Localization* radiograph is produced by an exposure which is short compared to the daily treatment time. It is processed and examined before the remainder of the treatment is delivered, so that any set-up errors can be detected and corrected in an interactive manner. However, this procedure is time consuming and impractical for routine implementation in every treatment fraction. A *verification* radiograph is produced when the film is exposed to the entire treatment delivered with that field, and therefore uses a less sensitive (ie. slow) film. Any set-up errors detected by this procedure can only be corrected on the following treatment. *Double exposure* radiograph is made when the treatment field is small making it difficult to determine the patient set-up accurately. As the name implies, two exposures are made, where one exposure is made with the blocked treatment field and the other uses a larger unblocked field. This procedure has the advantage of showing anatomical features located outside of the treatment field, which is useful in verifying the correct patient set-up.

High energy photons have similar energy absorption coefficients for bone and soft tissue, so that in comparison to diagnostic films, the contrast in portal films is extremely poor. Contrast is also degraded by the scattered photons since an anti-scatter grid is impractical at high energies. Although Droege et al.[2] have found that contrast

improvement can be achieved by maintaining an air gap between the patient and the film for ^{60}Co and 4 and 8 MV photons, scattering is highly forward directed at higher energies making air gaps less effective beyond 6 MV[3].

Many techniques have been proposed to improve portal film quality: by using metal screen cassettes[2,4-6], and by using metal/phosphor screen combination[7-9]. Reinstein and Orton[10] have used postprocessing enhancement by "gamma multiplication" to obtain an order of magnitude improvement in contrast in localization and verification films. Alternatively, a number of authors have developed methods to convert portal films into digital format and then to apply digital image enhancement techniques[11-17].

In order to circumvent the problem of inherently poor contrast in megavoltage portal films, imaging with low energy X-rays has been proposed. This idea was first explored as early as 1958 by Holloway[18] who mounted a diagnostic X-ray tube on a cobalt unit. Later Biggs et. al.[19] mounted a diagnostic X-ray tube on the side of a 10 MV linac. Shiu et. al.[20]also reported a system where a commercially available X-ray tube was mounted on the head of a cobalt unit. An alternate approach suggested by Galbraith[21] involves replacing the high-Z target with a thin low-Z target so that sufficient low-energy photons will be produced to make a high contrast portal film. However these systems did not find wide enough acceptance by the community to be commercially available. Epp and Suit[22] recently stressed the importance of diagnostic quality portal imaging in verifying three-dimensional conformal treatments.

Despite these improvements, the procedures involved in making and evaluating portal films are time consuming making portal imaging with film an off-line imaging modality. Their use in each portal of every treatment is prevented by the cost and effort involved in the film method. Furthermore, the cost in the film is largely irrecoverable. Consequently, 60% of the radiotherapy centres limited the use of portal films to the first day of the treatment only[1].

2.2 Alternative off-line modalities

Xeroradiography has been shown to have certain advantages over the portal film in radiation therapy verification[23,24]. The xeroradiographic process exploits the photoconductive properties of amorphous selenium. The image receptor is a thin layer of selenium deposited on an aluminium backing plate. The detector is charged prior to irradiation, and the electron hole pairs generated by the deposited radiation energy form a latent image by subtraction from the original uniform charge distribution. The latent image is developed by spraying a fine aerosol of blue powder which sticks to the charge image. This image is then transferred to paper by contact and fused by heating to produce an opaque radiograph. Exposures of 3-6 s (4-9 cGy dose) are sufficient to produce satisfactory images on ^{60}Co or 4MV treatment machines. This technique produces images with strong edge enhancement, and the wide latitude of the process allows good visualization of anatomical details.

Computed radiography (CR) has also been used for megavoltage portal imaging as an alternative to portal film[25-29]. The image receptor or "imaging plate" is a flexible plastic plate less than 1 mm thick that is coated with minute polycrystals (4-5μm in diameter) of photostimulable phosphor combined with an organic binder. Photostimulable phosphors are capable of storing a fraction of the absorbed energy in the form of colour centres (F-centers) when irradiated by X-rays, ultraviolet light, electrons, or protons. They emit luminescence radiation whose intensity is proportional to the absorbed energy when stimulated by visible or infrared radiation. After the X-ray image is stored on the imaging plate as a latent image, it is read by sequentially scanning a laser beam and recording the luminescent light with a conventional photomultiplier tube. By flooding the image plate with light, any residual image can be erased and the plate can be reused. Advantages of CR are ease of storage and retrieval, high dynamic range (10^5), and the possibility of digital processing and analysis.

Despite the advantages of portal imaging with xeroradiography and CR compared to portal film, they are not considered as ideal methodologies for radiotherapy verification since they are not real-time modalities.

2.3 Electronic portal imaging devices

A number of alternative detectors called electronic portal imaging devices (EPID), have been developed in the past to overcome the limitation in these off-line imaging methods. EPIDs are capable of imaging in real-time (or near real-time) and generating digital data (images). Digital images open up new possibilities for automatic quantitative geometric comparison (e.g. registration) with simulator images or digitally reconstructed radiographs (DRR), and real-time capability allows interventional verification. Furthermore the availability of a digital image allows the application of digital image processing to overcome the poor contrast. Recently Boyer et. al.[30] reviewed the developments in various EPIDs, including solid state detectors, ionization chamber systems, and video based portal imaging systems.

2.3.1 Solid state detectors

Lam et. al.[31] constructed an EPID using a linear array of 256 silicon diodes. The center-to-center separation between adjacent diodes was 2 mm, and a microcomputer controlled stepping motor was used to scan the radiation transmitted through the patient in 2 mm intervals. When mounted at 150 cm from the radiation source, the resulting resolution at the isocenter was 1.3 mm. A 1.1 mm thick lead plate was used on top of the diodes for electronic build-up when imaging a 4 MV beam. The quality of the images allowed visualization of a 1 cm test object at 0.8% primary contrast level. Being a scanning detector system, the major drawback in this system is the long acquisition time.

Another solid-state scanning array was developed by Morton et al.[32] using zinc tungstate scintillating crystals. The crystals, 5x5x25 mm in size, were arranged in a

double row, 64 crystals per row. The light output from the crystals was read out by optically coupled photodiodes. The surfaces of the crystals were polished and coated with a reflective material for maximum light collection efficiency. The detector was mounted at 200 cm from the radiation source to reduce the effects of scatter radiation, giving a 19x19 cm^2 field of view at the isocenter. A complete scan over the full field of view takes about 4 s. The spatial and contrast resolutions for this system were found experimentally to be 3 mm and 0.5% respectively[32].

Scanning arrays are not efficient in detecting two-dimensional distribution of radiation, and therefore require long acquisition times unless spatial and/or contrast resolution is sacrificed. Consequently scanning detector systems do not offer "real-time" capabilities for verifying dynamic conformal therapy. In order to overcome this drawback an area detector based on amorphous silicon photodiodes and thin-film transistors was developed at the University of Michigan[33,34]. The detector is a multi-element amorphous silicon detector array (called MASDA array) which consists of a matrix of 256x240 photodiodes, each coupled to a thin film field effect transistor (FET). The detector array is positioned immediately below a metal/phosphor screen combination which has the same functionality as those used in video based systems. The major advantage of this system is that it can collect a large percentage of the light emitted by the metal/phosphor screen. Although initial results indicate that this technology has the potential to provide an efficient, high resolution, large area EPID, the technology has not matured enough to be commercially available.

2.3.2 Liquid ionization chambers

A scanning liquid ionization chamber (SLIC) EPID was developed at the Netherlands Cancer Institute. The original prototype had only 33x32 chambers[35] and the later version which evolved into the commercial system "Portal Vision" from Varian Inc. has 256x256 chambers[36]. The ion chambers are made of 1 mm liquid film of iso-octane,

and is sandwiched between two parallel circuit boards. In addition, there is a 1 mm thick stainless steel front screen to allow sufficient build-up. There are 256 strip-formed electrodes on the rear plate that serve as signal electrodes. Each electrode is connected to a sensitive electrometer, and the outputs of the electrometers are multiplexed to a single amplifier and a digitizer. On the opposite plate, at right angles to the signal electrodes, are 256 high voltage electrodes. The signal is read out from the chamber matrix row by row, by successively switching high voltage to different electrodes and measuring the currents in all 256 column electrodes. The 32.5x32.5 cm field of view is scanned in about 6 seconds, although faster acquisitions are possible with reduced spatial resolution. The resolution of the device is governed by the 1.27 mm spacing of the electrode plates.

2.3.3 Video based electronic portal imaging devices (VEPID)

In principle, a television/video camera tube is a convenient device of moderate spatial resolution and adequate quantum efficiency, which can serve as the basis of an area detector system. It is natural, therefore to employ standard television cameras which have been brought to a high state of perfection by long development and mass production. It is even highly desirable to retain as far as possible the scanning rates, ie. line and frame frequency standards adopted in commercial television practice so that standard off-the-shelf inexpensive devices such as display monitors, signal generators etc. can be used without modification. In fact, VEPIDs or the fluoroscopic portal imaging devices were the very first real-time EPIDs developed[37]. Although the image quality of these systems was rather poor, these original studies demonstrated the potential of real-time verification of radiation treatments using television technology.

Intense research and development on night vision capabilities for military and civilian applications resulted in the commercial availability of very sensitive video camera tubes such as Silicon Intensified Target (SIT) camera tubes. Utilizing these

developments, Baily et al. demonstrated fluoroscopic portal imaging using a large flat metal/phosphor screen viewed through a 45^0 mirror by a SIT camera[38].

A schematic diagram of a video based portal imaging system is shown in Fig. 2-1, and in general consists of the following components.

1. metal/phosphor screen to convert the X-ray image to a light image.
2. 45° front surface mirror to optically couple the screen to the video camera
3. very sensitive video camera fitted with a fast (low F/stop) lens
4. control system containing a computer/image processor combination.

The metal plate about 1-2 mm in thickness, acts as the build-up material for the phosphor screen, transferring part of the energies of the incident photons to secondary electrons. These electrons in turn interact with and deposit energy (dose) through excitations in the phosphor screen. The screen emits fluorescent light via de-excitation, the intensity of which is proportional to the deposited energy[39,40]. A very small fraction of this light (less than 0.05%) is detected by the video camera to form a video signal. The video signal is then digitized, processed, and stored by the computer system.

The system developed by Baily et. al. at the University of California at San Diego, contained a 1/16" stainless steel build-up plate onto which a 43x43 cm^2 E-2 fluorescent screen (Dupont) was cemented. A front surface mirror and an F/0.78, 13 mm focal length lens was used to optically couple the phosphor screen to a SIT camera. The scanning of the SIT camera was modified from RS-170 format to a square format to image the full field of view. A computer or an image processor was not used in this system, and images were stored either on video tape or video disk. The limiting resolution of the system measured at the input surface of the fluorescent screen was 0.8 lp/mm. This early system clearly demonstrated the capability of real-time visualization of organ motion during ^{60}Co and 6MV treatments.

At the Massachusetts General Hospital (MGH), Leong et. al. developed a similar system, incorporating a real-time digital image processing system and a host computer[41].

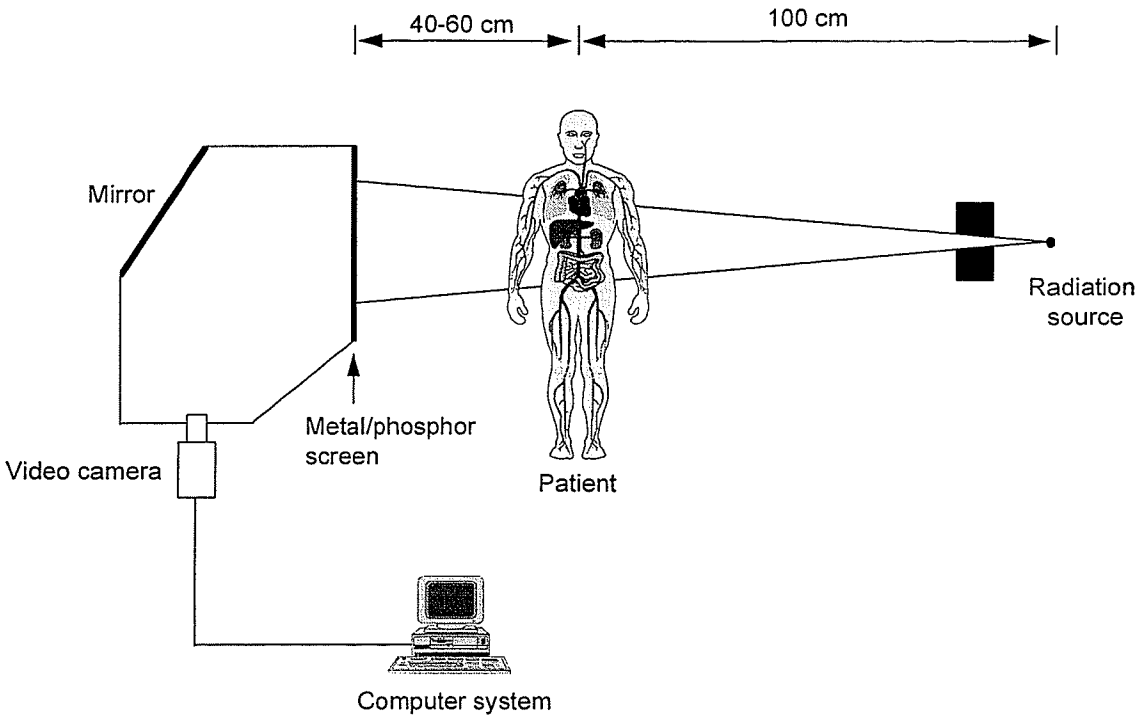

Figure 2-1 A Schematic diagram of a video based portal imaging system.

The video signal was digitized to 512x512 8-bit pixels and stored on frame buffers, and a pipeline image processor (PIP) was used to perform a host of arithmetic and logical operations, both at video frame rates. In addition to acquiring and processing digital portal images, the authors also described the attempts for quantitative dosimetric analysis on portal images, which was the first attempt on dosimetric verification of a radiation treatment using an EPID.

Munro et. al. at the University of Toronto have developed a VEPID using a plumbicon (lead oxide vidicon) camera[42,43]. A 400 mg cm^{-2} terbium activated gadolinium oxysulfide (Gd_2O_2S:Tb or P-43) phosphor layer bonded to 1 mm copper plate was used in their system, and signal integration on the camera target was used to reduce electronic noise. They have shown that the system is capable of detecting 0.7% contrast with 7cGy irradiation. This system is commercially marketed by Infimed Inc. under the trade name "THERAVIEW".

Visser et. al at the Daniel den Hoed Cancer Centre have developed a prototype system which is now marketed by the Philips Medical Systems as "SRI-100 MVI" portal imaging system[44]. The system consists of a Charge Coupled Device (CCD) camera (512x256 pixels) optically coupled to a 30x40 cm^2 rare earth fluorescent screen having a surface density of 411 mg cm^{-2} using two 45^0 mirrors. Initial signal integration was carried out on the CCD target for 0.1-1 seconds, and subsequent accumulation was carried out on a 16-bit frame processor. The spatial resolution of the system as measured by the FWHM was 1.5 mm. With 25 cm of water equivalent absorber, the signal-to-noise ratio of an image acquired with a 7 sec exposure was found to be 105. Huizenga et. al. later reported an improvement in the system by incorporating a large area CCD having a higher quantum efficiency[45].

Wong et. al. at the Mallincrodt Institute of Radiology have also developed a prototype VEPID using a Newvicon camera[46,47]. In order to overcome the bulkiness of the mirror based systems, the original design incorporated fibre optic coupling between

the video camera and the phosphor screen. However, a later version developed at the William Beaumont Hospital uses mirror coupling and a cooled CCD camera capable of target integration[48].

Shalev et. al. at the Manitoba Cancer Treatment and Research Foundation (MCTRF) in Winnipeg, developed a prototype real-time VEPID which later evolved into the BEAMVIEW^{PLUS} portal imaging system from Siemens Medical Systems[49]. The original prototype utilized a commercial phosphor screen (100 mg cm^{-2}) and a SIT camera combination to properly match the light output from the screen to the camera response. An ITI-151 real-time image processor from Imaging Technology Inc connected to a PC-286 host computer was used for image acquisition, process, and storage. The SIT camera was operated at RS-170 video rate (30 frames per sec.) and images were obtained by averaging 128 or 256 frames in real-time.

Although the images produced by this system were not ideal, the image quality was adequate after digital processing for the use in the evaluation of set-up errors[50]. The SIT camera which was necessary for imaging at the light level encountered with the 100 mg cm^{-2} screen, has a quantum efficiency of only 10-15%. This was a major drawback in the original system. After an extensive study on the performance of different metal/phosphor screen combinations for the use in real-time VEPIDs, Wowk developed thick screens that produced four fold increase in light output[51]. Consequently, and also partly due to recommendations based on the work of this thesis, the BEAMVIEW^{PLUS} commercial system uses a 150 mg cm^{-2} screen and a Newvicon camera.

2.4 Thesis overview

In the case of verification of static beam therapy, continuous real-time imaging is required only when patient and/or organ motion during a single fraction has to be studied. However, due to ever increasing utilization of dynamic therapy techniques, such as dynamic intensity modulation and dynamic wedge, the need for continuous real-time

portal verification becomes more and more important. Although, in principle, these treatments may be verified by a single long exposure, practical limitations such as instabilities in detector housing make the usefulness of such cumulative exposures somewhat questionable. In order to handle the demands in dynamic therapy verification, portal imaging systems must be capable of imaging in real-time or near real-time continuously during the whole treatment without any dead time.

The images produced by the MCTRF prototype portal imaging system have low contrast-to-noise ratios, making the geometric verification process difficult. Although post processing can increase the contrast in the portal images[50] the noise characteristics in the portal images determine the amount of contrast enhancement that can be performed. Furthermore, real-time portal images obtained by the system contain artifacts due to combined effects of accelerator pulsation and conventional video scanning. In the context of this thesis, the term noise is used to describe the presence of unwanted information in images. Noise, whether random or otherwise, also limits the accuracy with which quantitative information can be extracted from portal images. Therefore, identification and reduction of imaging system noise is necessary for optimizing the system performance for quantitative as well as qualitative measurements.

The first objective of this work was to optimize the noise characteristics of the prototype portal imaging system developed at the MCTRF. In order to achieve this, all the significant noise sources in the imaging system are identified and the contribution from each source is quantified either by theoretical modeling or by experimental measurements. Both hardware and software methods are utilized to optimize the system noise characteristics. Particularly, the video camera optimization was a major step in the optimization of the system. Once the system is optimized for noise characteristics, the second objective was to evaluate the ability of the system for quantitative imaging. The final objective was to develop suitable quality assurance tests for commissioning and routine quality control purposes.

Part II of the thesis describe the systematic and detailed investigation carried out to identify all the significant noise sources in the system and to quantify the contribution from each source. Possible ways of reducing all the contributions from these noise sources so that the system can operate close to the quantum noise limited regime are also described.

Noise in video-based digital portal imaging can be categorized into three parts: **random or stochastic noise, fixed pattern noise**, and **artifactual noise**. **Random noise** comprises *quantum noise*, due to the counting statistics of the input X-ray flux, the conversion of X-rays to light quanta, and the formation of a signal in the video camera, *electronic noise* which arises in the camera and the rest of the electronics, and *quantization noise* which is due to rounding off and truncation errors in the A/D conversion and digital frame averaging. **Fixed pattern noise** is due to defects in the phosphor screen and non-uniformities in the camera target and the A/D converter. The **artifactual noise** arises due to combined effects of linac pulsation and conventional video scanning.

Artifactual noise and whether, and under what conditions, pulsation artifacts will affect the measurement of random noise are described in Chapter 3. The quantization noise is handled in Chapter 4, and the rest of the random noise is dealt with in Chapter 5. Chapter 6 deals with the fixed pattern noise. Chapter 7 covers the frequency spectra of the image noise variance which involve the determination of Noise Power Spectra (NPS).

Part III covers the quality control aspects of the VEPID system. **Part IV** contains the applications of the optimized portal imaging system. Chapter 9 demonstrates the on-line imaging of electron treatments, which is a very demanding static imaging application. Chapter 10 describes an application of real-time continuous imaging, where stability of an accelerator during first three seconds of operation is measured with the VEPID. Chapter 11 handles the quantitative portal imaging, where the ability of the

system for exit dosimetry is described. Finally, the conclusions are summarized in Chapter 12.

References

[1] L. E. Reinstein, H. I. Amols, P. J. Biggs et al. *Radiotherapy portal imaging quality (AAPM report No. 24),* (AAPM, New York, NY., 1987).

[2] R. T. Droege and B. E. Bjarngard, "Influence of metal screens on contrast in megavoltage X-ray imaging," Med. Phys. **6,** 487-493 (1979).

[3] H. I. Amols, L. E. Reinstein, and B. Lagueux, "A quantitative assesment of portal film contrast as a function of beam energy," Med. Phys. **13,** 711-716 (1986).

[4] A. G. Haus, S. M. Pinsky, and J. E. Marks, "A technique for imaging patient treatment area during a therapeutic radiation exposure," Radiology **97,** 653-656 (1970).

[5] M. M. Hammoudah and U. K. Henschke, "Supervoltage beam films," Int. J. Radiat. Oncol. Biol. Phys. **2,** 571-577 (1977).

[6] R. T. Droege and B. E. Bjarngard, "Metal screen-film detector MTF at megavoltage X-ray energies," Med. Phys. **6,** 515-518 (1979).

[7] E. B. Springer, L. Pape, F. Elsner, and M. L. Jacobs, "High-energy radiography (Cobalt 60 and Cesium 137) for tumor localization and treatment planning," Radiology **78,** 260-262 (1962).

[8] B. M. Galkin, R. K. Wu, and N. Sunthatalingam, "Improved technique for obtaining teletherapy portal radiographs with high-energy photons," Radiology **127,** 828-830 (1978).

[9] R. Sephton, M. Green, and C. Fitzpatrick, "A new system for port films," Int. J. Radiat. Oncol. Biol. Phys. **16,** 251-258 (1989).

[10] L. E. Reinstein and C. G. Orton, "Contrast enhancement of high-energy radiotherapy films," B. J. R. **52,** 880-887 (1979).

[11] J. Leong, "A digital image processing system for high energy X-ray portal images," Phys. Med. Biol. **29,** 1527-1535 (1984).

[12] S. Shalev, C. Cheng, and J. Arenson, "Port film enhancement by digital processing," SPIE **555,** 103-108 (1985).

[13] H. Meertens, "Digital processing of high-energy photon beam images," Med. Phys. **12,** 111-113 (1985).

[14] H. I. Amols and T. Lowinger, "An inexpensive Microcomputer based port film image enhancement system," Med. Phys.**14** 483(1987).

[15] V. Smith, "Routines for enhancement of radiation therapy images," The Use of Computers in Radiation Therapy 37-40 (1987).

[16] G. W. Sherouse, J. Rosenman, H. L. McMurray, S. M. Pizer, and E. L. Chaney, "Automatic digital contrast enhancement of radiotherapy films," Int. J. Radiat. Oncol. Biol. Phys. **13,** 801-806 (1987).

[17] I. Crooks and B. G. Fallone, "PC-Based selective histogram equalization for contrast enhancement of portal films," Med. Phys.**18** 618(1991).

[18] A. F. Holloway, "A localising device for a rotating cobalt therapy unit," B. J. R. **31,** 227 (1958).

[19] P. J. Biggs, M. Goitein, and M. D. Russell, "A diagnostic X-ray field verification device for a 10 MV linear accelerator," Int. J. Radiat. Oncol. Biol. Phys. **11,** 635-643 (1985).

[20] A. S. Shiu, K. R. Hogstrom, N. A. Janjan, R. S. Fields, and L. J. Peters, "Technique for verifying treatment fields using portal images with diagnostic quality," Int. J. Radiat. Oncol. Biol. Phys. **13,** 1589-1594 (1987).

[21] D. M. Galbraith, "Low energy imaging with high-energy bremsstrahung beams," Med. Phys. **16,** 734-746 (1989).

[22] E. R. Epp and H. D. Suit, "The need for on-line portal images of diagnostic X-ray quality from linear accelerators," Int. J. Radiat. Oncol. Biol. Phys. **30,** 495-496 (1994).

[23] J. N. Wolfe, L. Kalisher, and B. Considine, "Cobalt 60 treatment field verification by xeroradiography," Am. J. Roentgenol. **118,** 916-918 (1973).

[24] A. G. Fingerhut and P. M. Fountinelle, "Xeroradiography in a radiation therapy department," Cancer **34,** 78-82 (1974).

[25] R. M. Wilenzick, C. R. B. Merritt, and S. Balter, "Megavoltage portal films using computed radiographic imaging with photostimulable phosphors," Med. Phys. **14,** 389-392 (1987).

[26] D. Gur, M. Deutsch, C. R. Fuhrman, P. A. Clayton, J. C. Weiser, M. S. Rosenthal, and A. G. Bukovitz, "The use of storage phosphors for portal imaging in radiation therapy: Therapists' perception of image quality," Med. Phys. **16,** 132-136 (1989).

[27] H. Roehrig, W. Lutz, G. Barnea, G. D. Pond, and W. Dallas, "Use of computed radiography for portal imaging," SPIE **1231,** 492-497 (1990).

[28] G. Barnea, E. Navon, A. Ginzburg, J. Politch, H. Roehrig, C. E. Dick, and R. C. Placious, "Use of storage phosphor imaging plates in portal imaging and high-energy radiography: The intensifying effect of metallic screens on sensitivity," Med. Phys. **18,** 432-438 (1991).

[29] R. J. Scheck, T. Wendt, and M. Panzer, "Digital storage phosphor radiography for treatment verification in radiotherapy," B. J. R. **66,** 801-806 (1993).

[30] A. L. Boyer, L. Antonuk, A. Fenster, M. van Herk, H. Meertens, P. Munro, L. Reinstein, and J. Wong, "A review of electronic portal imaging devices (EPIDs)," Med. Phys. **19,** 1-16 (1992).

[31] K. S. Lam, M. Partowmah, and W. C. Lam, "An on-line electronic portal imaging system for external beam radiotherapy," B. J. R. **59,** 1007-1013 (1986).

[32] E. J. Morton, W. Swindell, D. G. Lewis, and P. M. Evans, "A linear array, scintillation crystal-photodiode detector for megavoltage imaging," Med. Phys. **18,** 681-691 (1991).

[33] L. Antonuk, J. Yorkston, J. Boudry, M. J. Longo, and R. A. Street, "Large area amorphous silicon photodiode arrays for radiotherapy and diagnostic imaging," Nucl. Instr. and Meth. **A310,** 460-464 (1991).

[34] L. E. Antonuk, J. Boudry, W. Huang, D. L. McShan, E. J. Morton, J. Yorkston, M. J. Longo, and R. A. Street, "Demonstration of megavoltage and diagnostic x-ray imaging with hydrogenated amorphous silicon arrays," Med. Phys. **19,** 1455-1466 (1992).

[35] H. Meertens, M. van Herk, and J. Weeda, "A liquid ionisation detector for digital radiography of therapeutic megavoltage photon beams," Phys. Med. Biol. **30,** 313-321 (1985).

[36] H. Meertens, M. van Herk, J. Bijhold, and H. Bartelink, "First clinical experience with a newly developed electronic portal imaging device," Int. J. Radiat. Oncol. Biol. Phys. **18,** 1173-1181 (1990).

[37] J. R. Andrews, R. W. Swain, and P. Rubin, "Continuous visual monitoring of 2 MeV. Roengen therapy," Am. J. Roentgenol. **79,** 74-78 (1958).

[38] N. A. Baily, R. A. Horn, and T. D. Kampp, "Fluoroscopic visualization of megavoltage therapeutic X ray beams," Int. J. Radiat. Oncol. Biol. Phys. **6,** 935-939 (1980).

[39] N. A. Baily and B. E. Keller, "The response of fluoroscopic image intensifier-TV systems," Invest. Radiol **11,** 335-337 (1976).

[40] N. A. Baily, "Video techniques for X-ray imaging and data extraction from roentgenographic and fluoroscopic presentations," Med. Phys. **7,** 472-491 (1980).

[41] J. Leong, "Use of digital fluoroscopy as an on-line verification device in radiation therapy," Phys. Med. Biol. **31,** 985-992 (1986).

[42] P. Munro, J. A. Rowlinson, and A. Fenster, "A digital fluoroscopic imaging device for radiotherapy localization," Int. J. Radiat. Oncol. Biol. Phys. **18,** 641-649 (1990).

[43] P. Munro and J. A. Rawlinson, "Therapy imaging: A signal-to-noise analysis of a fluoroscopic imaging system for radiotherapy localization," Med. Phys. **17,** 763-772 (1990).

[44] A. G. Visser, H. Huizenga, V. G. M. Althof, and B. N. Swanenburg, "Performance of a prototype fluoroscopic radiotherapy imaging system," Int. J. Radiat. Oncol. Biol. Phys. **18,** 43-50 (1990).

[45] H. Huizenga, V. G. M. Althof, A. G. Visser, and B. N. Swanenburg, "Ultimate achievable contrast to noise ratio of a CCD-camera based fluoroscopic radiotherapy imaging system (SRI-100)," Med. Phys.**19** 839(1992).

[46] J. W. Wong, W. R. Binns, A. Y. Cheng, L. Y. Geer, J. W. Epstein, J. Klarmann, and J. A. Purdy, "On-line radiotherapy imaging with an array of fiber-optic image reducers," Int. J. Radiat. Oncol. Biol. Phys. **18,** 1477-1488 (1990).

[47] J. Wong, A. Y. Cheng, W. R. Binns, J. W. Epstein, J. Klarmann, and C. A. Perez, "Development of a second-generation fiber-optic on-line image verification system," Int. J. Radiat. Oncol. Biol. Phys. **26,** 311-320 (1993).

[48] J. W. Wong, C. X. Yu, D. Yan, and A. Mazur, "On-line double-exposure small field verification," Med. Phys.**20** 871(1993).

[49] S. Shalev, T. Lee, K. Leszczynski, S. Cosby, T. Chu, L. Reinstein, and A. Meek, "Video techniques for on-line portal imaging," Comp. Med. Imag. Graph. **13,** 217-226 (1989).

[50] K. Leszczynski, *Digital imaging techniques for radiotherapy treatment verification,* (Ph.D. Thesis, University of Manitoba, Winnipeg, Manitoba, 1991).

[51] B. Wowk, *Phosphor screens for on-line portal imaging,* (M.Sc. Thesis, University of Manitoba, Winnipeg, Manitoba, 1993).

Chapter 3

Artifactual noise

3.1 Introduction

In most cases electronic portal imaging devices (EPIDs) are mounted on linear accelerators, which produce short pulses of x-radiation with a repetition rate in the range 50 to 300 pps. Under certain circumstances an aliasing situation may exist between the bursts of radiation and the read-out cycle of the detector, with the result that pulsation artifacts are introduced into the digitized portal image which may reduce their clinical efficacy, or may interfere with accurate measurements of the signal level and its noise characteristics. Such pulsation artifacts will not occur if the radiation source is not pulsed, such as with a cobalt therapy unit, or if the detector signal is extracted in a manner totally uncoupled from the radiation pulsation frequency. However, several types of EPIDs do exhibit pulsation artifacts, and therefore their nature is investigated in this chapter for the case of video-based electronic portal imaging systems (VEPIDs).

In order to facilitate the evaluation of artifacts, pulse repetition rates were deliberately chosen to give rise to a single artifact in an image, and the nature and the amplitude of the artifacts for different types of video camera with dissimilar signal read-out techniques were compared. Comparative measurements were also made between a linear accelerator and a cobalt therapy unit. The goal was to define the nature of the pulsation artifacts and to investigate under which conditions they can be reduced or eliminated. While it is shown that pulsation artifacts can be significantly reduced by frame averaging, this is not always an option in clinical radiation therapy, since it increases the image acquisition time. In many cases short exposures are required to investigate patient or organ movement, or to improve image quality by reducing their blurring effect. Short acquisition times are also necessary for intra-treatment verification,

as well as for the verification of dynamic collimators, rotational treatments, and dynamic beam modulation techniques such as tomotherapy[1]. Where frame averaging is not appropriate, pulsation artifacts can be eliminated by using on-target integration in the video camera combined with suitable signal extraction. It is hoped that the analysis of this approach will encourage the development of VEPIDs which do not exhibit pulsation artifacts.

3.2 Video imaging of pulsed sources

Pulsation artifacts arise from the combined effects of linear accelerator pulsation and video camera read-out technique. A good understanding of video read-out techniques is necessary to understand these effects, and in the following brief description the discussion is restricted to RS-170 (continuous, real-time) standard video cameras[2]. A detailed description of standard video scanning is given by Harshbarger[3].

Conventional vacuum tube based video cameras operate by sequentially scanning the camera target with a narrow electron beam, one pixel at a time. Two read-out modes are used in vacuum tube cameras: progressive read-out mode and interlaced read-out mode. Each pixel in the target integrates the image for 33.3 ms (frame time), which is the time interval between two read-outs. This is due to the fact that integration is tied to the read-out. However, in the case of progressive scanning, pixels are read out sequentially, and therefore the integration periods of different pixels do not overlap in time. This is shown in Fig. 3-1 for four neighboring pixels. Furthermore, in the case of interlaced scanning, odd and even fields are read out one after the other. Therefore integration periods of two adjacent pixels in the vertical direction are displaced in time by 16.6 ms (field time) which corresponds to half the integration period. This displacement in integration periods between pixels is a major drawback in vacuum tube video cameras, when continuous imaging of rapid events is required.

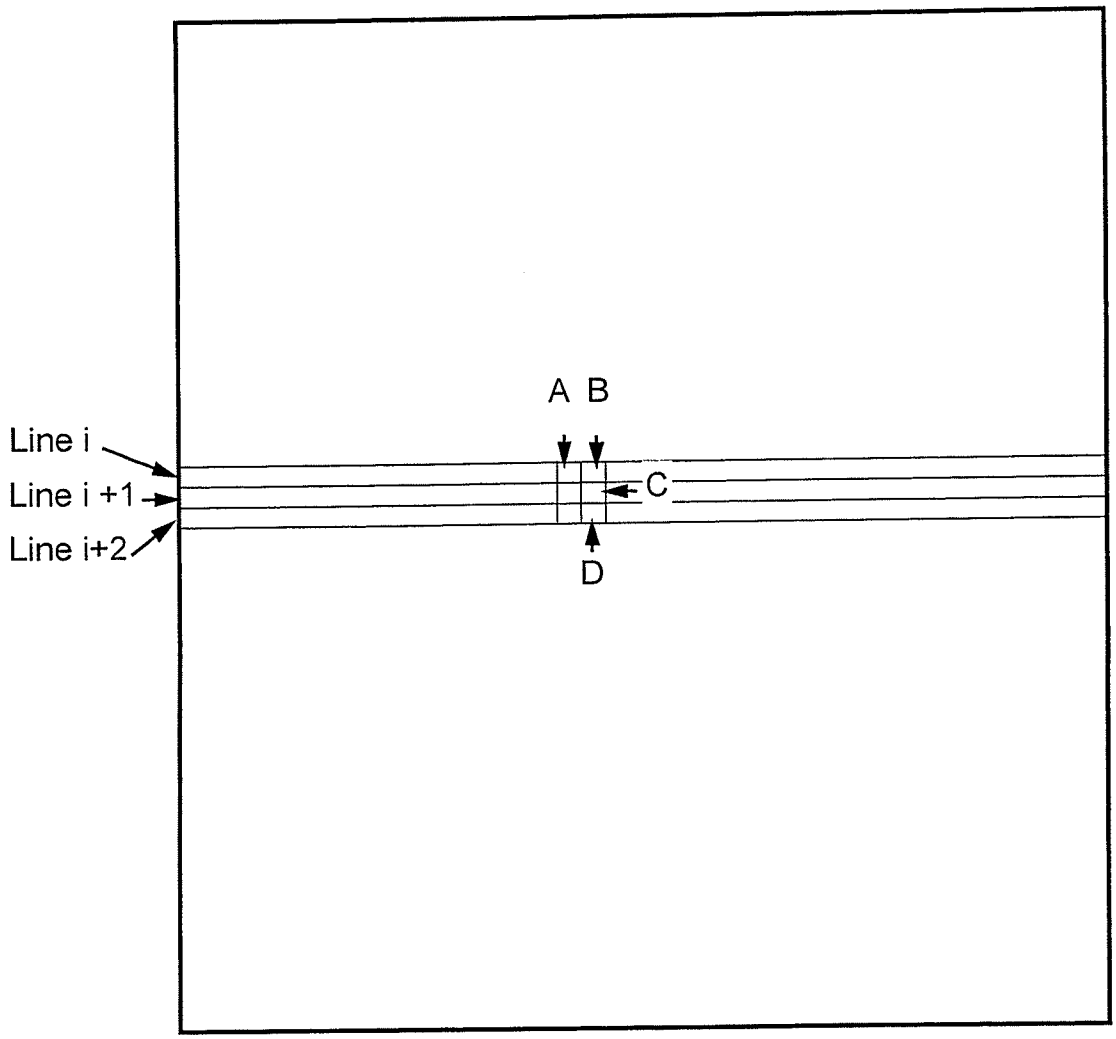

Figure 3-1. a) Spatial arrangement of four pixels in a camera target.

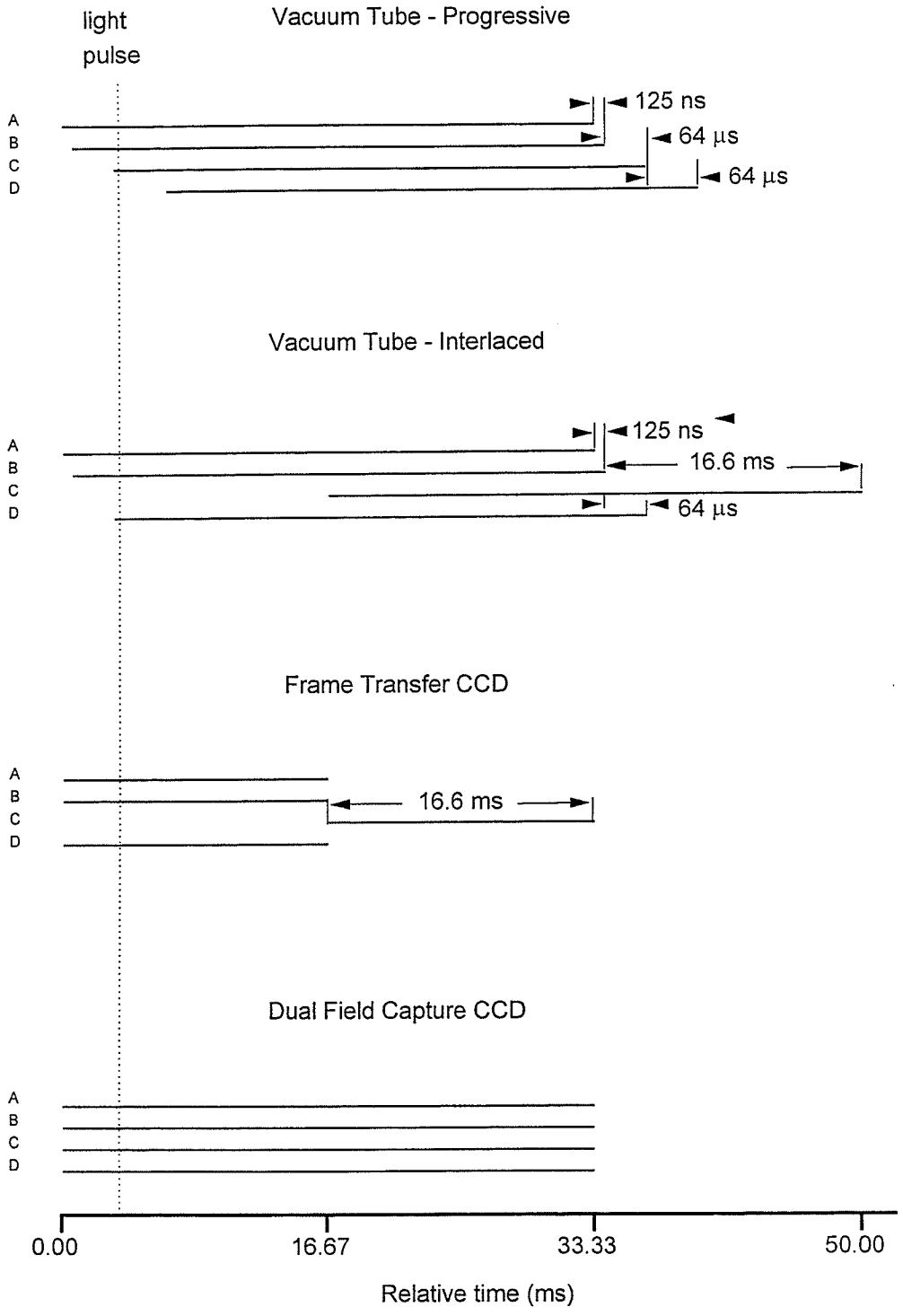

Figure 3-1 b. Temporal arrangement of the image integration times of the pixels shown in Fig. 3-1 a for four different types of cameras. Simultaneous image capture by all the pixels is performed only by the dual field capture CCD camera.

Solid state CCD cameras, on the other hand, use somewhat different read-out methods. An important difference between CCD and vacuum tube cameras is that image acquisition is not coupled to signal read-out in CCD cameras. An image is formed on the CCD target by generating electron-hole pairs, which are trapped in an array of potential wells created by applying potentials to on-chip electrodes. The trapped electrons are then transferred to an on-chip amplifier in a controlled fashion by changing the potentials applied to each electrode, and read out sequentially. Three types of CCD read-out architectures are in use[4]: full frame CCD, frame transfer CCD, and interline transfer CCD. A discussion of the differences in resolution between CCD and vacuum tube cameras due to the differences in the read-out techniques is given by Gurley and Haslett[5].

Most of the commercially available CCD cameras operating in the RS-170 standard use either interline or frame transfer architecture. As far as the pixel integration period is concerned, both of these read-out architectures are identical. Every pixel in a single field integrates the image simultaneously in 1/60 s, and hence the integration periods of every pixel in a single field completely overlap in time. All the pixels in the other field also integrate the image simultaneously but exactly 1/60 s later. The integration period of one field, therefore, does not overlap in time with the integration period of the other; the two fields contain completely independent information as far as temporal sampling is concerned.

A new generation CCD chip (TC 217*), which is a modified frame transfer CCD, has recently been introduced. This device is similar to a frame transfer CCD, but it has two separately addressable storage regions for storing odd and even fields. In one mode of operation of this device, called dual field capture mode, a complete frame is integrated on the image area during a frame time of 33.3 ms. Then the whole frame is transferred quickly to the storage region from which each field is read-out sequentially to generate a true interlaced video signal, or the two fields are read out together as a single frame to

* Texas Instruments Inc. Dallas, Texas.

generate a progressive video signal. During the reading of the stored frame the image area continues to integrate the next video frame. The operation of this CCD is similar to that of a full frame CCD, but the charge transfer to the storage region is very fast so that shuttering is not required.

Figure 3-1 shows schematically the comparison between the integration periods for four adjacent pixels for the four types of cameras. Figure 3-1a shows the spatial arrangement of the four pixels in the camera target and Fig. 3-1b shows the temporal relationships between the integration periods. It can be seen that simultaneous data capture by all the pixels is performed only by the dual field capture CCD camera.

If a strobed light source with a narrow pulse width (<1 ms) and a frequency comparable to the video scanning frequency is imaged with a vacuum tube camera in non-interlaced mode, only a part (upper or lower) of the image will contain the information due to the pulse. For example, if a narrow pulse of light is incident on the camera target at the time shown by the dashed line in Fig. 3-1b, pixels A, B, and C will capture the pulse, but not the pixel D. All the pixels to the top and to the left of pixel C will also capture the pulse, but all the pixels to the right and below pixel D will not capture the pulse. This is due to the temporal shift in the integration period of each pixel, and leads to a horizontal **banding artifact** in single frame images. Even though the imaged object is illuminated uniformly with each pulse, the resultant image will contain the banding artifact. The artifact arises purely due to conventional video scanning. Moreover, if interlaced scanning is used, even and odd fields may contain different levels of signal as the integration periods of adjacent lines are separated in time by half the integration period. This is illustrated also in Fig 3-1b, for the three vertically adjacent pixels B, C, and D. Pixel C does not capture the pulse but the pixels B and D do so. This introduces an **interlace artifact** in real time video images, which will be severe in the regions where the difference in the two fields is greatest. This interlace artifact has been

observed in real-time digital radiography as well[6]. These artifacts will be referred to as **pulsation artifacts**

If a strobed source is imaged with an interline or frame transfer CCD camera operating in real-time, only the interlace artifact will appear when the strobe frequency is comparable to the video frequency. Moreover, the artifact will be severe when the strobe frequency is about 30 Hz since only one field captures the strobe light, as shown in Fig 3-1b. The result will be a frame consisting of a bright field interlaced with a dark field. Both the dual field capture CCD and the full frame CCD are inherently insensitive to both the banding artifact and the interline artifact because every pixel in the whole frame integrates the image simultaneously. However, a shutter must be used to stop light falling on a full frame CCD during the read-out which make it unsuitable for continuous real-time imaging. Therefore video cameras based on the dual field capture CCD are the only ones capable of continuously operating in real-time without generating pulsation artifacts.

Linear accelerators used in radiotherapy produce bursts of X-rays lasting about 250 μs at a rate between 30 - 200 Hz. Since these frequencies are comparable to the video frequency, real time portal imaging with linear accelerators will be sensitive to these artifacts to an extent dependent on the video camera used. The dose rate delivered by some accelerators, particularly the one used in this study, is monitored and adjusted to the specified value during treatment by changing the pulsation frequency. Consequently the beam pulsation frequency does not remain constant during the operation, and is dependent on the beam energy and dose rate mode. These variations in the pulsation frequency lead to an instability of the dose rate as seen by the video camera. Table 3-1 shows the measured average pulsation frequencies of the KD-2* linear accelerator used in this study.

* Siemens Medical Systems Inc. Concord, California.

3.3 Materials and method

3.3.1 Materials

The prototype portal imaging system used in this study has a metal/phosphor screen consisting of a 500 mg/cm^2 Gd_2O_2S:Tb (P-43) phosphor layer on a 2.25 mm copper plate which was placed at a source-detector distance of 140 cm for all the measurements. Optical coupling between the metal phosphor screen and the video camera was achieved with a F/0.85, 25 mm c-mount lens and a 45° front coated glass mirror. Four types of video cameras were investigated: a SIT (Silicon Intensified Target), a Newvicon, a frame transfer CCD, and a dual field capture (DF) CCD camera. Two different systems were used for image acquisition: a PC- 386 equipped with an ITI series 150 image processor**, and a PC- 486 equipped with a Coreco Oculus 500 (OC500)*** processing board.

Dose rate	Energy			
	6 MV		23 MV	
High	195 Hz	(200 cGy/min)	140 Hz	(300 cGy/min)
Low	55 Hz	(50 cGy/min)	30 Hz	(50 cGy/min)

Table 3-1. Pulsation frequencies of the Siemens KD-2 linear accelerator for different modes of operation.

The ITI-150 system digitizes RS-170 video into 512x480 pixels using an 8-bit analog-to-digital (A/D) converter. It has a 16-bit Arithmetic Logic Unit (ALU) capable of summing up to 256 8-bit images in real time into a 16 bit frame buffer. The OC500

** Imaging Technology Inc. Bedford, Massachusetts.
*** Coreco Inc. Quebec, Canada.

system uses a 10-bit A/D converter which digitizes the RS-170 video signal into 640x480 array (square pixels). ITI-150 system was used with SIT, Newvicon, and frame transfer CCD camera, whereas the OC500 system was used with the DF CCD camera. All the results obtained with the OC500 system were normalized to 8-bit so that comparisons between the systems could be made.

A KD-2 linear accelerator operated in the 23 MV X-ray mode at a dose rate of 300 cGy/min and a 15 cm water phantom were used for this study unless otherwise specified. A 20x20 cm^2 field size was used in all cases.

CCD sensors are subject to radiation damage, and should be shielded from the direct treatment field[7]. They are also sensitive to incident X-rays, and image noise due to this effect has been noted previously[8]. The DF CCD camera was found to be especially sensitive to X-ray noise, even when it is located well outside of the field. When the beam is on, the image rapidly fills with single- or few-pixel spurious events, and on occasion distinct tracks are seen due to high energy electrons traveling through the CCD chip. It was found that shielding the camera with 5 cm lead reduced scattered radiation from the collimator, and resulted in a considerably lower spurious event rate.

It has been shown that video cameras and frame grabbers require a long warm-up time to stabilize reference voltages after being switched on[9]. During this warm-up period the video black level changes, resulting in higher temporal noise in real time video imaging. Therefore the measurements taken with the prototype system described in this work were made after 5 hour warm-up period.

3.3.2 Pulsation artifacts

Figure 3-2 shows a single frame open field image acquired with a SIT camera using a KD-2 linac operated in the 23 MV X-ray mode at a dose rate of 50 cGy/min. This low dose rate was selected to obtain a pulsation rate of about 30 Hz, producing a single radiation pulse for each video frame. The horizontal banding artifact due to the pulsation

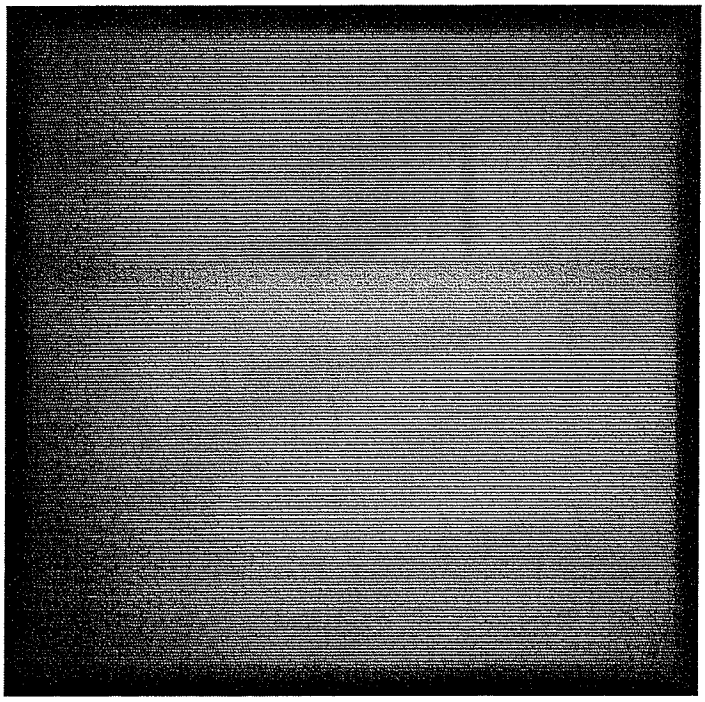

Figure 3-2. An open field portal image acquired with a SIT camera using a KD-2 linac operated in the 23 MV X-ray mode at a dose rate of 50 cGy/min. The horizontal banding artifact and the interline artifact due to linac pulsation are clearly visible in this image.

is clearly visible in this image. The vertical intensity profiles I(y) at the center of the image for individual fields are shown in Fig. 3-3a and for the full field in Fig. 3-3b. It can be seen that a burst of light due to the radiation pulse was incident on the camera when the electron beam had scanned about one third of field 1 so that the pixel intensity is higher in the lower part of the image. The intensity of the pixels that were read out at a later time is higher due to the higher charge accumulated in these lower pixels. The severity of the interlace artifact (zig-zag variation of the intensity along vertical direction) can be seen in Fig. 3-3b.

An intensity profile of a single field from an image obtained by averaging 256 frames is also shown in Fig. 3-3a for comparison, and the interlace artifact is seen to be considerably reduced. It is also interesting to note the severity of the non-uniform response of the SIT camera across the target. Fig. 3-3a also shows that the intensity of field 2 has dropped in the lower part of the field. This was believed to be due to the readout of one field discharging some of the charge from the other field. It was also found that the SIT camera has other irregularities in readout, for example, charge decay in the target before the readout. This makes the SIT camera unsuitable for quantitative imaging.

Figure 3-4 shows similar results for open field images acquired with a Newvicon camera. The banding artifact and the interlace artifact can be seen in this case also, but the effects are much smaller than for the SIT camera. The explanation is probably due to the longer lag in the Newvicon camera at the low light level encountered in portal imaging. Note that the non-uniform response across the camera target is less severe in the Newvicon than in the SIT camera.

Vertical intensity profiles of an image obtained with a frame transfer CCD camera are shown in Fig. 3-5. As expected, the banding artifact is absent in this case. However, a severe interlace artifact can be seen in the intensity profile of the full frame as shown in Fig. 3-5b.

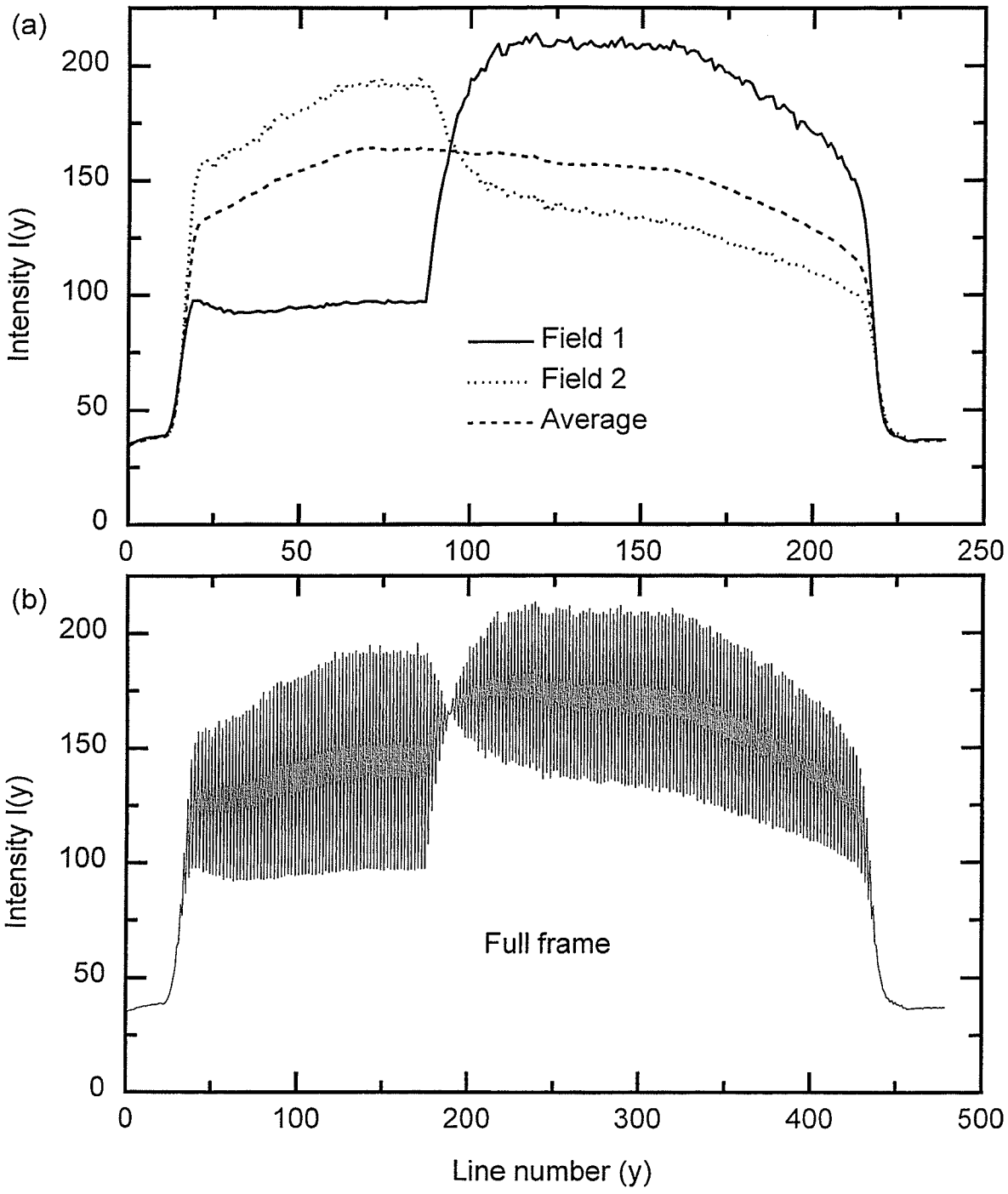

Figure 3-3. Vertical intensity profiles of the image shown in Fig. 3-2. a) Profiles of each field displayed separately and a single field profile obtained by averaging 256 frames. b) Profile of the complete frame. Line numbers are counted downwards from the top of the image.

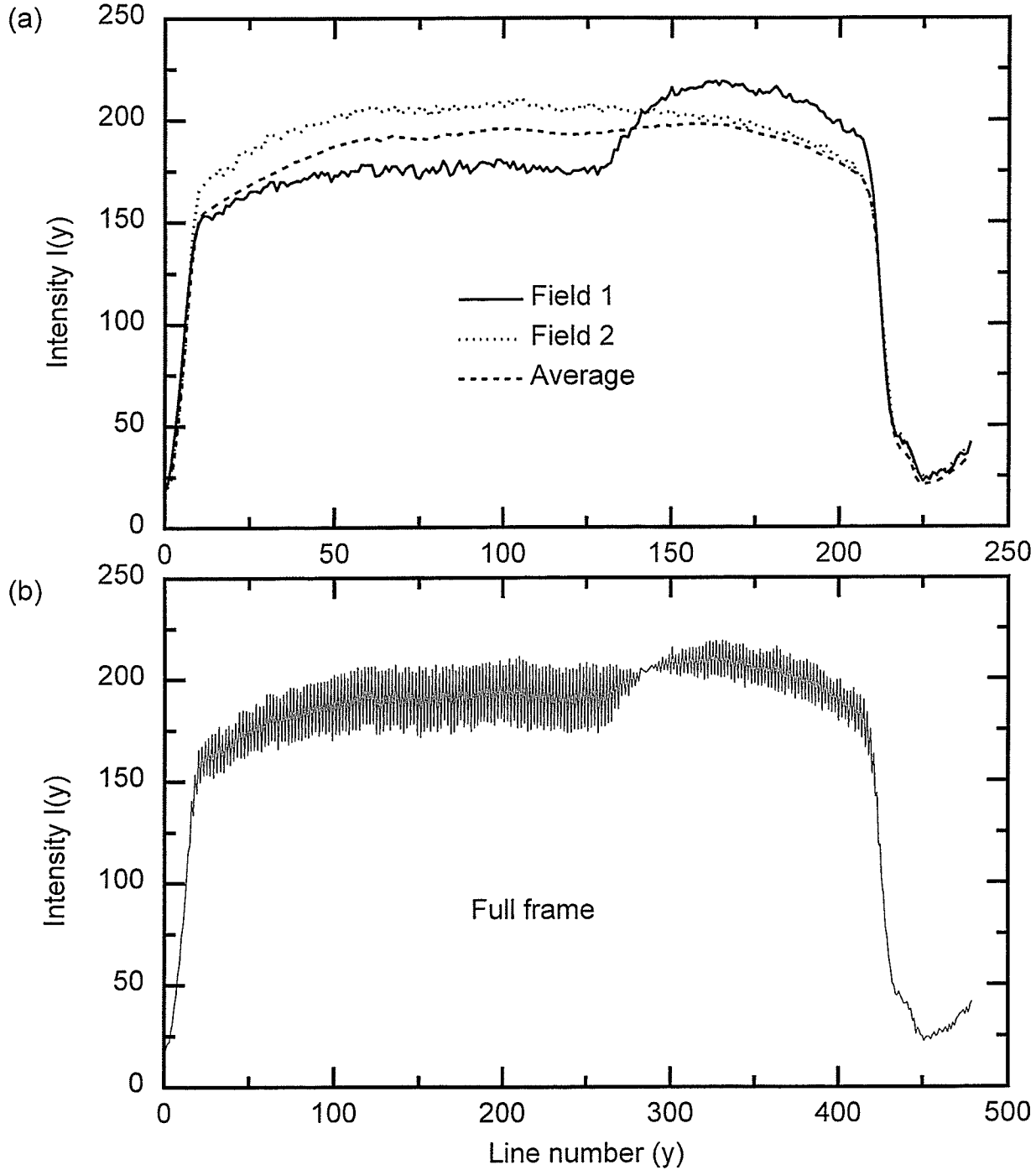

Figure 3-4. Vertical intensity profiles of a single frame image acquired with a Newvicon camera at the 50 cGy/min dose rate. a) Profiles of each field displayed separately and a single field profile obtained by averaging 256 frames. b) Profile of the complete frame.

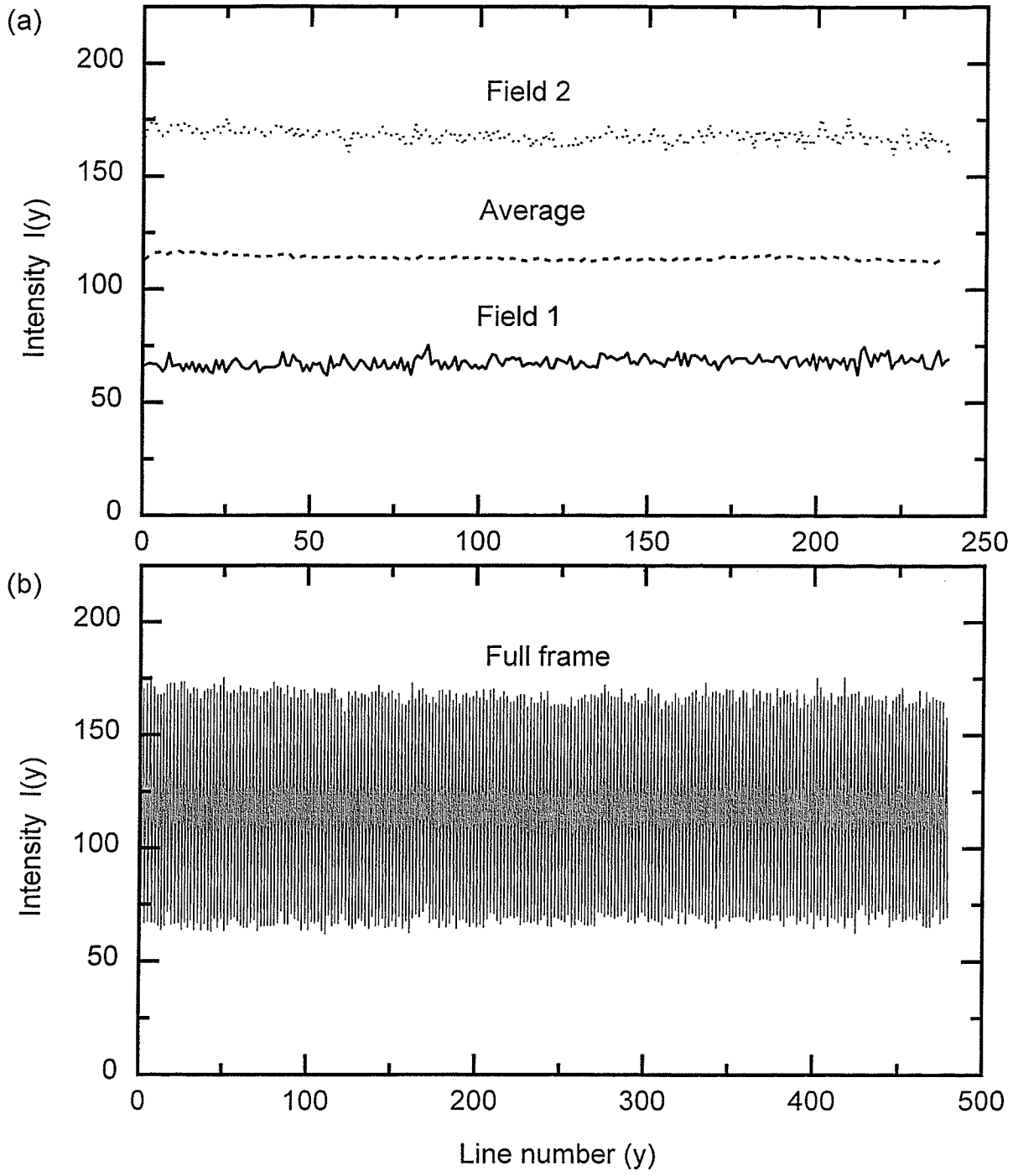

Figure 3-5. Vertical intensity profiles of an image acquired with a frame transfer CCD camera. a) Profiles of each field and a profile of an image averaged over 256 frames. b) Profile of the complete frame. The interline artifact which is uniform across the image is very large in this case but the banding artifact is absent.

Vertical intensity profiles of an image obtained with the dual field capture CCD camera are shown in Fig. 3-6. As expected, both artifacts are absent in this case. Note the relatively uniform camera response over the whole field. This result clearly indicates that this CCD camera is to be preferred over SIT and Newvicon cameras for quantitative portal imaging, due to the absence of pulsation artifacts and superior camera uniformity.

The previous tests were performed at a low dose rate in order to investigate the relationship between beam pulsation and camera readout, for which a single beam pulse per video frame is convenient. However, in clinical practice higher dose rates are used, and it is necessary to evaluate the noise due to pulsation artifacts under these conditions. Figure 3-7a shows the vertical intensity profile I(y) of a single frame image acquired with the SIT camera using the linac at 23 MV with the 300 cGy/min dose rate mode. The intensity profile $I_{512}(y)$ of a 512 frame averaged image is also shown. The corresponding normalized profile $I_c(y)$ for the full frame is shown in Fig. 3-7b. It is seen that four X-ray pulses have been incident on the camera during this particular frame, and pixel intensity changes up to 15% are present. Due to continuous changes in pulsation frequency of the KD-2 linac, pulsation artifacts will be randomly distributed in the consecutive video frames.

Figure 3-8 shows the histograms of the gray level values of the pixels comprising the normalized profiles $I_c(y)$ from a single frame, and 4- and 16-frame averaged images. The distribution for the single case has a bimodal shape with a long tail towards the upper end. When four or more frames are averaged, the distribution becomes a single mode distribution which resembles a Gaussian distribution. This implies that for images acquired by averaging more than four frames the noise due to the pulsation artifact will appear to be, and can be characterized as a random noise.

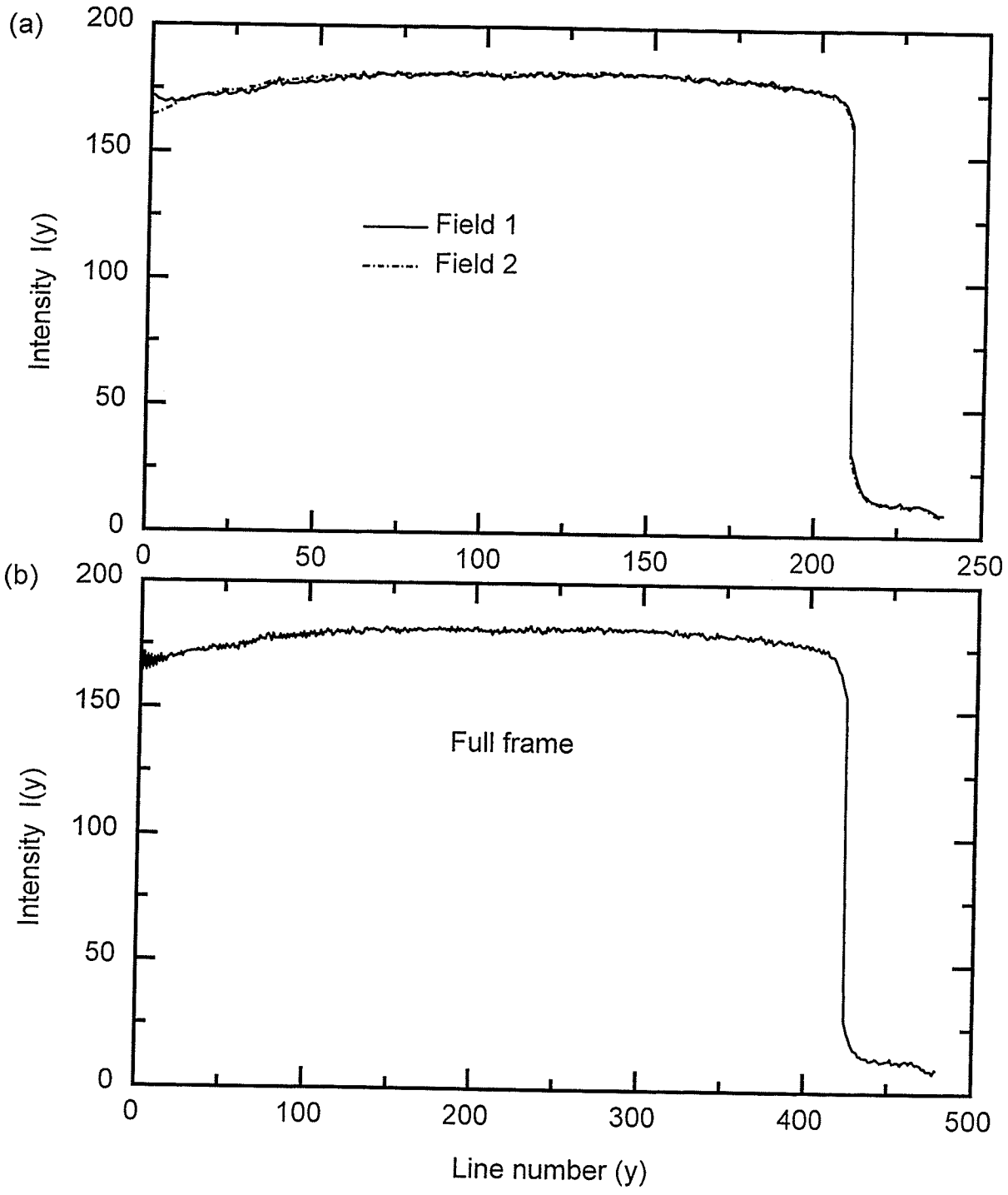

Figure 3-6. Vertical intensity profiles of an image acquired with a dual field capture CCD camera. a) Profiles of each field displayed separately. b) Profile of the complete frame. No pulsation artifacts are present.

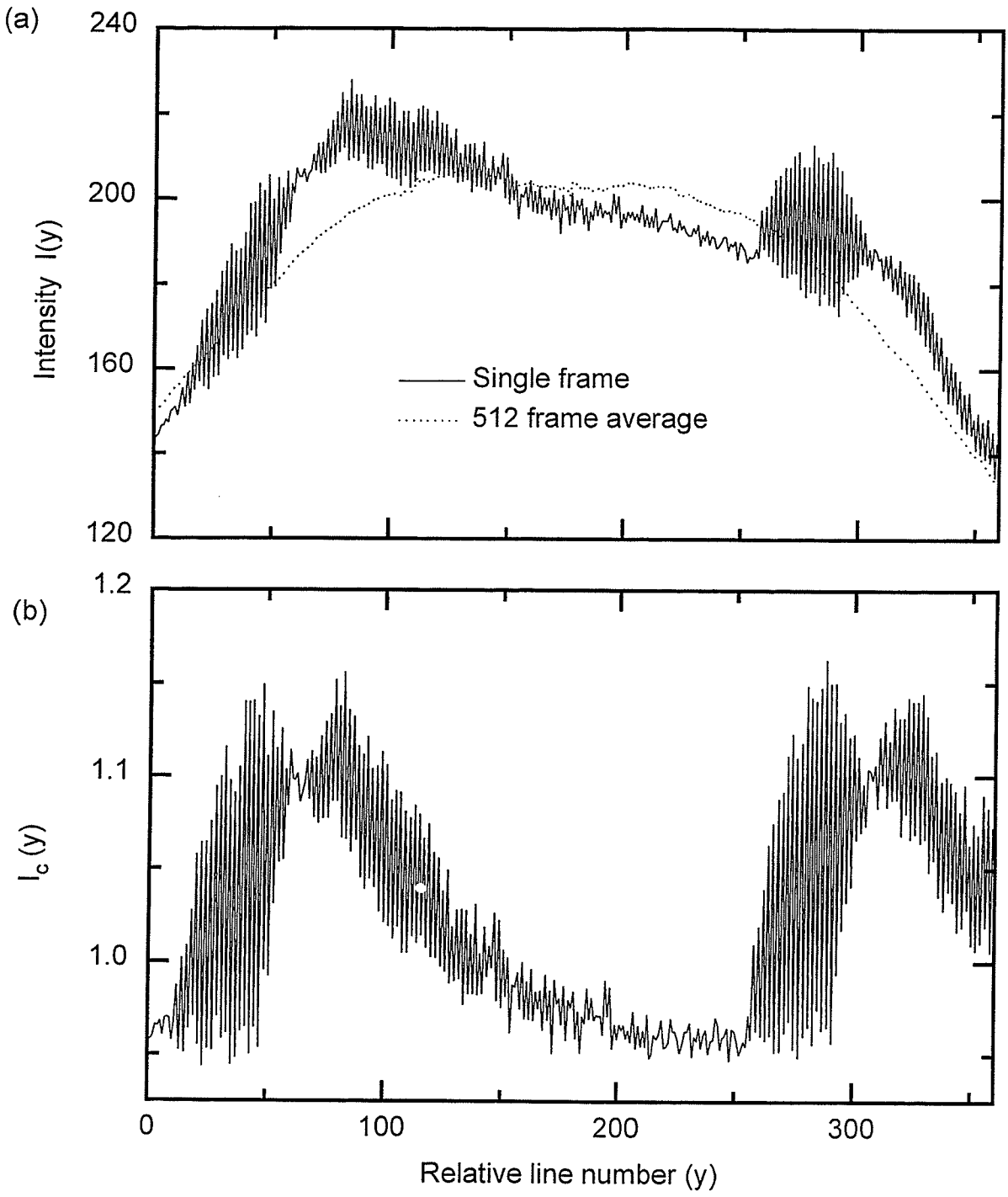

Figure 3-7. Vertical intensity profiles I(y) of a single frame open field image acquired at the dose rate of 300 cGy/min. a) Profiles of the complete frame and a profile of an image averaged over 512 frames. b) Normalized profile $I_c(y)$ obtained by dividing the single frame profile by frame averaged profile. Pixel intensity changes up to 15% are apparent.

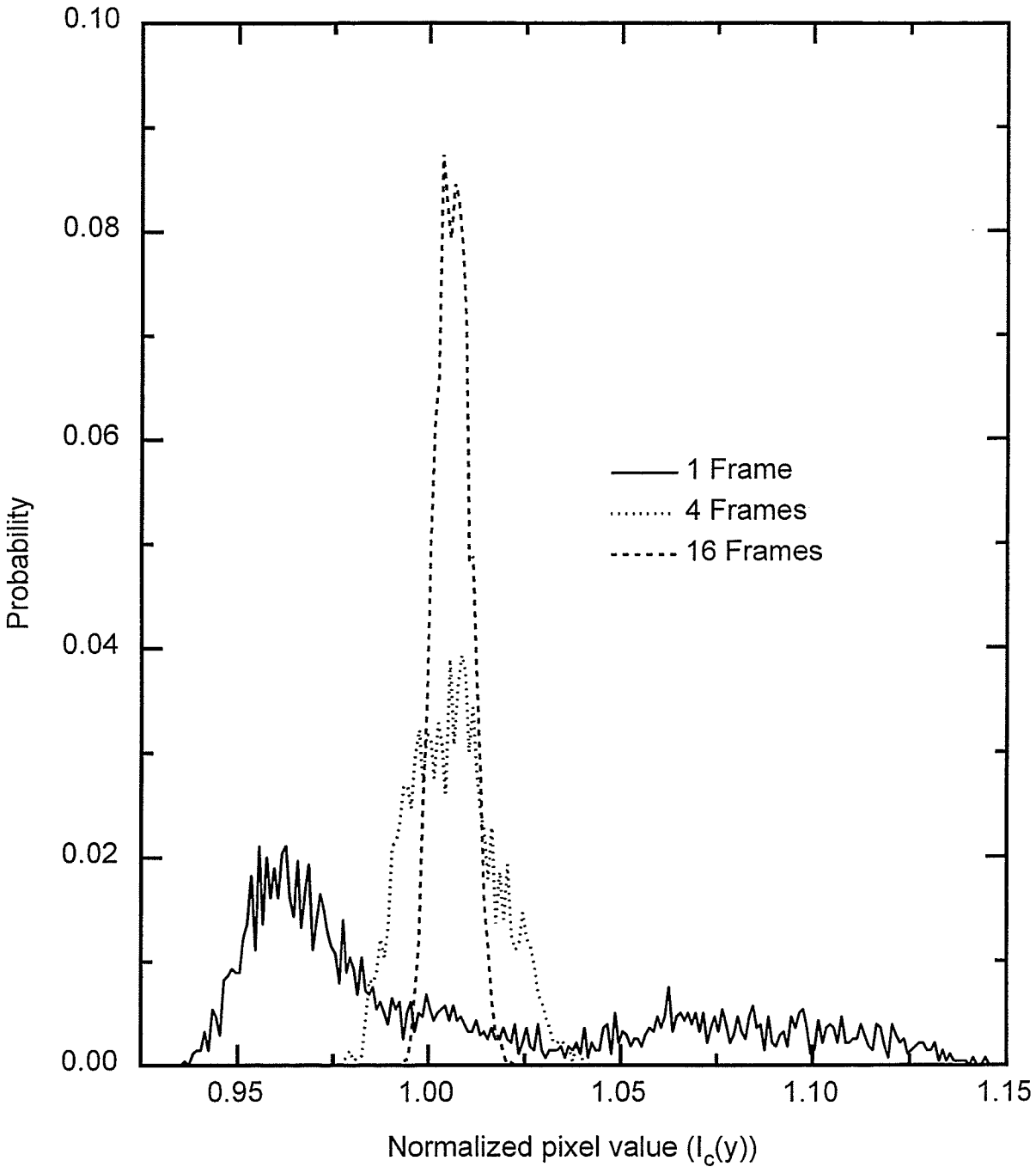

Figure 3-8. Probability distribution of the normalized intensity profiles $I_c(y)$ for a single frame image as well as 4- and 16 -frame averaged images obtained with a SIT camera at high dose rate.

3.3.3 Measurement of random noise

In characterizing the performance of a VEPID, it is useful to measure the various sources of random noise in the system, and compare their relative contributions to the overall signal to noise ratio (SNR). The design of the system, and the selection of operating parameters, can then be optimized to achieve maximal SNR. Pulsation artifacts are not random, but their presence will affect any noise measurements and give rise to incorrect predictions of SNR, as well as the inappropriate selection of operating parameters. Consequently an investigation was carried out to find whether, and under what conditions, pulsation artifacts will affect the measurement of random noise in the VEPID.

Random noise in real time video images can be characterized in either spatial or temporal terms. In the former case, the noise in a single pixel is estimated from the variance over a region of interest (ROI) containing many pixels. The ROI may be rectangular, giving the single-pixel noise variance estimate Σ_r^2, or it may be a section of the horizontal line running through the pixel in question, giving the estimate Σ_l^2. Alternatively, the noise variance in a single pixel can be determined from its gray-level variance over many sequential video frames, giving the noise variance estimate Σ_t^2. The spatial rectangle ROI approach and the temporal approach are shown diagramatically in Figs. 3-9a and 3-9b respectively. These three measures of noise differ in the way in which the video signal is sampled, and will give different results since each will be affected to a greater or lesser degree by the various types of noise present in the signal. A comparison of the values of Σ_l^2 (line ROI), Σ_r^2 (rectangular ROI), and Σ_t^2 (temporal measurement) provides an opportunity to identify and quantify the most significant noise sources in the imaging chain. Random noise from three sources (each of which is characterized by a variance σ^2) will contribute in a different way to the three measures of noise, Σ_l^2, Σ_r^2, and Σ_t^2. These are quantum noise (σ_D^2), electronic noise (σ_e^2), and noise due to instability of the incident photon beam or the black level (σ_s^2). Pulsation artifacts

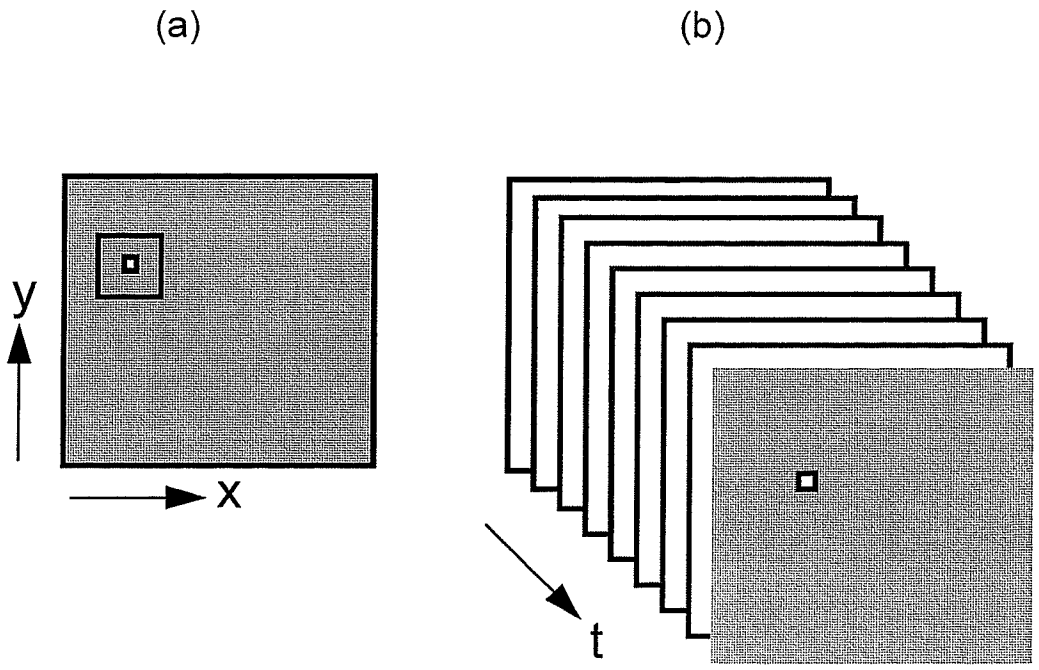

Figure 3-9. a) Measurement of spatial noise. b) Measurement of temporal noise.

affect the video signal by introducing variations in the vertical (y) scan direction, and their presence will contribute to the measured value of Σ_r but not to the value of Σ_l. This contribution will be considered as though it is a random effect, which was shown to be a reasonable approximation in section B above for the case of averaging at least four frames. Similarly, noise due to instabilities will contribute to Σ_t but not to the spatial noise measures Σ_l and Σ_r. These contributions are summarized in Table 3-2, from which the following relationship can be established:

$$\Sigma_r^2 = \Sigma_l^2 + \sigma_a^2 \qquad (3\text{-}1)$$

and

$$\Sigma_t^2 = \Sigma_r^2 + \sigma_s^2, \qquad (3\text{-}2)$$

when the contribution from pulsation artifacts and instabilities are considered to be random.

	Measure of noise		
Contribution	Σ_l	Σ_r	Σ_t
	Line ROI	Rectangle ROI	Temporal
Quantum (σ_D)	yes	yes	yes
Electronic (σ_e)	yes	yes	yes
Pulsation (σ_a)	no	yes	yes
Instability (σ_s)	no	no	yes

Table 3-2. Contributions from various sources to the noise measures Σ_l, Σ_r and Σ_t.

Spatial noise in a small ROI (either horizontal line or a rectangular) can be obtained by measuring the variance of the pixel intensity within the ROI, but it will include a contribution due to intensity gradients across the ROI. This effect can be

removed by subtracting a pair of identical images P_1 and P_2 and correcting for the increase in the variance due to subtraction. Let

$$\Delta(x,y,t) = P_1(x,y,t) - P_2(x,y,t)$$

where P(x,y,t) is a pixel value at spatial coordinates x, y and time (frame) t. Then the measured rms noise Σ_r^2 in a rectangular ROI can be defined as

$$\Sigma_r^2 = \frac{1}{2}\frac{\sum_{x=1}^{X_N}\sum_{y=1}^{Y_N}\Delta^2(x,y,t) - \frac{1}{X_N Y_N}\left[\sum_{x=1}^{X_N}\sum_{y=1}^{Y_N}\Delta(x,y,t)\right]^2}{X_N Y_N - 1} \qquad (3\text{-}3)$$

where X_N and Y_N are the dimensions (in pixels) of the ROI in the x and y directions. Similarly, the measured noise variance Σ_l^2 in a horizontal line ROI (Y_N =1) can be defined as

$$\Sigma_l^2 = \frac{1}{2}\frac{\sum_{x=1}^{X_N}\Delta^2(x,y,t) - \frac{1}{X_N}\left[\sum_{x=1}^{X_N}\Delta(x,y,t)\right]^2}{X_N - 1}. \qquad (3\text{-}4)$$

The measured temporal noise variance Σ_t^2 of a single pixel in a sequential series of identical images can be defined as

$$\Sigma_t^2 = \frac{\sum_{t=1}^{T_N}P^2(x,y,t) - \frac{1}{T_N}\left[\sum_{t=1}^{T_N}P(x,y,t)\right]^2}{T_N - 1}. \qquad (3\text{-}5)$$

where T_N is the total number of frames (images) used. These noise measures were determined for images that were acquired by averaging between 1 and 256 frames. The average of eight measurements was obtained in every case, and the standard deviation of the eight measurements was used for error bars.

It should be noted here that if any of these noise measures (say Σ_x) represent a Gaussian random noise, the measure for images obtained by averaging N frames will be

$$ {}_N\Sigma_x = \frac{\Sigma_x}{\sqrt{N}}. \qquad (3\text{-}6) $$

where frame averaging is performed without truncation[10].

3.3.4 Measurement of noise in the presence of pulsation artifacts

Open field images were acquired with a SIT camera using the KD-2 linac operated in the 23 MV mode at a dose rate of 300 cGy/min. Vertical intensity profiles I(y) from the middle of these images were extracted by averaging 20 pixels horizontally :

$$ I(y) = \frac{1}{20}\sum_{x=224}^{243} P(x,y,t), \qquad y = 61,.....420 \qquad (3\text{-}7) $$

An intensity profile $I_{512}(y)$ of a 512 frame average image at the same location is also used to correct for the image gradient:

$$ I_c(y) = \frac{I(y)}{I_{512}(y)} \qquad (3\text{-}8) $$

This was necessary to remove variations in the profile due to all factors except the pulsation artifacts. The standard deviation σ_α of $I_c(y)$ was taken as the contribution to the normalized rms noise due to the pulsation artifacts for a pixel value of one gray level. The effective contribution σ_a to the rms noise variance due to pulsation artifacts can then obtained by multiplying σ_α by the average pixel value for a particular situation.

3.4 Results and discussion

Spatial noise measures Σ_l and Σ_r were measured using a SIT camera with a 23 MV photon beam. For comparison, the same data were used to calculate the contribution to the measured noise due to the presence of pulsation artifacts. The results are shown in Fig. 3-10 as a function of N, the number of frames averaged when acquiring each image. Figure 3-10a shows that Σ_l decreases with N according to Eq. (3-6), and is well represented by a linear fit (on log-log axes) to a line with slope-0.5. While ${}_N\sigma_a$ is smaller than ${}_N\Sigma_l$ for $N \geq 4$, there is large increase in the measured value of the noise due to the presence of pulsation artifacts when less than four frames are averaged. This is expected

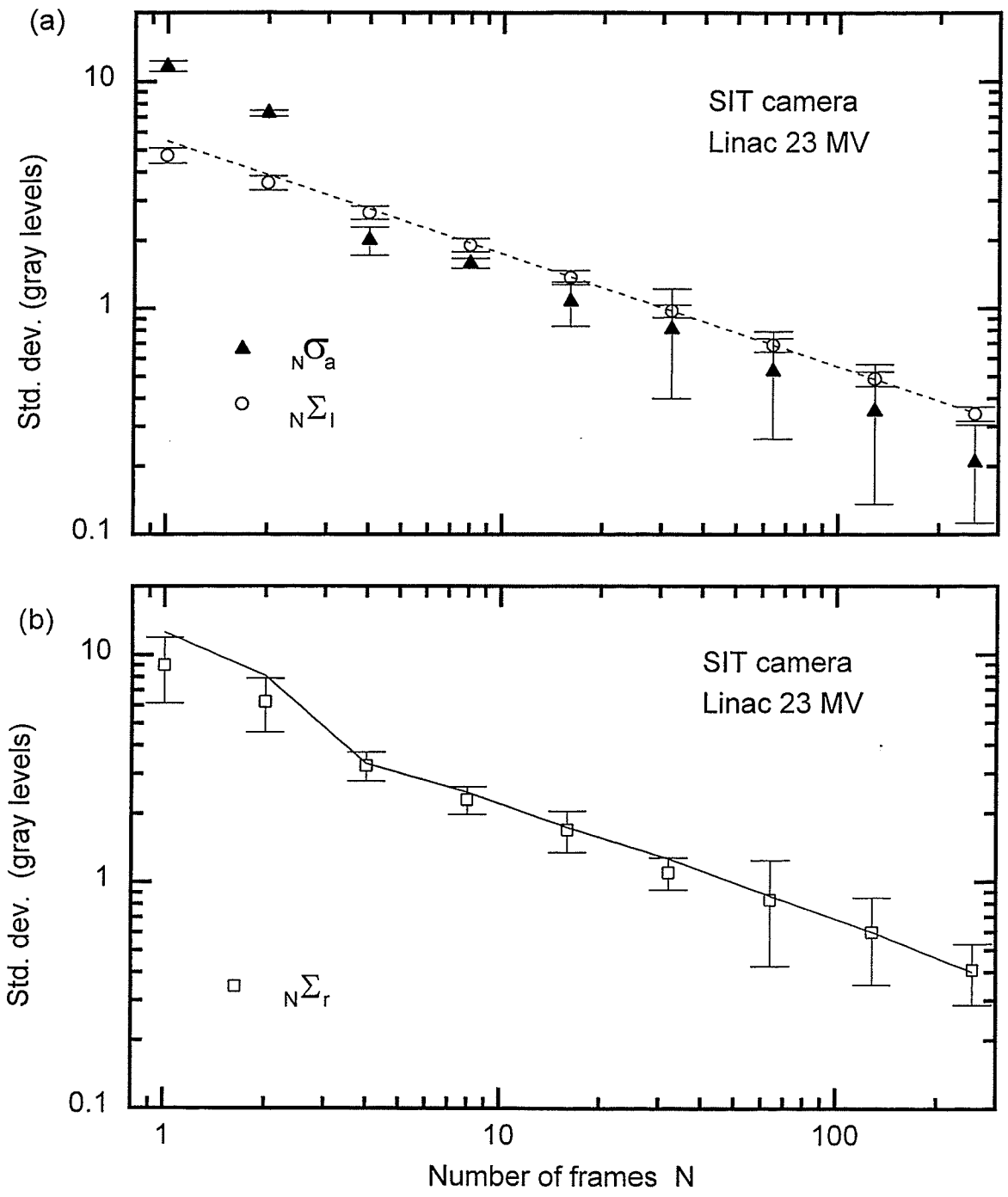

Figure 3-10. a) The effect of frame averaging on Σ_l and σ_a for the SIT camera. The line fitted to the Σ_l data has a slope of -0.5 according to the Eq. (3-6). b) The effect of frame averaging on Σ_r. The solid line is the sum of Σ_l and σ_a in quadrature.

since the distribution of pulsation artifact is not Gaussian when $N \leq 4$ as shown in Fig. 3-8. Figure 3-10b shows the comparison of Σ_r (data points) with the value obtained by adding Σ_l to σ_a in quadrature (solid line). These two results are almost identical for $N \geq 4$, indicating the validity of Eq. (3-1), and suggest that the contribution to the measured noise due to the presence of pulsation artifacts can be considered as a random noise for $N \geq 4$.

Figure 3-11 shows the change in the two spatial noise measures Σ_r and Σ_l as well as the temporal measure Σ_t when frames are averaged with a SIT camera using the linac at 23 MV with the 300 cGy/min dose rate mode. The straight line is a linear fit to the Σ_l data with a slope of -0.5 according to Eq. (3-6), and demonstrates that the Σ_l data behave as a pure random noise. The increased values of Σ_r are due to the pulsation artifacts. The temporal noise Σ_t is always higher than both spatial noise measures in this case since the linac output is not constant. The excursions in Σ_t larger than error bars are due to systematic changes in the linac output.

Figure 3-11b shows a similar comparison of the changes in Σ_r, Σ_l and Σ_t for the SIT camera when a ^{60}Co beam is used. A 20x20 cm field without a phantom was used for these measurements and the dose rate was 120 cGy/min. All three noise measures are identical in this case, since the output of the X-ray source is constant and therefore is statistically stationary over the time scale involved.

3.5 Conclusions

The nature of pulsation artifacts in certain types of video-based electronic portal imaging systems have been investigated. Two types of vacuum tube video cameras were evaluated (SIT and Newvicon), as well as two types of CCD camera (frame transfer and dual field capture). Pulsation artifacts were demonstrated at low radiation pulse rates, and it was shown that their relative magnitude decreased with increasing number of video frames averaged to form the final image. The dual field capture CCD camera does not

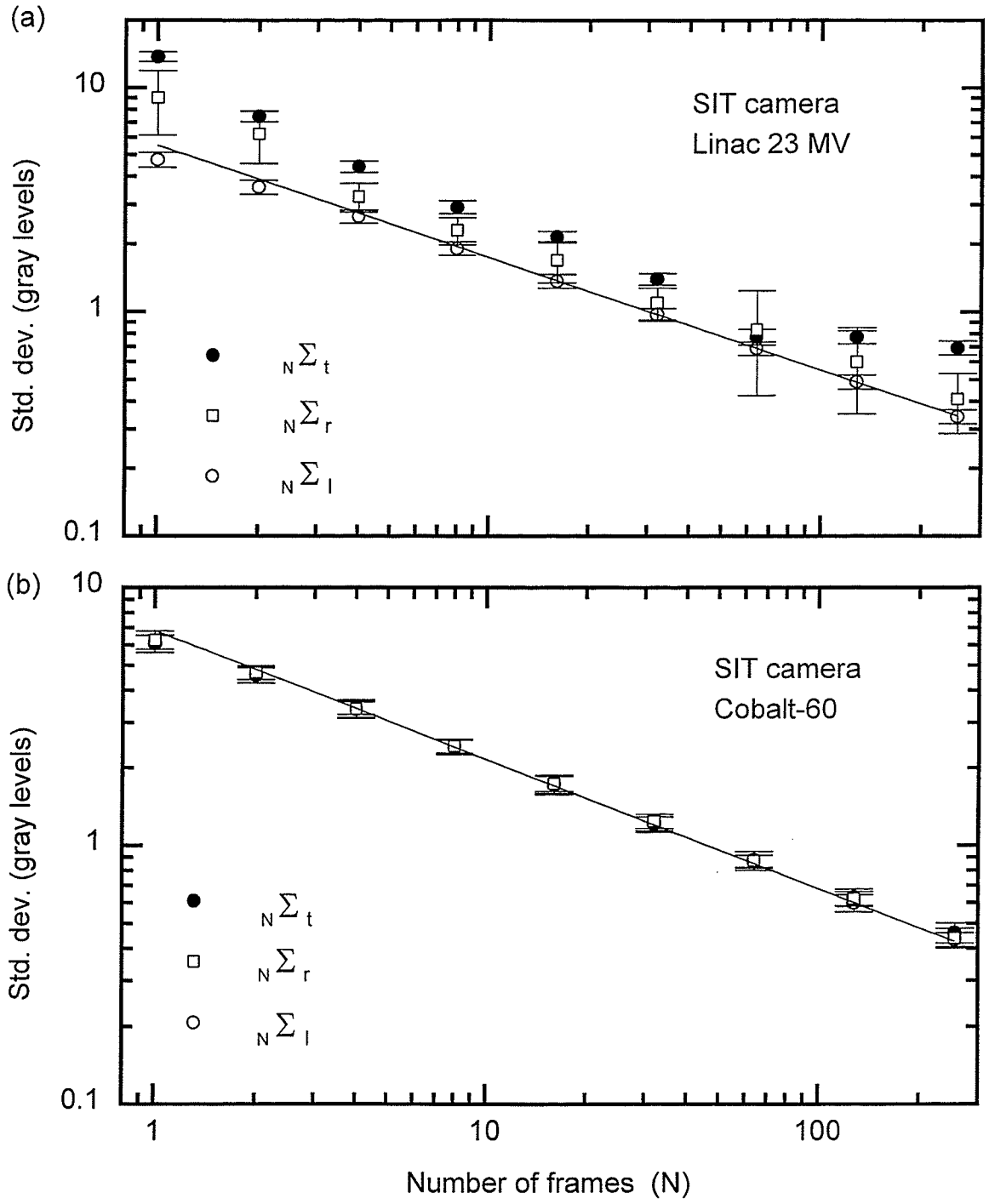

Figure 3-11. The effect of frame averaging on Σ_l, Σ_r and Σ_t for the SIT camera. a) Results for the linac images. b) Results for the ^{60}Co images.

exhibit pulsation artifacts due to the independence of signal acquisition and read-out, and therefore is the ideal camera for real-time portal imaging. A novel method was developed for the quantification of various contributions to the system noise, using noise measures based on line, area, and temporal signal acquisition. Measurements from a line give the level of quantum and electronic noise, while measurements from an area are higher due to the effect of pulsation artifacts. Temporal noise measurements give even higher values due to instabilities in the radiation source. Using a SIT camera and a pulsed linear accelerator at 300 cGy/min, it was found that the effect of pulsation artifacts can be expressed as a random contribution to the overall system noise for frame averaging with four or more frames. All noise measures were identical when a cobalt radiation source was used due to the absence of pulsation artifacts.

References

[1]T. R. Mackie, T. Holmes, S. Swerdloff, P. Reckwerdt, J. O. Deasy, J. Yang, B. Paliwal, and T. Kinsella, "Tomotherapy: A new concept for the delivery of dynamic conformal radiotherapy," Med. Phys. **20,** 1709-1719 (1993).

[2]D. G. Fink, "Television fundamentals and standards," in *Electronic engineers' handbook* (Second Edition), D. G. Fink ed. (McGraw-Hill, New York , 1982).

[3]J. H. Harshbarger, "Video standard and performance tests of video sytems," SPIE **84,** 72-78 (1994).

[4]C. H. Sequin and M. F. Tompsett, "Charge Transfer devices," Adv. Electron. Electron Phys., **Suppl. 8** Academic Press, New York (1975).

[5]T. M. Gurley and C. J. Haslett, "Resolution considerations in using CCD imagers in broadcast-quality cameras," SMPTE Journal **94** 882-895 (1985).

[6]J. A. Seibert, D. H. Barr, D. J. Borger, H. H. Hines, and H. G. Bogren, "Interlaced versus progressive readout of television cameras for digital radiographic acquisitions," Med. Phys. **11,** 703-707 (1984).

[7]R. Rajapakshe and S. Shalev, "Sources of Random Noise in real-time Portal Imaging," Med. Phys. **20** pp 870 (1993).

[8]J. Wong, A. Cheng, R. Binns, J. Epstein, J. Klarmann, and C. Perez, "Development of a second-generation fibre-optic on-line image verification system," Int. J. Radiation Oncology Biol. Phy. **26**, 311-320 (1993).

[9] R. Rajapakshe, T. J. Radcliffe, and S. Shalev, "Temporal and Spatial statistics of image noise in real time video imaging : A study on on-line portal imaging," SPIE **V 1896**, 62-72, (1993).

[10] R. Rajapakshe and S. Shalev, "Noise analysis in real-time portal imaging I : Quantization Noise," Med. Phys. **21**, 1263-1268 (1994).

Chapter 4

Quantization noise

4.1 Introduction

Random noise in real-time portal imaging comprises *quantum noise*, due to the counting statistics of the input X-ray flux, the conversion of X-rays to light quanta, and the formation of a signal in the video camera, *electronic noise* which arises in the camera and the rest of the electronics, and *quantization noise*. This chapter, the contents of which are published in parts elsewhere[1], is concerned with the effects of quantization noise.

Discrete representation of analog signals is necessary when digital transmission or processing is carried out on analog signals. Conversion of an analog signal to digital data occurs both in spatial coordinates (sampling) and in amplitude (quantization). Both of these processes can reduce the image quality as quantified by spatial resolution and noise, respectively. Coarse sampling degrades resolution directly and noise characteristics indirectly due to aliasing. Coarse amplitude quantization degrades the image by the addition of quantization noise.

All digital imaging systems use A/D converters which give integer output values obtained by rounding off real numbers. The quantization noise introduced by the A/D conversion is the amplitude quantization described widely in the literature[2-4]. However, there are other points in the imaging chain which involve some type of amplitude quantization. For example, real-time video based portal imaging systems perform video frame averaging in order to reduce the noise. It has been pointed out[4] that frame averaging should be carried out with a computing device having adequate precision in order to reduce the effect of the quantization noise of the input A/D. However, if the averaging is performed with integer arithmetic as in the case of frame buffer and

arithmetic logic unit (ALU) used in the prototype portal imaging system, information will be lost due to data truncation. This is an effective amplitude quantization which introduces quantization noise.

Consequently, there are two points in the portal imaging chain where quantization noise is introduced. The first is at the input A/D where the input video signal is quantized by rounding off input signal values. The contribution to the total noise from this process is usually negligible (two orders of magnitude lower) compared to the noise variance (~ 10 gray levels) in the analog video signal itself. The second point where quantization noise is added to the images is when frame averaging is performed using integer arithmetic, resulting in a truncation of real numbers to integers. In this chapter it is shown that the quantization noise due to truncation in digital frame averaging is more significant than the quantization noise due to round off errors in the input A/D.

4.2 Theoretical considerations

4.2.1 Quantization noise

Amplitude quantization is a non-linear transformation which maps the domain of continuous-amplitude inputs onto a finite number 2^n possible output values which are generally n-bit binary words (integers) where n is the number of bits used in the quantization process. These binary words are then used for digital transmission, processing and storage.

The simplest and most commonly used quantizer is the zero memory quantizer which determines the output value only from the corresponding analog input value. More complicated quantizers in which the output value also depends on other input values, such as block quantizers and sequential quantizers, are less commonly used. Zero-memory quantizers can have quantization steps which are either equal or unequal in size. Only the zero-memory uniform quantizer in which quantization steps are equal in size and denoted by Δ is considered here.

The amplitude quantization of a stationary, random, analog input signal x to the digital integer+ value **s**(x) can be treated as an additive noise operation[2,3]:

$$\mathbf{s}(x) = \gamma \cdot x + q \tag{4-1}$$

where γ is a constant and q, called the quantization error, is an additive noise which depends on the input signal. Quantization introduces an instrumental uncertainty which is stochastic in nature. If the input probability density distribution is assumed to be constant within a quantization bin Δ, it can be shown[2-4] that the mean square value σ_q of the quantization error q is

$$\sigma_q^2 = \frac{\Delta^2}{12} . \tag{4-2}$$

If the rms noise of the input analog signal is σ_x and the rms noise of the quantized output is σ_o, we have

$$\sigma_o^2 = \sigma_x^2 + \sigma_q^2 . \tag{4-3}$$

Barnes[4] has quoted the work of R. A. Sones which shows that the noise in the digitized signal in fact behaves as given by Eqs. (4-2) and (4-3) to a high degree of precision when $\Delta \leq 1.66\sigma_x$ irrespective of the signal value.

4.2.2 The effect of frame averaging

It has been claimed[6] that for a n-bit A/D where the bin with is equal to the rms noise in the analog signal, "the very best SNR of any system will be $\sqrt{12} \times 2^n$ irrespective of frame averaging". This corresponds to 886.8 for a 8-bit A/D. In the following

+ Variables which have integer values after digitization are written in **bold** type.

sections it is demonstrated by theoretical reasoning and experimental measurement that this statement is not true.

Consider the digitization of an analog signal x having a Gaussian rms noise σ_x with an 8-bit A/D converter such that $\Delta = 1.66\sigma_x$. Averaging N such signals using floating point arithmetic will yield a final signal S_{ave} with rms noise σ_{ave}:

$$S_{ave} = \frac{1}{N}\sum_{j=1}^{N} s(x_j) \tag{4-4}$$

$$\sigma_{ave} = \frac{1}{\sqrt{N}}\sigma_o = \frac{1}{\sqrt{N}}\sqrt{\sigma_x^2 + \sigma_q^2} \tag{4-5}$$

and the signal-to-noise ratio SNR is given by

$$SNR_{ave} = \frac{S_{ave}}{\sigma_{ave}} = \frac{\sum_{j=1}^{N} s(x_j)}{\sqrt{N(\sigma_x^2 + \sigma_q^2)}} . \tag{4-6}$$

Note that the signal is averaged after the input A/D conversion. Considering the example $\Delta = 1$ and $N = 256$, the maximum digitized output is 255 and the maximum SNR is 6130, which is much larger than 886.8. This result shows that with frame averaging according to Eq. (4-4) one can achieve a high value of SNR even with an 8-bit A/D converter.

4.2.3 The effect of integer arithmetic

Image processing systems capable of digital frame averaging usually make use of integer arithmetic. Consecutive frames are accumulated in a frame buffer using an ALU and the frame averaged image is then obtained by performing a (bit) shift-right operation. For example, in a system consisting of a 16-bit ALU and a 16-bit frame buffer with an 8-bit A/D, a maximum of 256 (2^8) frames can be added in the frame buffer and the

averaged image is obtained by dividing the accumulated signal by 2^8 (performing 8 shift-right operations). This is essentially an averaging process followed by a truncation. Since truncation is essentially an amplitude quantization process, a development analogous to section **4.2.1** for the increase in output noise can be used.

The truncated signal after integer frame averaging can be given as

$$\mathbf{S}_{\text{trunc}} = S_{\text{ave}} + q \ . \tag{4-7}$$

Then the rms noise σ_{trunc} in the averaged and truncated (digitally averaged) signal $\mathbf{S}_{\text{trunc}}$ will be given by:

$$\sigma^2_{\text{trunc}} = \sigma^2_{\text{ave}} + \sigma^2_q = \frac{(\sigma^2_x + \sigma^2_q)}{N} + \sigma^2_q \tag{4-8}$$

From Eq. (4-8) it is seen that σ_{trunc} is always higher than σ_q no matter how many frames are averaged. The 886.8 limit for SNR with an 8-bit A/D would be applicable to this situation.

However, if one opts to use digital frame *addition* instead of digital frame *averaging*, the quantization noise due to truncation can be avoided. In such a case the accumulated signal $\mathbf{S}_{\text{add}}$ will be

$$\mathbf{S}_{\text{add}} = \sum_{j=1}^{N} \mathbf{s}(x_j) \tag{4-9}$$

with rms noise

$$\sigma_{\text{add}} = \sqrt{N} \cdot \sigma_o = \sqrt{N(\sigma^2_x + \sigma^2_q)} \tag{4-10}$$

and the signal-to-noise ratio will be equal to SNR_{ave} as given in Eq. (4-6). Consequently the use of frame addition instead of frame averaging in real-time video based imaging systems can be used to overcome quantization noise due to truncation introduced by integer arithmetic.

4.3 Experimental methods

The prototype portal imaging system used was described in Chapter 3. Only two types of video cameras were investigated: a SIT (Silicon Intensified Target), and a Newvicon camera. The PC- 386 equipped with the IT-150 image processor containing an 8-bit A/D was used for image acquisition. This system has a 16-bit ALU unit capable of adding up to 256 8-bit images in real time into a 16-bit frame buffer. A 6 MV X-ray beam at a dose rate of 300 cGy/min at isocenter was used to acquire the images from which noise was measured. Water phantoms 15, 25, and 35 cm thick were used to simulate X-ray intensities corresponding to head and neck, anterior pelvic, and lateral pelvic fields respectively. The detector was located 140 cm from the X-ray source.

A sequence of N ($1 \leq N \leq 256$) 8-bit images can be averaged in a 16-bit frame buffer by adding the required number of frames in the frame buffer memory and then truncating all but the higher 8 bits. Routine clinical images are usually acquired with a 2 second exposure by averaging 64 frames. Subsequent image processing is performed on the truncated 8-bit clinical images.

Spatial noise in the portal images was determined by measuring the variance of the pixel intensities within a small (20x20) region of interest (ROI) according to Eq. (3-3). This noise measure was obtained for images that were acquired by adding between 1 and 256 frames.

One should measure the noise in the signal before and after the quantization in order to quantify the effect of quantization noise. This was done for the second quantization by using the computer to obtain the average image. The variance of the

signal at the input to the truncating quantizer was obtained by using double precision floating point numbers to calculate the image average. The variance of the output signal after the truncating quantizer was obtained by using integer arithmetic which produces the same effect as truncation by the frame buffer.

Images of the Las Vegas contrast-detail phantom[7] were also acquired. This phantom is constructed from commercial grade aluminium and has holes with diameters 1, 2, 4, 7, 10, and 15 mm and depths of 0.51, 1.0, 2.0, 3.2, and 4.8 mm. With a 6 MV X-ray beam, these thicknesses result in primary subject contrasts of 0.69, 1.36, 2.72, 4.36, and 6.54 % respectively. The calculation of these contrast values is described in Ref. 1.

Two 16 - bit images of the phantom were acquired by digitally adding 256 frames (~ 40 cGy) with a 6 MV beam at the dose rate of 300 cGy/min using Newvicon camera. One image was acquired using maximum input windowing so that only the range of video signal corresponding to the useful information was digitized into 256 gray levels. This corresponds to 0.5-0.7 V from a total video signal of 0.7 V and is referred to as fine input quantization. The other image was acquired with no input windowing, so that the full video signal of 0.0-0.7 V was digitized into 256 gray levels. This is referred to as coarse input quantization. Open field images were similarly acquired with a phantom containing no holes. 8-bit truncated versions of these images were obtained by dividing the images by 256 using integer arithmetic. This simulates the truncation that occur in the frame buffers when digital averaging is performed. These four phantom images were then corrected with corresponding open field images by division and the resultant images were windowed to show the maximum details within 8-bits.

4.4 Results and discussion

With the addition of sequential frames into a frame buffer, noise in the frame averaged images σ_{ave} is reduced in proportion to the square root of the number of frames according to Eq. (4-5). Figure 4-1 is a plot of σ_{ave} as frames are added together for the

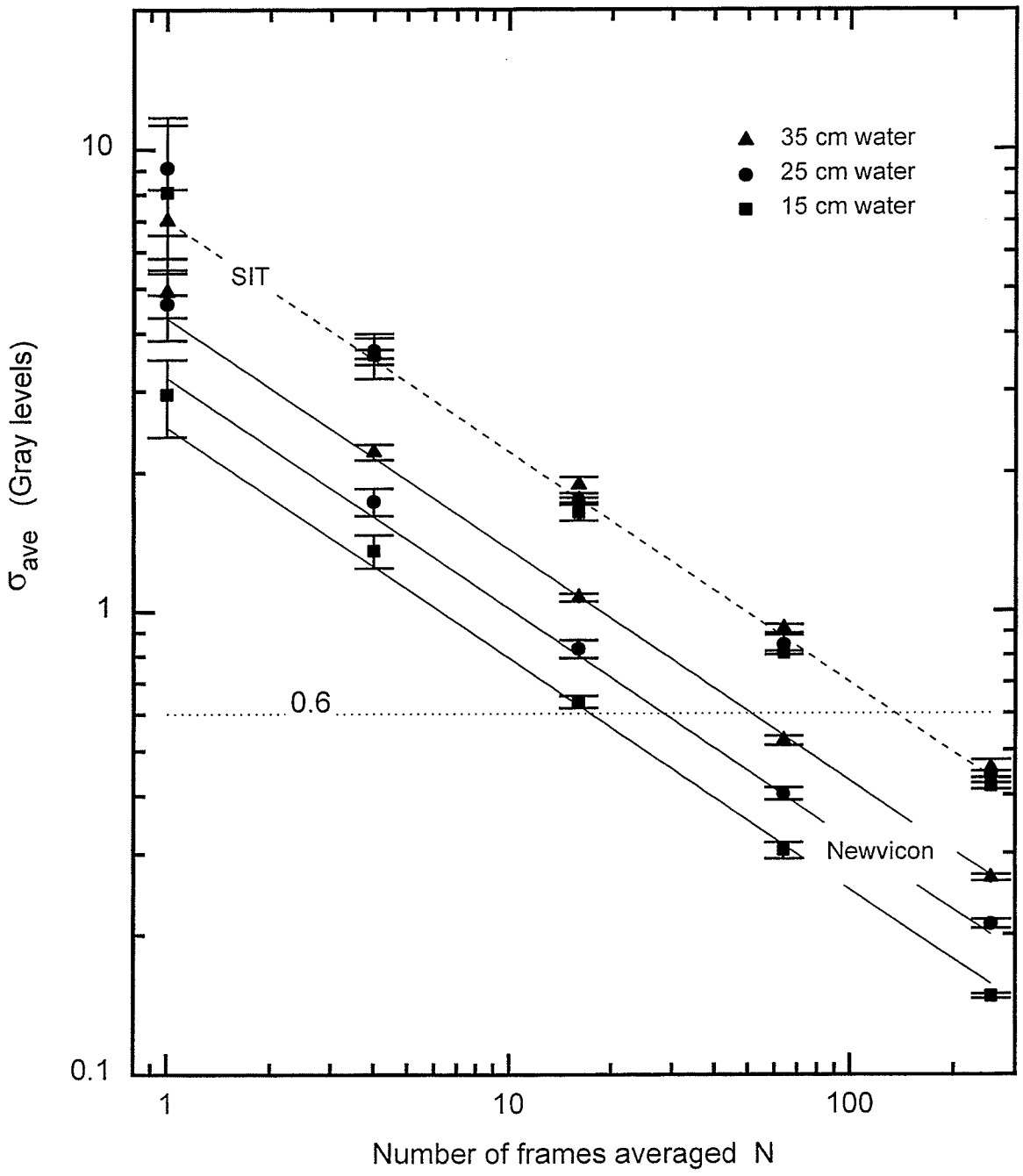

Figure 4-1. Reduction in rms noise in flat field images acquired with a SIT and Newvicon camera when frames are averaged. The horizontal dotted line indicates the level below which the quantization noise due to truncation becomes significant.

system using a SIT and a Newvicon camera and for the three different phantom thicknesses. Data have been fitted to a line with a slope of -0.5 as expected from Eq. (4-5). The dashed line indicates the level below which the quantization noise becomes significant. The SIT camera was operated at very low gain and KV values for these measurements since the light output from the phosphor screen was close to the saturation light level of the camera. As the image noise decreases, it reaches the point where quantization noise due to truncation starts to become significant. This occurs at 128 frames with the SIT camera.

The lower noise level in Newvicon images is due to the higher quantum efficiency and the longer (photo-conductive) lag in the Newvicon camera. The quantization noise due to truncation starts to become significant when averaging 16, 30, and 50 frames for 15, 25, and 35 cm phantoms respectively for this camera. Any phantom imaged with the Newvicon camera by averaging more than a 64 frames (2 second exposure) contains a significant amount of quantization noise.

Figure 4-2 shows the increase in SNR as frames averaged with the Newvicon camera using 15 cm phantom. SNR values for same images, before and after image truncation is shown in the figure for comparison. It is seen from this figure that an SNR higher than 886.8 is obtained with the system with proper averaging (or digital addition) even though an 8-bit input A/D is used. Clearly, the system SNR is not always determined by the number of bits used in the input A/D converter, but dependent on the random nature of the quantization noise added to the signal at the input A/D.

Images of the Las Vegas phantom which show the difference between a digitally added image with 16-bit processing and the digitally averaged (truncated) image with 8-bit processing are shown in Figure 4-3. The image in Fig. 4-3a was obtained with full 16-bit processing of the input windowed (fine quantization) image. Fig. 4-3b shows the corresponding image with 8-bit processing on the truncated 8-bit image. All the contrast detail objects in the phantom are visible in Fig. 4-3a, but the 1 mm object is visible only

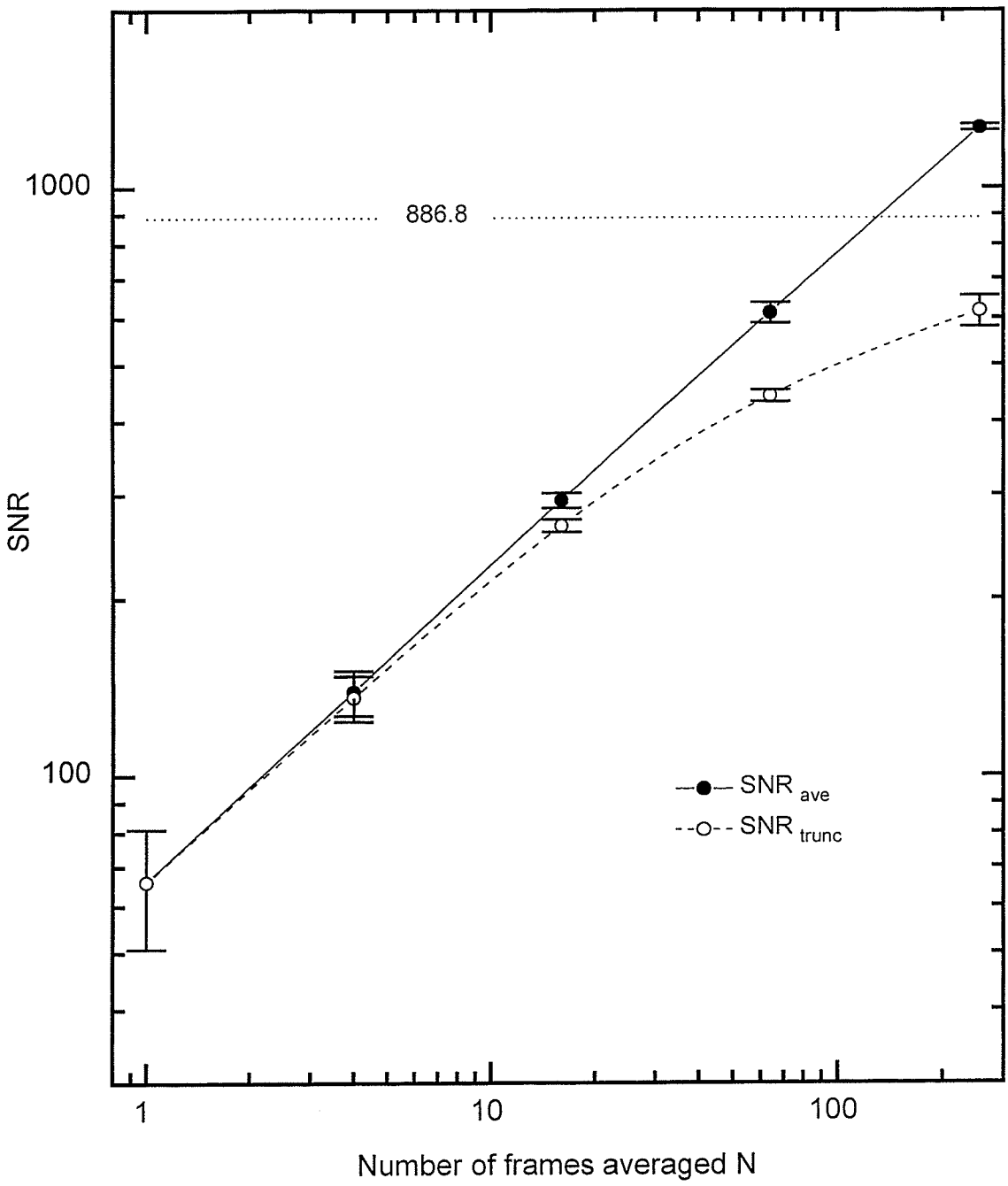

Figure 4-2. Comparison of the change in SNR before and after image truncation for 15 cm water phantom images when frames are averaged. A true SNR better than 886.8 is achieved in this system even with an 8-bit input A/D by frame addition.

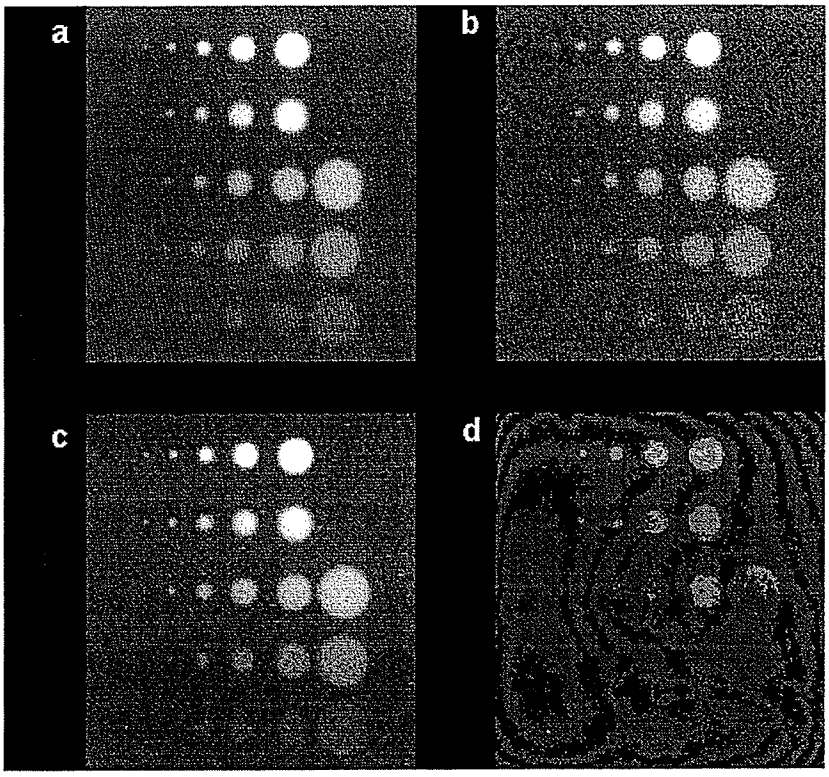

Figure 4-3. Images of the Las Vegas contrast-detail phantom showing the difference between digital frame addition with 16-bit processing and the digital frame averaging with 8-bit processing. a) 16-bit processing on digitally added image (with input windowing). b) 8-bit processing on digitally averaged image (with input windowing). c) 16-bit processing on digitally added image (no input windowing). d) 8-bit processing on digitally averaged image (no input windowing). See text for details.

at the 6.54% contrast level in Fig. 4-3b. The 2 mm object is also not visible at the 0.69% contrast level in Fig. 4-3b. This shows that digital frame addition together with 16-bit processing gives superior performance compared with digital frame averaging with 8-bit processing, even in this optimum case. Figs. 4-3c and 4-3d show a similar comparison for the worst case without input windowing (coarse quantization). All the objects, except for the 1 mm hole at the lowest two contrasts, are visible in Fig. 4-3c where 16-bit processing is used. Most of the objects are not visible in Fig. 4-3d due to the truncation. The visible contouring artifact due to truncation is also seen in Fig. 4-3d. The input windowing hampers the performance of quantitative measurements unless extensive calibrations are used. Therefore the dramatic difference between the two images in Figs. 4-3c and 4-3d clearly indicates that digital frame addition with 16-bit processing must be used for quantitative portal imaging.

4.5 Conclusions

An investigation has been carried out to identify and quantify the quantization noise sources in video based portal imaging. It has been found that the quantization noise due to integer averaging imposes a more serious problem than the quantization noise due to the input A/D for digital imaging systems capable of image averaging. It has also been shown that a SNR higher than 886.8 can be achieved with an 8-bit analog-to-digital converter (A/D) by using digital frame addition instead of frame averaging. Noise in any verification portal image acquired with a Newvicon camera by averaging more than 64 frames is found to be dominated by the quantization noise due to truncation. The full utilization of the improvement in SNR by frame averaging in verification portal images can only be achieved by using all the available bits (16 instead of 8 in our case) for all image processing and storing, and truncating images only for the purpose of display. Unfortunately, this imposes an increased computational burden on the imaging hardware.

References

[1]R. Rajapakshe and S. Shalev, "Noise analysis in real-time portal imaging I : Quantization Noise," Med. Phys. **21**, 1263-1268 (1994).

[2] W. R. Bennet, "Spectra of Quantized Signals, "Bell System Technical Journal **27**, 446-472 (1948).

[3] B. A. Widrow "A Study of Rough Amplitude Quantization by Means of Nyquist Sampling Theory " IRE Transactions in Circuit Theory **PGCT-3**, 266-276 (1956).

[4] G. T. Barnes, "Noise Analysis of Radiographic Imaging," in *Recent Developments in Digital Imaging*, edited by K. Doi, L Lanzl, and P. P. Lin 16-38 (AIP New York 1985).

[5] R. W Ramirez, *The FFT Fundamentals and Concepts*, (Prentice-Hall Inc., Englewood Cliffs New Jersey 1991).

[6] W. Swindell, E. J. Morton, P. M. Evans and D. G. Lewis, "The design of megavoltage projection imaging systems: Some theoretical aspects," Med. Phys. **18** 855-866 (1991).

[7] S. Shalev, Presented at the *Workshop on On-Line Radiotherapy Imaging*, Meeting of the Southern California Chapter of the AAPM, Las Vegas (1989) (unpublished).

Chapter 5

Random noise

5.1 Introduction

Random or spatially unstructured noise in real-time video based portal imaging systems includes *quantum noise*, due to the counting statistics of the input X-ray flux, the conversion of X-rays to light quanta, and the formation of a signal in the video camera, *electronic noise* which arises in the camera and the rest of the electronics, and *quantization noise* which is due to rounding off and truncation errors in the A/D conversion and digital frame averaging.

It was shown in Chapter 4 that the quantization noise from the 8-bit A/D is negligible when digitization is performed at video rates, and the second quantization can be avoided by digital frame addition instead of digital frame averaging. The remaining two parts of the random noise are considered in this Chapter. It was shown in Chapter 3 that the best camera for real-time continuous imaging with linacs is the dual field CCD camera, and therefore the focus of this chapter is mainly concentrated on the random noise in the CCD camera.

Near real-time imaging is adequate for some applications in radiotherapy verification using portal imaging. Consequently all the video based portal imaging systems, including the three which are available commercially, employ two signal averaging techniques to reduce random image noise. They are integration of the image on the camera target, and summation of sequential images in a digital memory, both of which reduce the time resolution.

One commercial system (Infimed Inc., Liverpool, NY) is based on the prototype portal imager designed by Munro et. al.[1]. It uses a Plumbicon camera and custom electronics to integrate the image on the camera target. Target integration is necessary

for this system since the camera noise is significant at the light levels encountered in portal imaging. Only preliminary results have been published[2] on the advantages of target integration for this device, and no quantitative comparison has been made between target integration and frame averaging.

Another commercial system (Philips Medical Systems, Shelton, CT) is based on the prototype developed by Visser et al.[3], and uses a Charge Coupled Device (CCD) video camera with a slow readout. Although this system is also capable of integrating frames on the CCD target for extended periods, the relative advantages of target integration and frame averaging have not been reported.

The BEAMVIEW^{PLUS} portal imager (Siemens Medical Systems, Concord, CA) is based on an earlier prototype system developed by Shalev et. al.[4]. A silicon intensified target (SIT) camera was used in the original design, and up to 256 video frames could be added in a frame buffer and subsequently truncated to 8-bits for display, processing, and storage. The current version of the system uses a Newvicon camera.

Wong et. al. have also developed a prototype video based system using a Newvicon camera[5,6]. The original design incorporated fibre optic coupling, while a later version uses mirror coupling and a cooled CCD camera capable of target integration[7]. Although good quality images have been produced by this system, no results have been reported on the advantages of target integration.

The purpose of this study is to investigate the random noise in the real-time portal imaging system using a custom designed camera based on a dual field capture CCD. Random noise in portal images acquired with SIT and Newvicon cameras is also measured for comparison. A simple model developed to predict the frequency dependent noise propagation through the imaging system to estimate the signal-to-noise ratio (SNR) of a single pixel is also reported. Furthermore, the advantages of Peltier cooling the CCD to further reduce the random noise is also investigated. A quantitative investigation was also carried out to identify relative advantages of target integration over summation of

sequential images in a computer frame buffer in order to reduce random noise, when near real-time imaging is performed using the custom designed CCD camera. Although the results of this study are only applicable to the imaging hardware under the investigation, the experimental techniques and the noise model used can be applied to study other video based systems.

5.2 Theory

5.2.1 Propagation of quantum noise

Radcliffe et. al. have presented an analysis of quantum noise in on-line video based portal imaging systems[8]. Here the analysis is extended by taking into account the Modulation Transfer Function (MTF) of the metal/phosphor screen using the model developed by Rabbani et al.[9]. A nomenclature somewhat similar to that of Ref. (8) is followed, but additional steps are included so that the effects of transfer functions at different stages in the imaging chain can be included. It should be noted here that the model is developed to predict the single pixel signal-to-noise ratio (SNR) of open field portal images (ie. zero frequency signal), which is defined as the ratio of the average value of region-of-interest (ROI) to the rms deviation in the pixels within the ROI. Since the open field images contain only the zero frequency information, the affects of the transfer functions are not applied to the signal propagation.

Let $\overline{N}_x$ be the average number of X-ray photons per pixel per frame incident on the screen, and p_x be the probability of interaction of those X-rays with the screen. Let $\overline{N}_p$ be the average number of optical photons produced per interacting X-ray photon with a variance of σ_p^2. The generation of these optical photons involves a complicated cascade process where secondary electrons are generated and scattered. Here a simple model is considered where each interacting X-ray photon generates some number of secondary electrons which are then scattered with a scattering transfer function $T_e(u,v)$ and result in the generation of $\overline{N}_p$ optical photons along the length of their tracks. Here u,v are the

two spatial frequencies in lp/pixel corresponding to orthogonal spatial coordinates. These optical photons are then scattered with a transfer function $T_p(u,v)$ and either absorbed or escape the screen with a probability of ξ. If $\overline{N}_T$ is the average number of optical photons created in the screen per pixel per frame with a variance of σ_T^2 having a noise power spectrum $NPS_T(u,v)$, we have

$$\overline{N}_T = \overline{N}_p \cdot p_x \cdot \overline{N}_x \tag{5-1}$$

and it can be shown[9] that

$$NPS_T(u,v) = \left((\overline{N}_p)^2 p_x \overline{N}_x + p_x \overline{N}_x \sigma_p^2 - p_x \overline{N}_x \overline{N}_p\right)\left|T_s(u,v)\right|^2 + p_x \overline{N}_x \overline{N}_p \tag{5-2}$$

where $$T_s(u,v) = T_e(u,v) \cdot T_p(u,v) \tag{5-3}$$

is the screen modulation transfer function (MTF). Note that the third term in Eq. (5-2) is always smaller than the sum of the first two terms. This expression is equivalent to that given by Rabbani et. al.[9] for screen-film radiography. Let p_p be the probability that an optical photon created in the phosphor screen will be detected by the video camera;

$$p_p = \xi \eta_c T_r \left[\frac{m^2}{4F^2(1+m)^2}\right] \tag{5-4}$$

where η_c is the quantum efficiency of the camera, T_r is the transmittance of the lens, F is the F/stop of the lens and m is the optical magnification[8]. Let $\overline{N}_D$ be the average number of optical photons per pixel per frame detected by the video camera, then the detected signal is

$$\overline{N}_D = p_p \cdot \overline{N}_p \cdot p_x \cdot \overline{N}_x \tag{5-5}$$

with a noise power spectrum

$$NPS_d = \left[p_p p_x \overline{N}_x \overline{N}_p + \left(p_p^2 p_x \overline{N}_x (\overline{N}_p)^2 + p_p^2 p_x \overline{N}_x \sigma_p^2 - p_p^2 p_x \overline{N}_x \overline{N}_p \right) |T_s(u,v)|^2 \right]. \tag{5-6}$$

This noise spectrum is affected by the transfer function of the anti-aliasing filter in the frame grabber $|T_{af}(u)|$, giving the noise spectrum in the digitized signal

$$NPS_D = \left[p_p p_x \overline{N}_x \overline{N}_p |T_{af}(u)|^2 + \left(p_p^2 p_x \overline{N}_x (\overline{N}_p)^2 + p_p^2 p_x \overline{N}_x \sigma_p^2 - p_p^2 p_x \overline{N}_x \overline{N}_p \right) |T_s(u,v)|^2 |T_{af}(u)|^2 \right]$$

or, (5-7)

$$NPS_D \approx \left[p_p p_x \overline{N}_x \overline{N}_p |T_{af}(u)|^2 + \left(p_p^2 p_x \overline{N}_x (\overline{N}_p)^2 + p_p^2 p_x \overline{N}_x \sigma_p^2 - p_p^2 p_x \overline{N}_x \overline{N}_p \right) |T_s(u,v)|^2 \right] \tag{5-8}$$

under the assumption $|T_s(u,v)| \cdot |T_{af}(u)| \approx |T_s(u,v)|$. The noise variance σ_D^2 of a single pixel is then given by the volume under the noise power spectrum[10],

$$\sigma_D^2 \approx \int_{-0.5}^{0.5} du \int_{-0.5}^{0.5} dv \left[p_p p_x \overline{N}_x \overline{N}_p{}^2 |T_{af}(u)|^2 + \left(p_p^2 p_x \overline{N}_x (\overline{N}_p)^2 + p_p^2 p_x \overline{N}_x \sigma_p^2 - p_p^2 p_x \overline{N}_x \overline{N}_p \right) |T_s(u,v)|^2 \right]$$

or

$$\sigma_D^2 = \int_{-0.5}^{0.5} du \int_{-0.5}^{0.5} dv \left[\overline{N}_D \left\{ |T_{af}(u)|^2 + \left(p_p \overline{N}_p + \frac{p_p \sigma_p^2}{\overline{N}_p} - p_p \right) |T_s(u,v)|^2 \right\} \right]. \tag{5-9}$$

A Monte Carlo study[8] has shown that $\sigma_p^2 \approx (\overline{N}_p)^2$, but a better estimate[#] is $\sigma_p^2 \approx 0.8(\overline{N}_p)^2$. So the noise variance for a single pixel becomes:

[#] T. Radcliffe, personal communication

$$\sigma_D^2 \approx \overline{N}_D\left\{\kappa + k\left(1.8p_p\overline{N}_p - p_p\right)\right\} \tag{5-10}$$

where

$$\kappa = \int_{-0.5}^{0.5} du\left|T_{af}(u)\right|^2 \tag{5-11}$$

and

$$k = \int_{-0.5}^{0.5} du \int_{-0.5}^{0.5} dv\left|T_s(u,v)\right|^2 \tag{5-12}$$

Writing the SNR per pixel per frame as

$$SNR_D = \frac{\overline{N}_D}{\sigma_D}, \tag{5-13}$$

we obtain:

$$SNR_D \approx \frac{\sqrt{\overline{N}_D}}{\sqrt{\kappa + 1.8 \cdot k \cdot p_p \cdot \overline{N}_p}}. \tag{5-14}$$

The third term in Eq. (5-10) was neglected in arriving the above expression for SNR, since it is about four orders of magnitude smaller than the second term.

So far it has been assumed that there was no phantom in the path of the X-ray beam. However, if the X-ray intensity is reduced by a factor ε due to the presence of a phantom, we then have

$$SNR_D \approx \frac{\sqrt{\varepsilon \cdot \overline{N}_D}}{\sqrt{\kappa + 1.8 \cdot k \cdot p_p \cdot \overline{N}_p}}. \tag{5-15}$$

If the frequency dependence of the noise propagation is not included as done in Ref 8, the SNR will be

$$SNR_D \approx \frac{\sqrt{\varepsilon \cdot \overline{N}_D}}{\sqrt{1+1.8 \cdot p_p \cdot \overline{N}_p}}. \qquad (5\text{-}16)$$

Equations (5-15) and (5-16) can be used to calculate SNR for images acquired with cameras in which camera noise in negligible, such as SIT camera.

5.2.2 The effect of CCD camera noise

Let $\overline{N}_b$ be the average number of thermally generated dark current electrons in each pixel per video frame with a variance σ_b^2. The target integration time n_t is usefully expressed in units of frame readout time (1/30 s), and then the signal in the CCD after the integration will be $n_t(\overline{N}_D + \overline{N}_b)$ with a variance of $n_t(\sigma_D^2 + \sigma_b^2)$. Signal readout introduces a readout noise per readout with a variance σ_r^2. The signal is then amplified and digitized, and corresponding pixels from n_f sequential frames can be added in a frame buffer to generate the output pixel value $\overline{N}_o$ given by:

$$\overline{N}_o = n_f g\ n_t(\overline{N}_D + \overline{N}_b) \qquad (5\text{-}17)$$

where g is the gain (electrons to gray level conversion factor) of the readout process. The variance in the output pixel value will then be

$$\sigma_o^2 = n_f g^2\left[n_t(\sigma_D^2 + \sigma_b^2) + \sigma_r^2\right] + n_f \sigma_q^2 \qquad (5\text{-}18)$$

where σ_q^2 is the variance of the quantization noise added by the analog-to-digital converter (A/D). However, if the A/D has sufficient number of bits one can neglect the quantization noise, in which case

$$\sigma_o^2 = n_f g^2\left[n_t(\sigma_D^2 + \sigma_b^2) + \sigma_r^2\right]. \qquad (5\text{-}19)$$

If a test is carried out without exposing the CCD to light and integrating n_t frames on the CCD, the output noise will be given by

$$\sigma_o^2 = g^2\left[n_t\sigma_b^2 + \sigma_r^2\right]. \tag{5-20}$$

In a plot of σ_o^2 vs n_t, the ratio of the slope to the intercept will yield the ratio of the dark current random noise variance σ_b^2 to the readout noise variance σ_r^2. The dark current noise can be reduced to a negligible level by sufficiently cooling the CCD. Then Eq. (5-19) reduces to

$$\sigma_o^2 = n_f g^2\left[n_t\sigma_D^2 + \sigma_r^2\right]. \tag{5-21}$$

In a plot of σ_o^2 vs n_t for the cooled CCD using only target integration without frame addition ($n_f = 1$), the slope to the intercept will give the ratio of σ_D^2 / σ_r^2. On the other hand, for a similar test carried out using only frame addition without frame integration ($n_t = 1$), a plot of σ_o^2 vs n_f will yield a straight line through the origin with a higher slope than in the previous case due to the contribution from readout noise.

One can also make sure that $\overline{N}_b = 0$ by using a suitable black level setting. Under these conditions the output pixel value will be

$$\overline{N}_o = n_f g n_t \overline{N}_D, \tag{5-22}$$

and the signal-to-noise ratio (SNR) for combined target integration and frame averaging for the cooled CCD will be:

$$SNR_o = \frac{\overline{N}_o}{\sigma_o} = \frac{\sqrt{n_f n_t}}{\sqrt{1 + \sigma_r^2 / n_t\sigma_D^2}} \cdot SNR_D, \tag{5-23}$$

If one selects n_t such that $\sigma_r^2 << n_t\sigma_D^2$, ie., readout noise is much smaller than quantum noise, the SNR of the output will be

$$SNR_o = \sqrt{n_f n_t}\frac{\overline{N}_D}{\sigma_D} = \sqrt{n_f n_t}\cdot SNR_D. \tag{5-24}$$

Equation (5-24) can be interpreted to mean that both n_f and n_t influence SNR in the same way as long as $\sigma_r^2 << n_t\sigma_D^2$, quantization noise due to the A/D is negligible, and the CCD target is not saturated.

5.2.3 The effect of camera noise in the Newvicon camera

The Newvicon is a vidicon type camera. The electronic noise added by the amplifier is significant in the images acquired with vidicon type cameras[11], and therefore camera noise must be taken into account in calculating SNR. Let σ_e^2 be the noise variance in the electronic noise added by amplifier with a zero mean value. Then the variance in the output pixel value of an image acquired by addition of n_f sequential frames will be given by

$$\sigma_o^2 = n_f g^2\left[\sigma_D^2 + \sigma_e^2\right]. \tag{5-25}$$

The corresponding SNR of the output will be

$$SNR_o = \frac{\sqrt{n_f}}{\sqrt{1+\sigma_e^2/\sigma_D^2}}\cdot SNR_D. \tag{5-26}$$

5.3 Materials and methods

The prototype portal imaging system used was described in Chapter 3. Three types of video cameras were investigated for random noise: a SIT (Silicon Intensified Target), a Newvicon, and a custom designed dual field capture (DF) CCD camera*. A KD-2** linear accelerator operated in the 23 MV X-ray mode at a dose rate of 300 cGy/min was used to image a 15 cm water phantom. A 20x20 cm^2 field size was used to acquire open field images from which the random noise is measured.

Random noise in real time video images can be characterized in either spatial or temporal terms (see Chapter 4). In this study only the spatial noise estimated from the variance over a region of interest (ROI) containing many pixels is used. A section of a horizontal line running through the pixel in question was used, giving the estimate Σ_l^2. The SNR was estimated by taking the ratio of maximum signal to Σ_l.

Experiments on cooling and target integration were performed using the CCD camera. The CCD can be Peltier cooled to 0° C, and the camera is capable of integrating up to 99 video frame readout periods on the CCD. Readout is in the RS-170 video mode.

Experimental measurements to find the effect of cooling on dark current random noise were performed without exposing the CCD to light. Dark current images were obtained by integrating frames on the CCD target with and without cooling. The spatial random noise variance Σ_r^2 using a rectangular ROI was calculated using the method described in Chapter 4, and the SNR was estimated by taking the ratio of maximum signal to Σ_r.

For the comparison of target integration and frame averaging, one should perform the experiments using a stable X-ray source so that exposure can be properly controlled. This was not possible with the Linacs used in our institution, and the ^{60}Co unit was taken out of commission due to its age. Therefore these experiments were carried out using a

* Paultek Imaging, Grass Valley, CA
** Siemens Medical Systems Inc. Concord, California.

light box. Although the light box operates at the 60 Hz line frequency, there are no pulsation artifacts since the CCD camera timing is synchronized with the line frequency. Furthermore, the light box contains an incandescent bulb producing light with exponential decay constant of 156 ms. The stability of the light box was also monitored for two hour period, and the rms changes were only 0.17%.

Initial experiments were performed using the experimental portal imaging system with the CCD camera to estimate the required camera gain for real-time portal imaging. For these tests a 15 cm water phantom was imaged with a 300 cGy/min 23 MV X-ray beam to simulate clinical conditions. Two different camera gains were found to be necessary, corresponding to two different metal/phosphor screens. One setting corresponded to the use of a custom screen consisting of a 500 mg/cm^2 Gd_2O_2S:Tb (P-43) phosphor layer on a 2.25 mm copper plate ("thick screen"). The second setting corresponded to the 150 mg/cm^2 screen used in the BEAMVIEW^{PLUS} portal imaging system ("thin screen").

The light level on the CCD for the experiments was controlled by properly closing the F/stop until the camera is producing the full video signal (0.7 V) in real-time with the corresponding camera gain. Flat field images were obtained by integrating frames on the CCD target, or addition of frames on the frame buffer, or by using both. All the experiments with light were carried out by cooling the CCD. The random noise and the SNR were measured as described above using a rectangular ROI.

5.4 Results and discussion

5.4.1 Single pixel SNR for a single frame

Figure 5-1 shows a plot of $|T_s(u,0)|^2$ and $|T_{af}(u)|^2$. The transfer function of the screen is the "thick screen" MTF obtained by Wowk[12], and the estimate for transfer function of the anti-aliasing filter was obtained from the manufacturer. It can be seen that the assumption $|T_s(u,v)|\cdot|T_{af}(u)| \approx |T_s(u,v)|$ used in arriving Eq. (5-8) is well justified.

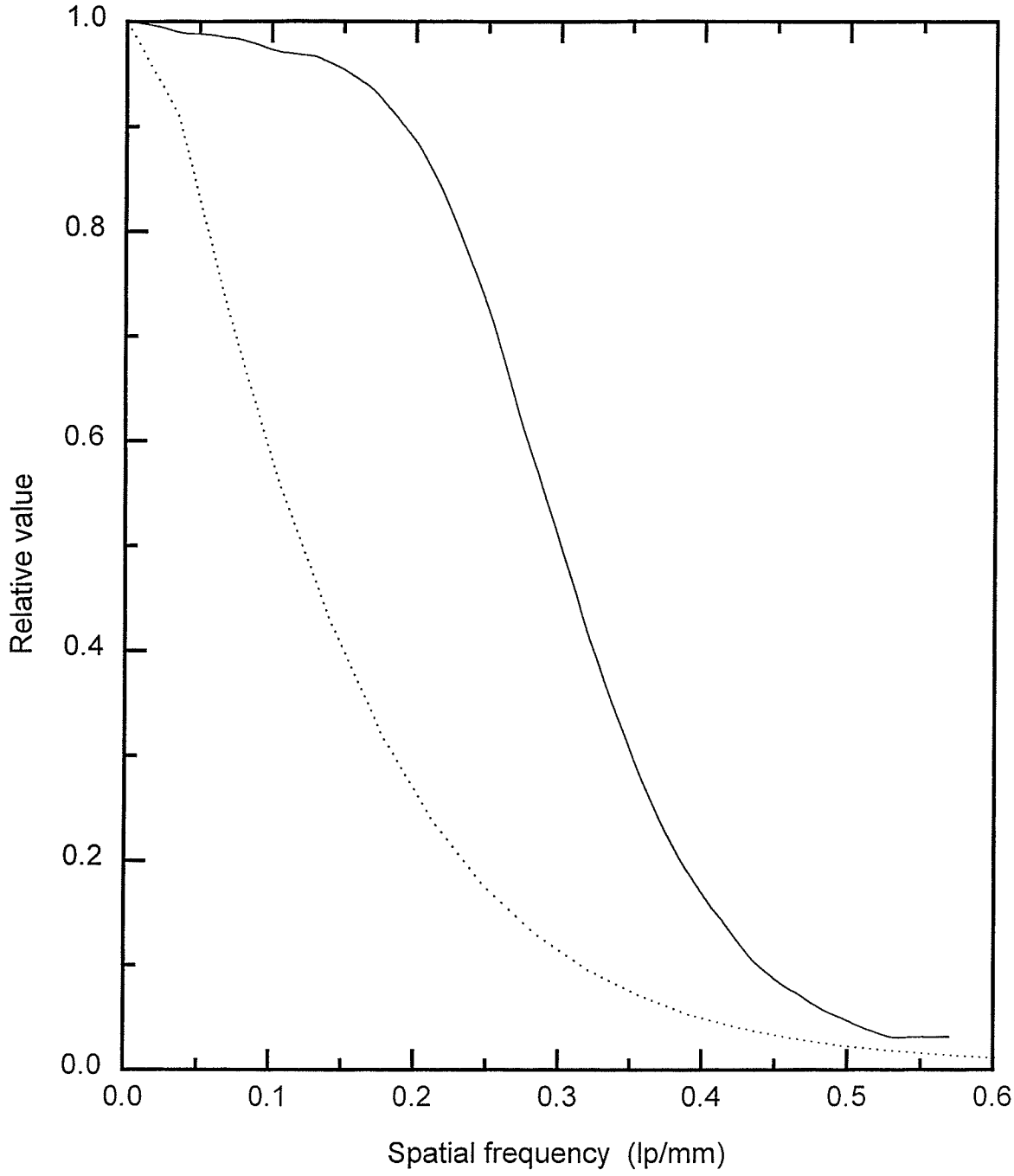

Figure 5-1. A plot of $|T_s(u,0)|^2$ (dotted line) and $|T_{af}(u)|^2$ (solid line).

Integration of these functions as shown in Eqs. (5-11) and (5-12) yield values of $\kappa \approx 0.5$ and $k = 0.046$ for the CCD camera.

Table 5-1 shows the SNR_D values calculated using Eq. (5-15). The values of $\overline{N}_x = 1.2x10^6$ (for a 1 mm^2 pixel) $p_x = 0.046$, $\overline{N}_p = 72240$, for the "thick screen" were obtained in a Monte Carlo study of video based portal imaging systems[8]. The value of ε is taken as 0.78 to accommodate the decrease in $\overline{N}_x$ due to the attenuation in a 15 cm water phantom. Other parameters used are also given in Table 5-1. The SIT and Newvicon cameras are of 1" format and the CCD camera is of 2/3" format. A 90% quantum efficiency for the Newvicon camera is used for the calculation even though "nearly equal to 1" quantum efficiency and quantum yield of higher than 1 are claimed[13]. A 10% quantum efficiency was assumed for the S-20 photocathode used in the SIT camera at 550 nm[14]. The quantum efficiency of the CCD camera was taken as 50%. The effects of camera noise is not included in these calculations, so the values correspond to the maximum possible SNR_D under the stipulated conditions.

Camera	dx (mm)	dy (mm)	η	p_p	κ	k	$\sqrt{\varepsilon \cdot N_D}$	**SNR_D** Eq. (5-15)	SNR_D Eq. (5-16)
SIT	0.86	0.68	0.1	$3.9x10^{-6}$	0.5	0.08	60	**81**	48
Newvicon	0.83	0.65	0.9	$4.0x10^{-5}$	0.5	0.073	178	**192**	73
CCD	0.57	0.57	0.5	$1.4x10^{-5}$	0.5	0.046	84	**110**	50

Table 5-1. Predicted SNR_D from Eq. (5-15) and (5-16). See text for details.

The calculations show that the Newvicon camera has the highest SNR_D, while the SIT camera has the lowest. Even with it's small target size, the CCD camera performs

better than SIT, since the difference in target size is more than compensated by the difference in quantum efficiency. The last column shows the SNR_D values calculated according to Eq. (5-16), where the frequency dependence of the noise propagation is not taken into account, ie $k=1$ and $\kappa=1$. Therefore these values correspond to the zero frequency SNR_D. The transfer function of the screen and the anti-aliasing filter makes the magnitude of the noise at higher frequencies to be lower, leading to the higher SNR_D calculated for small pixels. There are significant differences between the SNR_D calculated using the two equations for the Newvicon and CCD camera while the difference is much smaller for the SIT camera. This is due to the fact that the noise in the SIT camera is dominated by the optical photon noise[8], so the changes in X-ray and non-poisson noise have less effect on the SNR.

5.4.2 Effects of Peltier cooling the CCD

Figure 5-2a shows the increase in the random noise variance σ_o^2 in the dark current images as frames are added on the uncooled CCD. The straight line is a fit to the data according to Eq. (5-20). The fit indicates that the variance of the dark current noise σ_b^2 is 66% of the variance of the readout noise. Figure 5-2b shows similar results for the cooled CCD. Once again the straight line is a fit to the data according to Eq. (5-20), and indicates that σ_b^2 is only 5% of the readout noise variance σ_r^2. These results show that cooling the CCD reduced σ_b^2 by a factor of 13.2 so that it can be neglected when compared to σ_r^2.

5.4.3 Frame averaging vs. target integration

Figure 5-3a shows the change in the random noise variance σ_o^2 for both target integration alone (circles) and for frame addition alone (squares) for the light level corresponding to the thick screen. A maximum of 7 frames were integrated in this case to avoid CCD saturation. The straight line is a fit to the target integration data according to

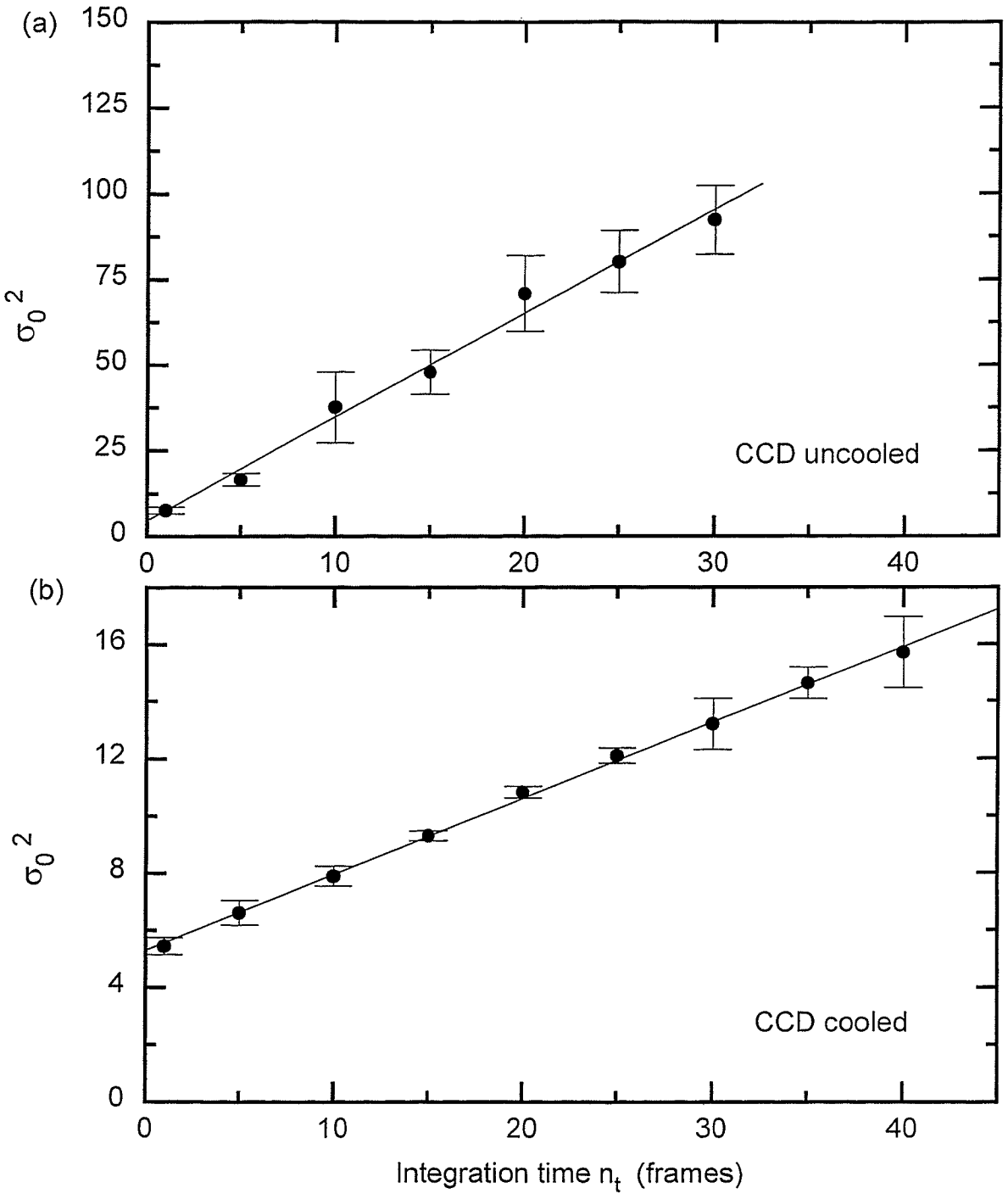

Figure 5-2. a) The increase in σ_o^2 when dark current images are integrated on the uncooled CCD. The straight line is a fit to the data according to Eq. (5-20). b) Similar results when the CCD is cooled to 0° C.

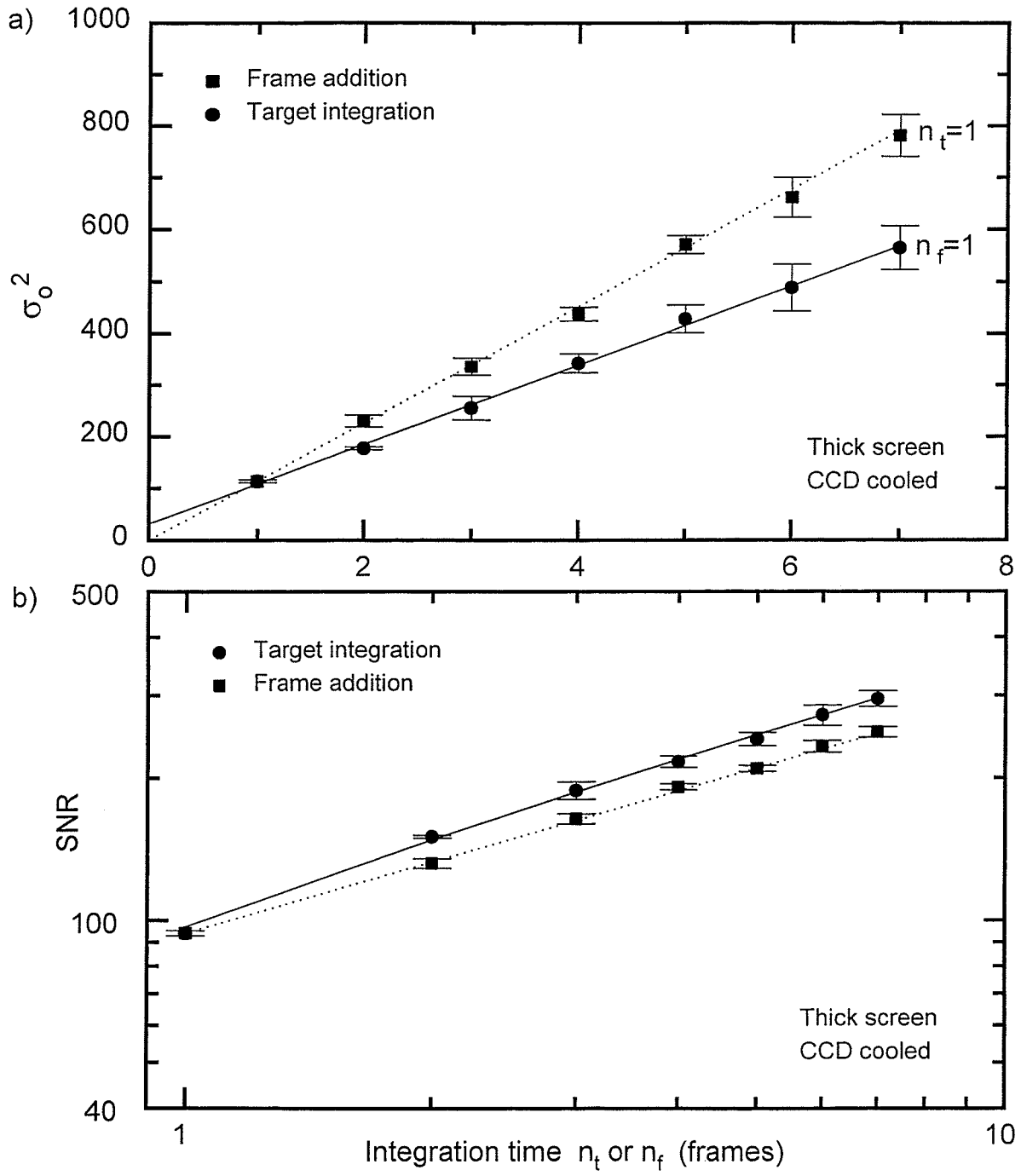

Figure 5-3. a) The increase in σ_o^2 when target integration alone is used (circles) and when frame averaging alone is used for the light level corresponding to the thick screen. b) The increase in SNR values for the two type of acquisition. The frame addition degrades the SNR by 16% due to the readout noise.

Eq (5-21) with $n_f = 1$, which indicates that the photon noise variance σ_D^2 in a single frame is 245% of the readout noise variance σ_r^2. The dotted line is a fit to the frame addition data according to Eq. (5-21) with $n_t = 1$.

The Figure 5-3b shows the corresponding increase in the SNR values for the two types of acquisition. The dotted line is a fit to the frame addition data and the curve line is a fit to the target integration data according to Eq. (5-23). The ratio of σ_r^2/σ_D^2 for these fits was obtained from the target integration results in Fig 5-3a. The fit to the target integration data indicates that the SNR_D is 112, and the frame averaging degrades the SNR by about 16% due to the camera readout noise. This degradation can be recovered by integrating 6 frames on the camera target, at which point the increase in SNR becomes proportional to n_t. The theoretical model predicted an SNR_D value of about 110 which agrees very well with the experimental measurement.

Figure 5-4a shows the increase in σ_o^2 for the light level corresponding to the thin screen. The variance σ_D^2 due to photon noise in a single frame is 111% of the readout noise variance according tho the straight line fit to the target integration data using Eq (5-21). Figure 5-4b shows the corresponding increase in the SNR values for this screen. Once again the dotted line is a fit to the frame addition data and the curve line is a fit to the target integration data according to Eq. (5-23). The ratio of σ_r^2/σ_D^2 for these fits was obtained from the target integration results in Fig 5-4a. The fit to the target integration data indicates that SNR_D is 76, and frame averaging degrades the SNR by 27 % due to the camera readout noise.

Figure 5-5a shows the effect of combined use of target integration and frame addition on σ_o^2 for the thin screen. Six frames were integrated on the target first and n_f such images were then added in the frame buffer. The straight line is a fit to the data according to Eq (5-21) with $n_t = 6$. Figure 5-5b shows the corresponding increase in SNR. The straight line is a fit to the SNR data according to Eq (5-23) with $n_t = 6$ and $\sigma_r^2/\sigma_D^2 = 0.89$.

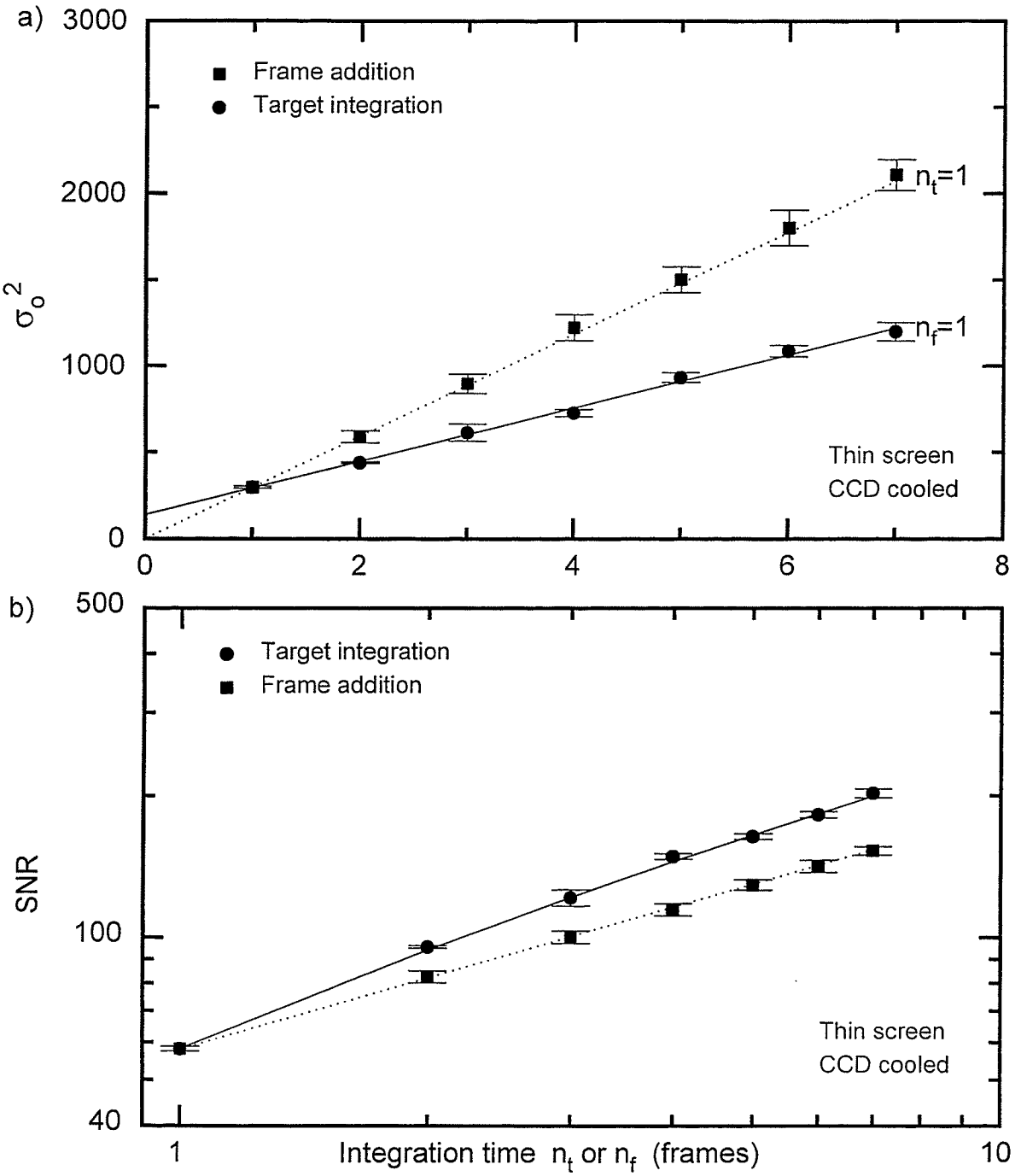

Figure 5-4. a) The increase in σ_o^2 when target integration alone is used (circles) and when frame averaging alone is used for the light level corresponding to the thin screen. b) The increase in SNR values for the two type of acquisition. The frame addition degrades the SNR by 27% due to the readout noise in this case.

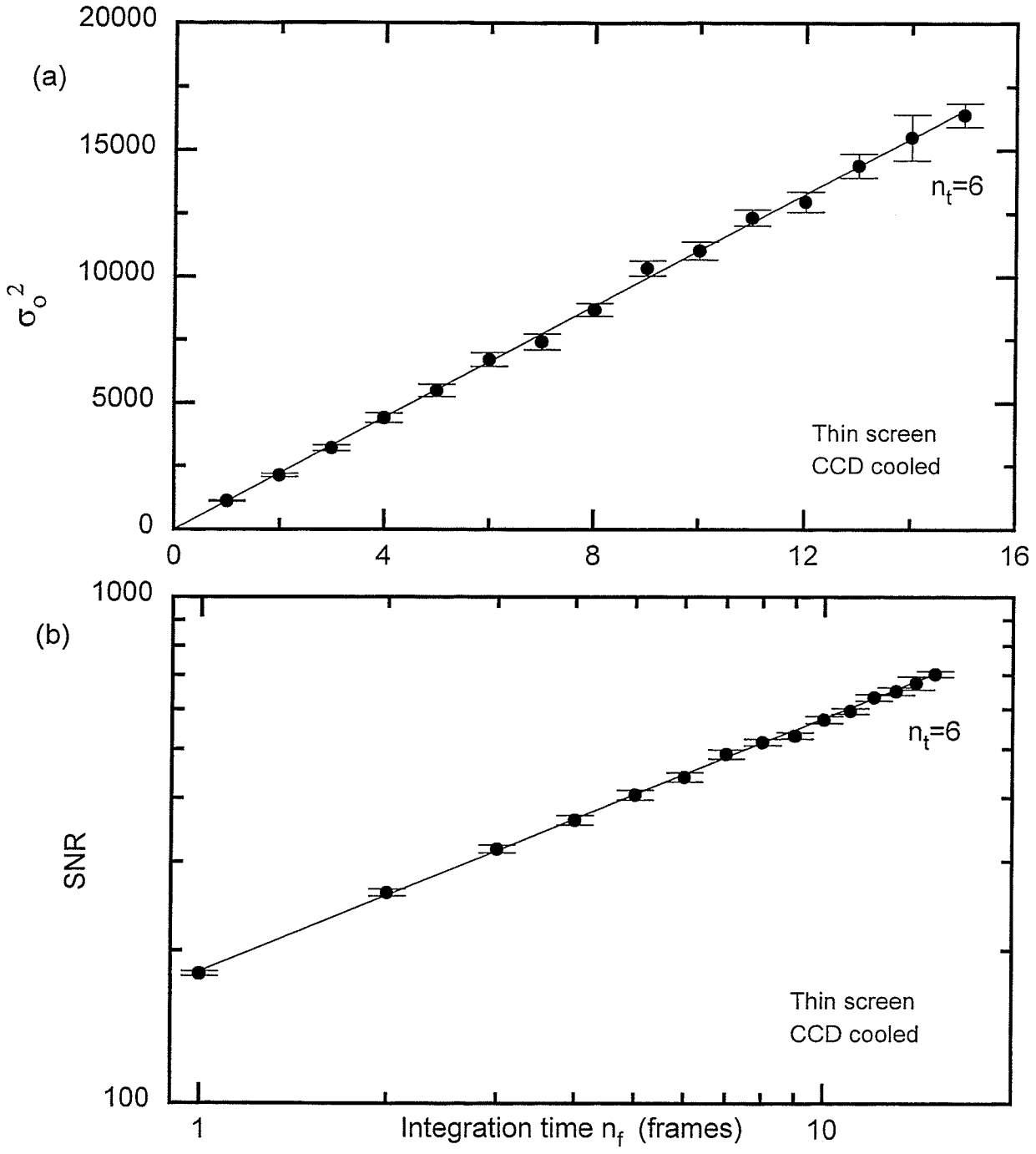

Figure 5-5. a) The increase in σ_o^2 due to combined use of target integration and frame addition. The straight line is a fit to the data according to Eq. (5-21) with $n_t = 6$. b) Corresponding increase in the SNR. The straight line is a fit to the SNR data according to Eq. (5-24) with $n_t = 6$.

These tests were carried out for the light levels encountered in portal imaging with 15 cm water phantom, which simulate a head and neck field. But for thicker fields such as pelvic fields, the light levels encountered would be lower, and therefore the ratio of σ_r^2/σ_D^2 would be higher by a similar factor. According to Eq. (5-23), higher σ_r^2/σ_D^2 ratio implies greater degradation of SNR due to frame averaging. For example, a decrease in light level by a factor of 2 would increase the ratio σ_r^2/σ_D^2 by factor of two, leading to a SNR degradation of 25% and 40% for the thick screen and the thin screen respectively. Consequently, the improvements in SNR by target integration will be higher.

Each component of the rms noise in the images acquired by the CCD camera having a signal value of 255 gray levels is summarised in Table 5-2.

Type of noise	Thick screen	Thin screen
σ_D	2.0	3.2
σ_b (without cooling)	1.04	2.4
σ_b (with cooling)	0.28	0.6
σ_r	1.28	3.0

Table 5-2. The rms noise measured in gray levels for the single frame images acquired with the CCD camera.

5.4.4 SIT and Newvicon cameras

Figure 5-6a shows the increase in the measured SNR_D when sequential frames are added in the frame buffer using the SIT camera. The straight line is a fit to the SNR_D data with a slope of 0.5 according to Eq (5-26) with $\sigma_e^2 = 0$, and indicates that the SIT camera has a quantum efficiency of only 2%. However, the S-20 photocathode used in the SIT camera has about 10% quantum efficiency at 550 nm[14]. Usually video cameras

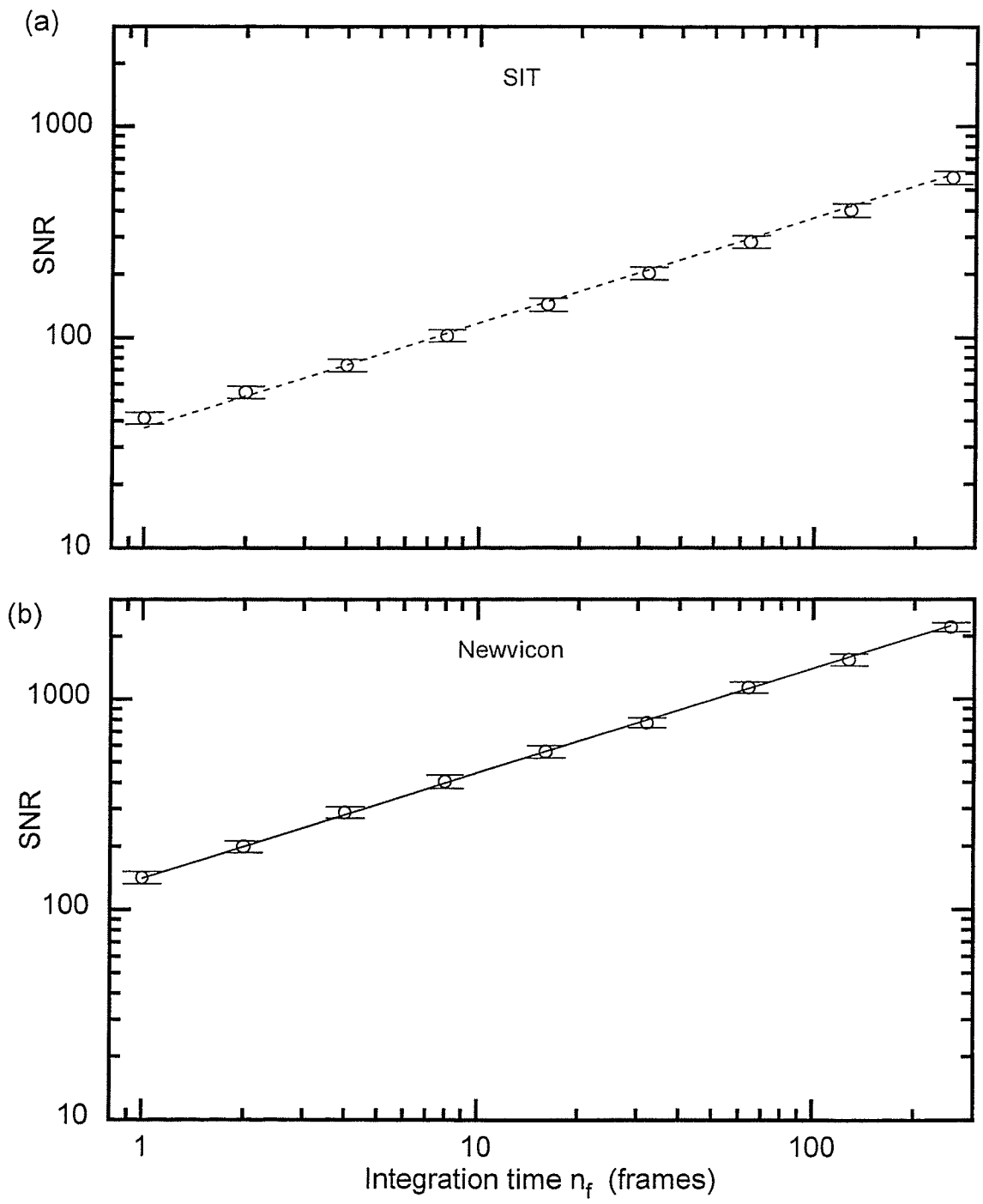

Figure 5-6. a) The effect of frame averaging on SNR for the SIT camera. b) Results for the Newvicon camera. See text for details.

are graded by the sensitivity (quantum efficiency) and defects, and 10% quantum efficiency is a nominal value for a very sensitive camera. However, some of the cameras may have low quantum efficiency due to variations in the production quality. Furthermore, the operation at low KV setting may also have an effect on the sensitivity of the camera. An independent measurement of the camera quantum efficiency is required to verify the 2% value obtained from the SNR measurements, but such a measurement could not be performed in the framework of this thesis.

Figure 5-6b shows the increase in the measured SNR_D when sequential frames are added in the frame buffer using the Newvicon camera. The straight line is a fit to the SNR_D data with a slope of 0.5 according to Eq (5-26) which indicates that the camera electronic noise variance σ_e^2 is 120% of the quantum noise variance σ_D^2. Therefore the electronic noise in the Newvicon camera degrades the SNR by more than $\sqrt{2}$. Even with the electronic noise, Newvicon has the highest SNR for a single frame due to its very high quantum efficiency. The CCD camera has the second highest SNR and the SIT camera has the lowest.

The rms noise in the single frame portal images acquired with the SIT and Newvicon cameras using the thick screen are summarised in Table 5-3. The signal value in the images is assumed to be 255 gray levels.

Type of noise	SIT	Newvicon
σ_D	5.5	0.99
σ_e	-	1.1
σ_a	11.6	1.8

Table 5-3. The rms noise measured in gray levels for single frame images acquired with SIT and Newvicon cameras.

5.5 Conclusions

A study carried out to investigate the random noise in a real-time portal imaging system has been presented. Three video cameras were under investigation: A SIT camera, a Newvicon camera and a dual field capture CCD camera. Frequency dependent noise propagation through the system was modelled to predict the single pixel SNR for the three cameras when real-time imaging is carried out. Measurements have shown that the images acquired with the Newvicon camera have the highest SNR, while images of the SIT camera have the lowest SNR. The SNR for the CCD camera was better than that of the SIT camera in spite of its smaller target size. The theoretical predictions for the CCD and Newvicon camera are in good agreement with the measurements. The effects of cooling the CCD on camera noise were also investigated. The noise model was further extended to account for the dark current and readout noise in the CCD camera. Cooling the CCD was found to reduce the dark current random noise by a factor of 13 or more so that its contribution to the output noise negligible. Readout noise in the CCD camera was found to be of 40% and 90% of the photon noise for the thick and thin screens respectively. Consequently frame averaging was found to degrade the SNR by 16% and 27% for the thick screen and thin screen respectively. The relative advantages of target integration versus frame addition were also investigated using the CCD camera. It is shown that the degradation of the SNR due to readout noise can be recovered by target integration.

References

[1] P. Munro, J. A. Rowlinson, and A. Fenster, "A digital fluoroscopic imaging device for radiotherapy localization," Int. J. Radiat. Oncol. Biol. Phys. **18,** 641-649 (1990).

[2] P. Munro and J. A. Rawlinson, "Therapy imaging: A signal-to-noise analysis of a fluoroscopic imaging system for radiotherapy localization," Med. Phys. **17,** 763-772 (1990).

[3] A. G. Visser, H. Huizenga, V. G. M. Althof, and B. N. Swanenburg, "Performance of a prototype fluoroscopic radiotherapy imaging system," Int. J. Radiat. Oncol. Biol. Phys. **18,** 43-50 (1990).

[4] S. Shalev, T. Lee, K. Leszczynski, S. Cosby, T. Chu, L. Reinstein, and A. Meek, "Video techniques for on-line portal imaging," Comp. Med. Imag. Graph. **13,** 217-226 (1989).

[5] J. W. Wong, W. R. Binns, A. Y. Cheng, L. Y. Geer, J. W. Epstein, J. Klarmann, and J. A. Purdy, "On-line radiotherapy imaging with an array of fiber-optic image reducers," Int. J. Radiat. Oncol. Biol. Phys. **18,** 1477-1488 (1990).

[6] J. Wong, A. Y. Cheng, W. R. Binns, J. W. Epstein, J. Klarmann, and C. A. Perez, "Development of a second-generation fiber-optic on-line image verification system," Int. J. Radiat. Oncol. Biol. Phys. **26,** 311-320 (1993).

[7] J. W. Wong, C. X. Yu, D. Yan, and A. Mazur, "On-line double-exposure small field verification," Med. Phys.**20** 871(1993).

[8] T. Radcliffe, G. Barnea, B. Wowk, R. Rajapakshe, and S. Shalev, "Monte Carlo optimization of metal/phosphor screens at megavoltage energies," Med. Phys. **20 (4),** 1161-1169 (1993).

[9] M. Rabbani, R. Shaw, and R. L. Van Metter, "Detective quantum efficiency of imaging systems with amplifying and scattering mechanisms," J. Opt. Soc. Am. **4,** 895-901 (1987).

[10] J. C. Dainty and R. Shaw, *Image Science,* (Academic Press, London, 1974).

[11] O. H. Schade, *Image Quality A comparison of photographic and television systems,* (RCA Laboratories, Princeton, NJ, 1975).

[12] B. Wowk, *Phosphor screens for on-line portal imaging,* (M.Sc. Thesis, University of Manitoba, Winnipeg, Manitoba, 1993).

[13] S. Fujiwara, T. Chikamura, and M. Fukai, "The heterojunction ZnSe-$(Zn_{1-X}CdxTe)_{1-y}(In_2Te_3)_y$ having high sensitivity in the visible light range and its applications," J. Crystal Growth **61,** 567-575 (1983).

[14] E. L. Dereniak and D. E. Crowe, *Optical Radiation Detectors,* (John Wiley & Sons, New York, 1984).

Chapter 6

Fixed pattern noise

6.1 Introduction

The fixed pattern noise (FPN) always imposes the upper limit on the SNR since it can not be decreased by signal integration. FPN in video based portal imaging comes from different sources: defects in the phosphor screen, defects in the camera target, and from the A/D conversion in the frame grabber. It is the author's experience that most of the frame grabber boards used to capture and digitize video signals have a FPN at the level of the least significant bit. The ITI-150 frame grabber in the original prototype system digitizes the video signal to an 8-bit digital word. Preliminary measurements have shown that the FPN in this frame grabber amounts to a half of a bit making the maximum possible SNR achievable with the system only 512. The current prototype system uses the Oculus 500 imaging system from Coreco Inc. which digitizes the video signal to 10-bit, and this reduces the effects of FPN from digitization by a factor of four. The structure of the FPN introduced by the two frame grabbers will be discussed in Chapter 7.

The FPN introduced by the phosphor screens is negligible for properly manufactured screens, and therefore is not considered in this thesis. This chapter concentrates on the FPN introduced by the CCD camera.

6.2 Theory

CCD dark current generates a significant amount of FPN. This is due to the spatially uneven generation of thermal electrons in CCD pixels. Since the rms value of the FPN increases linearly with the number of frames integrated, FPN imposes the

ultimate limit on SNR if not removed by a correction. FPN is usually removed by subtracting off a dark current image.

As before, the target integration time n_t can be expressed in units of frame readout time (1/30 s), and then the total spatial noise variance σ_T^2 in the dark current images including the FPN can be given as

$$\sigma_T^2 = n_f g^2 \left[n_t \sigma_b^2 + \sigma_r^2 \right] + n_f^2 g^2 n_t^2 \sigma_{fpn}^2 \qquad (6\text{-}1)$$

where σ_{fpn}^2 is the noise variance due to FPN. Other terms are defined in Chapter 5 (page 86). When the dark current is integrated either on the CCD target, or on the frame buffer, the FPN starts to dominate the total noise. If the dark current is integrated on the CCD target, ie. $n_f = 1$, the total noise can be given as

$$\sigma_T^2 = g^2 \left[n_t \sigma_b^2 + \sigma_r^2 + n_t^2 \sigma_{fpn}^2 \right]. \qquad (6\text{-}2)$$

6.3 Materials and methods

Experiments were performed using the custom designed CCD camera based on the TC-217 dual field capture CCD. The details of the experimental set-up were described in Chapter 5. Dark current images were acquired by integrating thermally generated charge on the CCD target with and without cooling the CCD. The target integration time is measured in units of frame readout time (1/30 s) for convenience. The total noise σ_T which contains the FPN was obtained by measuring the variance in a 40x40 central ROI in these images.

6.4 Results

Figure 6-1 shows two vertical intensity profiles of dark current images, obtained by integrating 10 frames on the CCD target. Figure 6-1a is the result without cooling the

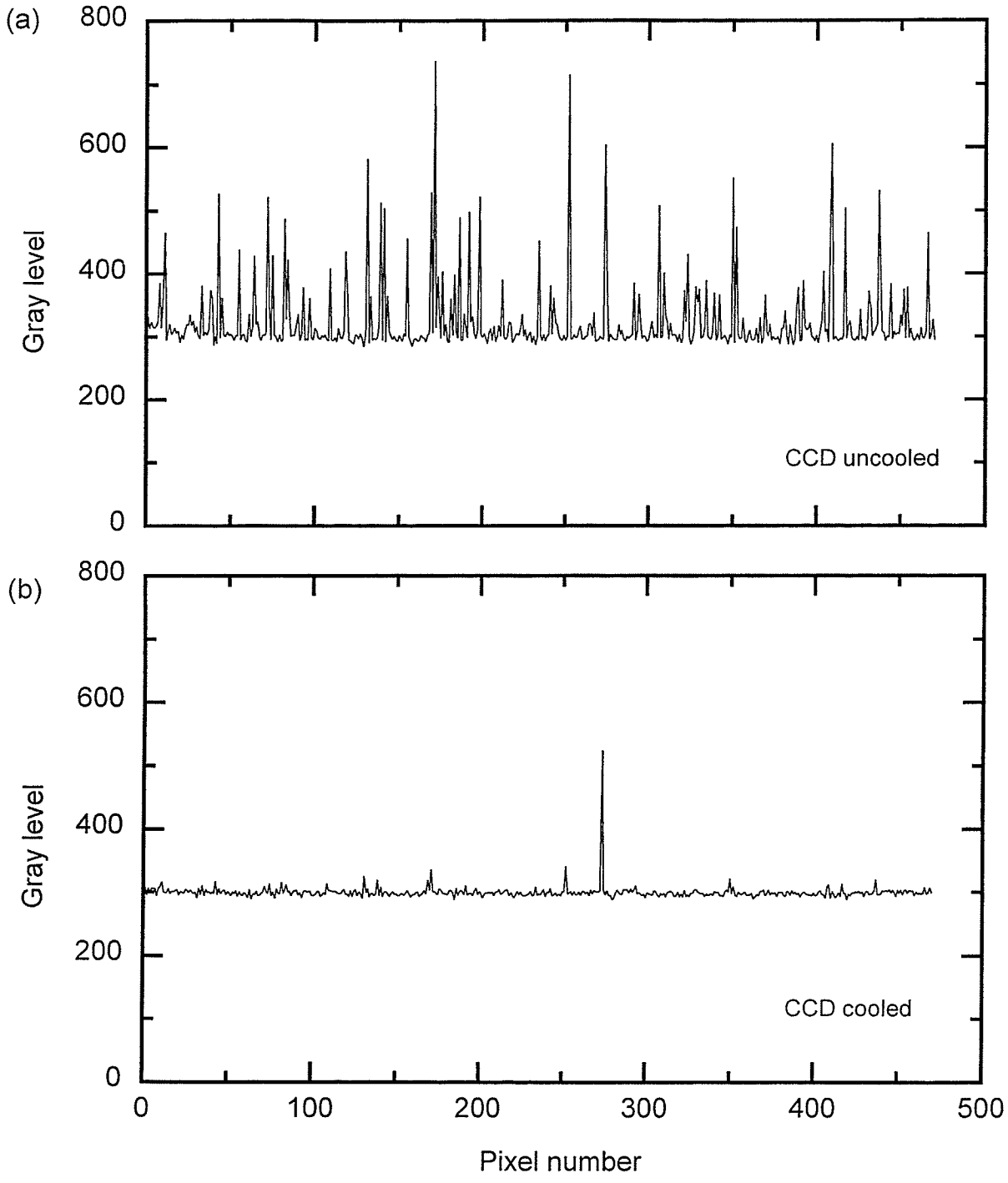

Figure 6-1. Vertical intensity profiles of dark current images obtained by integrating charge for 0.33 s on the CCD target. a) The result without cooling the CCD. b) The result with cooling the CCD.

CCD, and Fig. 6-1b is the result with cooling the CCD to 0° C. It can be seen that there are no gradients in the profiles indicating that the variance in a 40x40 ROI represent the total noise.

Figure 6-2a shows the increase in the total noise σ_T in the dark current images when frames are integrated on the CCD target without cooling. The FPN σ_{fpn} dominates the total noise in this case. For low number of frames, σ_T increases linearly with the number of frames integrated and starts to roll off due to the saturation of pixels contributing to the FPN at this temperature. The straight line section of the data indicates that the contribution from σ_{fpn} to σ_T is 6 ± 2 gray levels, limiting the spatial SNR to about 170 if FPN is not removed by dark image subtraction. Figure 6-2b shows the similar increase in σ_T when the CCD is cooled to 0° C. The curve is a fit to the data according to Eq. (6-2), and indicates that contribution from σ_{fpn} to σ_T is reduced to 0.470 $\pm$ 0.007 gray levels. This makes the maximum possible SNR due to the FPN in the camera about 2000.

6.5 Conclusions

The FPN in the dual field capture CCD camera has been investigated, in particular, the effect of cooling on the FPN. It was found that cooling the CCD reduced the rms FPN by a factor of about 13, making its magnitude about half a gray level.

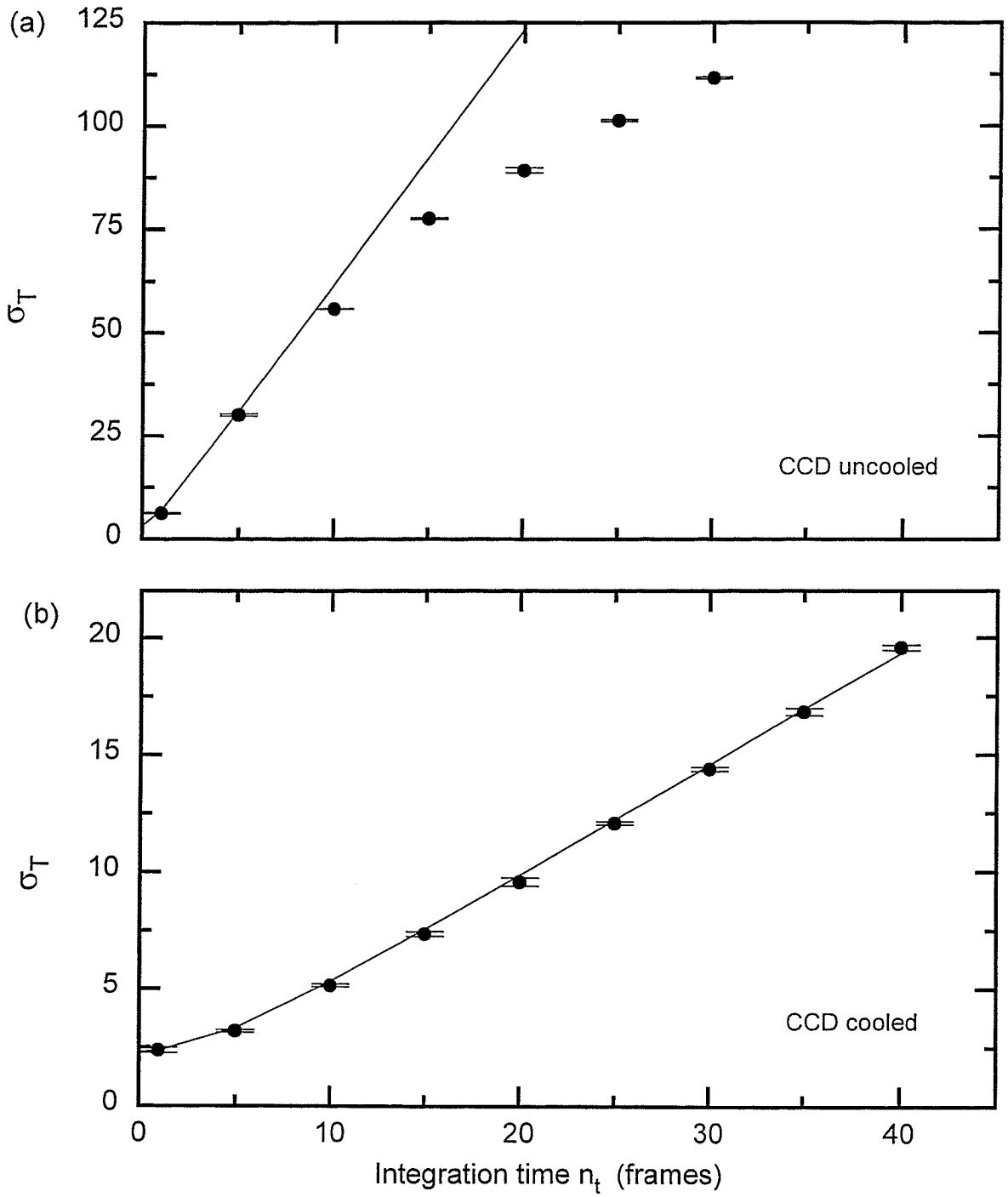

Figure 6-2. a) The increase in the total noise variance σ_T^2 including the fixed pattern noise (FPN) when the dark current is integrated on the uncooled CCD. b) Similar results for the cooled CCD. The curve line is a fit to the data according to Eq. (6-2), and indicates that the contribution from the FPN to σ_T is only 0.47 gray levels.

Chapter 7

Noise power spectra

7.1 Introduction

The theoretical and experimental analysis of the noise variances due to different sources in the real-time portal imaging chain were presented in chapters 3 - 6. However, a detailed analysis of system noise must always involve the determination of Noise Power Spectrum (NPS). Based on Fourier analysis of noise variance, the NPS describes the frequency distribution of the image noise variance, and provides information additional to the noise variance[1]. In this chapter the application of this Fourier method of noise analysis to the real-time portal imaging system is presented.

Investigation of image noise based on Fourier methods were first developed in photographic science for analysing photographic granularity. Elias et. al.[2], Elias[3], and Fellgett[4] have pointed out the relevance of Fourier analysis of noise developed in communication theory to optics, but R. Clark Jones[1] pioneered in describing and using this method for analysing film granularity. The generic name "Wiener Spectrum" instead of power spectrum was also proposed by Jones[1] to honour the person who developed the mathematical concepts. The ambiguity in the use of the term "power" in optics had been pointed out previously[3]. Furthermore, the technique of scanning a film with a long narrow slit to obtain a section of the noise spectrum was also proposed by Jones[1], and later verified theoretically and experimentally by Doi[5].

The finished product in film based imaging is a developed film and the spatial variation of transmittance or the optical density of the film is required to obtain the Wiener spectrum. Both analog[1,4,6,7] and digital[8] techniques have been used to measure the NPS of the developed film. Show[9] has given an excellent review on the historical development of the subject. The advent of Fast Fourier Transform (FFT) and the

availability of faster computers have made the digital technique popular, and most of the NPS measurements with radiographic film screen systems have been carried out using the digital technique.

It has been shown that special precautions have to be used in scanning a portion of the film for NPS measurements[7]. Furthermore, corrections due to the finite size of the scanning aperture are necessary for film NPS measurements since scanning with a microphotometer is required to obtain the data. However, the NPS of film are circularly symmetric due to the isotropic nature of the film, and therefore the central slice of the 2-D NPS provides the complete picture of the spectrum[7]. Consequently the central slice of the 2-D NPS has been mainly used in film studies.

NPS measurement techniques were also used for analysing noise in film based radiographic imaging[10-13]. It has been customary in the past to simply adopt the techniques used for film NPS measurements to digital systems[14-18]. Most of this work was lead by the NPS measurements performed on a film based digital radiographic system[19], where a virtual scan of the digital data was performed using a digitally synthesized long narrow slit to simulate the film measurement technique. This method is known as the synthesized slit method.

However, in the case of digital imaging, the sampling is an inherent property of the imaging process[19] and the finite pixel size is a part of the digital imaging system. The final product in digital imaging is a set of digital data representing an image in contrast to the developed film in film based imaging. Although necessary for performance analysis in analog fluoroscopic systems[20,21], and analysing "pre-sampled" data in digital systems, pixel size correction in the NPS measurement is not necessary if one is interested in the analysis of the digital system. Moreover, video based digital imaging systems are not always isotropic and sometimes are not spatially invariant either, as shown later in this chapter. Consequently the central slice of the NPS may not provide

the complete picture of the spectrum[21], and the two dimensional structure of the spatial NPS is necessary to identify any off-axis spectral components.

7.2 Theory

Although the image data representing a physical process can have more than 3 dimensions[2], data from real-time monochrome video imaging can be restricted to three dimensions, consisting of two spatial and one temporal dimension[20,21]. However, the temporal and spatial dimensions are separated for simplicity, and only the two dimensional spatial noise power spectrum is considered here. A two dimensional noise data sequence in an image (either digital or analog) with a zero mean can be denoted by n(x,y) where x and y are the two spatial coordinates.

For an analog noise data set, the 2-D NPS is defined as[22]

$$\mathrm{NPS}(u,v) = \underset{X,Y \to \infty}{\text{limit}} \left\langle \frac{1}{2X}\frac{1}{2Y}\left| \int_{-X}^{X}\int_{-Y}^{Y} n(x,y)\ \exp\left[-2\pi i(ux+vy)\right] dx\ dy \right|^2 \right\rangle \tag{7-1}$$

where X and Y are the limits of the analog image dimensions. Here u and v are the analog frequency variables corresponding to x and y directions respectively. The double integral represents the 2-D analog Fourier transform and the $\langle\ \rangle$ symbol represents the process of taking an ensemble average.

Similarly for a two dimensional digital noise data set n(x,y), we can define the two dimensional NPS by

$$\mathrm{NPS}(u,v) = \left\langle \frac{dx.dy}{N_x.N_y}\left| \sum_{x=0}^{N_x-1}\sum_{y=0}^{N_y-1} n(x,y)\ \exp\left[-2\pi i(ux/N_x + vy/N_y)\right] \right|^2 \right\rangle \tag{7-2}$$

where dx, dy are the pixel sizes in two spatial directions, N_x and N_y are the number of pixels in each spatial direction. Here u and v are the digital frequency variables corresponding to horizontal and vertical directions respectively. The double summation represents the 2-D discrete Fourier transform.

Once a two-dimensional spectrum is calculated according to Eq. (7-2), the central slices of the spectrum can be extracted simply by using $NPS(u,0)$ and $NPS(0,v)$. On the other hand, an average value of the noise power spectrum in one direction can be obtained by averaging along the other direction. ie.,

$$\overline{NPS(u)} = \frac{1}{N_y} \sum_{v=0}^{N_y-1} NPS(u,v) \tag{7-3}$$

and

$$\overline{NPS(v)} = \frac{1}{N_x} \sum_{u=0}^{N_x-1} NPS(u,v) \tag{7-4}$$

These one-dimensional spectra can also be calculated by performing a one-dimensional Fourier transform. The exact central slice along the u axis can be obtained by

$$NPS(u,0) = \left\langle \frac{dx.dy}{N_x \cdot N_y} \left| \sum_{x=0}^{N_x-1} n_y(x) \exp[-2\pi i(ux/N_x)] \right|^2 \right\rangle \tag{7-5}$$

where

$$n_y(x) = \sum_{y=0}^{N_y-1} n(x,y). \tag{7-6}$$

This follows directly from Eq. (7-2) when v = 0. This method is known as *scanning synthesized slit method* to obtain the central slice of the NPS[19,20].

Similarly, a statistical realization of the average value along the u axis can be obtained using

$$\overline{NPS(u)} = \left\langle \frac{dx.dy}{N_x} \left| \sum_{x=0}^{N_x-1} n_y(x,0)\ \exp[-2\pi i(ux/N_x)] \right|^2 \right\rangle. \qquad (7\text{-}7)$$

7.3 Materials and methods

The prototype portal imaging system used this study was described in Chapter 3. Three types of video cameras were used for image acquisition: a SIT , a Newvicon, and a dual field capture (DF) CCD camera. The Newvicon camera had no manual gain control, so automatic gain-control was used. The pixel size at the metal/phosphor screen for the three cameras were 0.863 x 0.682 mm^2, 0.827 x 0.645 mm^2, and 0.64 x 0.64 mm^2 respectively. Both ITI-151 and OC-500 frame grabbers were used for image acquisition. ITI-151 was used for acquiring images from the SIT and Newvicon cameras, and the OC-500 was used to acquire images from the CCD camera. Dark current images of the SIT camera were also acquired by OC-500 for comparison.

A 6 MV X-ray beam at a dose rate of 300 cGy/min at isocenter was used to acquire portal images. A 15 cm thick water phantom was used to simulate X-ray intensities encountered in the clinical settings. Images were also acquired using the SIT and CCD cameras with a light box. The light level falling on the cameras was adjusted to that encountered in portal imaging. Dark current images of all the three cameras were also acquired.

The two dimensional noise power spectra were calculated using Eq. (7-2). The central slices were directly extracted from the two dimensional spectra, and the average values along the two directions were calculated using Eq.(7-3) and (7-4). The central slices and the averages were also calculated using Eq. (7-5) and (7-7) for comparing the one- and two- dimensional calculation methods.

The middle 256x256 section of 512x480 or 640x480 pixel images were used to evaluate the NPS. The 2-D image data were Fourier Transformed using a general n-dimensional discrete Fast Fourier Transform (FFT) algorithm[23]. The noise power was obtained by scaling the squared modulus of the Fourier transformed data by the pixel size (dx·dy) and the number of pixels ($N_x = 256$, $N_y = 256$) used in the transform. NPS of 25-100 image pairs were averaged to reduce the variance in the spectra. No data smoothing window is applied before the FFT, as it did not make significant changes to the NPS in the preliminary NPS calculations. A previous study[20] has also reported that data windowing had little effect on the NPS of video based X-ray images.

No pixel size correction is made in the spectra since we are interested in the noise performance of the entire system. The spectra were normalized by the square of the mean signal value of the 256x256 region used for the NPS calculations. The spectral values shown, therefore, correspond to the central 256x256 region of the images only. This is due to the fact that lens vignetting and any non uniform response of the camera leads to different gray values at the edge of the images[18]. The program used to calculate 2-D NPS was written for a PC-486 using Microsoft C-7 compiler to run under Microsoft Windows 3.1.

A 4x4 frequency bin average of the 256x256 NPS array was used for plotting the 2-D NPS as the plotting routine could not handle the full data set. The central slices of the 2-D spectra (NPS(u,0) and NPS(0,v)) were extracted from the 2-D results, and the averages of the spectra taken along the two directions (($\overline{NPS}(u)$ and $\overline{NPS}(v)$) were also obtained as shown in Eq. (7-3) and (7-4). The conventional 1-D calculation of the central slices using the "synthesized slit" method and the calculation of the average value along the two directions were also performed according to Eqs. (7-5) and (7-7). This 1-D calculation was carried out only for the single frame images of the water phantom acquired by the SIT camera, for both horizontal and vertical directions.

7.4 Results and discussion

7.4.1 SIT and Newvicon cameras

The two dimensional noise power spectrum of single frame portal images of the water phantom acquired with the SIT camera is shown in Fig. 7-1. The high value (peak) of the NPS at the Nyquist frequency in the v axis is due to the interlace artifact (different intensities in the two interlaced fields). The increase in the spectral values along the v axis is due to the banding artifact. The banding artifact changes from image to image and this leads to a randomly distributed noise power along the v axis. Both these artifacts influence the noise power only along the v axis. The use of the central slice NPS(0,v) of this spectrum as a representation of the noise power in the v direction will lead to an over-estimate the magnitude of the 2-D spectrum due to the increase in the spectral values along the v axis. This emphasizes the fact that 2-D spectral calculation is necessary to properly estimate the spatial noise spectrum in video based digital imaging.

Figure 7-2 shows the 2-D spectrum of the images obtained with the SIT camera using a light box. The central spike is due to excess variability in the mean brightness of the images. There are no extra spectral components along the v axis due to pulsation artifacts since the intensity of the light box is very stable. However, a small increase in the spectral values along the v axis can be seen in this spectrum. The video noise spectrum published by Tapiovaara also exhibits a similar behaviour[21], but no explanation was given for the increase. The author believes that this is due to the clamping error; the error in detecting the black level in each horizontal video line in the RS-170 video signal. The clamping error is a systematic error for each individual video line, and will not affect the noise power in the horizontal direction. However, the random nature of the clamping error makes the noise power along v axis higher than the average.

Figure 7-3 shows the comparison of 1-D slices obtained by 2-D calculation using Eqs. (7-2) - (7-4), and 1-D calculation using Eqs. (7-5) - (7-7) for the images used in calculating the NPS shown in Figure 7-1. Figure 7-3a shows the horizontal slices

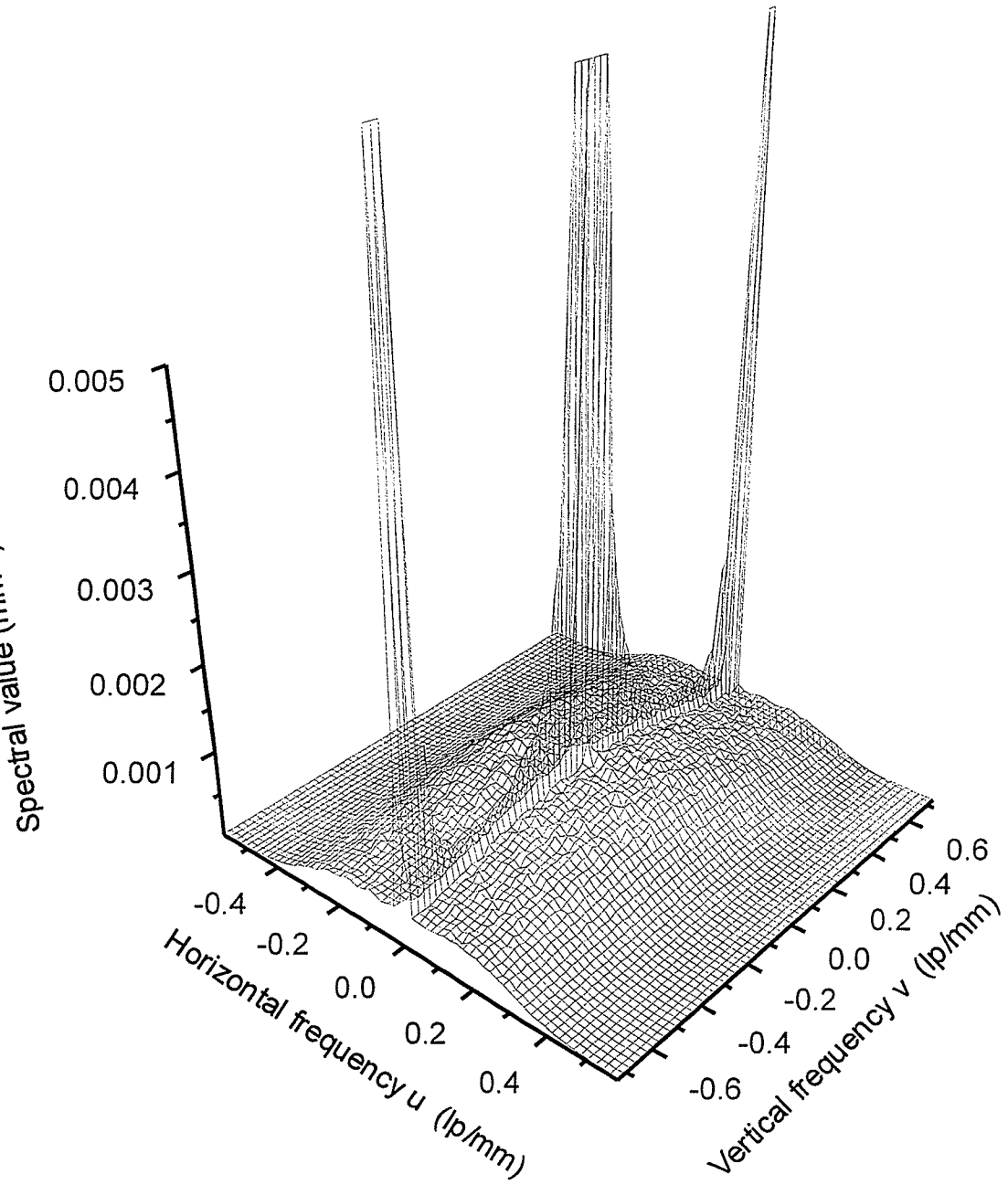

Figure 7-1. Two dimensional noise power spectrum of single frame water phantom images acquired with the SIT camera. The increase in the spectral values along the v axis is due to the pulsation artifacts.

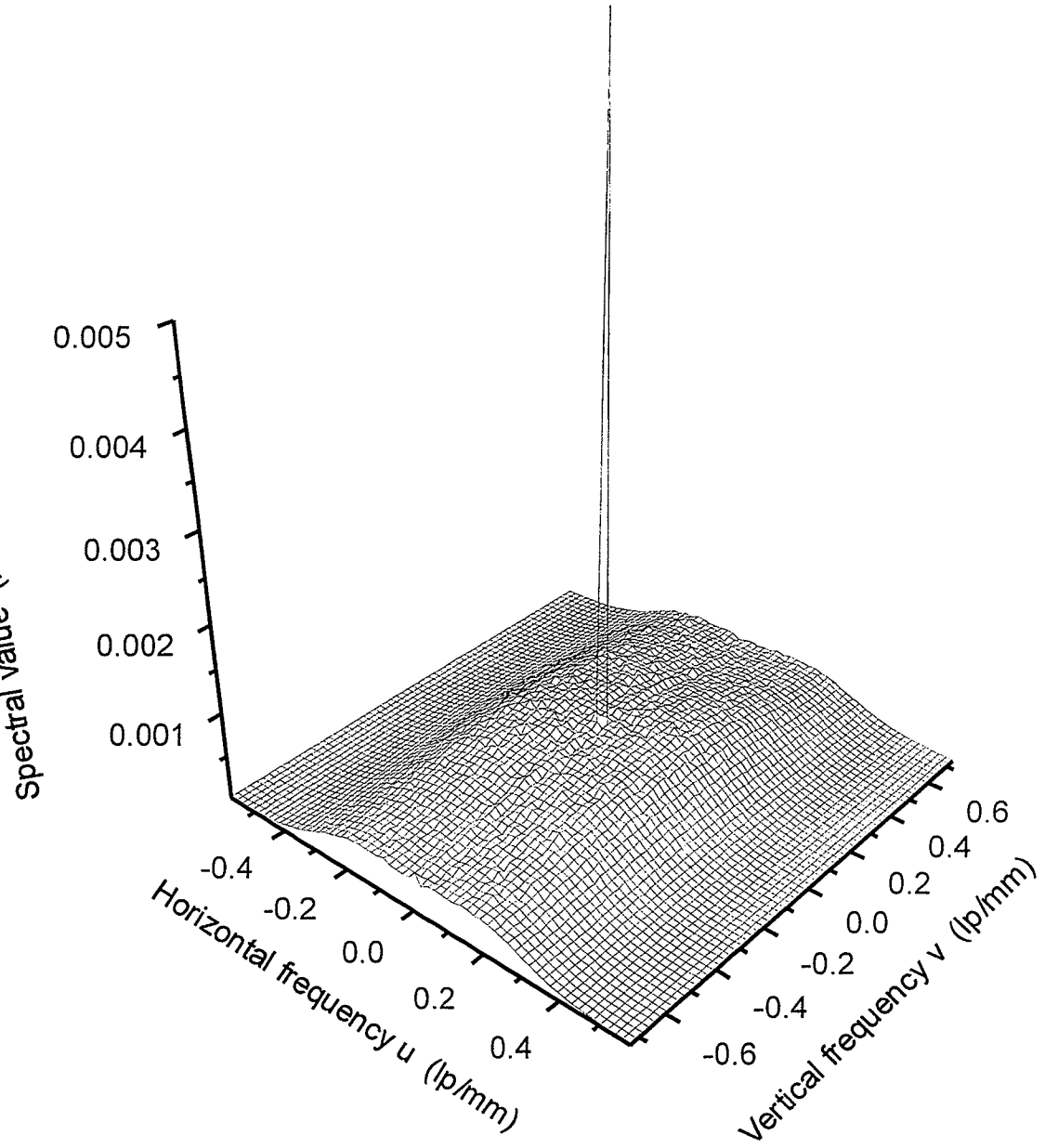

Figure 7-2. Noise power spectrum of images acquired with the SIT camera when illuminated with a light box.

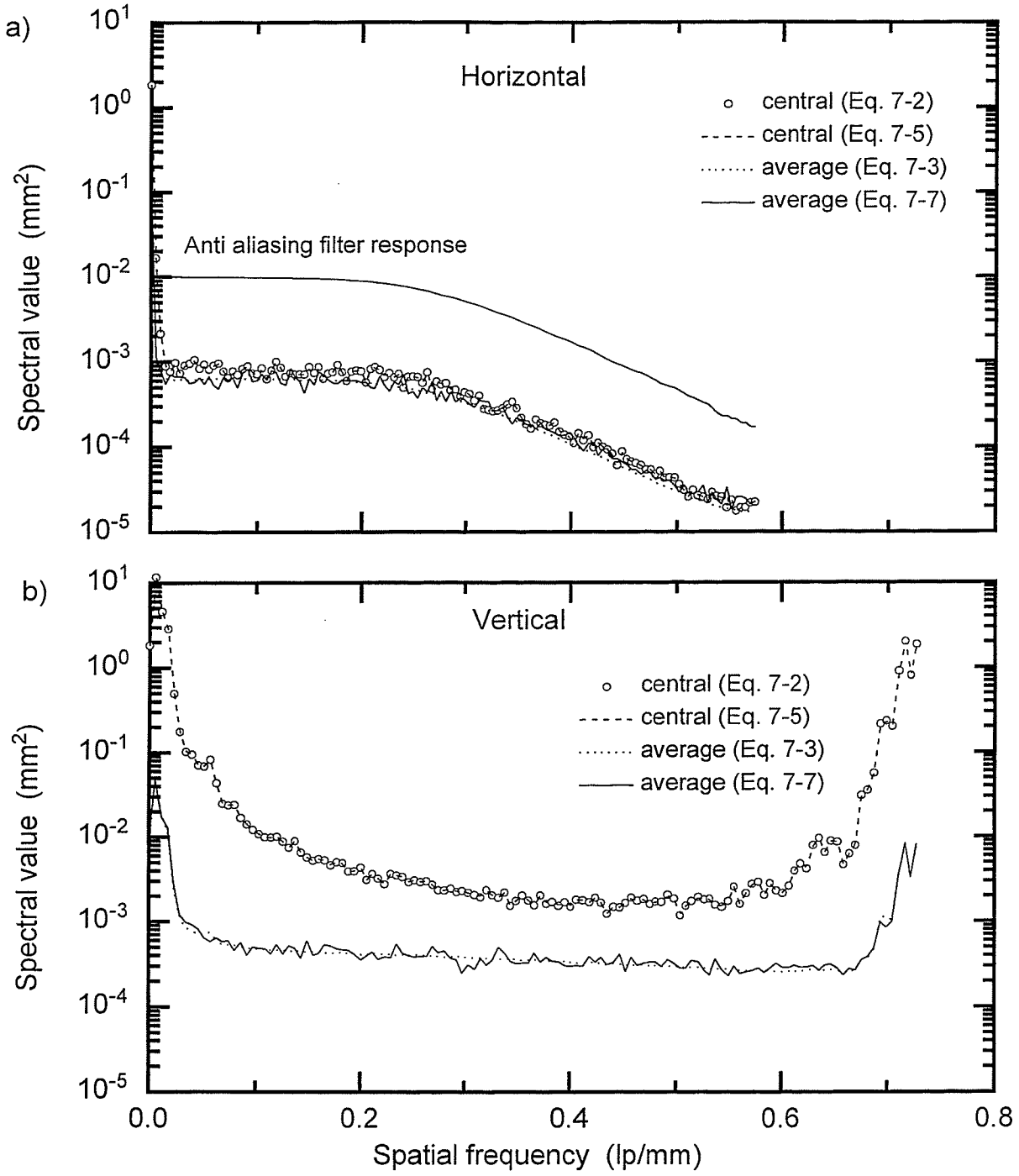

Figure 7-3. a) Comparison of the central slices and the averages of the 2-D NPS in the u direction obtained by the 2-D calculation (using Eqs. (7-2) - (7-4)) and by the 1-D calculation (using Eqs. (7-5) - (7-7)) . b) Similar comparison in the v direction. These results show that the two methods give almost identical results.

NPS(u,0) and $\overline{NPS}(u)$, and Figure 7-3b shows the vertical slices NPS(0,v) and $\overline{NPS}(v)$. It can be seen that the slices calculated by the two methods agree very well. The relative effect of the anti aliasing filter obtained from the data shown in Fig. 5-1 is also shown in Fig. 7-3a. The data were scaled down by a factor of 100 for easy comparison.

NPS of the SIT camera images must be "white" (uniformly distributed), as the noise in the SIT camera images are dominated by the optical photon noise. However, a decrease in the spectral values in the u direction at higher frequencies is clearly seen. This roll-off in the NPS in u direction is consistent with the shape of the anti aliasing filter characteristics indicating that this roll-off is due to the anti-aliasing filter.

Figure 7-4 shows the 2-D NPS of single frame dark current images from the SIT camera acquired by the ITI-151. The spectrum in the horizontal direction increases initially at low frequencies, and then starts to decrease at higher frequencies due to the anti-aliasing filter. The increase in the camera noise power in the horizontal direction is typical of vacuum tube cameras[24]. The differences between the magnitude and the shape of this spectrum and that of the Fig. 7-2a confirm that the camera noise in the images acquired with the SIT camera is negligible.

Figure 7-5 shows the 2-D NPS of single frame dark current images from the SIT camera acquired by the OC-500. The spectral peaks that were present in Fig. 7.4 are absent in this spectrum indicating that this feature is introduced by the ITI-151 frame grabber. However, there is an increase in spectral values at u = 0.219, 0.326, 0.45, and 0.568 mm^{-1} due to the fixed pattern noise introduced by the OC-500 system. These differences in the spectra acquired by the two frame grabbers clearly indicate that frame grabbers can introduce spatial fixed pattern noise.

Two dimensional noise power spectrum of single frame images of the water phantom acquired with the Newvicon camera are shown in the Fig. 7-6. Although the dose delivered to the phantom during a video frame is only 0.167 cGy, the lag in the Newvicon makes the effective dose used in producing the images somewhat higher. The

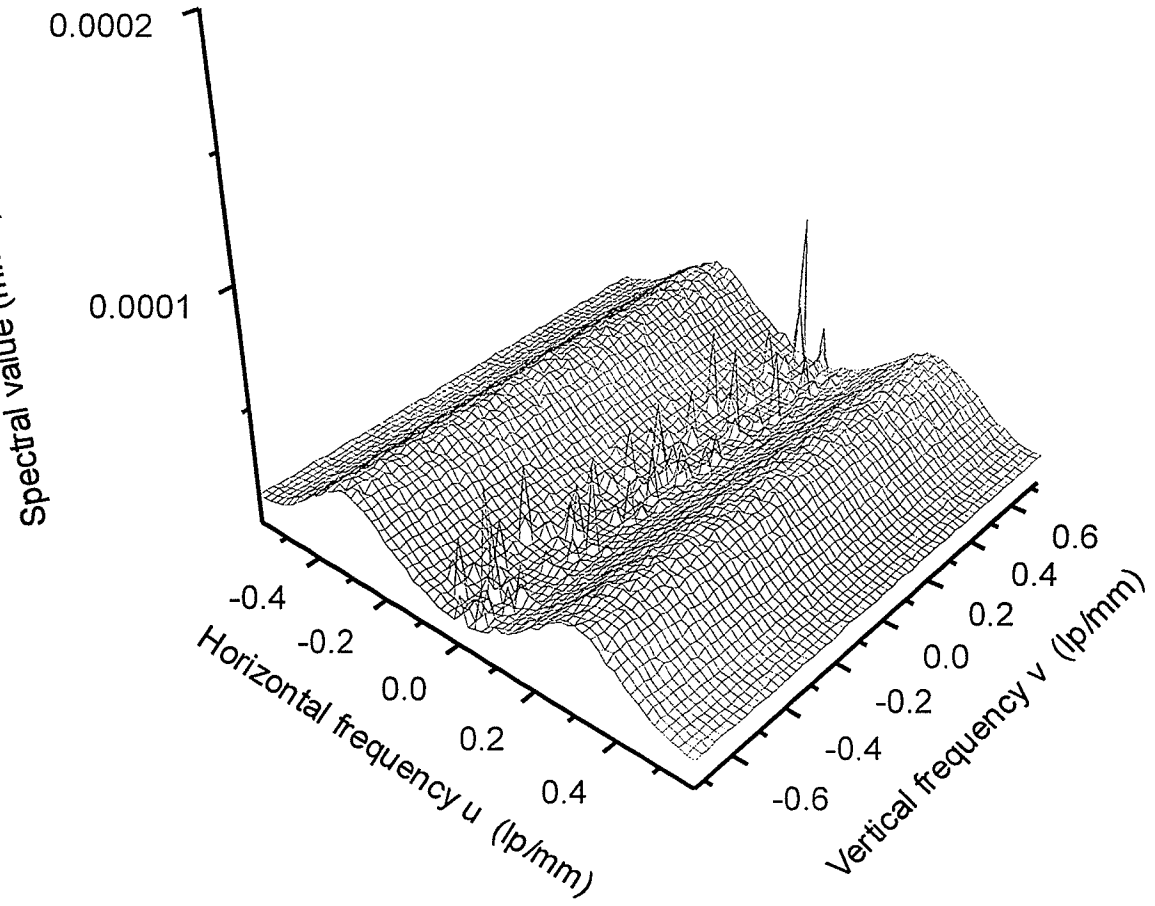

Figure 7-4. 2-D noise power spectra of single frame dark current images of the SIT camera acquired by the ITI-151 grabber.

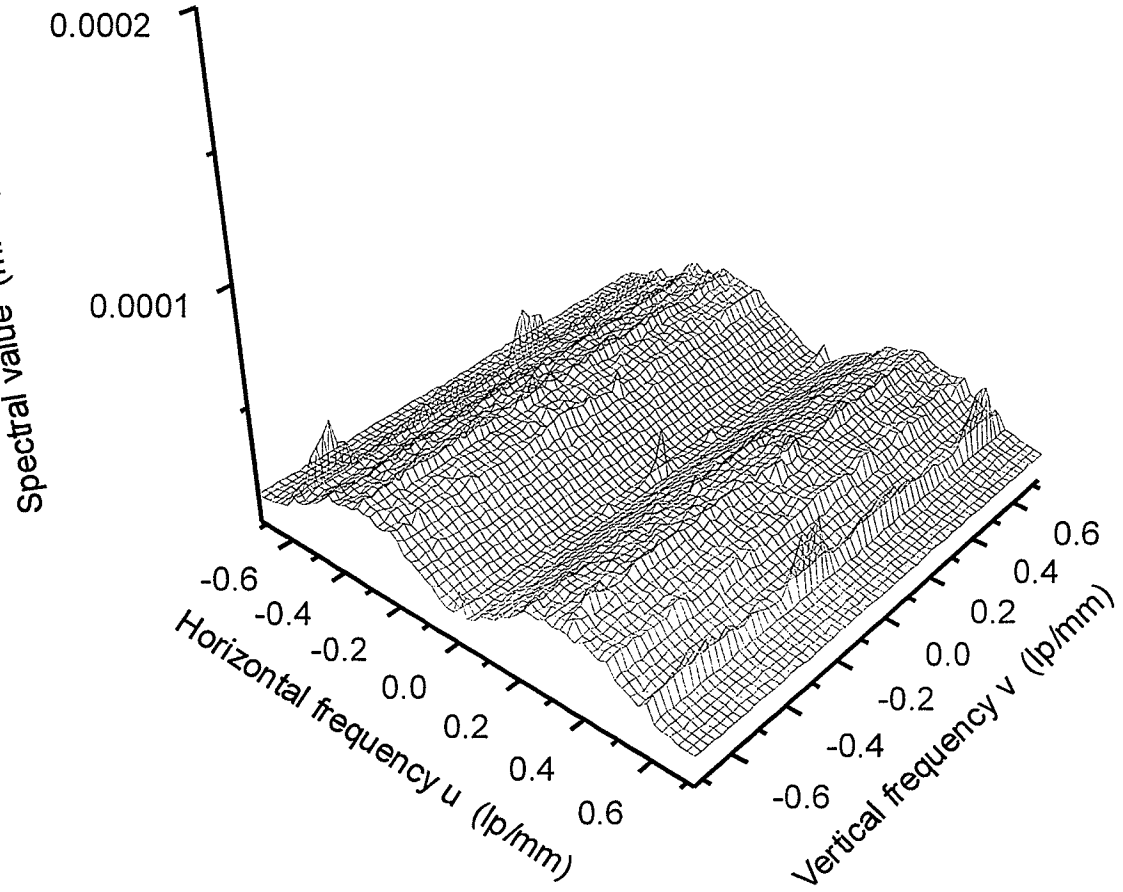

Figure 7-5. 2-D noise power spectra of single frame dark current images of the SIT camera acquired by the OC-500 grabber.

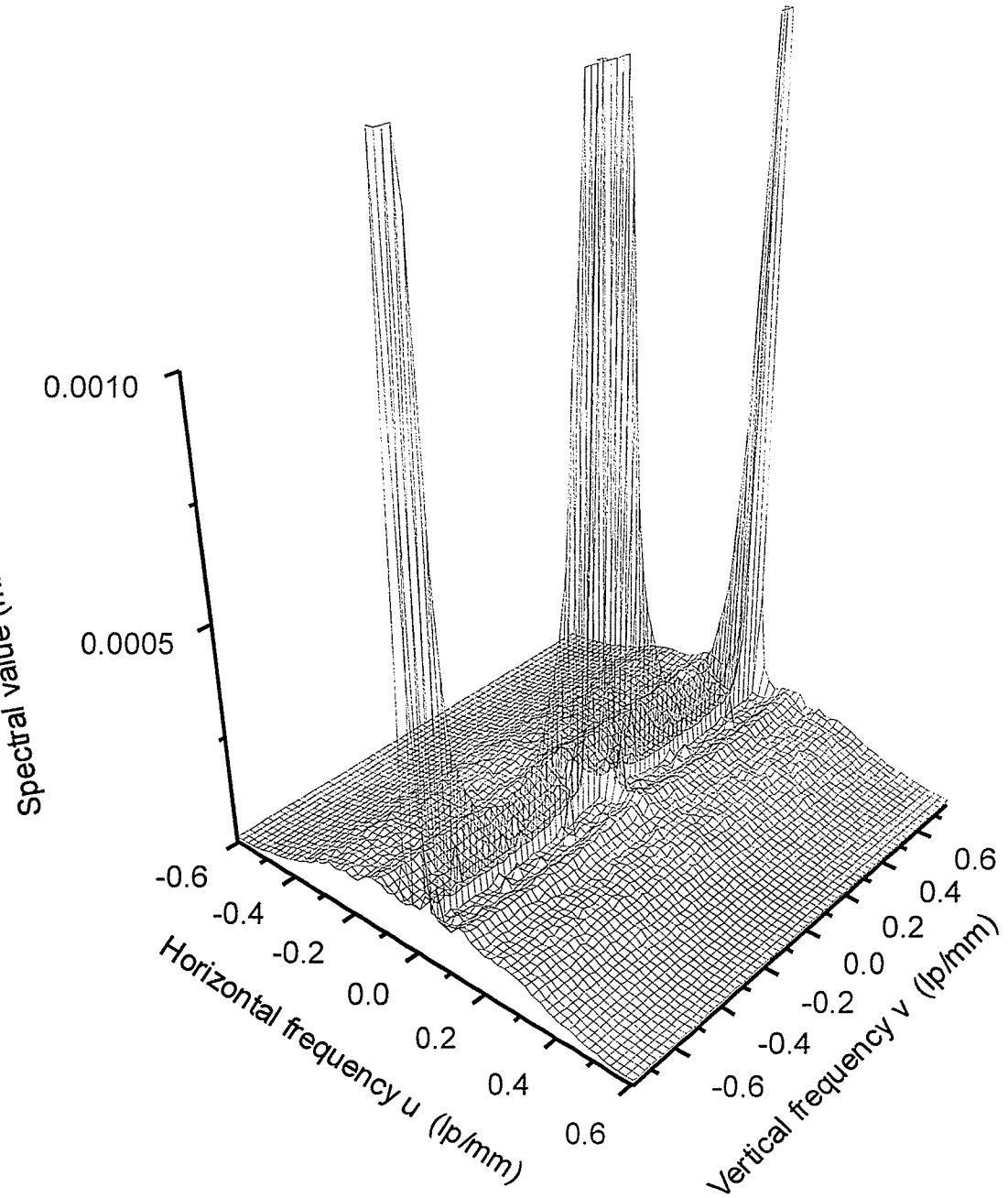

Figure 7-6. Two dimensional noise power spectrum of single frame water phantom images acquired with the Newvicon camera. Fixed pattern noise introduced by the ITI-151 grabber is also seen in this spectrum.

increase in the spectral values along the v axis due to the two pulsation artifacts can be seen. The roll-off in the NPS in u direction due to the anti-aliasing filter can also be seen.

Figure 7-7 shows the 2-D NPS of single frame dark current images of the Newvicon camera acquired by the ITI-151. The similarity of the shape of this spectrum to that of the Fig. 7-6 confirms that the noise in the images acquired with the Newvicon camera is dominated by the camera electronic noise. The spatial fixed pattern noise introduced by the frame grabber is not visible in this spectrum since the camera noise is much higher in the Newvicon camera.

7.4.2 The effect of second quantization

Noise power spectra of the phantom images acquired with the Newvicon camera by averaging 256 video frames are shown in the Fig. 7-8. Figure 7-8a is the spectrum of the images obtained by floating point frame averaging, and Fig. 7-8b is the spectrum of the images obtained by integer (digital) frame averaging. It was shown in Chapter 3 that the integer frame averaging used in the portal imaging system introduces quantization noise. The increase in the NPS due to the second quantization (integer frame averaging) is quite significant in these 256 frame averaged images. It can be seen that the effect of quantization noise is almost white (equally distributed within the whole spectrum). The three small spikes in the horizontal frequency axis and the small spike in the vertical frequency axis are due to the temporal variation in the spatial fixed pattern noise in the Newvicon camera. It was shown earlier that time jitter converts some of the spatial fixed pattern noise into random noise[25].

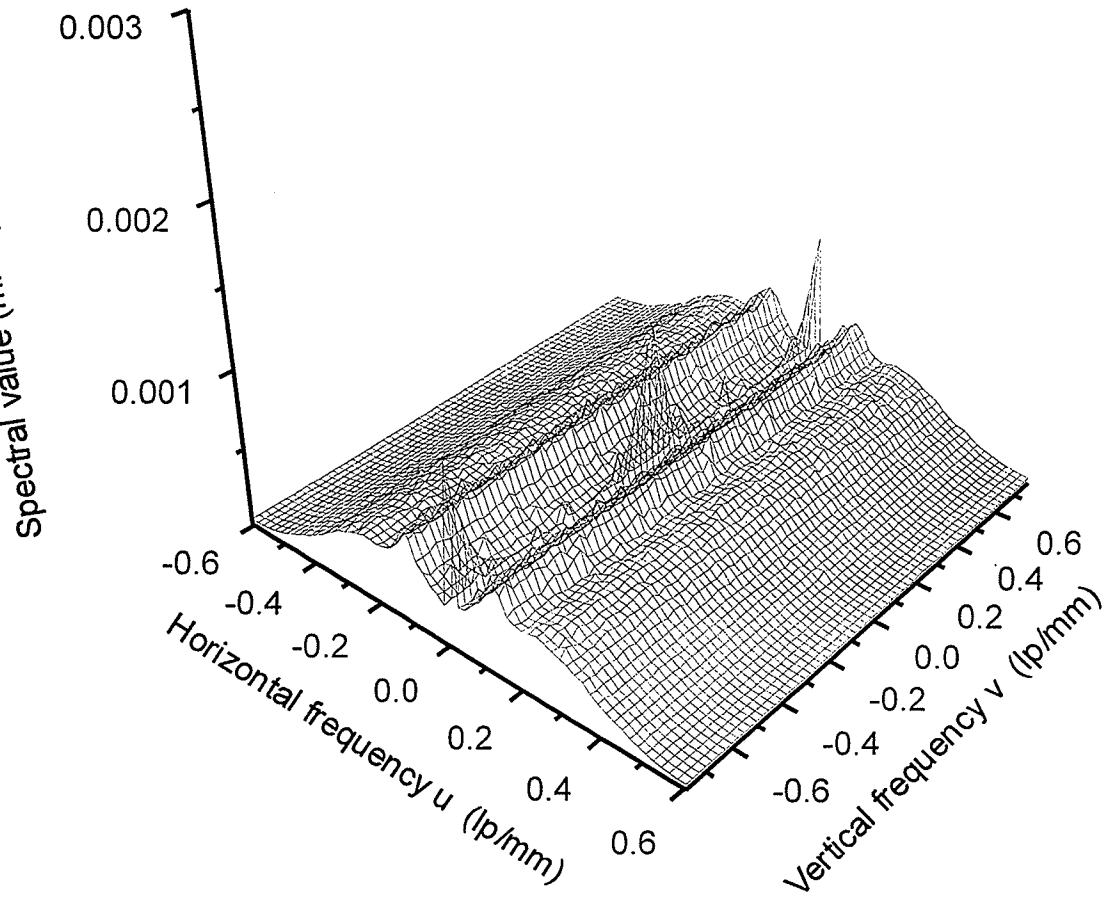

Figure 7-7. 2-D noise power spectra of single frame dark current images of the Newvicon camera acquired by the ITI-151 grabber. Similarity in this spectrum and that of Fig 7-6 indicates that the noise in portal images acquired by the Newvicon camera is dominated by the camera electronic noise.

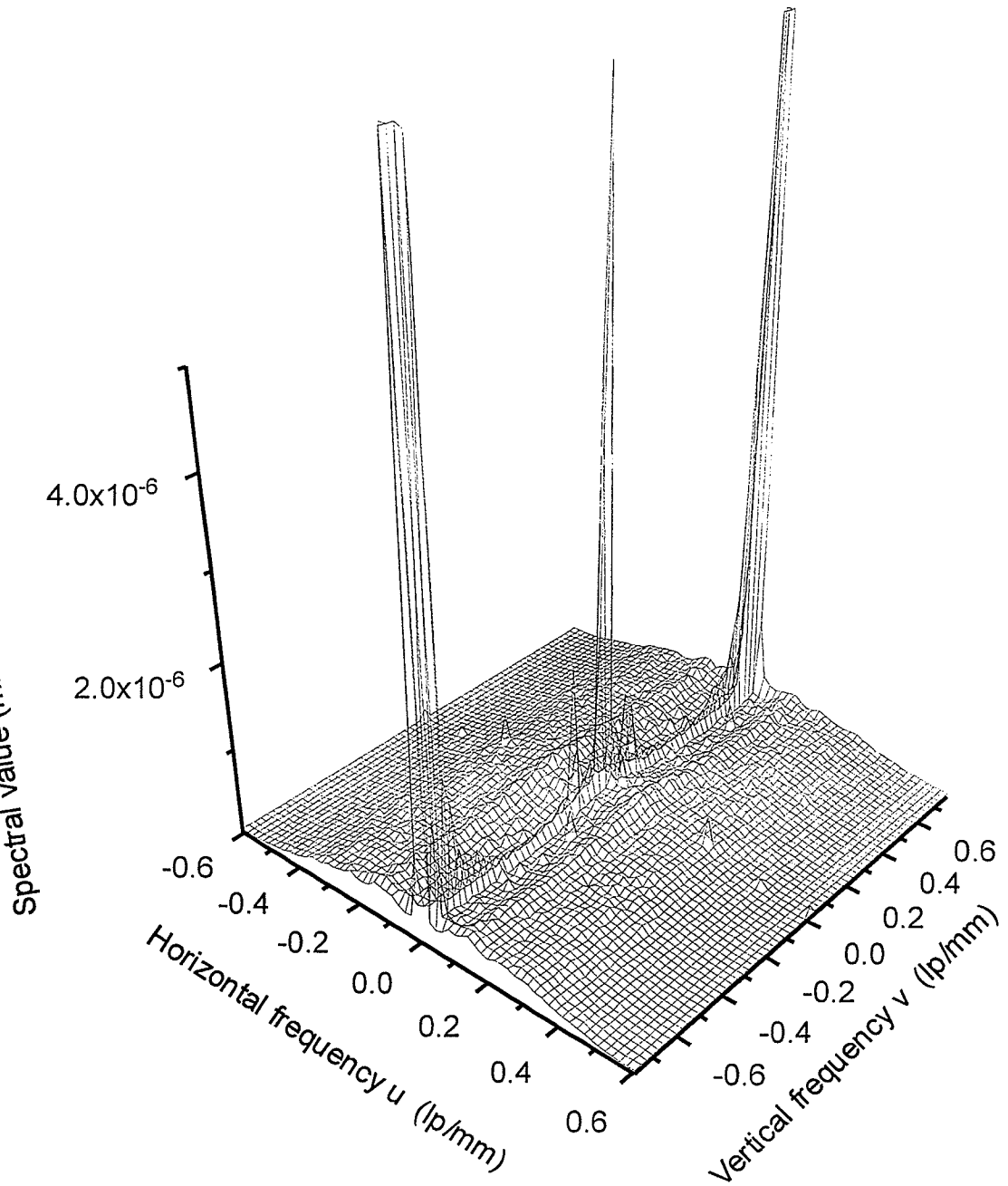

Figure 7-8. a) 2-D noise power spectra of water phantom images acquired with the Newvicon camera by averaging 256 frames in floating point (or digital addition).

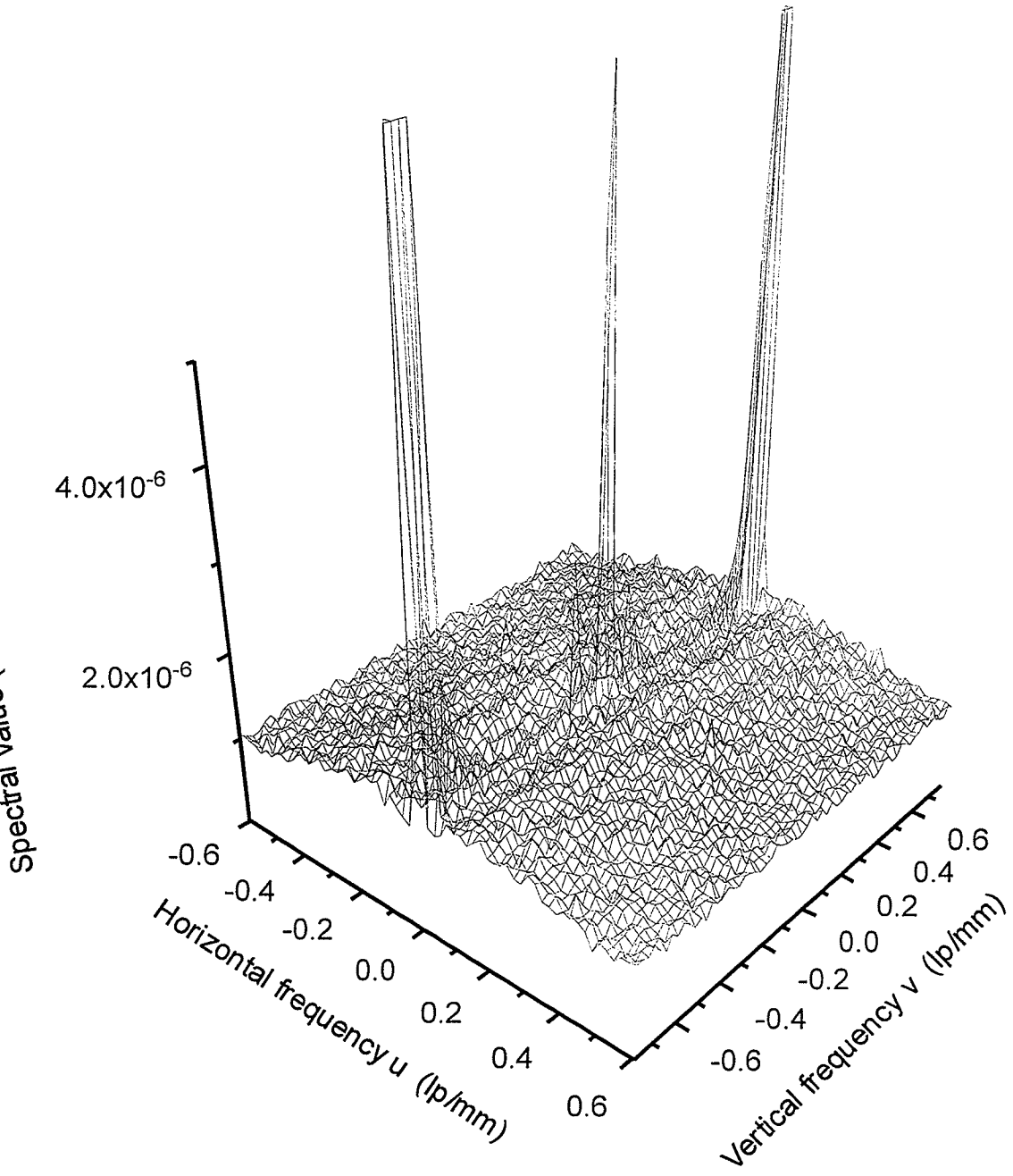

Figure 7-8. b) 2-D noise power spectra of water phantom images acquired with the Newvicon camera by digitally averaging 256 frames. The increase in the noise power is due to the second quantization.

7.4.3 Results of the CCD camera

Figure 7-9 shows the 2-D NPS of single frame water phantom images of the CCD camera. The fixed pattern noise from the OC-500 frame grabber can be clearly seen in this spectrum. The extra noise due to pulsation artifacts is absent, but an increase in the spectral values along the central slice of the vertical direction due to the clamping noise is seen. It is clearly seen that the two dimensional nature of this spectrum can not be represented by the two central slices. Figure 7-10 shows the similar spectrum obtained by using the light box, which also exhibits similar clamping noise. Comparison of the two spectra indicates that the spectra of the portal images have higher spectral values at low frequencies due to the X-ray quantum noise.

The differences in the noise power at low frequencies between portal images and that of the light box images can not be observed properly along the u direction due to the effects of the anti aliasing filter. Furthermore, the central slice along the vertical direction can not be used either due to the effects of clamping noise. Therefore the average of the two vertical slices NPS(0.00609,v) and NPS(0.01219,v) are shown in Fig. 7-11 for water phantom images and for light box images. Comparison of the results between water phantom images and the light box images clearly show the increase in spectral value in the portal images due to X-ray quantum noise at low frequencies.

7.5 Conclusions

A novel method has been used to measure the 2-D NPS of real-time portal images. Comparison of the NPS of the images obtained with different cameras and different frame grabbers have been used to identify the sources of noise which contribute to the NPS. It has been shown that pulsation artifacts introduce extra noise along the vertical frequency axis in real-time portal images. It has also been shown that the 1-D and 2-D calculations of the central slices of the 2-D NPS and the averages of the 2-D spectra taken over one direction, give the same results. However, it has been shown that

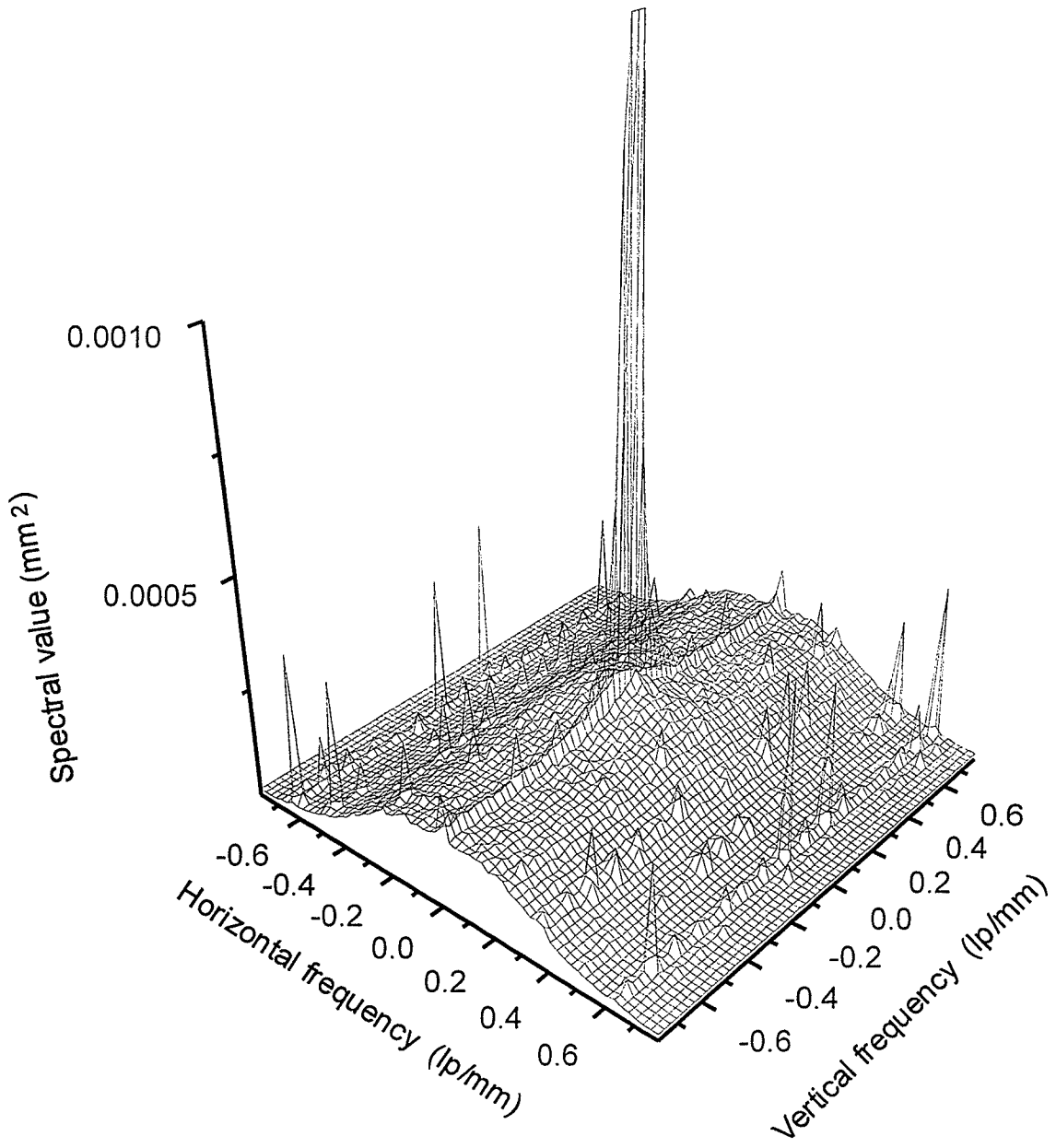

Figure 7-9. Two dimensional noise power spectrum of single frame water phantom images acquired with the CCD camera.

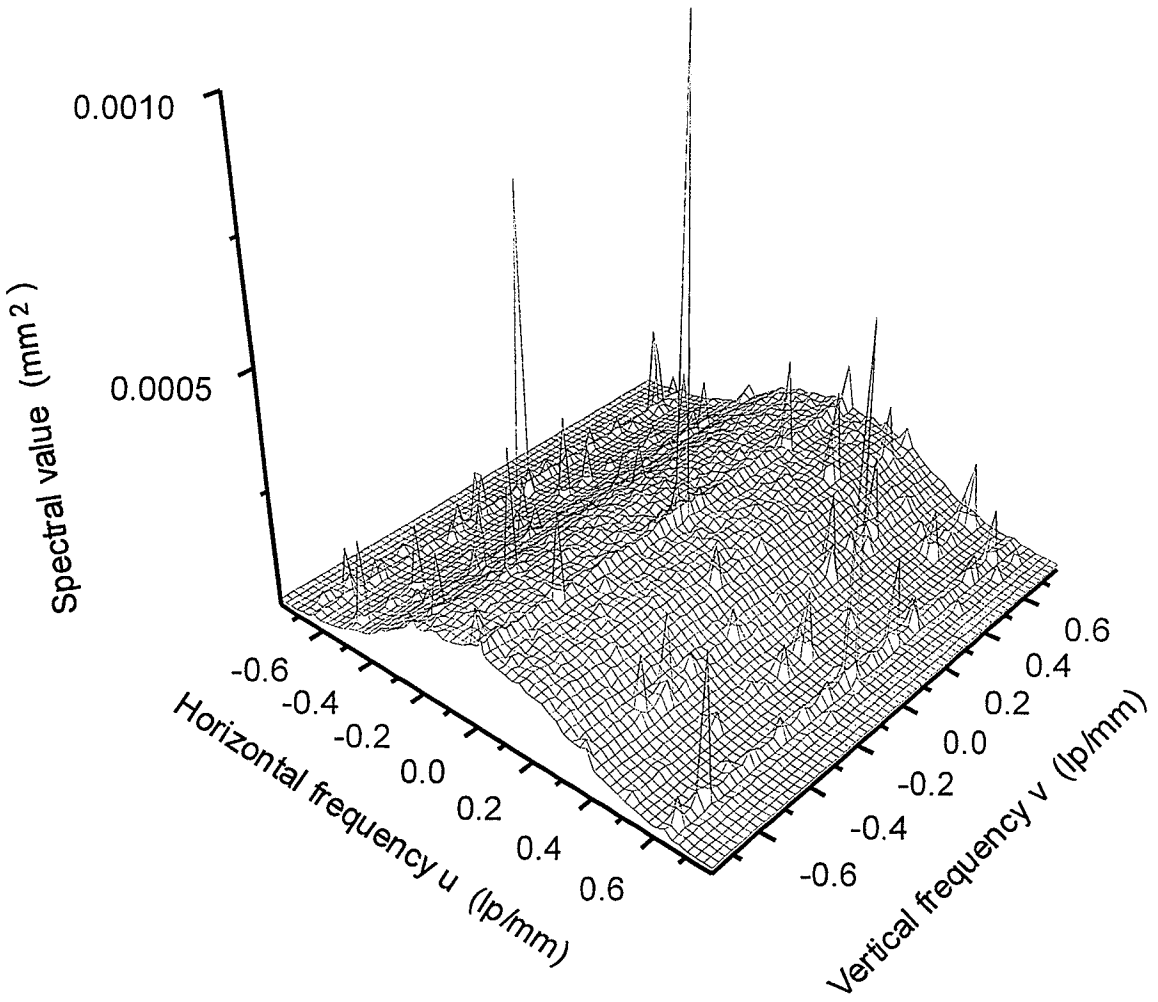

Figure 7-10. Noise power spectrum of images acquired with the CCD camera when illuminated with a light box.

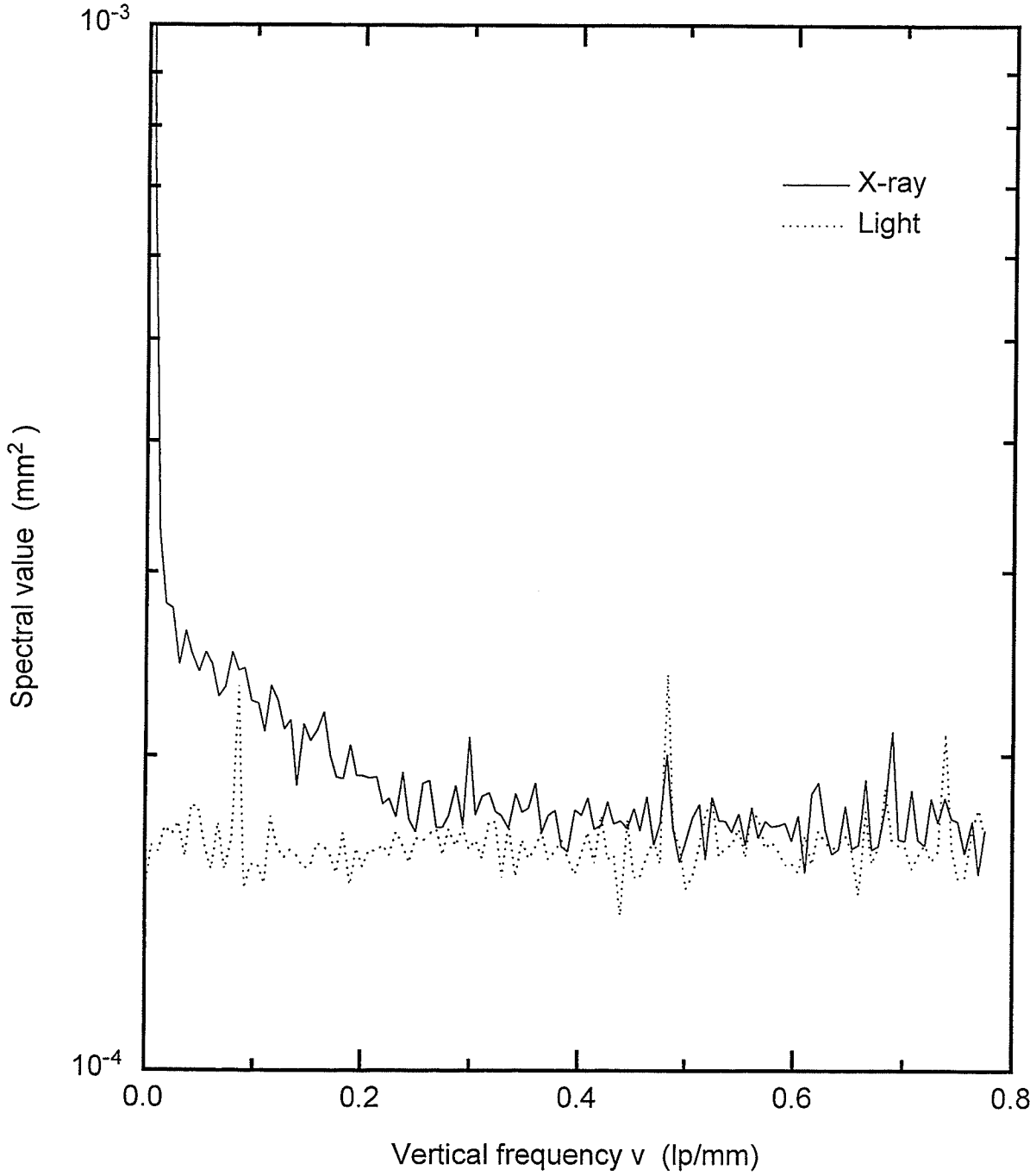

Figure 7-11. Average value of the vertical slices NPS(0.00609,v) and NPS(0.01219,v) for the water phantom images (X-ray) and light box images (Light) acquired with the CCD camera.

the central slice along the v axis can give an over-estimate of the spectra due to the extra clamping error and pulsation artifacts which contribute only to the noise power along the v axis. Noise in the portal images acquired by the SIT camera is shown to be dominated by the optical photon noise, whereas the noise in the images acquired by the Newvicon camera is dominated by the camera noise. X-ray quantum noise is significant in the portal images acquired by the CCD camera at low spatial frequencies. It is also shown that frame grabbers can introduce temporally variable, but spatially fixed noise, and the noise power due to the second quantization is "white". It is shown that 2-D noise power spectra calculations are necessary for real-time video based imaging since NPS in these situations can have 2-D structure.

References

[1] R. C. Jones, "New method of describing and measuring the granularity of photographic materials," J. Opt. Soc. Am. **45,** 799-808 (1955).

[2] P. Elias, D. S. Grey, and D. Z. Robinson, "Fourier treatment of optical processes," J. Opt. Soc. Am. **42,** 127-134 (1952).

[3] P. Elias, "Optics and communication theory," J. Opt. Soc. Am. **43,** 229-232 (1953).

[4] P. Fellgett, "Concerning photographic grain, signal-to-noise ratio and information," J. Opt. Soc. Am. **43,** 271-282 (1953).

[5] K. Doi, "Scans in measuring Wiener spectra for photographic granularity," Japanese Journal of Applied Physics **5,** 1213-1216 (1966).

[6] H. Frieser, "Noise spectrum of developed photographic layers exposed by light, X-rays and electrons," Phot. Sci. Eng. **3,** 164-169 (1959).

[7] E. Klein and G. Langner, "Relations between granularity, graininess and the Wiener-spectrum of the density deviations," The Journal of Photographic Science **11,** 177-185 (1963).

[8] M. De Belder and J. De Kerf, "The determination of the Wiener spectrum of photographic emulsion layers with digital methods," Phot. Sci. Eng. **11,** 371-378 (1967).

[9] R. Shaw, "Evaluating the efficiency of imaging process," Rep. Prog. Phys. **41,** 1103-1155 (1978).

[10] K. Rossmann, "Modulation transfer function of radiographic systems using fluorescent screens," J. Opt. Soc. Am. **52,** 774-777 (1962).

[11] K. Rossmann, "Recording of X-ray quantum fluctuations in radiographs," J. Opt. Soc. Am. **52,** 1162-1164 (1962).

[12] K. Rossmann, "Spatial fluctuation of x-ray quanta and the recording of radiographic mottle," Am. J. Roentgenol. **90,** 863-869 (1963).

[13] K. Doi, "Wiener spectrum analysis of quantum statistical fluctuations and other noise sources in radiography," in *Television in diagnostic radiology*, edited by R. D. J. Mosely and J. J. Rust (Aesculapius Publishing Company, Birmingham, Alabama, 1969), pp. 313-331.

[14] T. Fu and H. Roehrig, "Noise power spectrum, MTF, and DQE of photoelectronic radiographic systems," SPIE **454,** 377-386 (1984).

[15] H. Fujita, K. Doi, and M. L. Giger, "Investigation of basic imaging properties in digital radiography. 6. MTFs of II-TV digital imaging systems," Med. Phys. **12,** 713-720 (1985).

[16] M. L. Giger, K. Doi, and H. Fujita, "Investigation of basic imaging properties in digital radiography. 7. Noise Wiener spectra of II-TV digital imaging systems," Med. Phys. **13,** 131-138 (1986).

[17] Y. Kume, K. Doi, K. Ohara, and M. L. Giger, "Investigation of basic imaging properties in digital radiography. 10. Structure mottle of II-TV digital imaging systems," Med. Phys. **13,** 843-849 (1986).

[18] P. Munro and J. A. Rawlinson, "Therapy imaging: A signal-to-noise analysis of a fluoroscopic imaging system for radiotherapy localization," Med. Phys. **17,** 763-772 (1990).

[19] M. L. Giger, K. Doi, and C. E. Metz, "Investigation of basic imaging properties in digital radiography. 2. Noise Wiener spectrum," Med. Phys. **11,** 797-805 (1984).

[20] L. W. Goldman, "Fluoroscopic performance tests using a portable computer/frame grabber: Wiener spectra measurements," Med. Phys. **19,** 45-52 (1992).

[21] M. J. Tapiovaara, "SNR and noise measurements for medical Imaging: II. Application to fluoroscopic x-ray equipment," Phys. Med. Biol. **38,** 1761-1788 (1993).

[22] J. C. Dainty and R. Shaw, *Image Science,* (Academic Press, London, 1974).

[23] W. H. Press, S. A. Teukolsky, W. T. Vetterling, and B. P. Flannery, *Numerical recipes in C : The art of scientific computing,* 2nd (Cambridge University Press, Cambridge, 1992).

[24] J. A. Rowlands, "Optimazation of readout rate of television cameras in pulsed digital radiography," Med. Phys. **14,** 341-348 (1987).

[25] P. O. Scheibe and A. J. Thomas, "Noise sources in digital fluoroscopy," SPIE **314,** 202-209 (1981).

Chapter 8

Quality control for VEPIDs

8.1 Introduction

Verification of field placement is an essential part of a comprehensive quality assurance program for radiation oncology, and a recent AAPM Task Group Report[1] recommends acquiring portal images at least once a week. With the development of electronic portal imaging devices[2] (EPIDs), verification is now much simpler and can be carried out on a more frequent basis, with the expectation of reducing gross field placement errors and increasing overall treatment accuracy. However, the efficacy of an EPID depends on the image quality[3], and so it is essential to devise quality control (QC) tests for the devices themselves. Such tests are required by the manufacturer at installation, and by the user throughout the lifetime of the equipment. In particular, when the optimized portal imaging system described in this thesis is clinically implemented, it is very important that the users can verify that it is operating at the optimal level

Unfortunately the quality assurance of EPIDs is not mentioned in the recently published AAPM code of practice for radiotherapy accelerators[4]. However, as these systems become part of regular clinical practice, it will be necessary to ensure their correct and reliable operation at all times. Even if the image quality is optimal at installation, a number of factors can lead to deterioration over time. Specially, video-based electronic portal imaging devices (VEPIDs) may suffer from shifting or deformation of the detector housing, dust or dirt on lenses and mirrors, loose or unfocused optical components, improper frame grabber or computer control settings, or malfunctioning electronic equipment. Qualitative visual QC checks have been suggested[5] using the Lutz[6,7] and the Las Vegas[8,9] phantoms, but a less subjective approach is necessary for routine daily quality control. A recent proposal involves the

construction of contrast-detail curves using the spectral properties of the radiation beam to compute the contrast of the test objects[10], but its implementation with EPIDs has yet to be evaluated.

The development of an objective, quantitative QC test for VEPIDs which is simple to perform and which requires no observer skills or subjective decisions is presented. It is designed to test for acceptable performance in high contrast spatial resolution and contrast-to-noise ratio (CNR). Daily measurements have been made over a period of several months, and the test is shown to be sensitive to variations in the measured parameters when preventative maintenance procedures are carried out or when system parameters are adjusted.

8.2 Experimental method

A QC phantom was designed for use in the test, which consists of five sets of high-contrast rectangular bars with spatial frequencies of 0.1, 0.2, 0.25, 0.4, and 0.75 lp/mm. A schematic diagram of the QC phantom is shown in Fig. 8-1. The frame of the phantom is made of aluminum, and the five test sections are made of lead and Delrin (Acetal) plastic (density : 1.42 g cm^{-3}). The phantom is 15 mm thick and has 3 mm Acrylic and 2 mm aluminum cover plates on the top and the bottom respectively. With the VEPID located under the patient (0° in the Siemens gantry coordinate system), the phantom is placed on the top of the VEPID detector housing in order to acquire test images. This location preferred rather than the isocenter in order to minimize blurring due to the beam penumbra, since the test is intended to monitor the performance of the VEPID and should be independent of the linac source size. The phantom is rotated to 45° relative to the video scan lines to prevent aliasing in the images of the bar patterns. A simple frame to attach the phantom on the detector housing was also designed in order to be able to acquire images at all gantry angles.

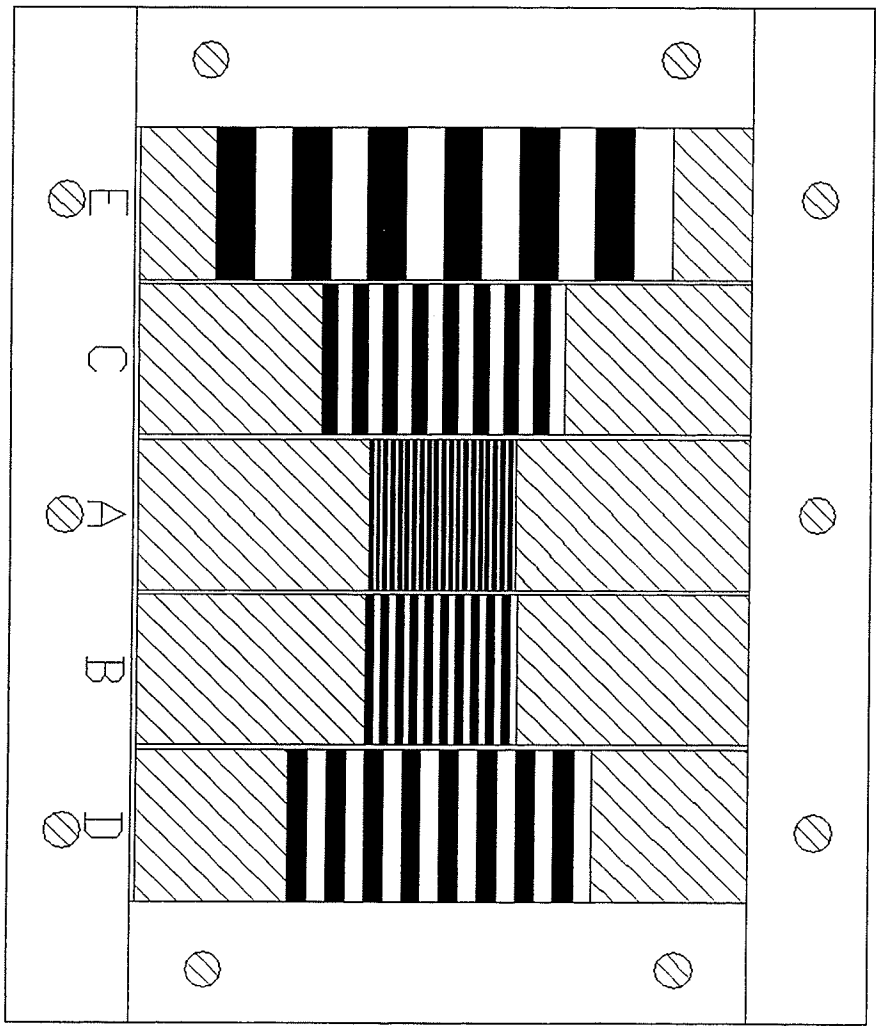

Figure 8-1. A schematic diagram of the QC phantom. See text for details.

The QC phantom has been used on two different VEPIDs. The first was the prototype BEAMVIEW system* which used a PC-386 computer for image acquisition, processing, display and storage. Only spatial resolution tests were made with this system. The second VEPID was the BEAMVIEW^{PLUS} system* based on a Sun workstation, from which images were downloaded via PC-NFS to a PC-386 for analysis of both spatial resolution and CNR. The experimental technique consists of four steps: first, the phantom is placed on the VEPID housing, the radiation beam is switched on, and the digital gain and offset (threshold) are adjusted to achieve maximum contrast without saturating the video signal. Second, two video images are acquired, each the average of 16 video frames (0.54 s or about 2 MU). Third, the images are ported to the analysis program, and the position of the phantom is delineated on the monitor by the operator. The fourth step is the totally automatic analysis of the images without operator interaction.

The analysis program places a region of interest (ROI) over each set of bars as shown in Fig. 8-2. The frequency dependent Square Wave Modulation Transfer Function (SWMTF) is determined by the method proposed by Droege[11] and the frequency for 50% modulation (f_{50}) is compared with the predetermined critical frequency f_c as a test of system performance. In addition, values of the CNR are calculated and compared with the predetermined critical value CNR_c.

8.2.1 Determining the SWMTF

The SWMTF of an imaging system is defined as[12]

$$SWMTF(f) = \frac{\Delta E(f)}{\Delta E_0} \qquad (8\text{-}1)$$

* Siemens Medical Systems Inc., Concord, CA.

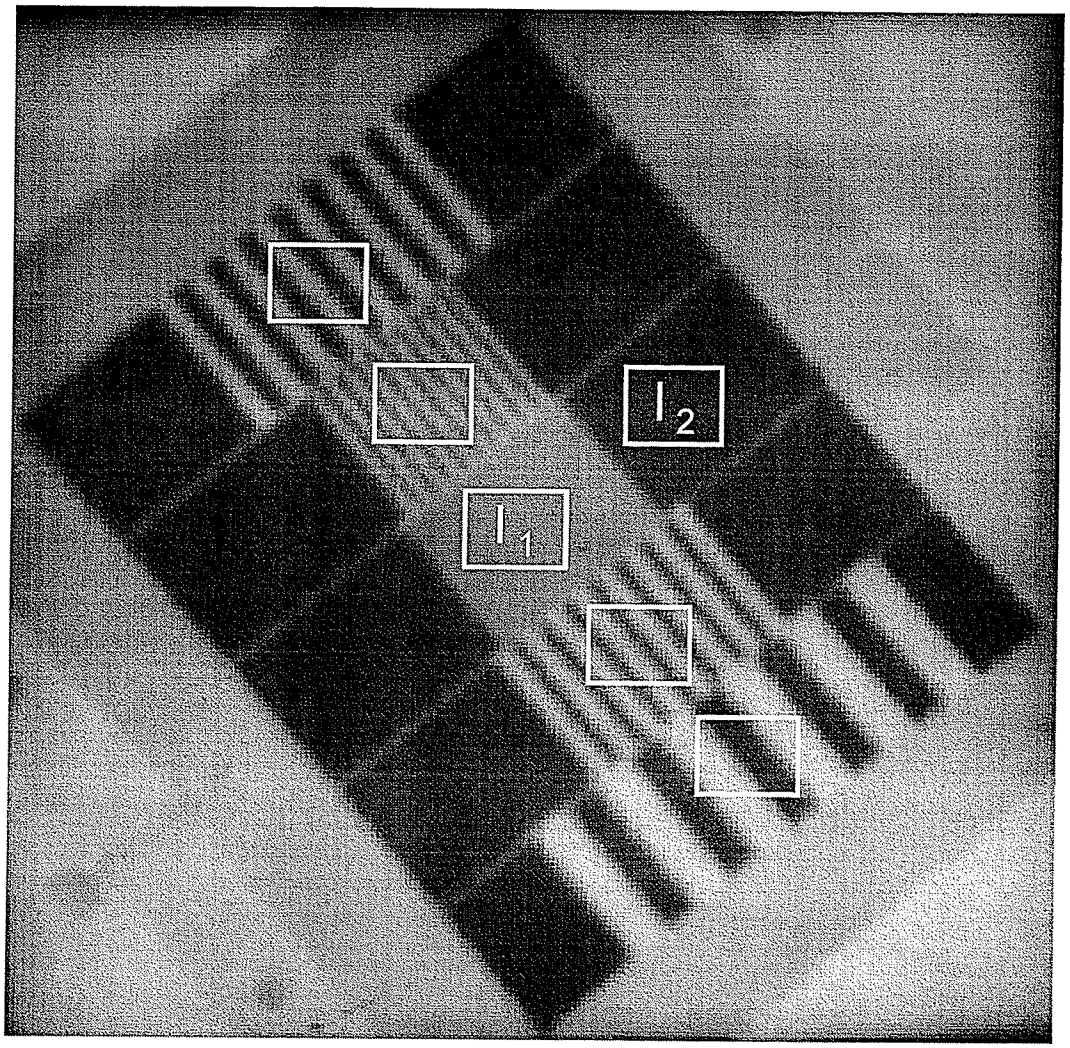

Figure 8-2. A portal image of the QC phantom at diagonal orientation obtained with the BEAMVIEW portal imaging system. The ROI's used for the QC test are marked on the image.

where ΔE_0 and $\Delta E(f)$ are the modulations of input to and output from the system. Since an absolute measure of the SWMTF is not necessary in determining day-to-day variations in the system resolution, a relative measure (RMTF) of the SWMTF can be used by calculating;

$$RMTF(f) = \frac{\Delta E(f)}{\Delta E(f_l)} \tag{8-2}$$

where $\Delta E(f_l)$ is the output modulation for the lowest frequency. Usually the output modulation $\Delta E(f)$ is difficult to obtain from a noisy image, and therefore Droege and Morin[13] suggested using the relationship between a signal amplitude and its variance. For a sinusoidal output, $(\Delta E)^2$ is proportional to the variance $(M)^2$ within an ROI containing the bar pattern, and the above relation can be rewritten as

$$RMTF(f) = \frac{M(f)}{M(f_l)}. \tag{8-3}$$

In the presence of random image noise, $M(f)$ can be obtained by

$$M^2(f) = \sigma_m^2(f) - \sigma^2(f) \tag{8-4}$$

where $\sigma_m^2(f)$ and $\sigma^2(f)$ are the measured total variance and the variance due to random noise, respectively. The total variance $\sigma_m^2(f)$ is obtained by measuring the variance of the pixels in the ROI corresponding to frequency f. In order to measure the random noise in an image, a pair of similar images are subtracted and the standard deviation obtained from the difference, thus avoiding contributions from fixed pattern noise. In this case, the variance of the subtracted ROI (σ_{sub}^2) will be

$$\sigma_{sub}^2 = \sigma_1^2 + \sigma_2^2 \tag{8-5}$$

where σ_1^2 and σ_2^2 are the random noise variances of the ROI's for each image. Assuming that these two variances are equal we get;

$$\sigma_1 = \sigma = \sigma_{sub}/\sqrt{2}. \tag{8-6}$$

The variance $\sigma^2(f)$ is calculated once using Eq. 8-6, for the set of bars with the highest frequency (0.75 lp/mm) on the assumption that random noise is same for all ROI's.

8.2.2 The extraction of f_{50}

Three methods were tested for obtaining the critical frequency f_{50} for which the response is 50% of the maximum from the RMTF(f) data. In the first method, f_{50} was obtained by interpolating between the two data points immediately below and above the 50% response. A check is carried out before evaluating the RMTF(f) to verify $\sigma_m^2(f)$ decreases as the frequency inc.eases. The second method used a second order least squares polynomial fit to the RMTF(f) data, and the third method incorporated a least squares fit to the logit function. Figure 8-3 shows the RMTF data for the test image pair with the three different fits to extract f_{50}.

A series of tests was carried out using a pair of test images as well as four additional image pairs intended to simulate the degradation of imaging performance[14]. These additional images were obtained from the original pair of test images by (a): adding Gaussian noise with σ = 5, (b): adding Gaussian noise with σ = 10, (c): performing a 3x3 blur, and (d): performing a Gaussian blur with σ = 5. Figure 8-4 shows the results of the three different fits to extract f_{50} from the image pair obtained by

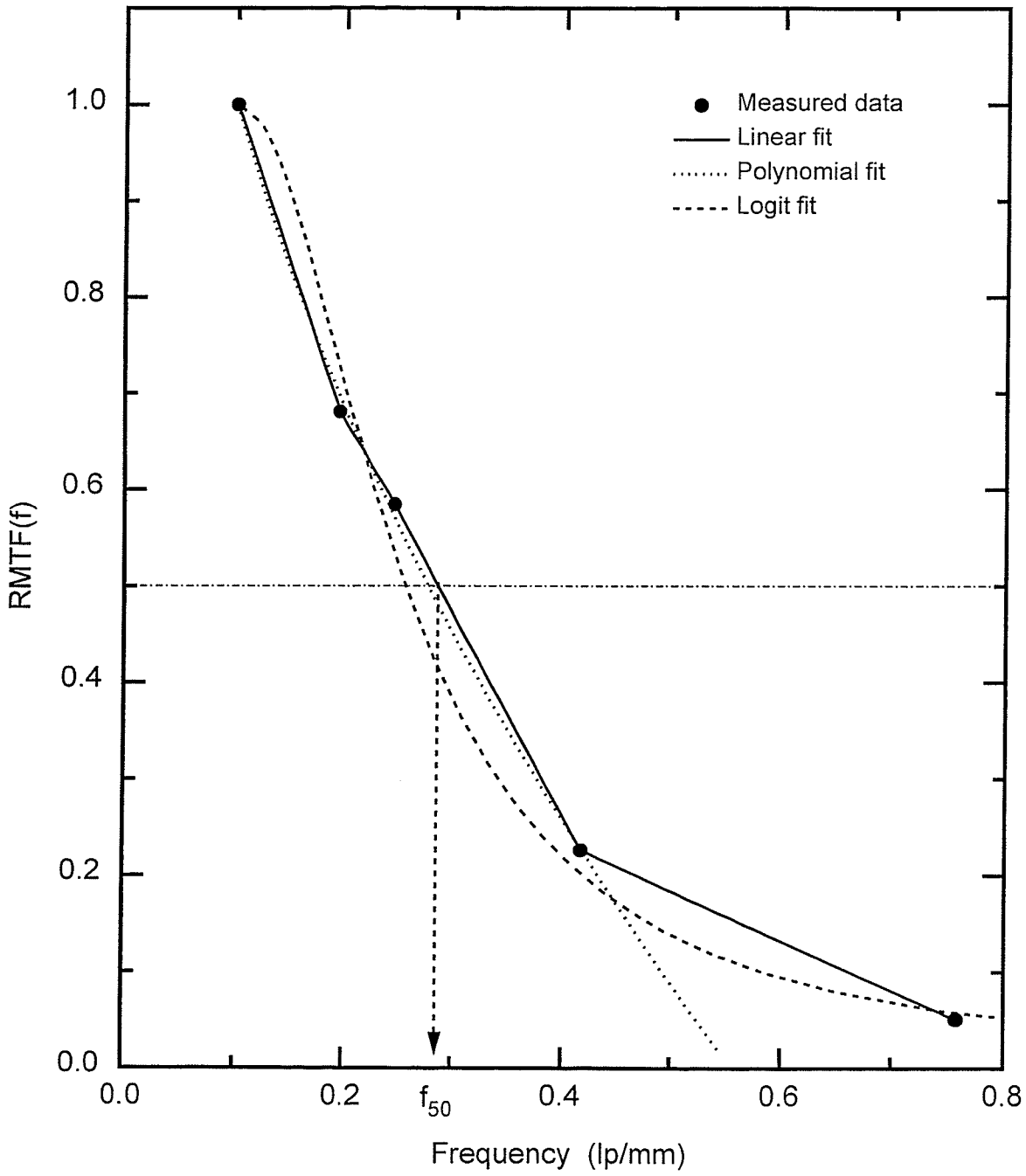

Figure 8-3. The RMTF curve for the test image pair showing the three types of fitting used to obtain the value of f_{50}.

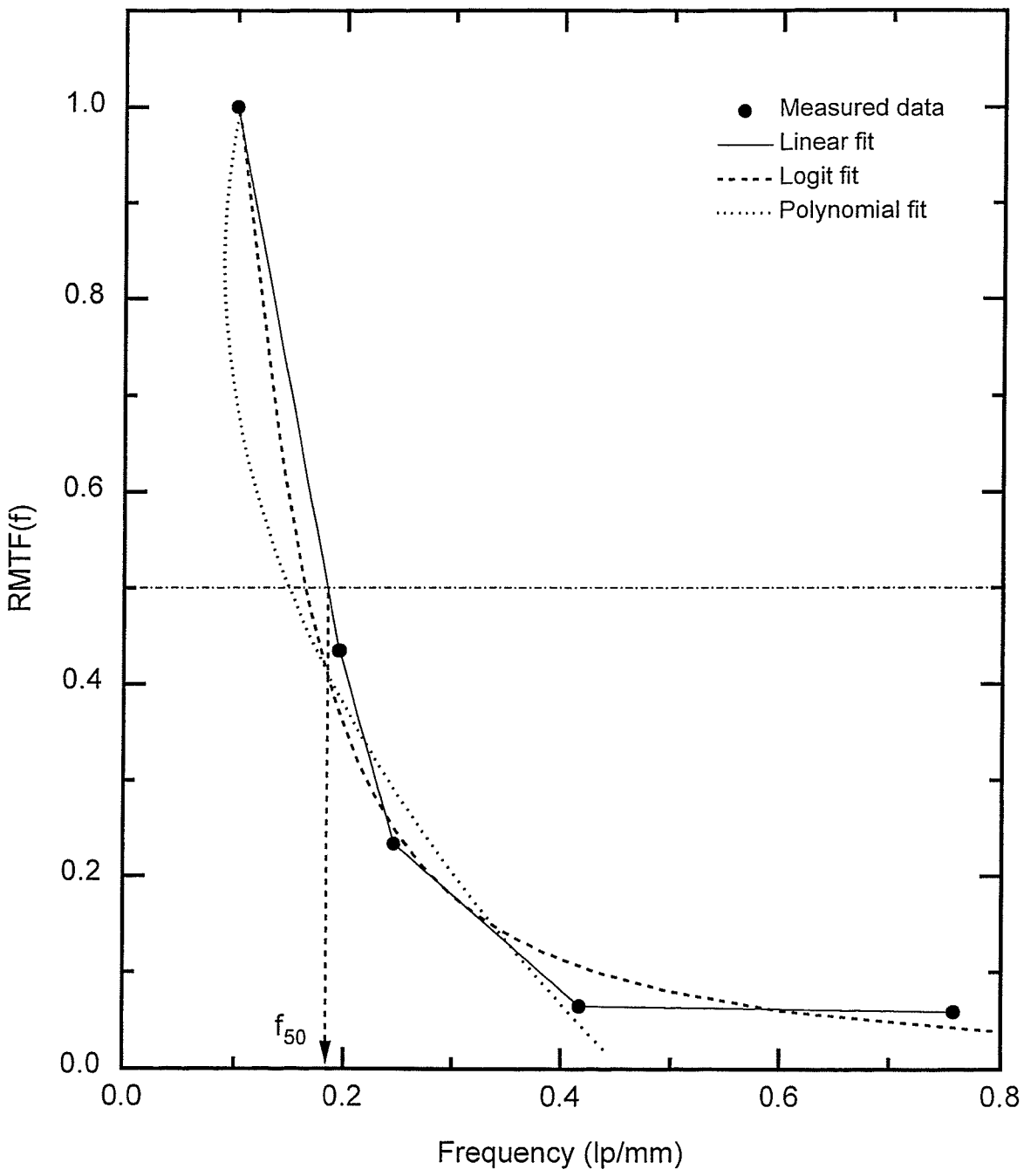

Figure 8-4. The results of the three different fits to extract f_{50} from the image pair obtained by performing a 3x3 blur.

performing a 3x3 blur. Figures 8-3 and 8-4 clearly indicate that linear interpolation is the most reliable criterion for determining f_{50}, and therefore was adopted for use in the routine QC test.

8.2.3 Determining the CNR

The CNR for the QC test was calculated by

$$CNR = \frac{I_1 - I_2}{\sigma} \tag{8-7}$$

where I_1 and I_2 are the average gray values of the brightest and darkest ROI's as shown in Fig. 8-2. The calculation of random image noise, σ, was described in section **8.2.1**.

8.2.4 Phantom alignment

The BEAMVIEW and BEAMVIEW^{PLUS} portal imaging systems utilize non-square pixels giving rise to different MTF's in horizontal and vertical directions. By using the diagonal phantom orientation, as shown in Fig. 8-2, a combined measure of resolution in both directions could be obtained, as well as a reduction in errors due to possible changes in ROI size and positioning[11]. The robustness of the algorithm for the determination of RMTF(f) was tested against the ROI size and positioning for this phantom orientation using the 0.2 lp/mm section of a test image. The result was found to vary with an rms deviation less than 0.7% for a change in ROI dimensions and position by $\pm$ 5 pixels. The robustness of the complete QC procedure was tested by repeating the test 10 times, and the rms deviation of the results was less than 0.6%. Changes in field size and increasing the image acquisition times did not have a significant impact on the measured results.

8.3 Results

Measurements were made daily on the BEAMVIEW imaging system mounted on a KD-2 dual energy linear accelerator. System performance was monitored during a calibration period of 18 days, and these data were used to determine the mean and standard deviation of f_{50}. Subsequently the value of f_c was arbitrarily set to be three standard deviations below the mean value. Any subsequent measurement in which the $f_{50} < f_c$ would be deemed a failure of the test, and a warning message displayed to the operator.

Figure 8-5 shows the daily plot of f_{50} for the BEAMVIEW portal imaging system during the calibration period and a later test period, for two treatment energies. Since the VEPID was mounted on a dual energy linac, it was possible to perform the QC test at both 6 and 23 MV. The dotted and dashed lines represent the ± 3 standard deviations determined during the calibration period and extrapolated to the test period for 6 and 23 MV respectively. It is seen that system resolution at 6 MV is superior to that at 23 MV, an effect which has been observed previously and is a result of the larger physical beam penumbra at higher energies[15,16]. There is a close correlation between the f_{50} values for the two energies, since changes in resolution are due to problems in the detector system. A trend in worsening resolution is seen from test day 29, and even though a number of tests failed, no action was taken to service the system. The BEAMVIEW imaging system was replaced by a BEAMVIEW^{PLUS} system at this time.

Figure 8-6 shows a plot of f_{50} recorded on a daily basis for the BEAMVIEW^{PLUS} system which includes the first 25 day calibration period and the subsequent test period. The dotted and dashed lines once again represent the ± 3 standard deviations determined during the calibration period and extrapolated over the test period. It is seen that f_{50} values at both 6 and 23 MV lie around 0.18 lp/mm for the BEAMVIEW^{PLUS} whereas values for the BEAMVIEW system are 0.29 and 0.23 lp/mm respectively. The superior resolution of the prototype VEPID is attributed to the Silicone Intensified Target camera

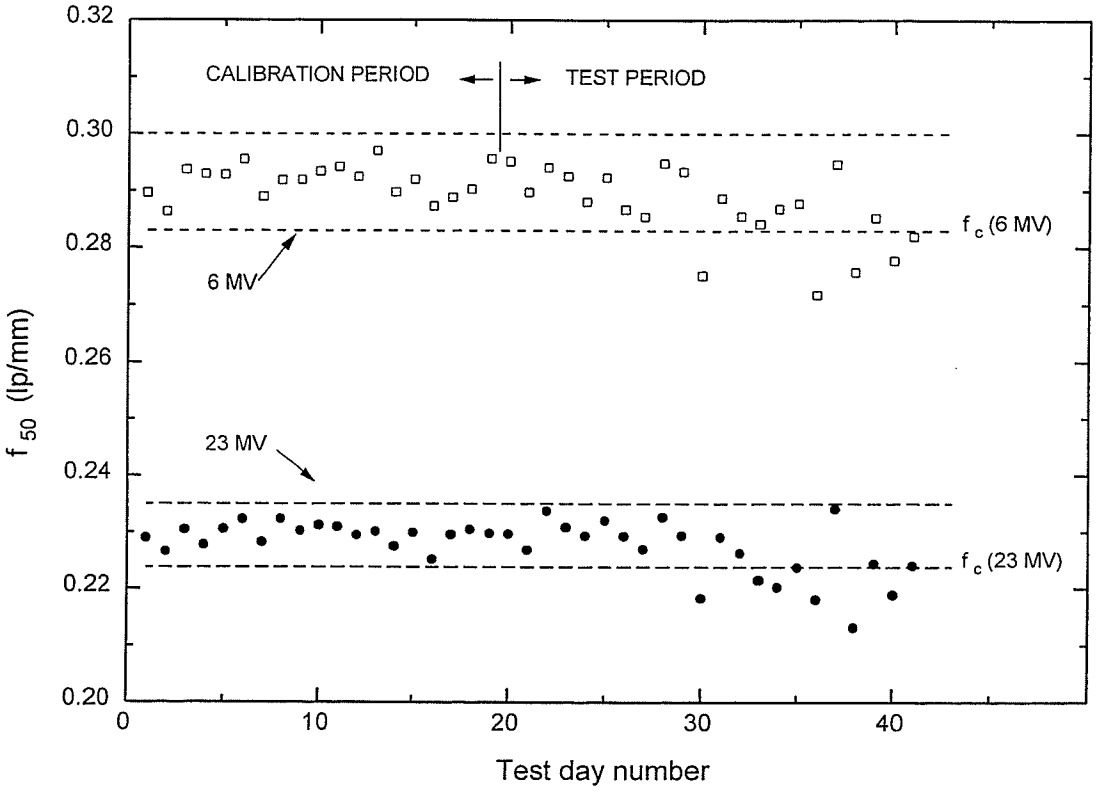

Figure 8-5. Plot of f_{50} recorded on a daily basis for the BEAMVIEW portal imaging system at gantry angle 0° at 6 and 23 MV. The two dotted and dashed lines indicate ± 3 standard deviations from the mean which were calculated from data taken during the first 18 test days.

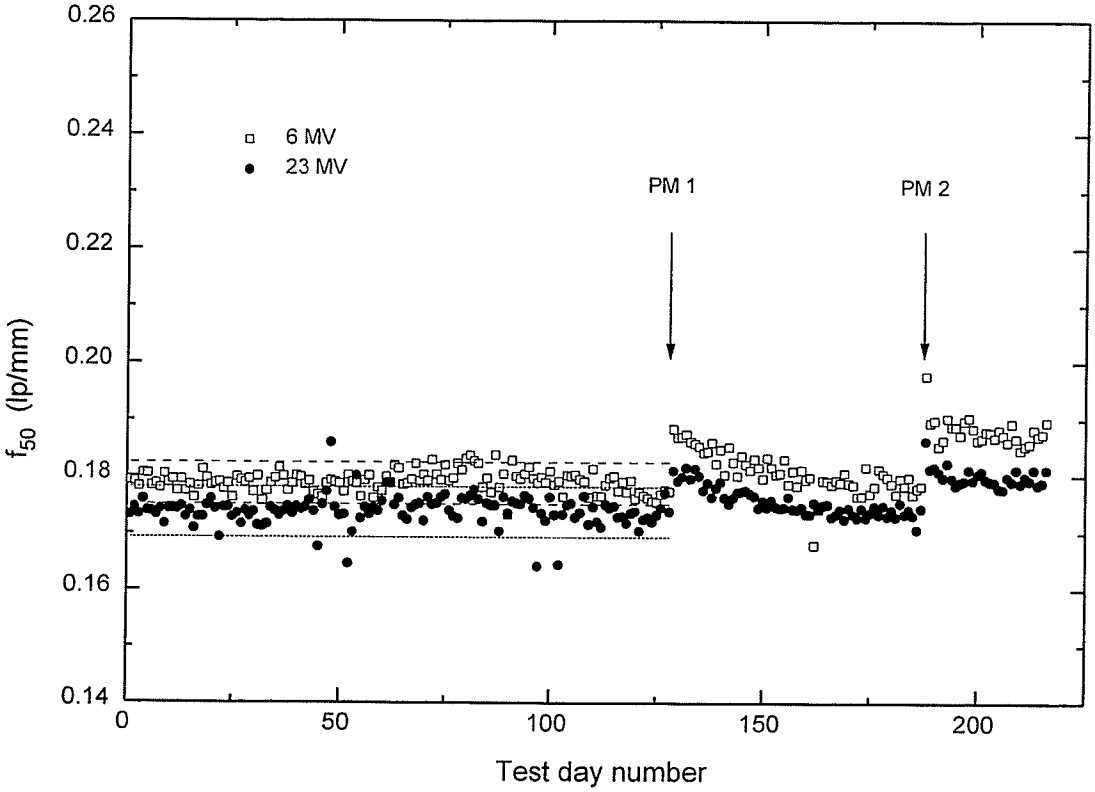

Figure 8-6. The plot of f_{50} for the BEAMVIEW^{PLUS} portal imaging system at gantry angle 0°. PM1 and PM2 indicate the days when preventative maintenance was performed on the system. The F/stop of the lens was changed from F/1.1 to F/1.4 during PM1.

tube used in the earlier system, which was replaced by a lower resolution Newvicon tube in the later model.

Preventative maintenance (PM) was performed on the imaging system after test day number 128 at which time the optical components were cleaned and the lens was refocused. The maximum lens shutter opening of F/1.1 had been used up to this point. Video lenses do not have the best Modulation Transfer Function (MTF) at the maximum shutter opening (i.e. lowest F/stop), and therefore it was decided to close down the F/stop to F /1.4 in an attempt to obtain improved spatial resolution. The f_{50} values for both 6 and 23 MV increased significantly after this PM, but for some unknown reason the f_{50} values fell back to the previously recorded values over a period of several weeks. Another preventative maintenance was performed on test day 187 where once again the lens was refocused, and f_{50} returned to the previous high values. These results suggest that regular preventative maintenance and routine QC tests are beneficial for VEPIDs.

Figure 8-7 shows a plot of CNR values recorded on a daily basis for the BEAMVIEW^{PLUS} portal imaging system. The dotted and dashed lines represent ± 3 standard deviations determined during the calibration period of 25 days. It is seen that CNR for 23 MV is higher than that for 6 MV, which is due to the higher dose rate (300 cGy/min) at 23 MV compared to that at 6 MV (200 cGy/min). Since the QC images were acquired by averaging 16 video frames (0.53 sec), the dose utilized in acquiring the images was 2.67 cGy and 1.78 cGy at 23 and 6 MV respectively. Although the primary subject contrast is higher at 6 MV, the decrease in image noise at the higher dose rate results in higher CNR values at 23 MV than at 6 MV.

The sharp drop in CNR after the first PM is due to the change in F/stop, which reduces the amount of light reaching the camera, and increases the noise. No such change is seen at the second PM, since the lens aperture was not changed at that time.

Figures 8-8a and 8-8b show the plot of f_{50} values recorded daily for four gantry angles; 0°, 90°, 180°, and 270°. Figure 8-8a shows the results at 6 MV, and Fig. 8-8b

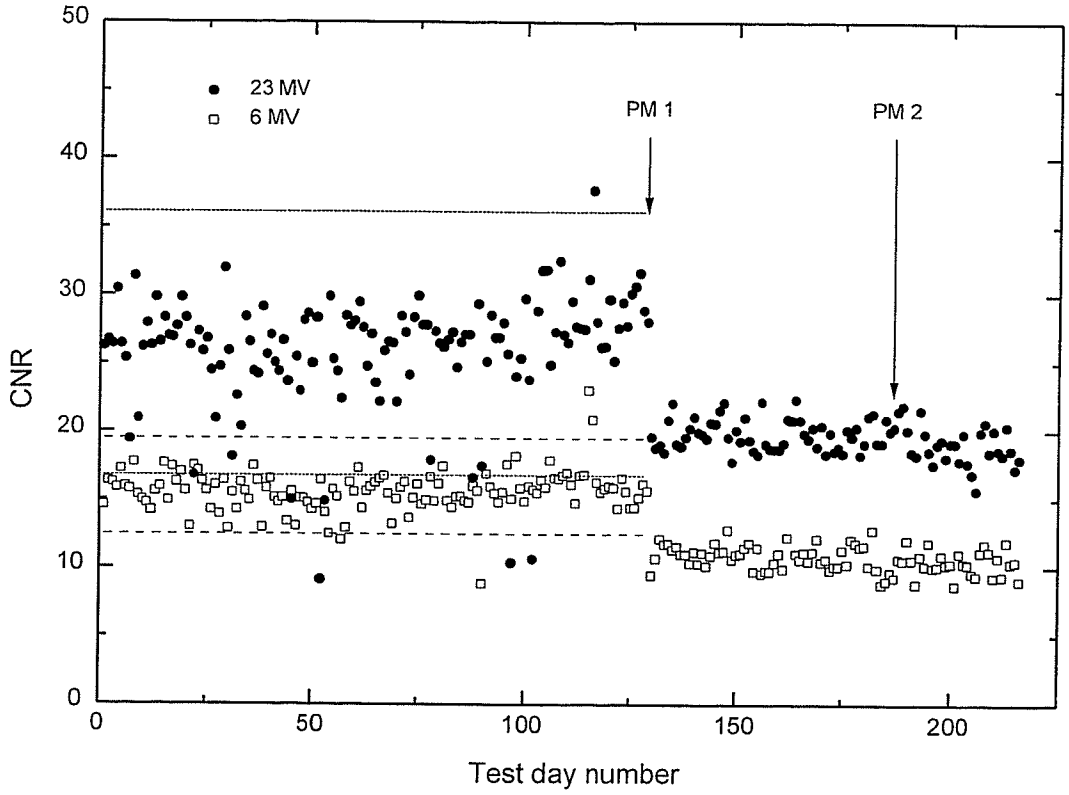

Figure 8-7. The plot of contrast-to-noise ratio (CNR) for the BEAMVIEW^{PLUS} portal imaging system.

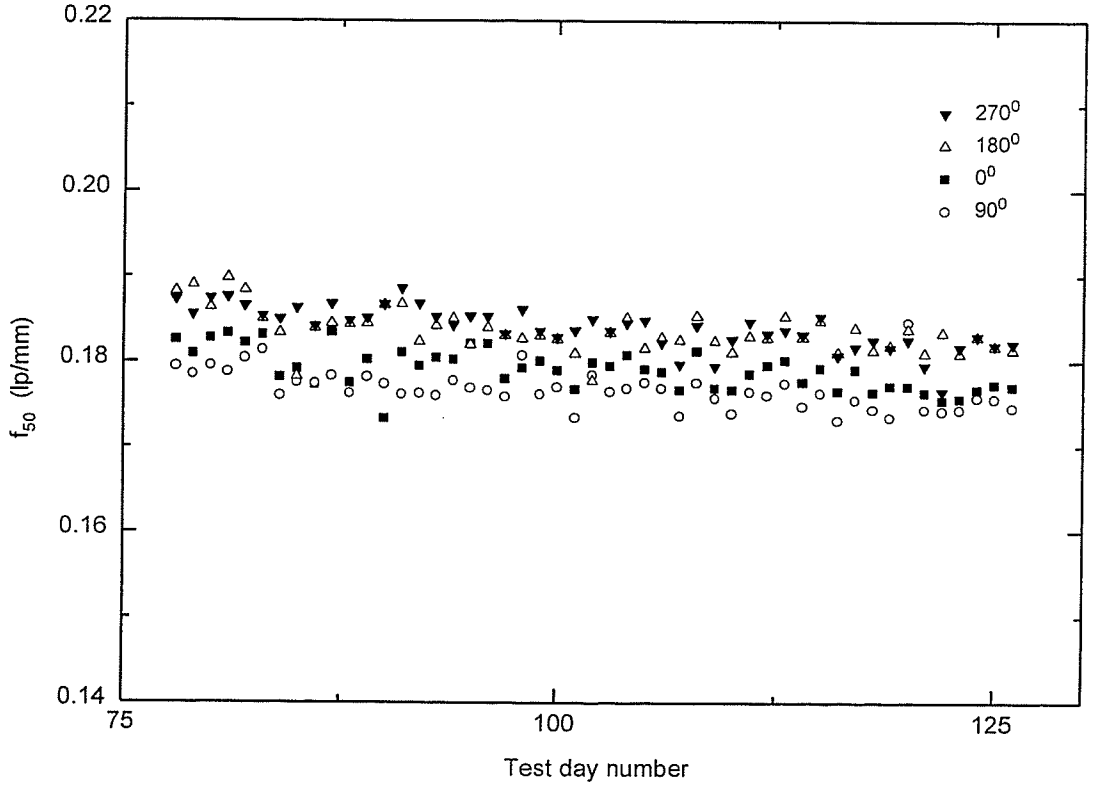

Figure 8-8. a) Plot of f_{50} for the BEAMVIEW^{PLUS} portal imaging system obtained at four gantry angles, at 6 MV.

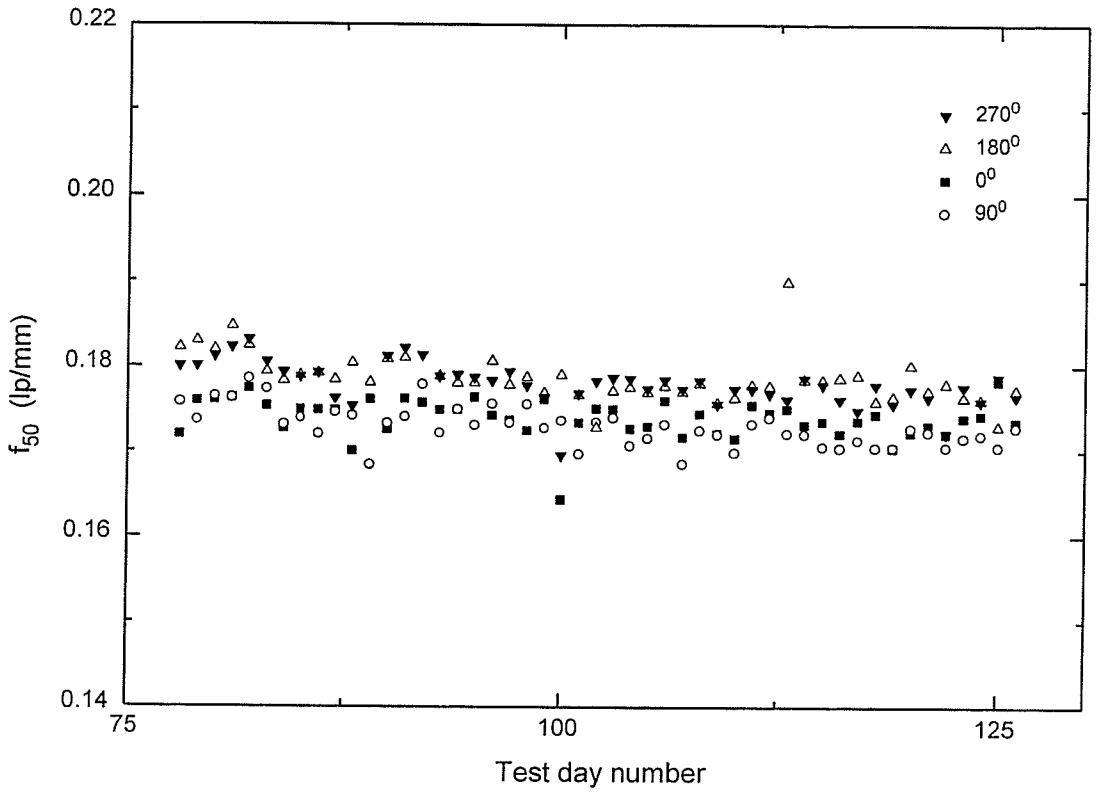

Figure 8-8. b) Plot of f_{50} for the BEAMVIEW^{PLUS} portal imaging system obtained at four gantry angles, at 23 MV.

shows the results at 23 MV. Significant differences are seen between the f_{50} values obtained at some gantry angles, showing that the test is very sensitive to changes in imaging performance of the system at both 6 and 23 MV. On average, the highest values of f_{50} are obtained at gantry angle 270°, since it is at this gantry angle that the lens is focused during preventative maintenance. The reduced performance at other gantry angles is suspected to be due to flexing of the detector housing and possible changes in the camera-screen distance.

8.4 Spurious results due to image artifacts

Figure 8-9 shows the RMTF curves for three test days for the BEAMVIEW^{PLUS} portal imaging system: test day 26 which gave an average f_{50} value, test day 45 which gave a f_{50} value above the ± 3 standard deviation range, and test day 52 which gave a f_{50} value below the ± 3 standard deviation range. When the QC images for test day 45 were investigated, it was found that the images were saturated in the region containing the lowest frequency bar pattern. Since the RMTF is defined with respect to that set of bars, the RMTF values at other frequencies increased giving a spurious high value for f_{50} on that day.

When the QC images obtained on test day 52 were investigated, it was found that one image contained significantly high pulsation artifacts. Since random image noise is obtained by subtracting the image pair, the noise due to the pulsation artifact was also included in the random noise estimation. Figure 8-10 shows the comparison of vertical intensity profiles across the center of the image obtained by subtracting one QC image from the other for the test day 26 (a) and for the test day 52 (b). This result clearly shows the increase in noise in the center of the images on test day 52. The higher value of random noise made the RMTF to fall below zero at higher frequencies as seen in Figure 8-9. This led to a 5% decrease in f_{50} value on day 52 as well as on test days 97 and 102. It must be noted here that the influence of these artifacts are maximum when they appear

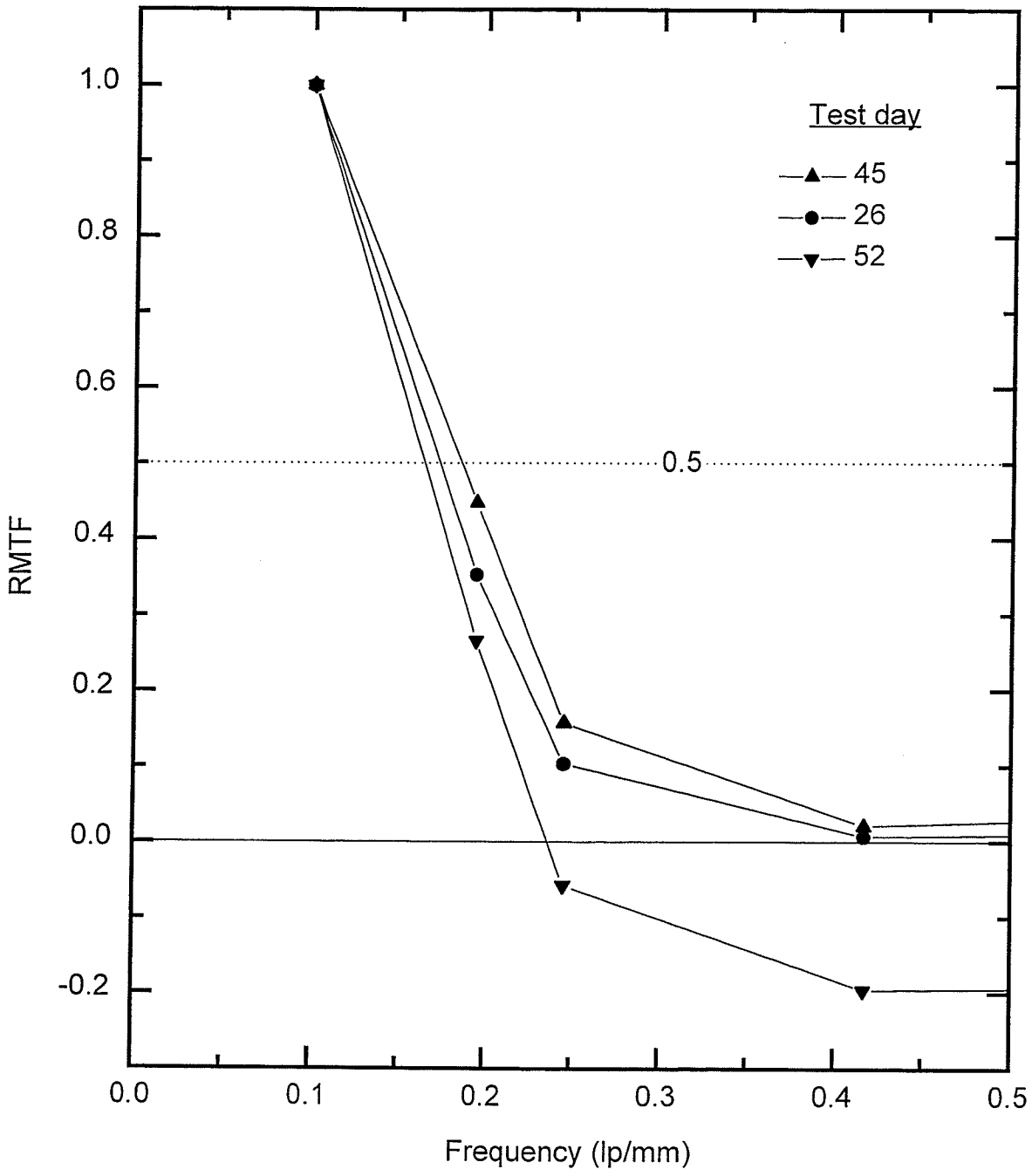

Figure 8-9. The RMTF curves for three test days. Test day 26 gave an average f_{50} value, test day 45 gave f_{50} value above the $\pm$ 3 standard deviation range, and test day 52 gave f_{50} value below the $\pm$ 3 standard deviation range.

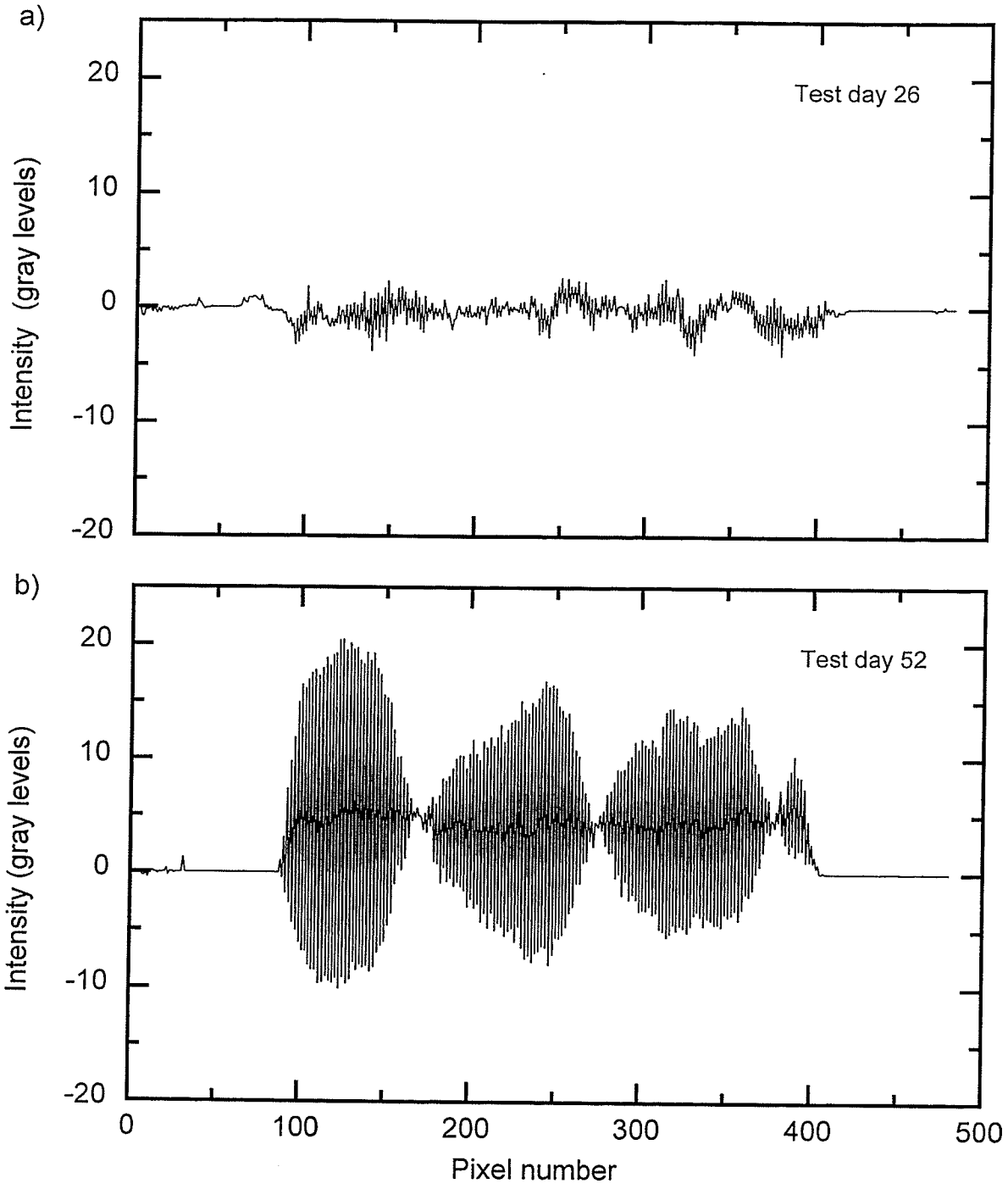

Figure 8-10. The vertical intensity profiles of the image obtained by subtracting two 16 frame QC images acquired on the same day. a) Profile from the QC images acquired on test day 26. b) Profile obtained from the QC images acquired on test day number 52.

at the ROI corresponding to the highest spatial frequency which has the lowest variance (ie. at the centre of the phantom), and therefore the influence of these artifacts on the f_{50} value will not be higher than 5% when appear at other places of the QC images.

Other artifacts due to the electrical interferences have also been observed in the images acquired by the BEAMVIEW^{PLUS} portal imaging system. The presence of these artifacts in the QC images can lead to spurious failures of the test, and therefore the test must be repeated by physics personnel if it failed at the first attempt.

8.5 Conclusions

The development of a Quality Control (QC) test for video based on-line portal imaging systems suitable for routine daily use which tests the system for acceptable performance in high contrast spatial resolution and contrast-to-noise ratio has been presented. A QC phantom consisting of five sets of high-contrast rectangular bars was designed for use in the test. A series of QC measurements has shown that this method provides an automatic, objective, and sensitive measure of the system's imaging performance and is a useful tool for routine daily quality control as well as for commissioning new installations.

References

[1] G. J. Kutcher, L. Coia, M. Gillin, W. F. Hanson, S. Leibel, R. J. Morton, J. R. Palta, J. A. Purdy, L. E. Reinstein, G. K. Svensson, M. Weller, and L. Wingfield, "Comprehensive QA for radiation oncology: Report of AAPM Radiation Therapy Committee Task Group 40," Med. Phys. **21**, 581-618 (1994).

[2] A. Boyer, L. Antonuk, A. Fenster, M. Van Herk, M. Heertens, P. Munro, L. Reinstein and J. Wong, "A review of electronic portal imaging devices (EPIDs)," Med. Phys. **19**, 1-16 (1992).

[3] D. Verellen, W. De Neve, F. van den Heuvel, M. Coghe, O. Louis, and G. Storme, "On-line portal imaging: Image quality defining parameters for pelvic fields - clinical evaluation," Int. J. Radiat. Onc. Biol. Phys. **27**, 945-952 (1993).

[4] R. Nath, P. J. Biggs, F. J. Bova, C. C. Ling, J. A. Purdy, J. van de Geijn, and M. S. Weinhous, "AAPM code of practice for radiotherapy accelerators: Report of AAPM Radiation Therapy Task Group No. 45," Med. Phys. **21,** 1093-1121 (1994).

[5] D. A. Low, E. E. Klein, D. K. Maag, and J. A. Purdy, "The commissioning of a Varian PortalVision electronic portal imaging device," Med. Phys. **20**, 898 (1993).

[6] W. Lutz and B. Bjarngard, "A test object for evaluation of portal films," Int. J. Radiat. Onc. Biol. Phys. **11,** 631-634 (1985).

[7] K. Leszczynski and S. Shalev, "Digital contrast enhancement for online portal imaging," Med. Biol. Eng. Comput. **27,** 507-512 (1989).

[8] J. W. Wong, A. Y. Cheng, W. R. Binns, J. W. Epstein, J. Klarmann, and C. A. Perez, "Development of a second-generation fiber-optic on-line image verification system," Int. J. Radiat. Onc. Biol. Phys. **26**, 311-320 (1993).

[9] M. G. Herman, R. A. Abrams, and R. R. Mayer, "Clinical use of on-line portal imaging for daily patient treatment verification," Int. J. Radiat. Onc. Biol. Phys. **28**, 1017-1023 (1994).

[10] R. M. Harrison and G. D. Lambert, "A method and contrast-detail phantom for the quantitative assessment of radiotherapy portal imaging systems," Brit. J. Radiol. **67**, 384-388 (1994).

[11] R. T. Droege, "A practical method to routinely monitor resolution in digital images," Med. Phys., **10**, 337-343 (1983).

[12] G. T. Barnes, "The use of bar pattern test objects in assessing the resolution of film/screen systems," in The physics of medical imaging: Recording system measurements and techniques, Ed. A. G. Haus, AIP, New York NY., 138-151 (1979).

[13] R. T. Droege and R. L. Morin, "A practical method to measure the MTF of CT scanners," Med. Phys., **9**, 758-760 (1982).

[14] R. Rajapakshe, T. J. Radcliffe, and S. Shalev, "Quality Control for on-line portal imaging systems," SPIE **V 1897**, 121-127 (1993).

15 B. Wowk, T. Radcliffe, K. W. Leszczynski, S. Shalev, and R. Rajapakshe, "Optimization of metal/phosphor screens for on-line portal imaging," Med. Phys. **21**, 227-235 (1994).

16 P. Munro and J. A. Rawlinson, "Therapy imaging: A signal-to-noise analysis of a fluoroscopic imaging system for radiotherapy localization," Med. Phys. **17**, 763-772 (1990).

Chapter 9

On-line imaging of electron treatments

9.1 Introduction

Verification of X-ray treatment fields by portal imaging is a standard procedure in most centers. Conventionally, portal films are used during the first treatment and on a weekly basis thereafter, although the advent of electronic portal imaging devices (EPIDs) provides the capability of verifying every treatment field on a daily basis. Verification of electron treatment fields is much less common, although the need to do so is well established. With electron applicators in place it is difficult to ensure accurate setup, and often the target volume is not located directly underneath the surgical scar for cosmetic reasons. For example, Regine et al. found that 12 out of 17 patients given electron boost fields for breast irradiation suffered from geographical misses when set up clinically[1]. They recommended the inclusion of surgical clips to mark the target volume, and 3-D planning following a CT scan to ensure delivery of an adequate treatment volume to the tumor bed, but did not address verification of the electron fields during treatment.

Keller[2] was probably the first to demonstrate portal imaging with electron beams, using a lead foil cassette and Kodak XRP-1 film. Clinical experience with film verification was reported by Grimm et al. for 10 MeV electrons[3], and by Gur et al. for a wide range of electron energies[4]. Storage phosphor technology has also been shown to be effective[4-8] in acquiring portal images of electron treatments, although Weiser et al. correctly pointed out that for superficial treatments the portal image will be more sensitive than the target volume to changes in beam angle[9]. The goal of the present study was to evaluate the possibility of using EPIDs for on-line verification of electron treatments, thus avoiding the difficulties and delays inherent in film and storage phosphor techniques.

Electrons are useful for superficial and local boost radiation treatments on account of their low range in tissue, so that structures underlying the target volume are spared high dose levels. However, portal imaging using radiation transversing the total patient thickness is still possible during electron treatments due to the contaminant bremsstrahlung, which contributes 4-5% of the maximum electron dose[10] in a typical clinical linear accelerator. These high energy X-rays are generated in the scattering foil of the treatment head, and their intensity has been shown to vary with the photon collimator settings[11]. This X-ray contamination of an 18 MeV electron beam was used to demonstrate the acquisition of on-line electronic portal images of a Rando anthropomorphic head phantom.

9.2 Materials and methods

The optimized version of the prototype video-based electronic portal imaging system was used to acquire on-line portal images of the Rando head phantom. The system uses a metal/phosphor screen consisting of a 500 mg/cm^2 Gd_2O_2S:Tb (P-43) phosphor layer on a 2.25 mm copper plate which was placed at a source-detector distance of 140 cm. Optical coupling between the metal phosphor screen and the video camera was achieved with a F/0.85, 25 mm c-mount lens and two 45° front surface glass mirrors. The video camera was the custom designed dual field capture CCD camera. The camera was Peltier cooled to 0° C to reduce dark current, and was shielded with 5 cm of lead to avoid noise due to direct detection of X-rays by the CCD. A PC-486 equipped with a Oculus 500 (OC500) processing board* was used to acquire images.

The KD-2 linear accelerator** used in this study was operated in the 18 MeV electron mode at a dose rate of 300 cGy/min with a 15x15 cm^2 accessory cone. The dose rate at the detector surface due to the X-ray contamination after passing through 15 cm

* Coreco Inc. Quebec, Canada.
** Siemens Medical Systems Inc. Concord, CA

water was measured with a Capintec F/type #64564 ionization chamber and a CNMC K616 electrometer. Measurements were taken with 2.8 cm build-up and 9 cm of backscatter material (Acrylic).

The Rando head phantom was irradiated at 110 cm source-to-surface distance (SSD). Exposures of one second were used (30 frames integrated on the CCD target), and eight similar images were averaged after applying a 3x3 median filter to remove noise due to direct detection of X-rays by the CCD. The final verification image thus corresponds to a 40 cGy dose to the phantom. A "open field" image of a 15 cm water phantom was also obtained for off-line image correction. The verification image was enhanced using contrast limited adaptive histogram equalization[12] (CLAHE), and corrections were made for the beam non-uniformity and detector response by dividing the portal image by the open field image.

Clinical linear accelerators are designed to provide uniform fields of high energy X-rays during photon treatments, but the X-ray contaminant in electron beams is far from uniform[11]. The uncorrected open field image is not a reliable measure of the spatial distribution of the contaminant X-rays due to non-uniform detector response and vignetting in the optical system. These effects can be reduced by using an image acquired with a uniform photon beam of any energy. Consequently the water phantom image of the 15x15 cm^2 electron beam was corrected by division with an open field image of a 40x40 cm^2 6 MV photon beam. The 6 MV photon beam was used for convenience. Horizontal and vertical central profiles of the corrected image were obtained by averaging 20 pixels in the direction perpendicular to the profile direction. Similar profiles were also obtained from an image of a 15 cm water phantom acquired with a 6 MV photon beam using a 15x15 cm^2 field.

9.3 Results

The dose rate at the detector due the contaminant X-rays after passing through a 15 cm water phantom was found to be 7.31 cGy/min. This corresponds to 2.5% of the electron dose at the D_{max}.

Figure 9-1a shows the original verification image of the Rando head phantom. This image was acquired with 0.975 cGy dose to the metal/phosphor screen which corresponds to 40 cGy electron dose to the phantom. The triangular object in the lower left corner of the image is a lead block used to stop direct irradiation of the detector in the region where there was no phantom. The contrast enhanced image without open field correction is shown in Fig. 9-1b. The four support struts and the inside edge of the 15x15 cm^2 accessory cone are clearly visible in this image. The contrast enhanced image after open field correction is shown in Fig. 9-1c. Comparison of Fig. 9-1b and 9-1c shows the suppression of the subject contrast due to the extreme non-uniformity of the bremsstrahlung beam profile. The quality of the fully corrected and enhanced image (Fig. 9-1c) is comparable to on-line portal images acquired with photon beams with an equally small dose to the detector. Portal images such as this can be used for the verification of electron beam shaping applicators[13] to ensure that they are correctly installed during every treatment session.

Figures 9-2a and 9-2b show the horizontal and vertical profiles of the corrected open field images respectively. The straight line corresponds to the contaminant X-rays in a 15x15 cm^2 18 MeV electron beam and the dashed line is the profile for the 15x15 cm^2 6 MV photon beam. These figures show that both horizontal and vertical profiles of the contaminant beam open field image are cone-shaped and decrease in a linear fashion to about 50% of the center value at the physical edge of the beam. This linear decrease of dose from the central value to 50% at 7.5 cm from the central axis is consistent with the earlier result obtained by Rutsgi and Rodgers[11]. The cone shape of the contaminant

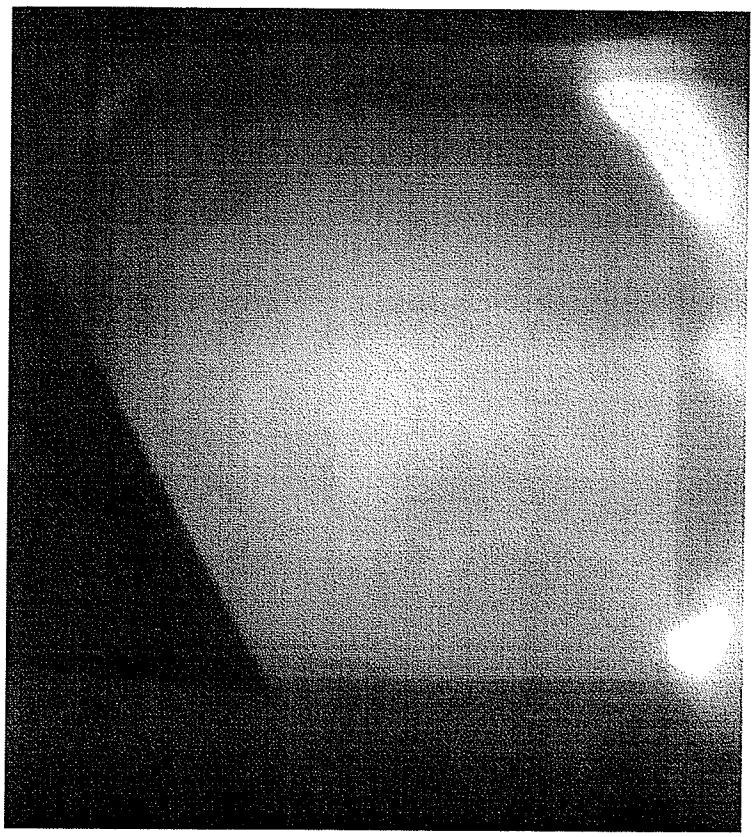

Figure 9-1. a) Original Image of the Rando head phantom acquired with an 18 MeV electron beam with a 15x15cm^2 accessory cone.

Figure 9-1. b) Contrast enhanced image without open field correction.

Figure 9-1. c) contrast enhanced image with an open field correction.

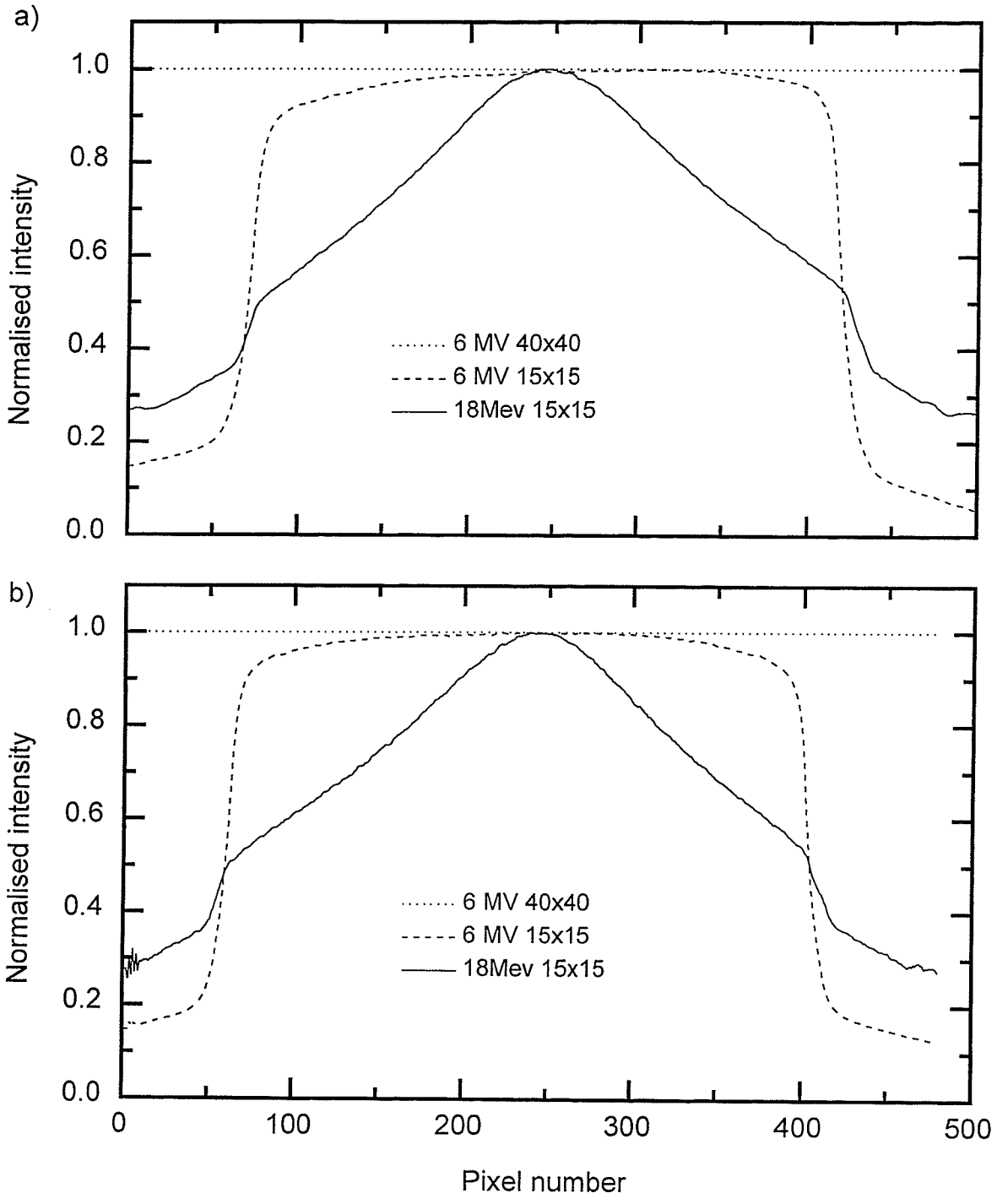

Figure 9-2. Intensity profiles of the bremsstrahlung component of the 15x15 cm^2 18 MeV electron beam (straight line) and a 15x15 cm^2 6 MV photon beam (dashed line) from a KD-2 linear accelerator after transmission through a 15 cm water phantom. a) horizontal profiles, b) vertical profiles.

X-ray dose profiles is to be expected since there are no flattening filters in the electron beam path. It is important to note that measurements of the dose due to the X-ray contamination in electron beams are usually performed at the central axis, and therefore any corrections applied using such estimates will over-estimate the dose to the patient.

9.4 Conclusions

This study shows that the optimized prototype portal imaging system is capable of acquiring verification portal images during 18 MeV electron treatments. It was also shown that portal images should be corrected by the open field in order to improve image quality. The fact that high quality transmission portal images can be obtained indicates that a major part of the contaminant X-rays in the electron beam is generated with an effective small focal spot.

References

[1] W. F. Regine, K. M. Ayyangar, L. T. Komarnicky, N. Bhandare, and C. M. Mansfield, "Computer-CT planning of the electron boost in definitive breast irradiation," Int. J. Radiat. Oncol. Biol. Phys. **20**, 121-125 (1991).

[2] B. Keller, "Electron-beam radiographs," Radiology **128**, 830-831 (1978).

[3] D. Grimm, M. Gillin, R. Kline, and N. Janjan, "Electron beam port films," Medical Dosimetry **14**, 31-33 (1989).

[4] D. Gur, J. Weiser, M. Deutsch, C. Fuhrman, R. Gennari, M. Rosenthal, "Verification of electron beam therapy with conventional and storage phosphor images: Preliminary experience," Int. J. Radiat. Oncol. Biol. Phys. **17,** 1337-1340 (1989).

[5] M. Kao, A. Chung-Bin, J. Lobec, and S. Balter, "Using computed radiography system for electron beam portal film," Med. Phys. **14**, 483 (1987).

[6] M. Kao, A. Chung-Bin, J. Lobec, and S. Balter, "Computed radiography system for therapeutic portal film applications," Int. J. Radiat. Oncol. Biol. Phys. **13**, Sup. 1, 178 (1987).

[7] J. Weiser, D. Gur, M. Deutsch, R. Gennari, W. Bloomer, A. Epstein, J. Flickenger, and S. Kalnicki, "Clinical applications of electron treatment portal images," Int. J. Radiat. Oncol. Biol. Phys. **17,** Sup. 1, 160 (1989).

[8] K. Nakagawa, Y. Aoki, A. Akanuma, K. Karasawa, and Y. Sasaki, "Applying computed radiography to the portal imaging in the verification of radiotherapy," Proc. ESTRO meeting, Montecatini, 28 (1990).

[9] J. Weiser, D. Gur, E. Cano, M. Deutsch, A. Wu, and R. Mogus, "Verification of electron beam therapy with storage phosphor images: Precision of field placement," Radiology **175**, 257-259 (1990).

[10] D. Gur, A. G. Bukovitz, and C. Serago, "Photon contamination in 8-20-MeV electron beams from a linear accelerator," Med. Phys. **6,** 145-146 (1979).

[11] S. N. Rustgi and J. E. Rodgers, "Analysis of the bremsstrahlung component in 6-18 MeV electron beams," Med. Phys. **14,** 884-888 (1987).

[12] G. Sherouse, J. Rosenman, S. Pizer, H. McMurry, and E. Chaney, "Automatic digital contrast enhancement of radiotherapy films," Int. J. Radiat. Oncol. Biol. Phys. **13**, 801-806, (1987).

[13] J. H. Plane and C. Usher, "A rapid method of production of irregular-shaped fields for use with patients receiving electron radiotherapy," B. J. R. **63**, 882-883 (1990).

Chapter 10

Output stability of a linear accelerator during the first three seconds

10.1 Introduction

High stability of a linear accelerator output during first few seconds of operation is of importance for a number of reasons. Some commercial electronic portal imaging devices (EPIDs) adjust image acquisition parameters automatically at the beginning of a treatment assuming the linac produces a stable output instantaneously. However, the acquisition parameters may not be optimized properly if the linac output is unstable during the time of these adjustments and may have a serious impact on portal image quality. Furthermore, a highly stable output is necessary for dynamic therapy such as arc therapy, dynamic intensity modulation, dynamic wedge, etc.

Although a study has been carried out to analyze the cumulative beam characteristics for different numbers of monitor units[1], the author is unaware of any published reports on measuring beam characteristics in real time. Therefore the output stability of a KD-2 linear accelerator* during the first three seconds of operation was measured with a real-time portal imaging system having a time resolution of 0.33 s. The output was measured for X-ray energies of 23 MV and 6 MV as well as for electron energies of 6, 9, 12 ,15 and 18 MeV.

10.2 Materials and methods

Figure 10-1 show the operating sequence of the KD-2 linac. When the "RAD ON" switch is pressed, all the parts except the electron gun start operating under the control of pre-set (soft-pot) parameters. These parameters, which may be different for

* Siemens Medical Systems, Concord, CA.

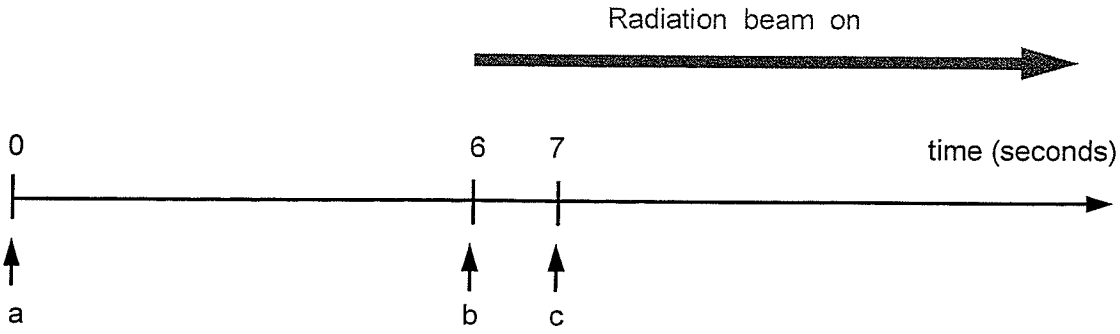

a : **Rad on switch pressed :** All parts except the electron gun start operating under the preset (soft-pot) parameters.

b: **Electron gun starts operating :** Delivers radiation beam under control of the soft-pot parameters.

c: **Dosimetry servo system starts operating :** Feedback controls the radiation output.

Figure 10-1. Operating sequence of the Siemens KD-2 linear accelerator.

each mode of operation, are set at the time of tuning the accelerator during installation and when maintenance is performed. After about 6 s, the electron gun starts operating and radiation is produced. After an additional 1 s the dosimetry servo system takes over control of the dose rate by modifying the pulse repetition rate through a feed-back loop. Consequently the output is initially controlled by the soft-pot parameters for a period of about 1s. If these parameters are not set correctly, there will be a step change in output when control is passed to the servo system.

The optimized prototype portal imaging system used for this study was described in Chapter 9. For this study, the 8 MB of frame buffer memory in the OC-500 frame grabber was configured to capture 128 consecutive frames each of 256x256 pixels, permitting the recording of 4.26 s of real-time digital video data. An input look up table (LUT) was used to scale the 10-bit digital data to the 8-bit frame memory.

Open field images of 15x15 cm^2 radiation beams were acquired with the portal imaging system. Two 40x40 pixel regions of interest (ROIs) were used to measure the average intensity of a section of the open field and the black level. The measured open field intensities were corrected for black level by subtraction, and then normalized by the average value of the signal while the beam was on. Effects due to optical glare are reduced by the black level subtraction. Therefore, any change in measured relative intensities will represent a change in output dose rate. The measurements were repeated four times in each mode of linac operation, and the results showed similar behaviour in all the four measurements.

Clinical linear accelerators deliver radiation in pulses, with a pulsation frequency in the range 30-200 Hz depending on the mode of operation. In one mode of operation (23 MV @ 300 cGy/min), the pulsation frequency of the KD-2 linac is about 135 Hz. When imaging is performed at the real-time video rate (ie. 30 Hz), each video frame will capture on the average about 4½ radiation pulses. Therefore, some video frames may capture 4 radiation pulses and other frames will capture 5 pulses as shown in Fig. 9-2.

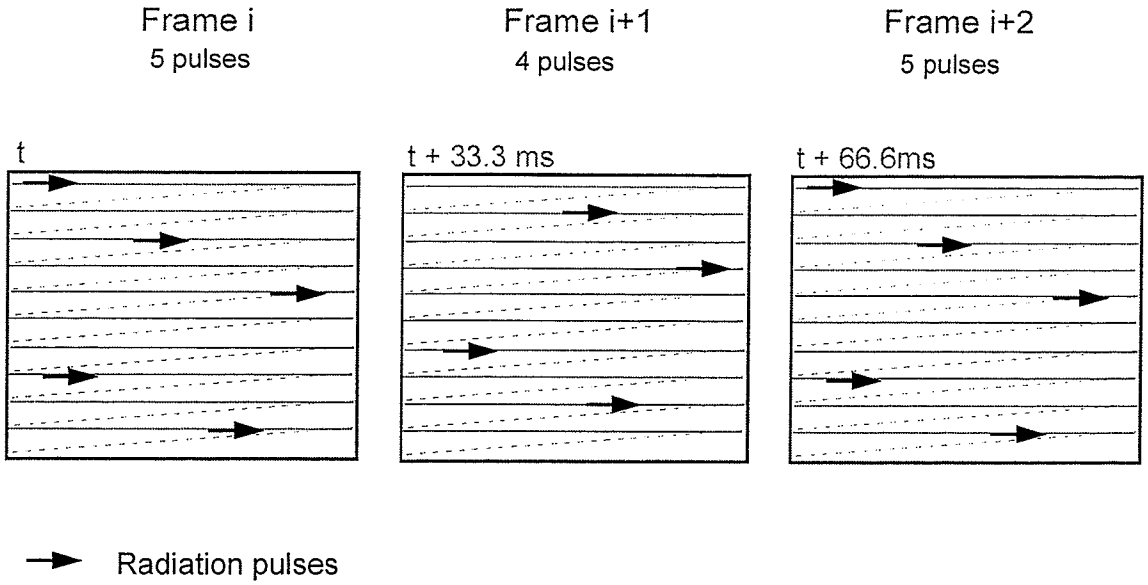

Figure 10-2. Schematic diagram showing the effect of monitoring 135 Hz linac pulsation with 30 Hz video imaging. Consecutive video frames may detect different numbers of radiation pulses because video scanning is not synchronised with accelerator pulsation.

Consequently, the output dose rate as measured by the real-time portal imaging system will vary due to this aliasing artifact. The effect is reduced by averaging 6 video frames, with a consequent reduction in temporal resolution to 200 ms.

10.3 Results

Figure 10-3a shows the output of the linac in the 23 MV x-ray mode as measured by the portal imaging system. The nominal dose rate in this mode is 300 cGy/min (5 cGy/s). The variation in the measured output due to the aliasing artifact is clearly seen. While the output reached the required dose rate instantaneously, it became unstable when the servo feed-back took control after 1 s. Figure 10-3b shows the linac output measured by frame averaging. It indicates that after the initial instability the machine delivered a relatively stable output.

Figure 10-4a shows the output of the linac in the 6 MV x-ray mode as measured by the portal imaging system. The nominal dose rate in this mode is 200 cGy/ min (3.33 cGy/s). The variation of the measured output due to the aliasing artifact can also be seen in this case. Figure 10-4b shows the output with reduced temporal resolution. The linac was properly tuned in this mode, and delivered a stable output after the initial build-up over a period of about 0.25 s.

Figure 10-5a shows the output of the linac in the 15 MeV electron mode as measured by the portal imaging system. The nominal dose rate in this mode is 300 cGy/ min (5 cGy/s). The change in the output after 1 s is clearly visible in this figure, even with the aliasing artifact present. Figure 10-5b shows the measured output with reduced temporal resolution. The linac was not tuned properly in this case so the output during the first second was lower by more than 10 % of the cumulative average during the first four seconds. The measured output for the other electron energies showed a similar behaviour, with various step changes in output after 1s.

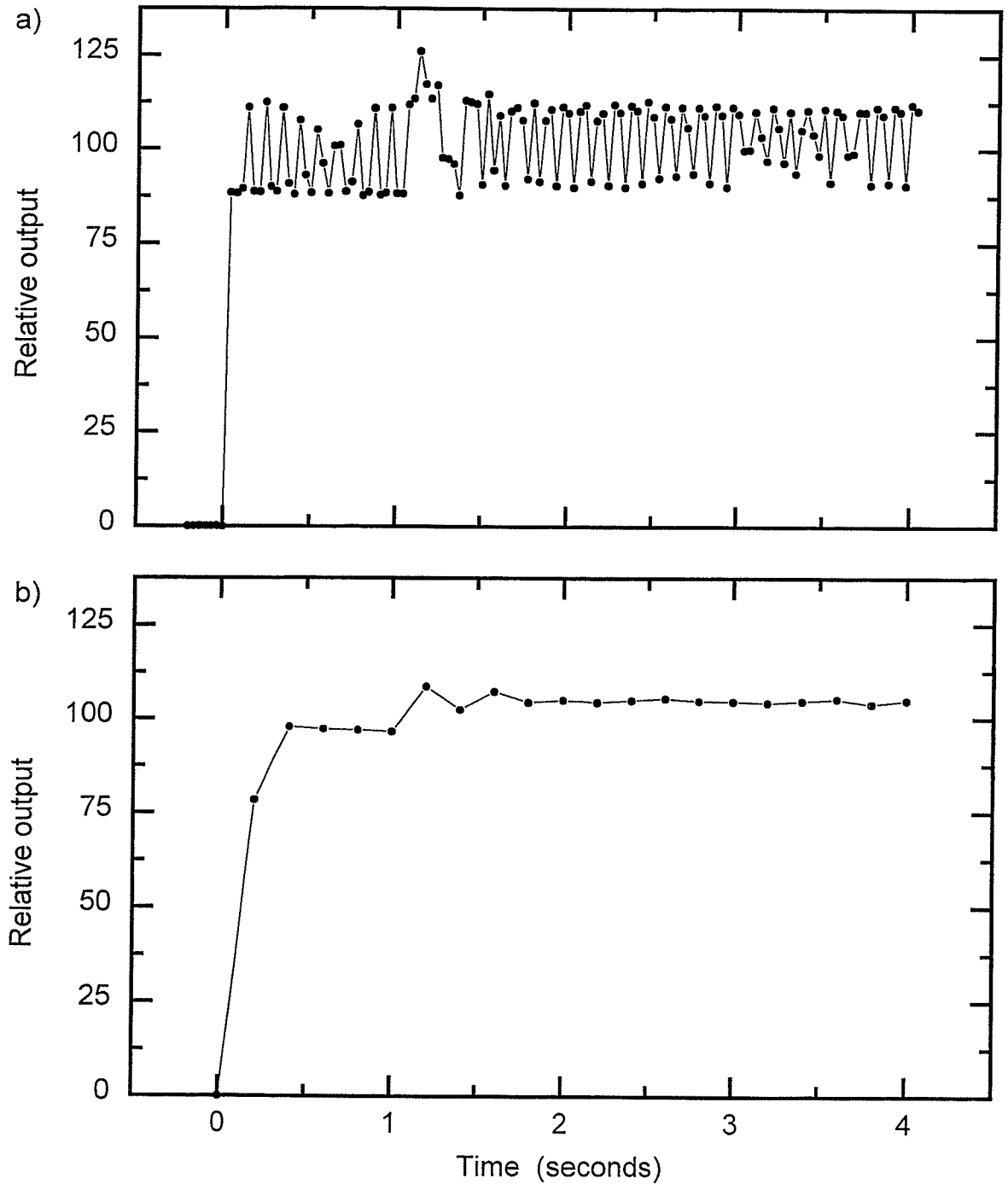

Figure 10-3. Output of the linac in the 23 MV X-ray mode as measured by the portal imaging system. a) 33.3 ms temporal resolution. b) 200 ms temporal resolution. The variation of the measured output due to aliasing artifact is seen in a). The linac achieved its required dose rate almost instantaneously in this mode.

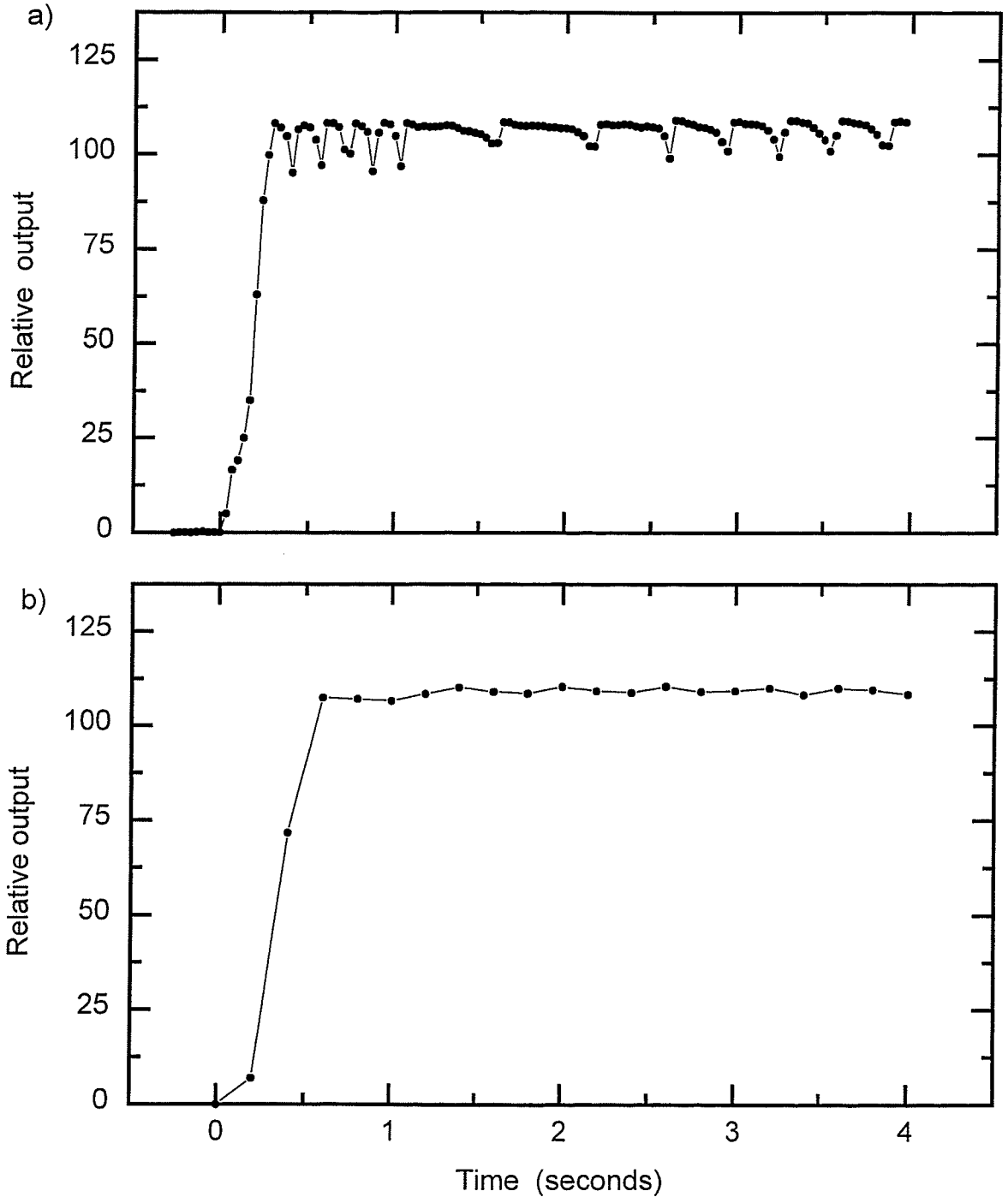

Figure 10-4. Output of the linac in the 6 MV X-ray mode as measured by the portal imaging system. a) 33.3 ms temporal resolution. b) 200 ms temporal resolution. The linac required 0.25 seconds to achieve the required dose rate in this case.

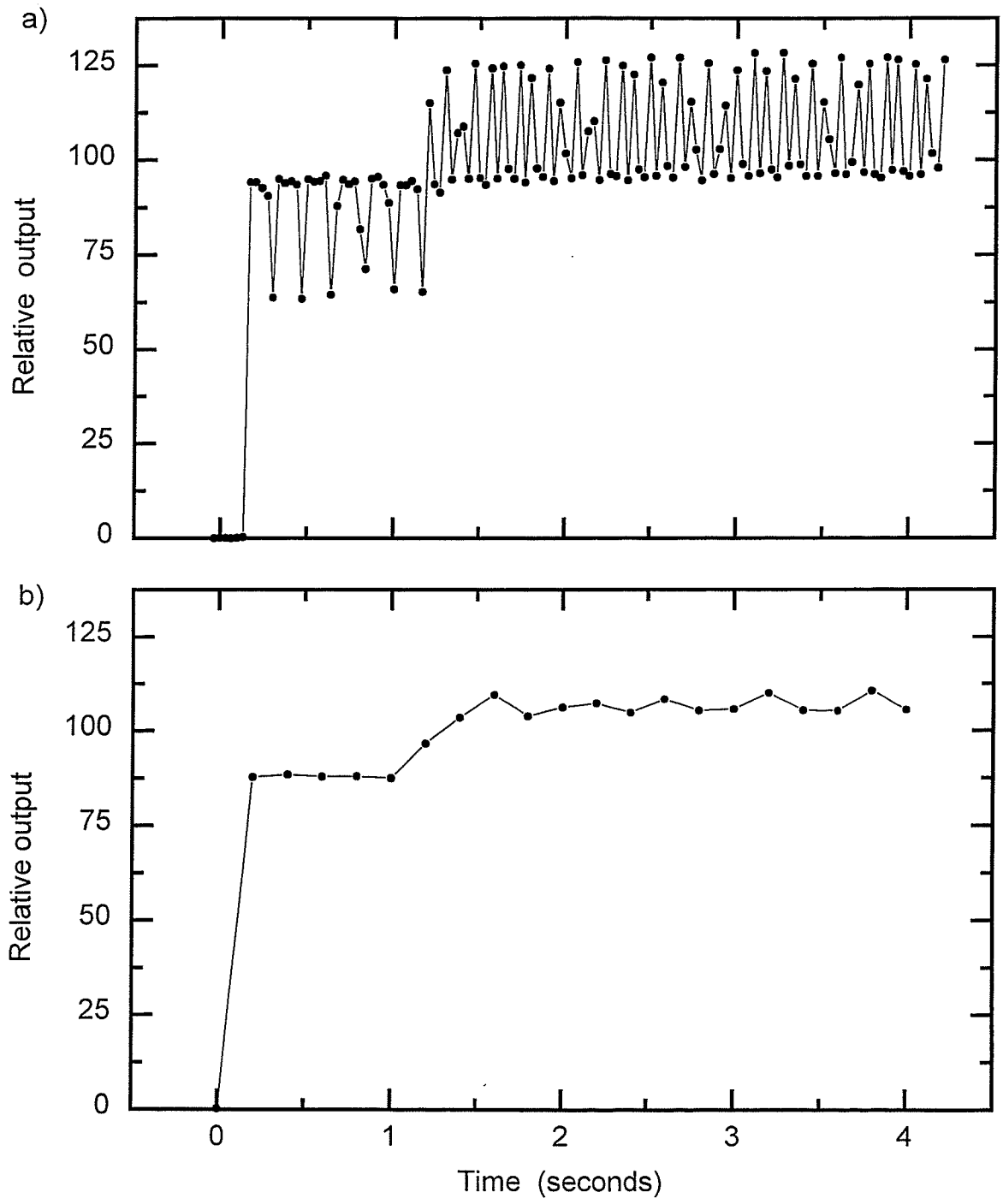

Figure 10-5. Output of the linac in the 15 MeV electron mode as measured by the portal imaging system. a) 33.3 ms temporal resolution. b) 200 ms temporal resolution. The linac was not properly tuned in this mode and a change in output of more than 10% is seen.

Clearly a dose rate instability can occur during the first second of operation, and particularly at the time when the servo feed-back takes control of the pulse repetition frequency. It is possible that there may also be a change in the spatial dose distribution during this time, and therefore an experiment to investigate this possibility was also designed. The soft-pot parameters were deliberately changed to set the initial dose rate 20% too high, so that a significant step change in dose rate would occur at 1s. Figure 10-6 shows two horizontal intensity profiles of open field images at 23 MV acquired by averaging six frames under these conditions. The two profiles are extracted from the images during the first 0.2 s (before feed-back control) and during the period 2.0-2.2 s (after feed-back control). No significant differences between the two profiles can be seen.

10.4 Conclusions

The dose rate stability of a linear accelerator during the first three seconds of operation has been measured with a real-time portal imaging system. Measurements have shown that a change in dose rate of more than 10% can occur after about 1s of operation, when the dosimetry servo system takes over control of the machine output. The magnitude of this effect can be reduced by properly setting the soft-pot parameters. These initial instabilities may have serious implications for electronic portal imaging devices which adjust image acquisition parameters automatically according to the measured signal. Furthermore, these instabilities must be taken into account in any dynamic therapy application.

It was shown that the optimized real-time portal imaging system has the capability to monitor the accelerator output, and can be used to assist in maintenance procedures.

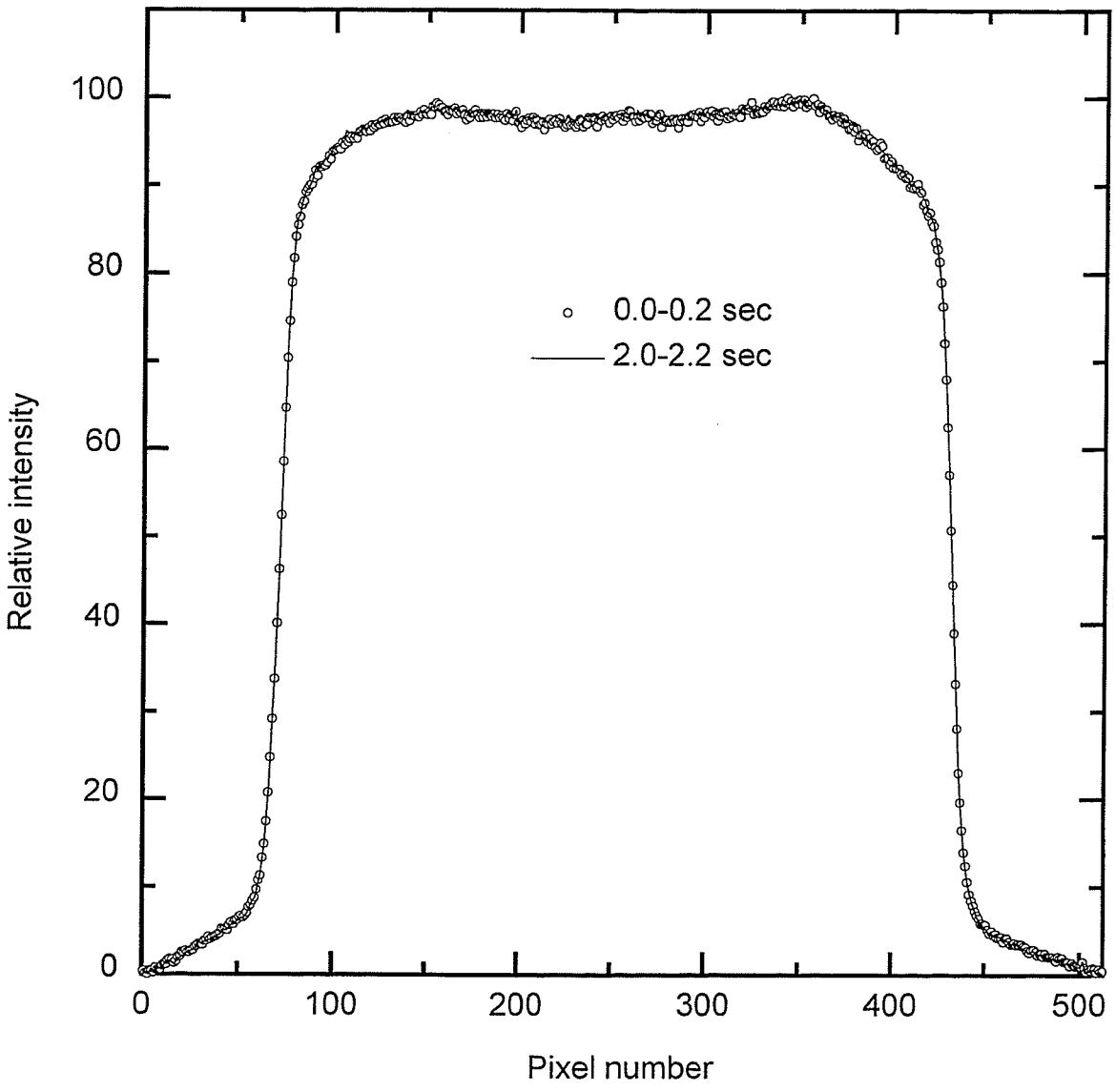

Figure 10-6. Two horizontal intensity profiles of 23 MV open field images acquired by averaging 6 frames with the soft-pot parameters set 20 % too high. The two profiles are taken from the very first 0.2 sec (before feed-back control) and the period 2.0-2.2 s (after feed-back control).

References

[1] R. J. Barish, R. C. Fleischman, and Y. M. Pipman, "Teletherapy beam characteristics: The first second," Med. Phys. **14,** 657-661 (1987).

Chapter 11

Portal dosimetry

11.1 Introduction

The use of electronic portal imaging devices (EPIDs) for verification of radiation treatments is increasing rapidly[1], and a number of centres are evaluating these tools in the clinical setting[2-8]. So far the emphasis has been on the relatively straightforward problem of geometric verification, in which the size, shape and position of the treatment field is compared to prescribed values. A more difficult problem is dosimetric verification, in which a quantitative measure of the dose distribution at the detector is compared to calculations of the predicted exit dose. While some progress has been made using film, TLD dosimeters, diodes, and ionization chambers[9-15], much less effort has been devoted to dosimetric verification using EPIDs. Since the pioneering efforts of Leong[16] and Wong and colleagues[17], a number of preliminary studies have demonstrated the possibility of quantitative dose measurements using fluoroscopic portal imaging systems[18-21].

Video based portal imaging systems use metal/phosphor screens for converting the transmitted X-rays to light. It is generally known that the light output from a phosphor screen when irradiated with X-rays is proportional to the energy deposited in the phosphor screen[22]. If the detection of the optical photons in the video camera and the rest of the electronic circuitry is linear, a measure of the exit (or transit) dose can be obtained by a portal imager as an intensity (gray) level. This chapter examines the ability of the optimized portal imaging system in measuring exit dose.

The relative accuracy of an exit dose measured with the VEPID is determined by the uncertainty in measuring the gray level value in the portal image. The primary limitation is imposed by the noise in the portal image. Although sub-millimeter

resolutions are required and available for qualitative geometric verification imaging and image alignment using anatomical features, such high spatial resolution is not required for dosimetric measurements. Ultimately one has to compare the measured dose with the estimated exit dose obtained from a treatment planning computer. Treatment planning systems do not calculate doses at resolutions higher than 1-2 mm, and 2 mm resolution (at the isocenter) would be adequate for dose measurements with an EPID. The optimized VEPID has a pixel size of about 0.4 mm at the isocenter. Therefore one can reduce the spatial resolution by a factor of 4 by averaging data in a 4x4 pixel area, and by doing so, improve the SNR. For such large pixel values, a conservative estimate of the single frame SNR is 200 which is obtained from the low frequency SNR of 50 given in Chapter 5. For a 0.25 s exposure (about 1 cGy delivered to the patient) this will result in an SNR value of more than 500, which is adequate for achieving quantitative accuracy of 1%. Consequently, the noise in the optimized system imposes no practical limitation on the ability of the system to measure exit dose.

Further limitations to the quantitative accuracy of video based portal imaging are imposed by issues such as distortions introduced by the frame grabber and the effects of lens vignetting, veiling glare, black level clamping, and the linearity of the system in detecting optical light. The effects of these artifacts on the accuracy of quantitative portal imaging are also investigated in this chapter.

11.2 Calibrations

11.2.1 Artifacts from the frame grabber

Investigation of the uniformity of a CCD dark current image indicated that the pixel intensities (gray values) get smaller and smaller towards the right side of the image. Observation of the video signal with a oscilloscope did not show any measurable nonuniformity in the signal. Therefore it was concluded that the frame grabber introduced this artifact. In order to investigate this artifact, an image was acquired with

the CCD camera by saturating the CCD. The uniform video signal generated by the saturated CCD was then captured by the frame grabber for analysis. Five horizontal and vertical intensity profiles were extracted from the images by averaging 8 pixels and are shown in Fig. 11-1. Figure 11-1a shows the horizontal profiles extracted at y = 80, 160, 240, 320, and 400. All five of the profiles are identical, but have a gradient of 0.065 gray levels per horizontal pixel giving a maximum error of about 5%. Figure 11-1b shows the vertical profiles extracted at x = 125, 225, 325, 425, and 525. The average value of profiles are different due to the gradient in the horizontal direction, but no significant gradient is seen in the vertical direction.

Further tests carried out without saturating the CCD indicated that the magnitude of this gradient in a given horizontal video line depends not only on the maximum gray value of the line, but also on the extent of the illuminated section in a complex manner.

The field of view of the camera always contains two dark vertical strips of about 20 pixels wide at the left and right hand edges. These regions correspond to the wood structure holding the phosphor screen. Since the sections are painted black, the corresponding pixel values denote the video black level. The difference between the leftmost and the rightmost dark regions (which are referred to as the left dark region and the right dark region in the following) can therefore be used to estimate the magnitude of the gradient in each video line, and an individual correction can be made to each video line according to the equation

$$I_g(x,y) = I(x,y) + x \cdot \frac{I(x_1,y) - I(x_2,y)}{x_2 - x_1}. \qquad (11\text{-}1)$$

Here $I(x_1,y) = \sum_{x_1-7}^{x_1+7} I(x,y)$ and $I(x_2,y) = \sum_{x_2-7}^{x_2+7} I(x,y)$ are the average gray values of the left and right dark regions in the video line y, estimated by averaging 15 pixels horizontally, and x_1 and x_2 are the central x coordinates of the left and right dark regions. $I_g(x,y)$ and

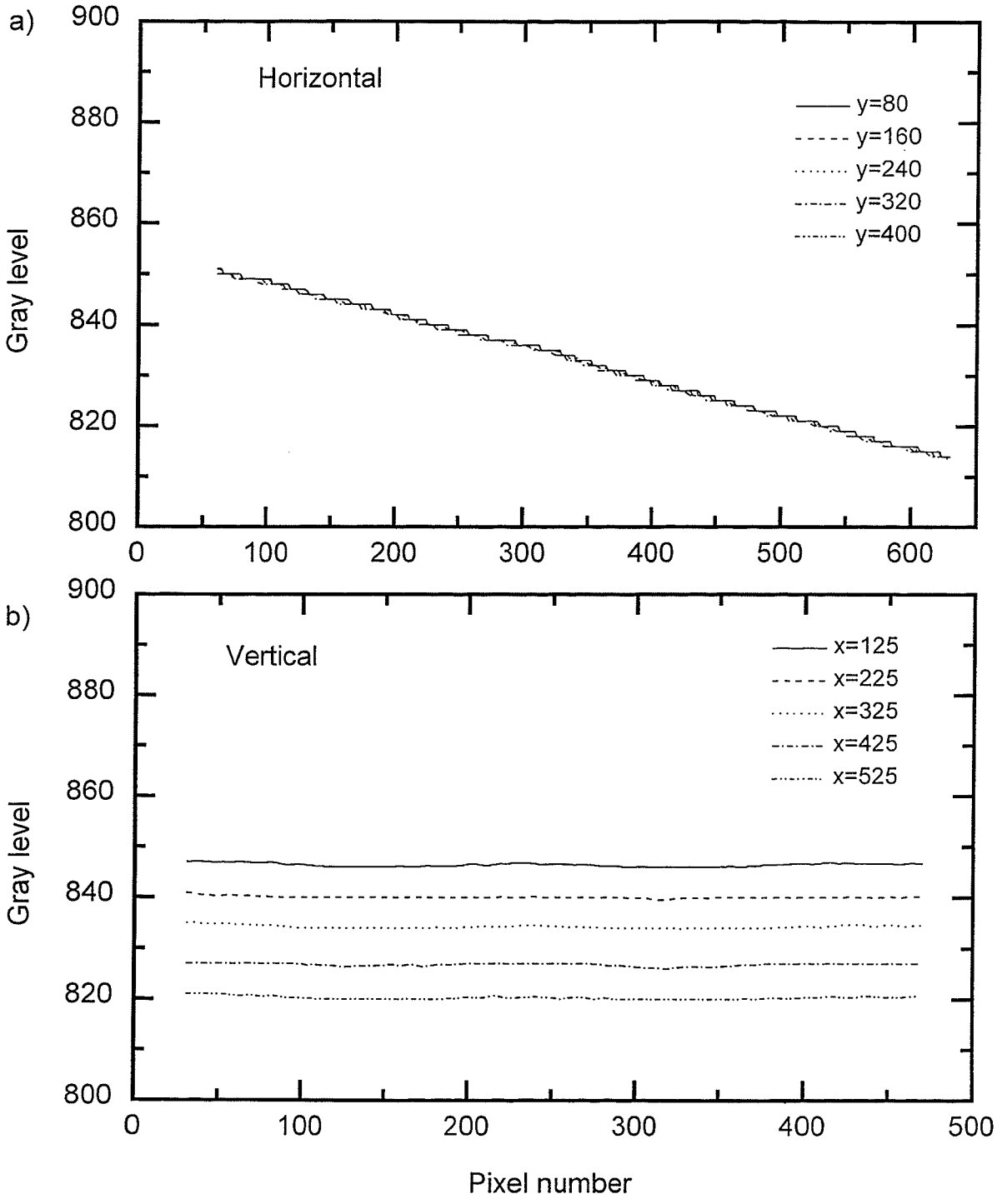

Figure 11-1. Five intensity profiles extracted from an image acquired by saturating the CCD camera. a) Horizontal profiles extracted at y = 80, 160, 240, 320, and 400. b) Vertical profiles extracted at x = 125, 225, 325, 425, and 525. See text for details.

$I(x,y)$ are corrected and uncorrected gray values at (x,y). Of course, for this correction to be applied, gray values of the left and right dark regions in all the images should be greater than zero.

11.2.2 Clamping error

The importance of the proper clamping of the RS-170 video signal in quantitative video imaging has been emphasized by Baily[22]. Any error in clamping the video black level in each video line to 0 V will lead to an error in the digitized pixel values in the corresponding video line. The ideal way to remove the clamping error is to digitize the video data before the RS-170 synchronization signals are added, ie. by using a digital camera. However, the CCD camera used in the current system uses RS-170 video, and consequently clamping errors must be corrected in the portal images before any quantitative measurements can be made.

The clamping circuitry in the OC-500 frame grabber is found to be very unstable, affected by the peak video signal as well as the horizontal extent of the illuminated region. This makes it necessary to correct for the clamping error in each video line. Figure 11-2 shows examples of the clamping errors introduced by the OC-500. Figure 11-2a shows vertical intensity profiles extracted at the left dark region (ie. $I(x_l,y)$) of three images: a dark current image, an image containing a 5 cm diameter circular bright region, and an image containing a 25 cm diameter circular bright region. Since the left dark region represents the video black level, the three profiles should be of similar magnitude and shape with ideal clamping. Figure 11-2b shows similar profiles of the dark current image and two images of a rectangular bright region having average signal values of about 50 and 750 gray levels. The deviation of the profiles of the images containing bright regions from that of the dark current image indicate the extent of the clamping error.

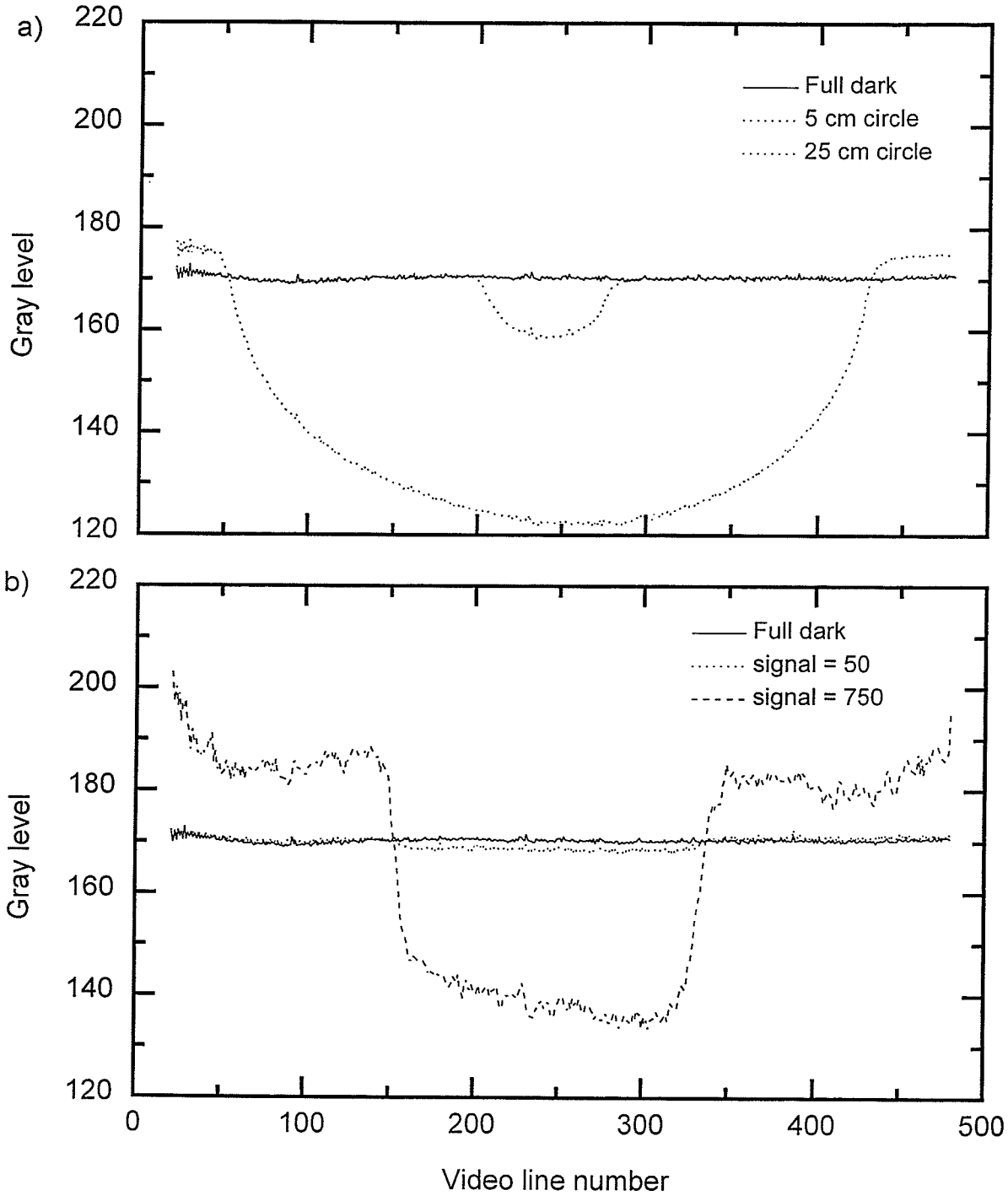

Figure 11-2. a) Vertical intensity profiles extracted at the left dark region from a dark current image, and images containing 5 and 25 cm diameter circular bright regions. b) Similar profiles of the dark current image and two images of a rectangular bright region having average signal values of about 50 and 750 gray levels.

Figure 11-3a shows the change in black level due to clamping error as a function of the extent of the illuminated region while the intensity of the illuminated region was kept constant. Figure 11-3b shows the change in black level due to the clamping error as a function of intensity of the illuminated region, while the extent of the illuminated region was kept constant. Clearly, the change in the black level in each video line depends on the extent of the illuminated section in the video line as well as the average intensity of the illuminated section in a non-linear fashion. It is also seen that unless corrected, inaccurate clamping can introduce errors of up to 55 gray levels which amounts to about 5.5 % error for a maximum signal of 1000 gray levels.

The clamping error can simply be corrected by subtraction of $I(x_1, y)$, the average gray value of the left black region, as long as the gray values of the left dark region are greater than zero. Eq. (11-1) can be extended to obtain $I_{g,c}(x, y)$, the gray value corrected for both gradient effect and clamping error as

$$I_{g,c}(x,y) = I(x,y) - I(x_1,y) + x \cdot \frac{I(x_1,y) - I(x_2,y)}{x_2 - x_1}. \qquad (11\text{-}2)$$

11.2.3 The cosine^4 law and lens vignetting

The Eq. (5-4) in Chapter 5 which describes the lens coupling efficiency between the phosphor screen and the camera target is derived under the assumption that both image and object subtend small angles at the lens. However, in a real case, even with an ideal thin lens, the illumination in the image plane (ie. on the camera target) is found to decrease away from the optical axis at least as the fourth power of the cosine of the angle[23]. Furthermore, with thick lenses used in practice, the illumination will fall off even more rapidly due to vignetting. Vignetting is caused due to the fact that some light entering the entrance pupil of the lens fails to emerge from the exit pupil. Vignetting

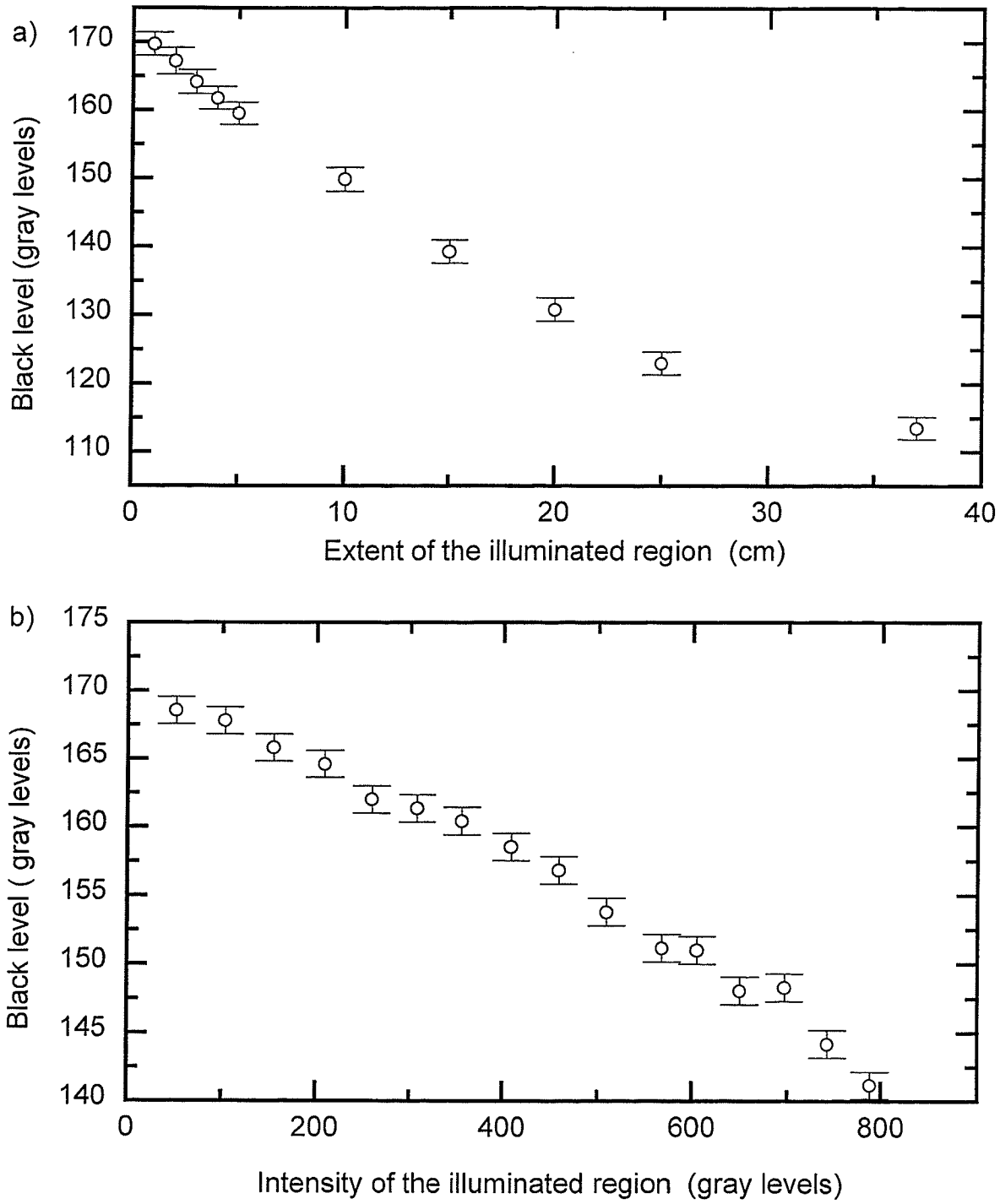

Figure 11-3. a) The change in black level due to clamping error as a function of the extent of the illuminated region while the intensity of the illuminated region was kept constant. b) The change in black level due to clamping error as a function of intensity of the illuminated region, while the extent of the illuminated region was kept constant.

usually depends on the F/stop setting of the lens, generally disappearing at small openings (large F/stops)[23].

In order to quantify the magnitude of these non-linear effects, the metal/phosphor screen was replaced by a translucent screen used in a light box, and the screen was illuminated with a circular (1 cm radius) light source placed at 2.6 m from the screen. The spatial variation in the illumination of the screen due to inverse square effects is less than 0.6 %. The light intensity at the screen surface is measured with a radiometer, and the maximum measured change within the field of view was 2% which is close to the accuracy of the radiometer.

Images of the uniformly illuminated translucent screen were acquired at 8 possible F/stop settings (0.85, 1.4, 2.0, 2.4, 4.0, 5.6, 8.0, and 11) of the Fujinon 25 mm focal length lens used in the system. Figure 11-4 shows a contour map of the image obtained with F/0.85 opening which clearly shows the effects of vignetting and $\cos^4$ law variations. It can be seen that this non-linearity is symmetric as one expects, but the point of symmetry does not coincide with the centre of the image. This may be due to mechanical misalignment of the lens axis with the centre of the CCD target. The displacement in the two centres are about 35 and 65 pixels in horizontal and vertical directions respectively, which amounts to about 0.5 mm and 0.9 mm at the camera target.

Figure 11-5 shows the horizontal intensity profiles extracted from the images acquired with an F/stop setting of 0.85, 1.4, 2.0, and 2.8. The profiles were obtained by averaging 24 pixels vertically. Note that the profiles were extracted from the images after corrections were applied for horizontal gradient error and clamping error as described above. The effect due to $\cos^4$ law is also shown for comparison. It can be seen that the effect of lens vignetting is severe at the lowest setting of F/0.85. The difference between the other three F/stop settings are less than 3%. The profiles of the images acquired at other F/stop settings are also very similar. This result clearly shows that F/1.4 is the optimal opening of the lens.

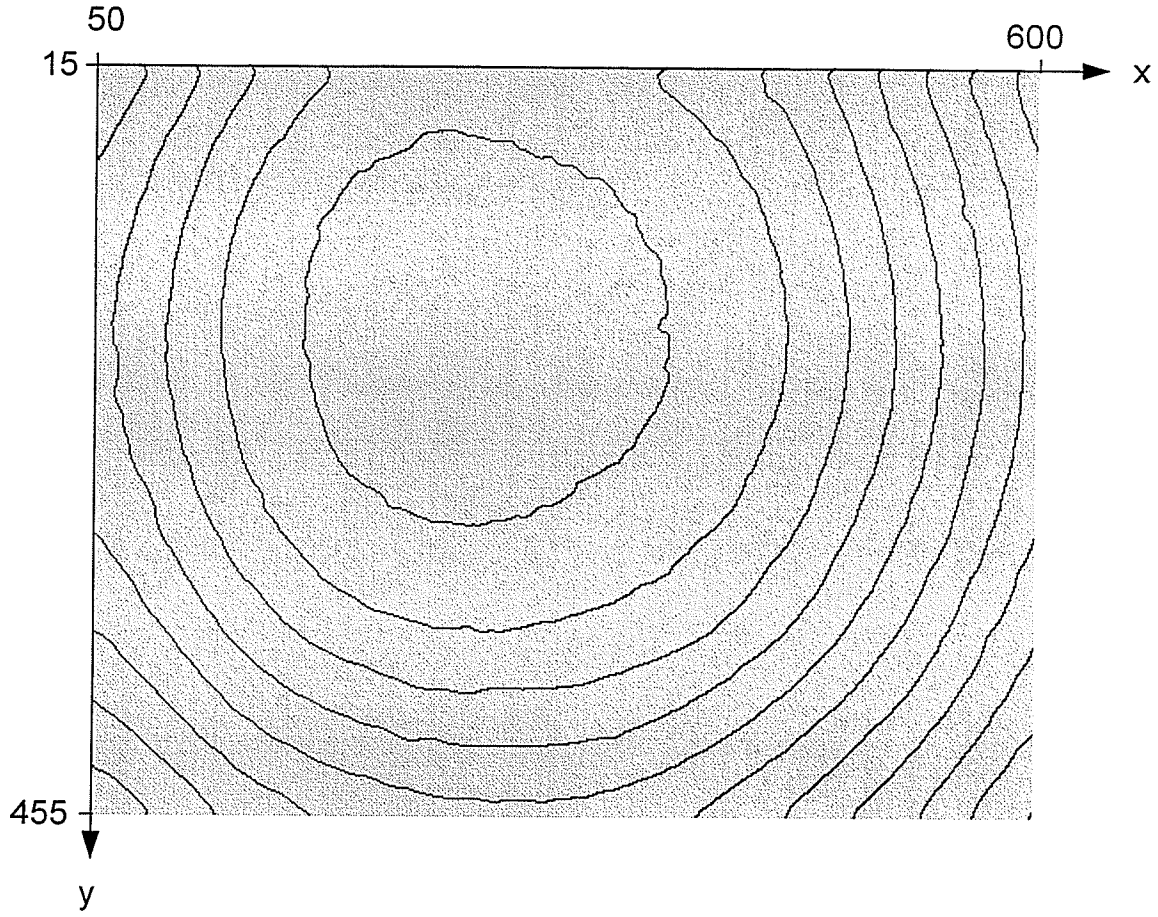

Figure 11-4. A contour map of an image acquired by imaging a flat light field with the F/0.85 opening of the lens showing the effects of vignetting and $\cos^4$ law variations. The difference between each contour line is about 10 gray levels.

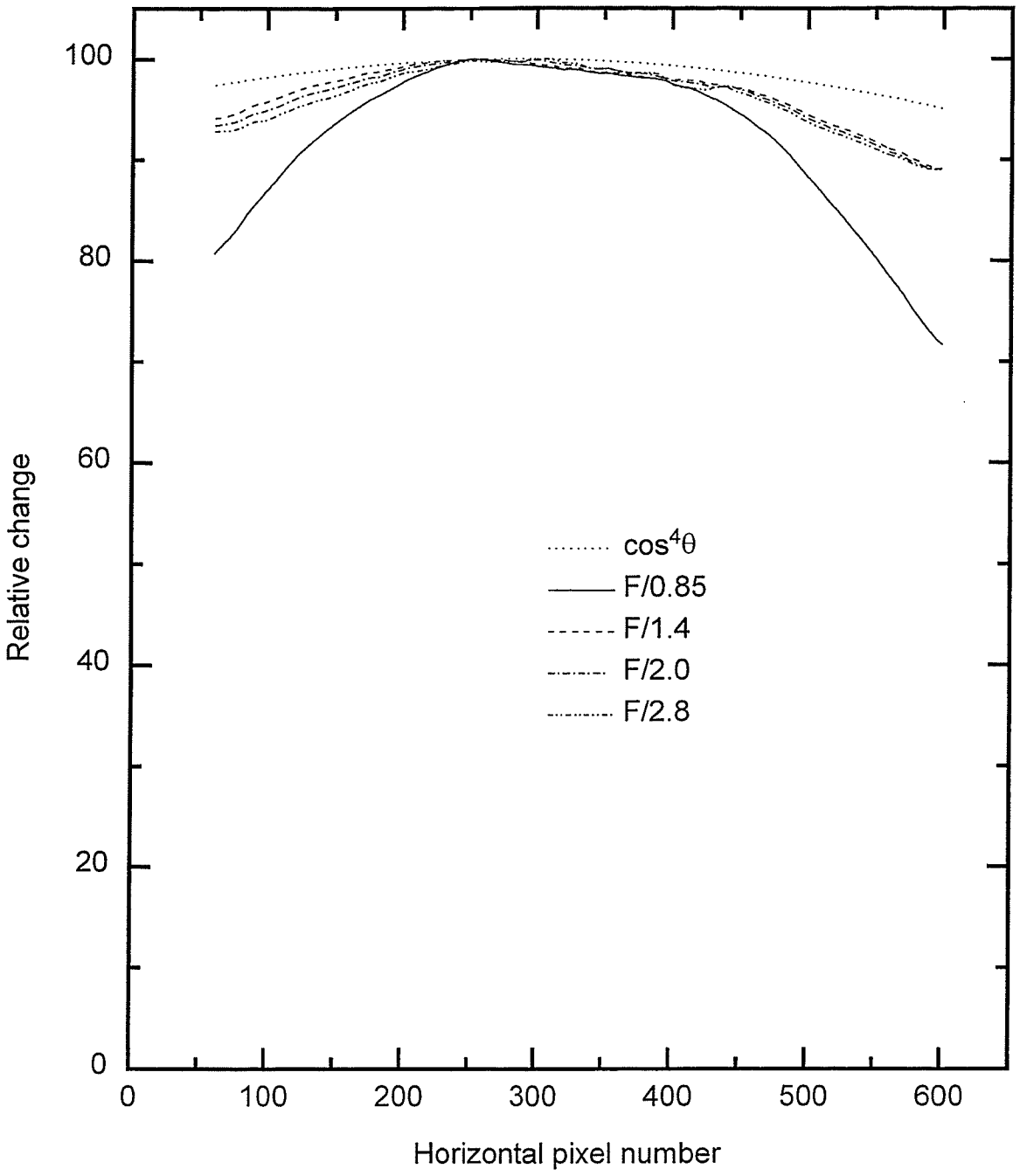

Figure 11-5. The horizontal intensity profiles extracted from the images of the flat light field acquired with F/stop settings of 0.85, 1.4, 2.0, and 2.8.

The correction for these nonlinearities can be expressed as

$$I_{g,c,v}(x,y) = \frac{I_{g,c}(x,y)}{I_{g,c}^{open}(x,y)} \qquad (11\text{-}3)$$

where $I_{g,c,v}(x,y)$ is the corrected gray level , $I_{g,c}^{open}(x,y)$ is the normalized (between 0 to 1) gray value of the flat light field image acquired at the same F/stop.

11.3 Other errors

11.3.1 Veiling glare and electronic instabilities

Veiling glare is caused by the scattering of visible radiation within the optical detection system. If the detection of optical photons by the system is linear, it is reasonable to assume that the magnitude of veiling glare is proportional to the illumination. Furthermore, it is assumed that the effect of the glare is uniform, which may not be true always[24].

In order to estimate the relative magnitude of the veiling glare, images were acquired with the translucent screen by illuminating circular regions having diameters of 2, 3, 4, 5, 10, 15, 20, and 25 cm, by keeping the intensity of the illuminated regions constant. Figure 11-6a shows the average gray value in an 8x8 ROI measured at the centre of the circular region. It can be seen that the intensity at the centre decreases with increasing diameter of the illuminated region, and then increases. The initial decrease in the intensity with increasing diameter is due to the instabilities in the camera and frame grabber electronics. The increase in the intensity with increasing diameter for diameters larger that 5 cm is due to the veiling glare. The curved line is a rough estimate of the change in intensity due to veiling glare, obtained by a second order polynomial fit to the last four data points. Roehrig and Fu[24] have reportaed a similar behaviour for the effect

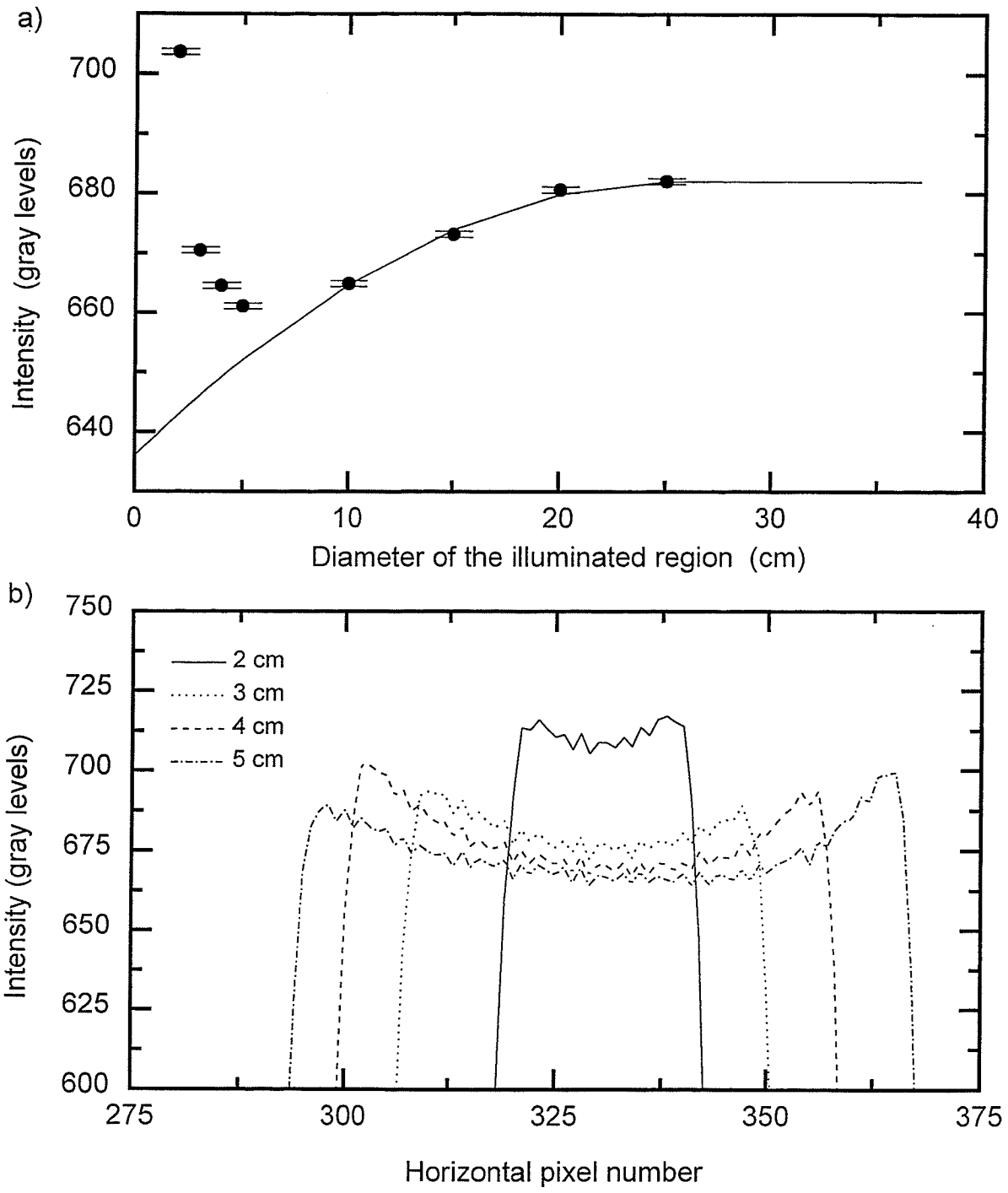

Figure 11-6. a) The change in the gray level in the centre of circular bright region as a function of the diameter of the illuminated region. b) The effect of electronic "over-shoot" on the measured gray level. See text for details.

of veiling glare in video based X-ray imaging. The fit indicates that the intensity for zero diameter is 636 ± 7 gray levels.

Figure 11-6b shows the corrected intensity profiles of the images acquired with 2, 3, 4, and 5 cm diameter regions, extracted at the centre of the illuminated regions. An electronic "over-shoot" effect due to the sharp gradient at the edges is seen. It is seen that the intensities in the central part are overestimated due to this effect.

Figure 11-7 show the relative error introduced by the electronic over-shoot and veiling glare. It is seen that errors in the order of 10% can be introduced by the over-shoot, whereas the veiling glare can introduce errors up to 7%. The error introduced by the veiling glare can be completely eliminated for any field size by calibrating the portal dose for a given field size. One should be able to eliminate the effect of electronic over-shoot by using a good digital CCD camera.

11.4 Linearity

The portal imaging system uses a CCD camera for detecting optical photons created by the phosphor screens. Response of CCD cameras are known to be highly linear, but the linearity of the associated electronic circuits in the camera and the frame grabber can make the optical detection process non-linear. Therefore the linearity of the optical photon detection process of the portal imager was tested by integrating different numbers of frames on the CCD target by properly adjusting the light falling on the CCD with the light box described in Chapter 5. Figure 11-8 shows the response of the camera. The straight line is a linear fit to data with a maximum deviation of only 3.2%.

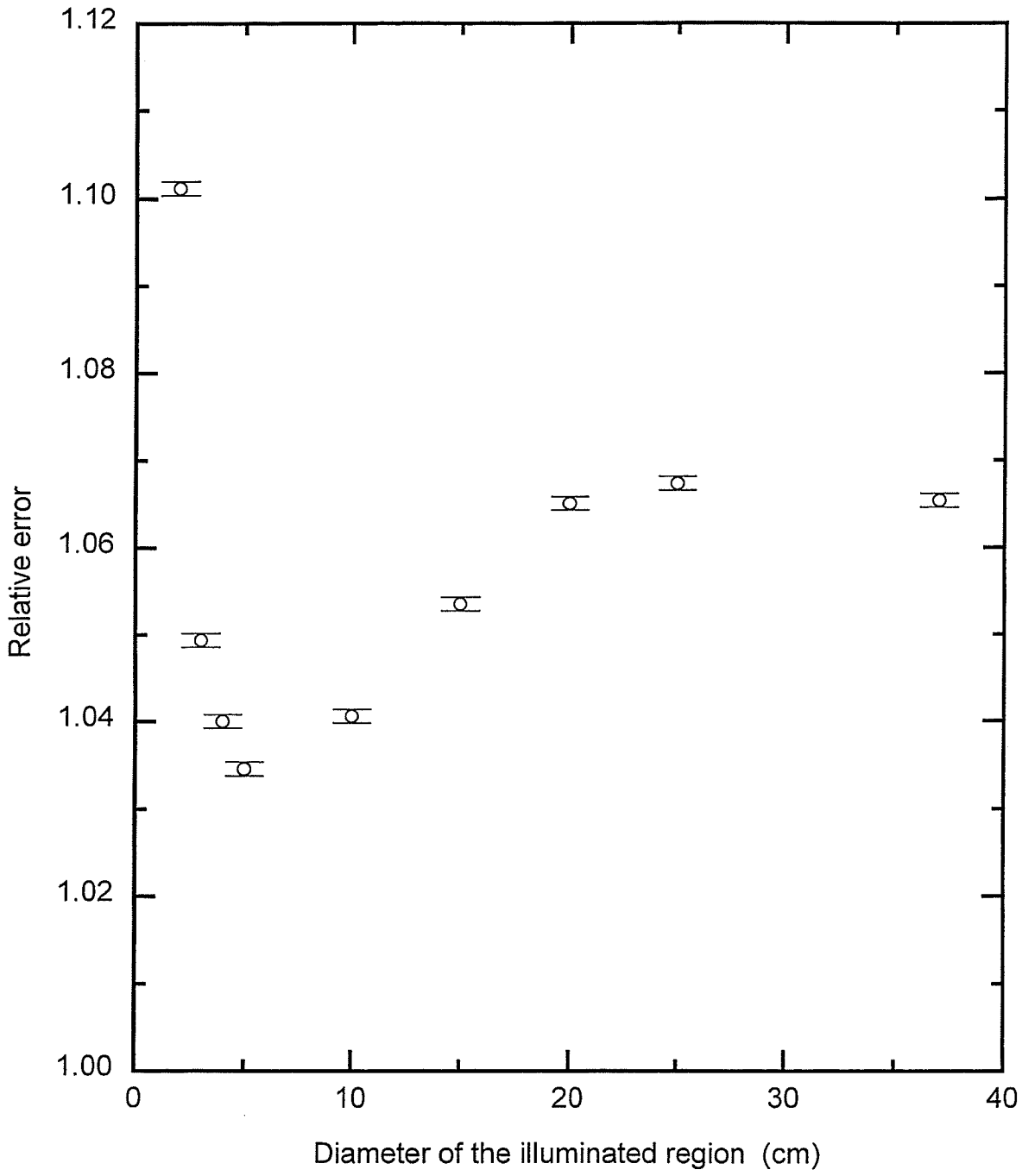

Figure 11-7. The relative error introduced by the electronic "over-shoot" and veiling glare.

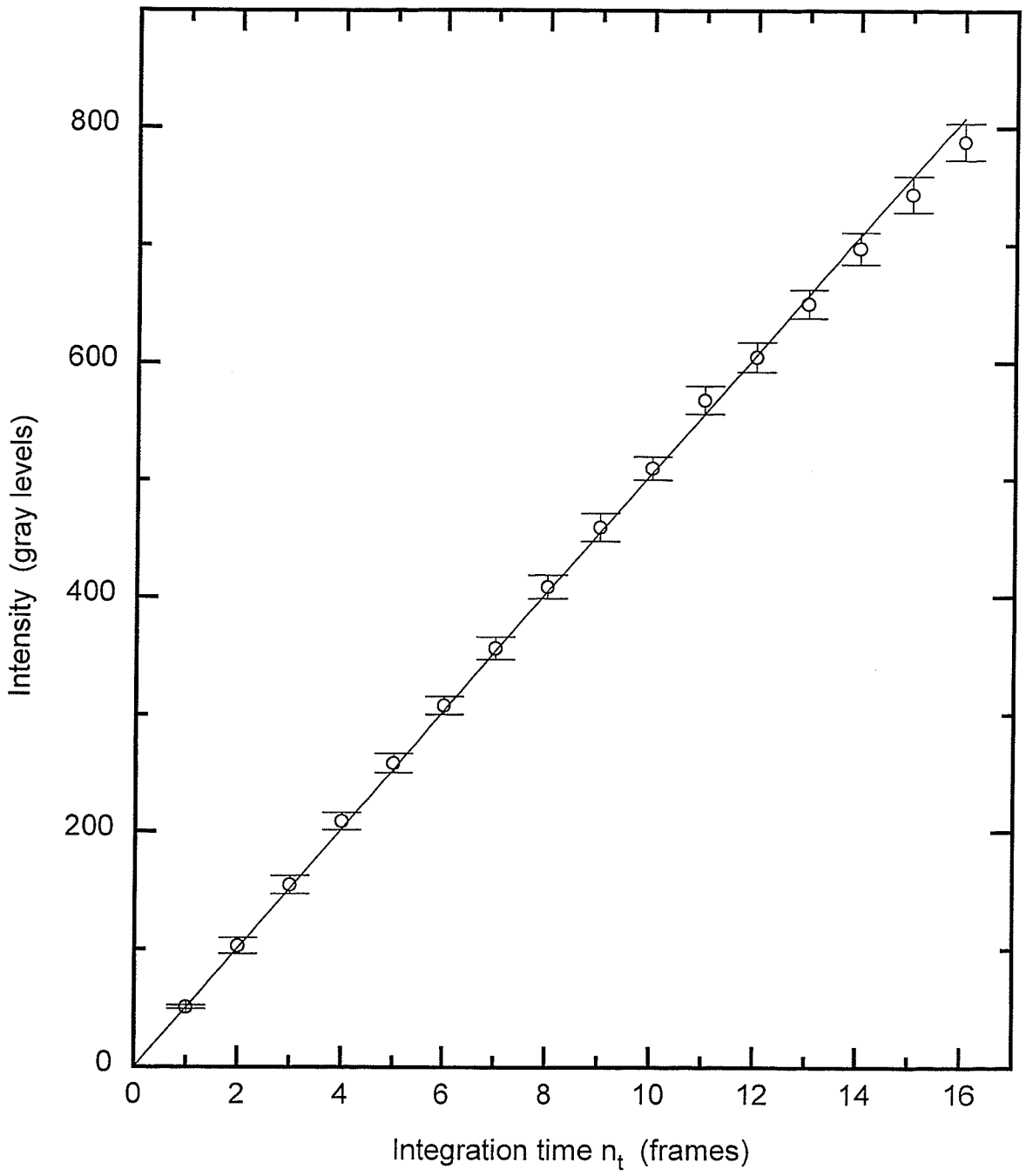

Figure 11-8. Linearity of the optical photon detection process of the portal imaging system. The straight line is a linear fit to the data. The maximum deviation of the data from the linear fit is only 3.2%.

11.5 Experimental measurements

11.5.1 Central axis dose

Portal images were acquired with a 10x10 cm^2 ^{60}Co beam by irradiating acrylic phantoms of varying thicknesses. The optimized portal imaging system incorporating the CCD camera was used to acquire the images by integrating 8 frames (0.267 s) on the CCD target. Images were also acquired with the prototype system incorporating a Newvicon camera by summing 8 sequential frames on the frame buffer. The experimental geometry used for measurements is shown in Fig. 11-9. The gray level intensity in a central 10x10 pixel ROI was measured after the three corrections were applied to the images. The exit dose at the detector surface was also measured with a Capintec F/type #64564 ionization chamber and a CNMC K616 electrometer for comparison. Both portal dose and ion chamber measurements were normalized by the corresponding open field dose (zero phantom thickness).

In order to find the effect of the air gap and the effect of the phantom material, similar measurements were carried out with a 1 cm thick lead phantom and a 10 cm acrylic phantom. Measurements with the lead phantom were carried out with 26.5 cm and 56.5 cm air gaps, and the measurements with the acrylic phantom were carried out at 26.5 cm and 52 cm air gaps.

11.5.2 Profiles

A 15x15 cm^2 field was used to obtain portal images of an open field, 15°, 30° and 45° wedges using a ^{60}Co beam. Images were acquired by integrating 8 frames on the CCD target using the optimized portal imaging system. The three corrections were applied to the images and profiles of the images at the centre of the images along the wedged direction were extracted by averaging 24 pixels in the non-wedged direction. A 24 pixel average was selected to simulate the scanning performed by the ion chamber

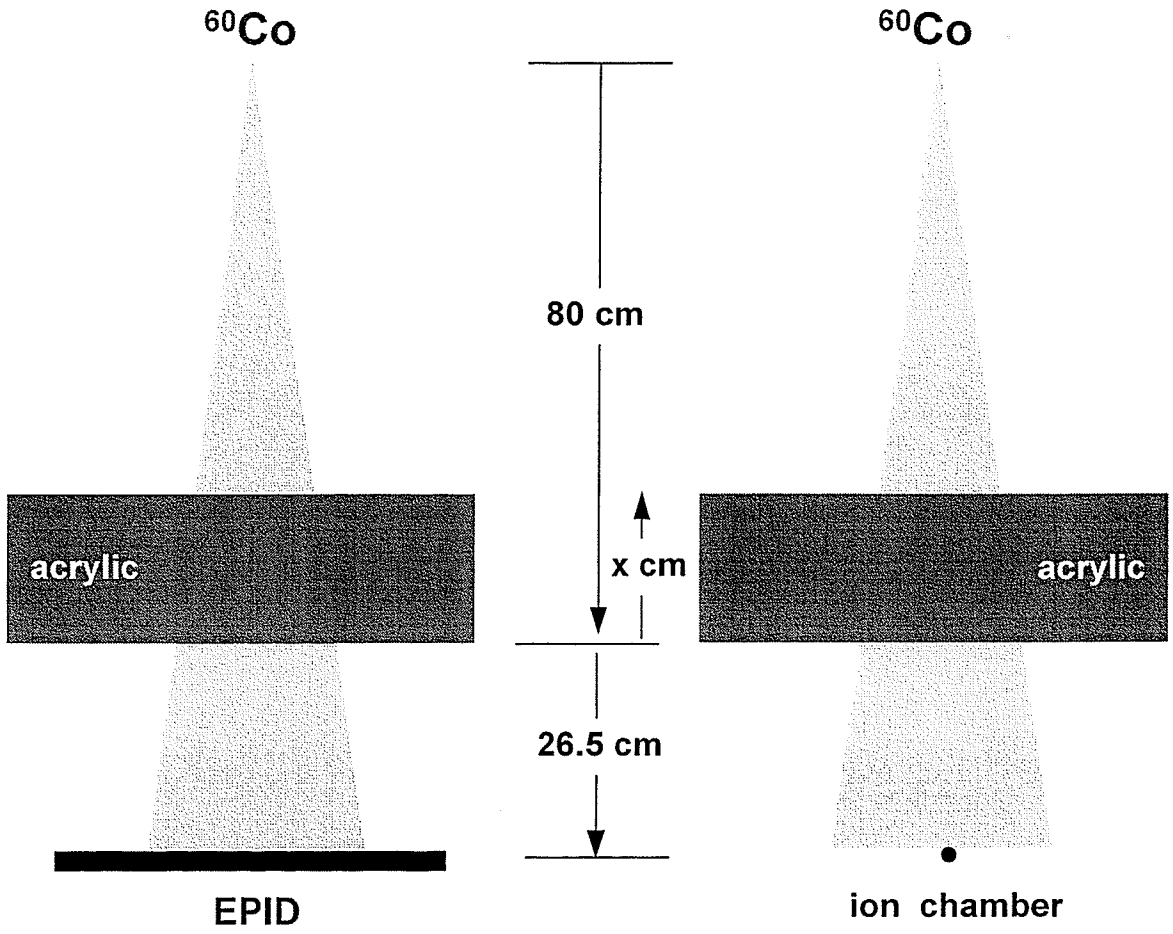

Figure 11-9. The experimental geometry used for measuring exit dose at the central axis of a ^{60}Co beam.

which has a chamber length of about 1.5 cm. The corresponding dose profiles were also scanned with a Therascan scanning ion chamber with a 0.5 cm build-up cap.

Similar portal dose profiles of 6 and 23 MV photons beams from a KD-2 linear accelerator were also obtained using a 15x15 cm^2 open field and 15°, 30°, 45°, and 60° wedged fields. Profiles of these images were extracted along the wedged direction as described above. The corresponding dose profile of each field was also scanned in water with a Multidata scanning ion chamber system at the detector level (140 cm from the source) with 1.5 and 3.5 cm build-up. In air dose measurements with build-up caps were not practical in this case due to the physical constraints of the scanning ion chamber.

11.6 Results and discussion

Figure 11-10 shows central axis portal dose plotted against the corresponding dose measured with the ion chamber, both normalized to the values of the zero phantom thickness. It is seen that the portal dose measured with the optimized system incorporating the CCD camera is highly linear, whereas the dose measured with the prototype system incorporating the Newvicon camera is somewhat non-linear. This clearly shows that the CCD camera is the best choice for quantitative portal imaging. It can be seen that the dose measured by the optimized portal imager is smaller than that of the ion chamber. This difference could be due to the difference in the energy response of the two detectors, but the two measurements agree well within the 5% limit.

Figure 11-11a shows a plot of the wedged dose profiles of the ^{60}Co beam obtained from the portal dose images and from the scanning ion chamber with a build-up cap. Both portal and ion chamber dose profiles were normalized to the corresponding central axis dose of the open field. It is seen that the un-wedged beam profiles agree very well while the wedged profiles obtained with portal dose images were significantly lower. The difference between the ion chamber dose and the portal dose at the central axis for the 45° wedge is about 15%. Since the dose measurements carried out with the acrylic

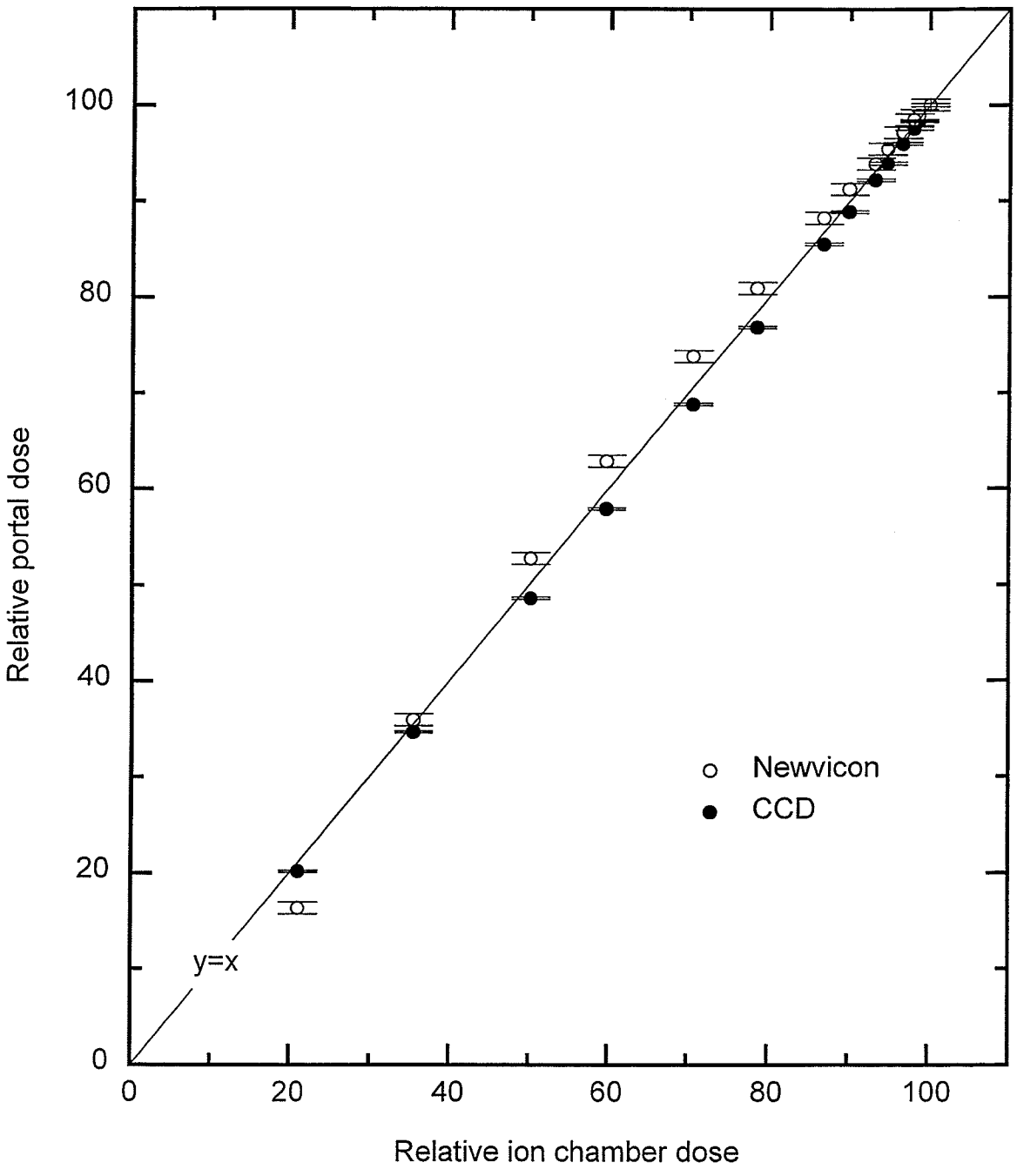

Figure 11-10. The plot of central axis portal dose against the corresponding dose measured with the ion chamber, both normalized to the values of the zero phantom thickness.

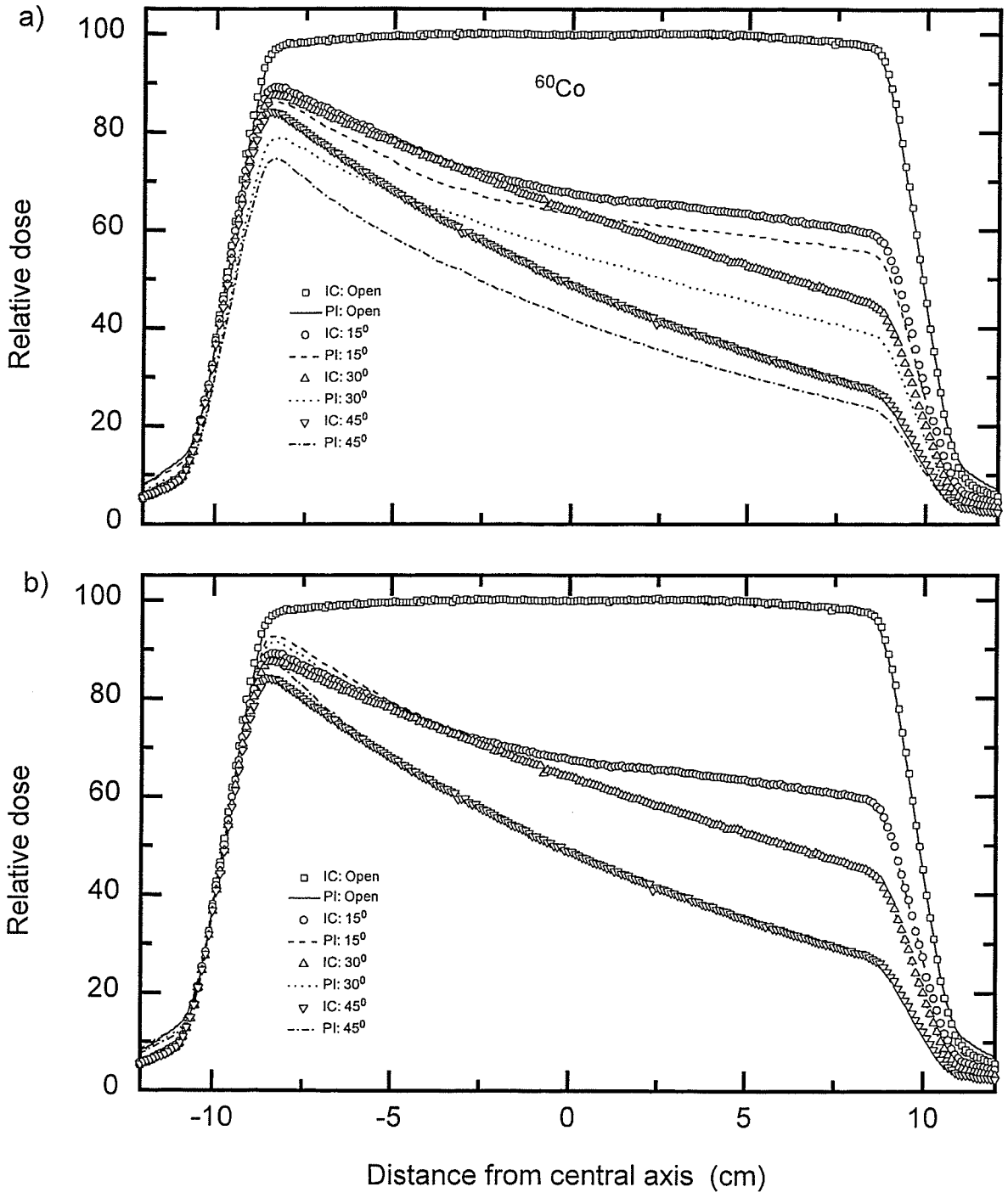

Figure 11-11. The comparison of open and wedged dose profiles of a 15x15 cm^2 ^{60}Co beam measured by the portal imager and by an ion chamber. a) Profiles were normalized to the corresponding central axis dose of the open field. b) Individual portal dose profiles were re-scaled to match the corresponding ion chamber dose at the central axis.

phantom agreed within 5% with the dose measured with the ion chamber, the discrepancy in the wedged dose profile suggests a significant change in the spectral distribution in the beam due to the heavy metals used in the wedges.

Figure 11-11b shows the same data, but the individual portal dose profiles were re-scaled to match the corresponding dose measured with the ion chamber at the central axis. It can be seen that except for the small discrepancy at the peak dose region, there is an excellent agreement between the two dose profiles after re-scaling. The discrepancy at the peak dose region is found to be due to the electronic over-shoot effect, since this discrepancy is reduced significantly when the wedges were rotated by 180°. One should be able to completely eliminate this discrepancy due to over-shoot effect by using a good digital CCD camera. For ^{60}Co beam, one can reasonably assume that for a given wedge, the spectral distribution within the field after passing the wedge is somewhat constant. Therefore the re-scaling of the portal dose profile to match the dose profile obtained with the ion chamber at the central axis would remove the effect of differential energy response of the two detectors for a given beam.

Figure 11-12 shows the comparison of open and wedged beam profiles of the linear accelerator. Figure 11-12a shows the profiles of the 6 MV photon beam, and Fig. 11-12b shows the profiles of the 23 MV photon beam. Both portal and ion chamber dose profiles were normalized to the corresponding central axis dose of the open field. There is a difference in the magnitude of the portal dose profiles and the profiles measured with the ion chamber at 6 MV, whereas the profiles of the 23 MV beam agree very well. However the discrepancy in the 6 MV profiles are smaller than that of the ^{60}Co beam. It is seen that the open field profiles of the 6MV beam show a significant discrepancy close to the field edge, indicating a change in spectral distribution in the radial direction. This clearly indicates that the energy response of the detector must be accounted for when portal dose measurements are compared with dose measured with an ion chamber.

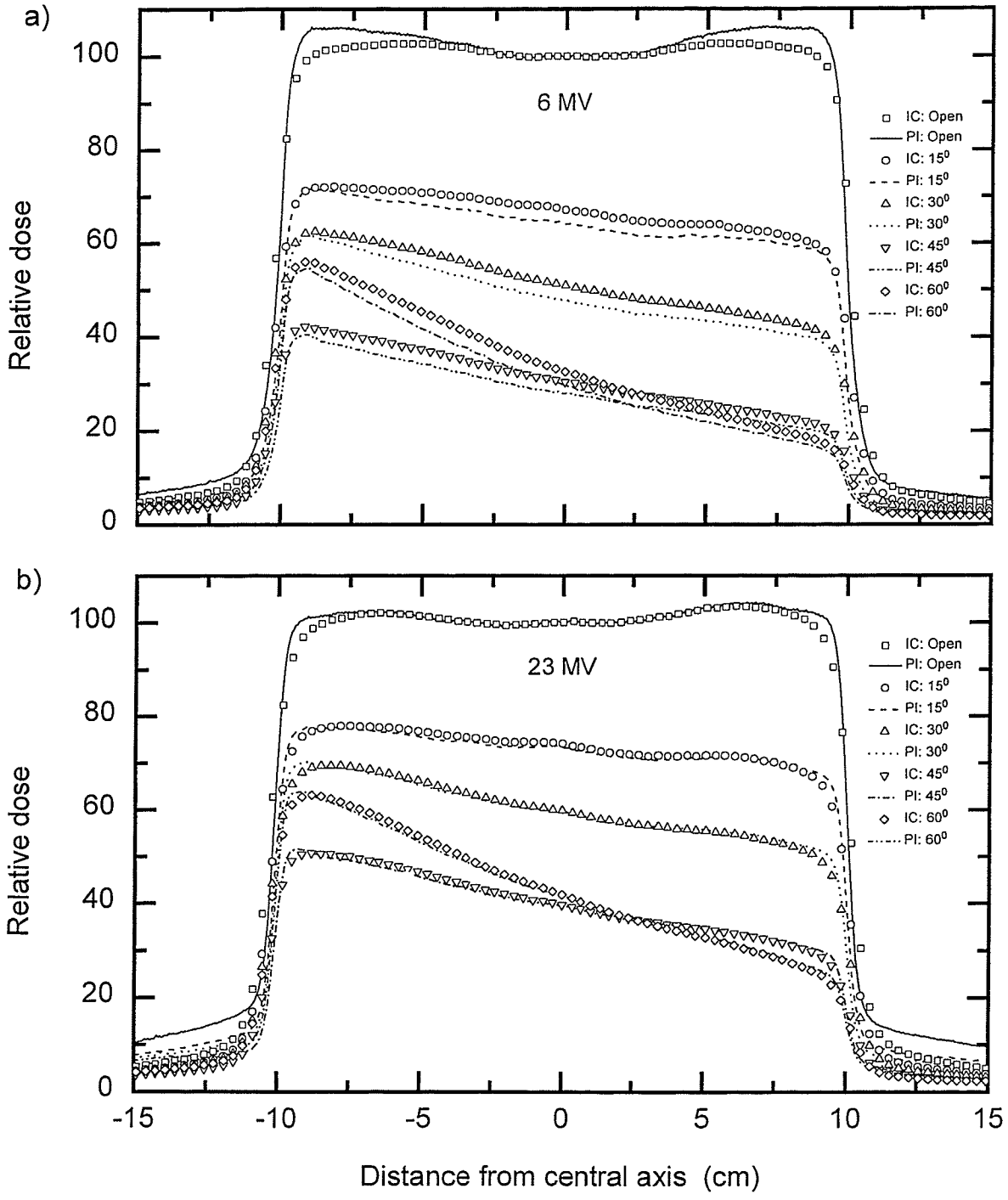

Figure 11-12. The comparison of open and wedged beam profiles of a linear accelerator. a) Profiles of a 6 MV photon beam. b) Profiles of a 23 MV photon beam. Both portal and ion chamber dose profiles were normalized to the corresponding central axis doses of the open field.

Figure 11-13 shows a plot of portal dose at the central axis against the corresponding ion chamber dose for all the profiles shown in Fig. 11-11 and 11-12. Also plotted are the relative exit doses measured with 10 cm acrylic and 1 cm lead phantoms using different air gaps. It is seen that the wedge dose measurements performed at 23 MV with the portal imager and with ion chamber agree very well. Measurements performed at 6 MV show a small but significant difference between the two types of exit dose measures, whereas the measurements from ^{60}Co have the greatest discrepancy.

It can be seen that irrespective of the air gap, the 1 cm lead phantom also produces a discrepancy between the portal and ion chamber doses which is consistent with that of the 30° and 45° wedges of the ^{60}Co beam. Irrespective of the air gap, the differences are smaller for the exit doses measured with the acrylic phantom. This leads to the conclusion that the phantom material can make a significant change in the spectral distribution of the exit fluence. The 15° wedge used with ^{60}Co is made of brass and all the other wedges are made mainly of lead. The discrepancy between the portal and ion chamber doses of the 15° wedge is smaller than the other two wedges indicating a smaller change in the spectral distribution for the 15° wedge.

The change in the spectral distribution of the exit fluence due to an insertion of a wedge made of metal into the beam path is not surprising. A Monte Carlo study carried out by Jaffray et. al.[25] has shown that the energy response of a metal/phosphor screen is relatively constant in the energy range of 5-25 MeV, but the response decreases with decreasing energy below 5 MeV with the minimum response around 0.5 MeV. Therefore the change in spectrum at 23 MV will have the least effect on the energy deposited in the screen whereas the change in the ^{60}Co beam will have the greatest effect on the deposited energy which is consistent with the results shown in Fig. 11-13. This effect of change in spectrum due to absorbing/scattering material in the beam path, and the resulting change in the portal dose due to the energy response of the portal detector must be explored in

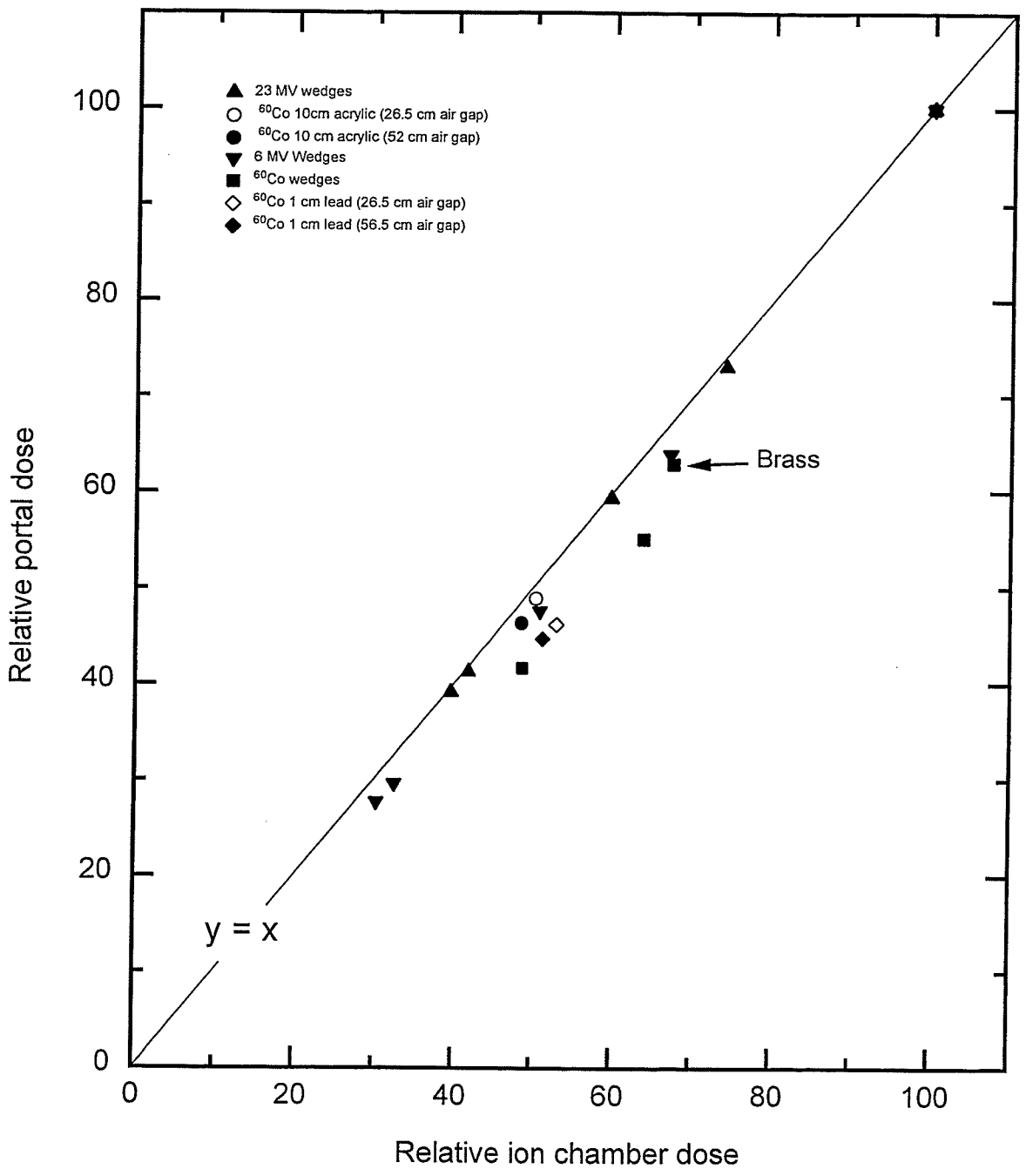

Figure 11-13. The plot of portal dose at the central axis against the corresponding ion chamber dose taken from the profiles shown in Fig. 11-11 and 11-12.

greater detail before one can safely use absolute values of exit dose measured with a portal imaging system in clinical practice.

11.7 Conclusions

The suitability of the optimized portal imaging system utilizing the CCD camera for exit dosimetry has been examined. The frame grabber used in the imaging chain introduces a "gradient" error with a magnitude of up to 5%, while the video clamping error is found to be as high as 5.5%. Lens vignetting introduces errors up to 30% depending on the lens aperture. Proper calibrations have been established to eliminate these sources of error. The response of the imager in detecting optical light is linear within 3% error. Veiling glare introduces a maximum of 7% error in the measured gray value whereas the over-shoot effects of the electronic circuitry can introduce errors up to 10%, which are the most significant errors introduced by the imager in detecting optical photons.

By far the most significant source of error in comparing portal dose with that measured with an ion chamber is due to the differences in the energy response of the two detectors. Therefore it is concluded that the comparison of portal dose measurements must be carried out against the exit dose calculations carried out either by Monte Carlo methods, or by analytical models, instead of ion chamber measurements.

References

[1] A. Boyer, L. Antonuk, A. Fenster, M. van Herk, H. Meertens, P. Munro, L. Reinstein and J. Wong, "A review of electronic portal imaging devices (EPIDs)," Med. Phys. **19**, 1-16 (1992).

[2] K. Halverson, T. Leung, J. Pellet, R. Gerber, M. Weinhous, and J. Wong, "Study of treatment variation in the radiotherapy of head and neck tumors using a fiber-optic on-line radiotherapy imaging system," Int. J. Rad. Onc. Biol. Phys. **21**, 1327-1336 (1991).

[3] M. Kirby and P. Williams, "Portal imaging for the verification of breast treatments," Radiother. Oncol. **22**, 314-316 (1991).

[4] J. Bijhold, J. Lebesque, A. Hart, and R. Vijlbrief, "Maximizing setup accuracy using portal images as applied to a conformal boost technique for prostatic cancer," Radiother. Oncol. **24**, 261-271 (1992).

[5] A. Ezz, P. Munro, A. Porter, J. Battista, D. Jaffray, A. Fenster, and S. Osborne, "Daily monitoring and correction of radiation field placement using a video-based portal imaging system: A pilot study," Int. J. Rad. Onc. Biol. Phys. **22**, 159-165 (1992).

[6] D.J. Gladstone, M. van Herk, and L.M. Chin, "Verification of lung attenuator positioning before total body irradiation using an electronic portal imaging device," Int. J. Rad. Onc. Biol. Phys. **27**, 449-454 (1993).

[7] W. De Neve, F. van den Heuvel, M. Coghe, D. Verellen, M. de Beukeleer, A. Roelstraete, P. de Roover, L. Thon, and G. Storme, "Interactive use of on-line portal imaging in pelvic radiation," Int. J. Rad. Onc. Biol. Phys. **25**, 517-524 (1993).

[8] C.L. Creutzberg, V.G.M. Althof, H. Huizenga, A.G. Visser, and P. Levendag, "Quality assurance using portal imaging: The accuracy of patient positioning in irradiation of breast cancer," Int. J. Rad. Onc. Biol. Phys. **25**, 529-539 (1993).

[9] J. Wong, E. Slessinger, R. Hermes, C. Offutt, T. Roy, and M. Vannier, "Portal dose images I: Quantitative treatment plan verification," Int. J. Rad. Onc. Biol. Phys. **18**, 1455-1463 (1990).

[10] J. Van Dam, A. Dutreix, N. Blanckaert, and E. van der Schueren, "About the use of conventional port films for in vivo dosimetry in radiotherapy," Med. Biol. Eng. Comp. **29 Suppl.**, p. 238 (1991).

[11] N. van Bree, L. van Battum, H. Huizenga, M. Idzes, and B. Mijnheer, "Film dosimetry of megavoltage photon beams for treatment planning verification," Radiother. Oncol. **24 Suppl.**, S25 (1992).

[12] J. Van Dam, C. Vaerman, N. Blanckaert, G. Leunens, A. Dutreix, and E. van der Schueren, "Are port films reliable for in vivo exit dose measurements?," Radiother. Oncol. **25**, 67-72 (1992).

[13] S. Heukelom, J. Lanson, and B. Mijnheer, "In vivo dosimetry during pelvic treatment," Radiother. Oncol. **25**, 111-120 (1992).

[14] G. Leunens, J. Verstraete, A. Dutreix, and E. van der Schueren, "Assessment of dose inhomogeneity at target level by in vivo dosimetry: can the recommended 5% accuracy in the dose delivered to the target volume be fulfilled in daily practice?," Radiother. Oncol. **5**, 242-250 (1992).

15 G. Leunens, J. Verstraete, A. Dutreix, and E. van der Schueren, "In vivo dosimetry in daily clinical practice," Radiother. Oncol. **24 Suppl.**, S23 (1992).

16 J. Leong, "Use of digital fluoroscopy as an on-line verification device in radiation therapy," Phys. Med. Biol. **31**, 985-992 (1986).

17 J. Wong, R. Binns, W. Ge, J. Epstein, J. Klarmann, and M. Israel, "Rapid areal dosimetry using a computer based plastic cintillator video camera system," In *The Use of Computers in Radiation Therapy* (I. Bruinvis, Ed.) Elsevier Science Publishers p. 417-420 (1987).

18 M. Takai and M. Kaneko, "Dosimetric verification using a fluoroscopic imaging device," Med. Biol. Eng. Comp. **29 Suppl.**, p. 860 (1991).

19 O. Holmberg, L. Ekberg, H. Widmark, L. Ahlgren, C. Larsson, and T. Knoos, "On-line monitoring of intracavitary dose in megavoltage radiotherapy using an array of diodes and an electronic portal imaging device," Radiother. Oncol. **24 Suppl.**, S26 (1992).

20 B. J. M. Heijmen, J. S. Stroom, H. Huizenga, and A. G. Visser, "Application of a fluoroscopic portal imaging system with a CCD camera for accurate in vivo dosimetry," Med. Phys. **20**, 870 (1993).

21 M.C. Kirby and P.C. Williams, "The use of an electronic portal imaging device for exit dosimetry and quality control measurements," Int. J. Rad. Onc. Biol. Phys. **27, Suppl. 1**, 165 (1993).

22 N. A. Baily, "Video techniques for X-ray imaging and data extraction from roentgenographic and fluoroscopic presentations," Med. Phys. **7,** 472-491 (1980).

23 W. F. Schreiber, *Fundamentals of electronic imaging systems,* 2nd (Springer-Verlag, Berlin, 1991).

24 H. Roehrig and T. Fu, "Physical properties of photoelectronic imaging devices and systems," in *Recent developments in digital imaging*, edited by K. Doi, L. Lanzl, and P. P. Lin (AIP, New York, 1985), pp. 82-140.

25 D. A. Jaffray, J. J. Battista, A. Fenster, and P. Munro, "X-ray scatter in megavoltage transmission radiography: Physical characteristics and influence on image quality," Med. Phys. **21 (1),** 45-60 (1994).

Chapter 12

Summary

The outcome of radiation therapy in treating cancerous tumour relies mainly on the ability to destroy the tumour with minimal damage to the surrounding normal tissues. Systematic and random errors occur during a course of therapy and will lead to under-treatment of the tumour or over-irradiation of adjacent healthy tissues. Accuracy and reproducibility in the radiation dose delivered to the target volume on a daily basis over a period of several weeks are important factors in improving overall precision of the treatment process. With the ever increasing use of oblique and even non-coplanar beams and the use of dynamic conformal therapy, this issue has become even more significant. Conventionally, treatment accuracy was verified using portal films on a very sparse sample, but their quality is often poor and the procedures involved in making and evaluating them are time consuming. Their use in each portal of every treatment is prevented by the cost in money and effort involved in the film method.

Several techniques have been proposed to overcome the difficulties encountered in the portal film method. The most important of these is the video based electronic portal imaging devices (VEPIDs). A prototype VEPID was developed in 1989 at the Manitoba Cancer Foundation for on-line verification of radiotherapy treatments. The system consisted of a metal/phosphor screen, a Silicon Intensified Target (SIT) camera and a PC-386 with an Imaging Technology series 151 image processor. The performance of this original system was far from ideal for both geometric and dosimetric verification.

Imaging performance of video based portal imaging systems is predominantly determined by the noise properties of the system. The ideal imaging system is a quantum noise limited system in which contributions from all other noise sources are smaller than the quantum noise. The major objective of this work was to optimize the noise

characteristics of the imaging system. In order to achieve this, all the significant noise sources in the imaging system were identified and the contribution from each source was quantified either by theoretical modeling or experimental measurements. Both hardware and software methods have been utilized to optimize the system noise characteristics. In particular, the optimization of the video camera played a major role in this process. It was shown that the dual field capture CCD camera is the best camera for real-time portal imaging, due to the linearity in detecting optical photons and the insensitivity to pulsation artifacts.

Figures 12-1 and 12-2 summarize the noise in the portal images acquired with the three video cameras concerned in this work when the 500 mg cm^{-2} phosphor screen ("thick screen") is used in a 23 MV photon beam. The figures show the plot of rms noise in gray levels for images with a maximum signal value of 256 gray levels against the integration time measured in number of frames (1/30 s). The definition of each noise source is given in part II, but repeated here for convenience. σ_o^2 is the total variance in the output pixel values (page 86, Eq. (5-18)). σ_D^2 is the quantum noise variance (page 84, Eq. (5-9). σ_a^2 is the noise variance due to pulsation artifacts (page 58, Eq. (3-1). σ_e^2 is the variance in the electronic noise added by amplifier in the Newvicon camera (page 88, Eq. (5-25). σ_r^2 is the variance in the readout noise of the CCD camera (page 86, Eq. (5-18). σ_b^2 is the variance in the dark current of the CCD camera (page 86, Eq. (5-18).

Figure 12-1a shows the change in noise in the images acquired with the SIT camera when frame averaging is performed. The values of the rms noise were obtained from Table 5-3 (page 101). The horizontal dotted line indicates the magnitude of second quantization noise. It is seen that when the integration time is more than 4 frames, the images acquired by the SIT camera are dominated by the quantum noise. Figure 12-1b shows the corresponding change in noise in the images acquired with the Newvicon camera. The values were obtained from Table 5-3 (page 101). Once the pulsation noise

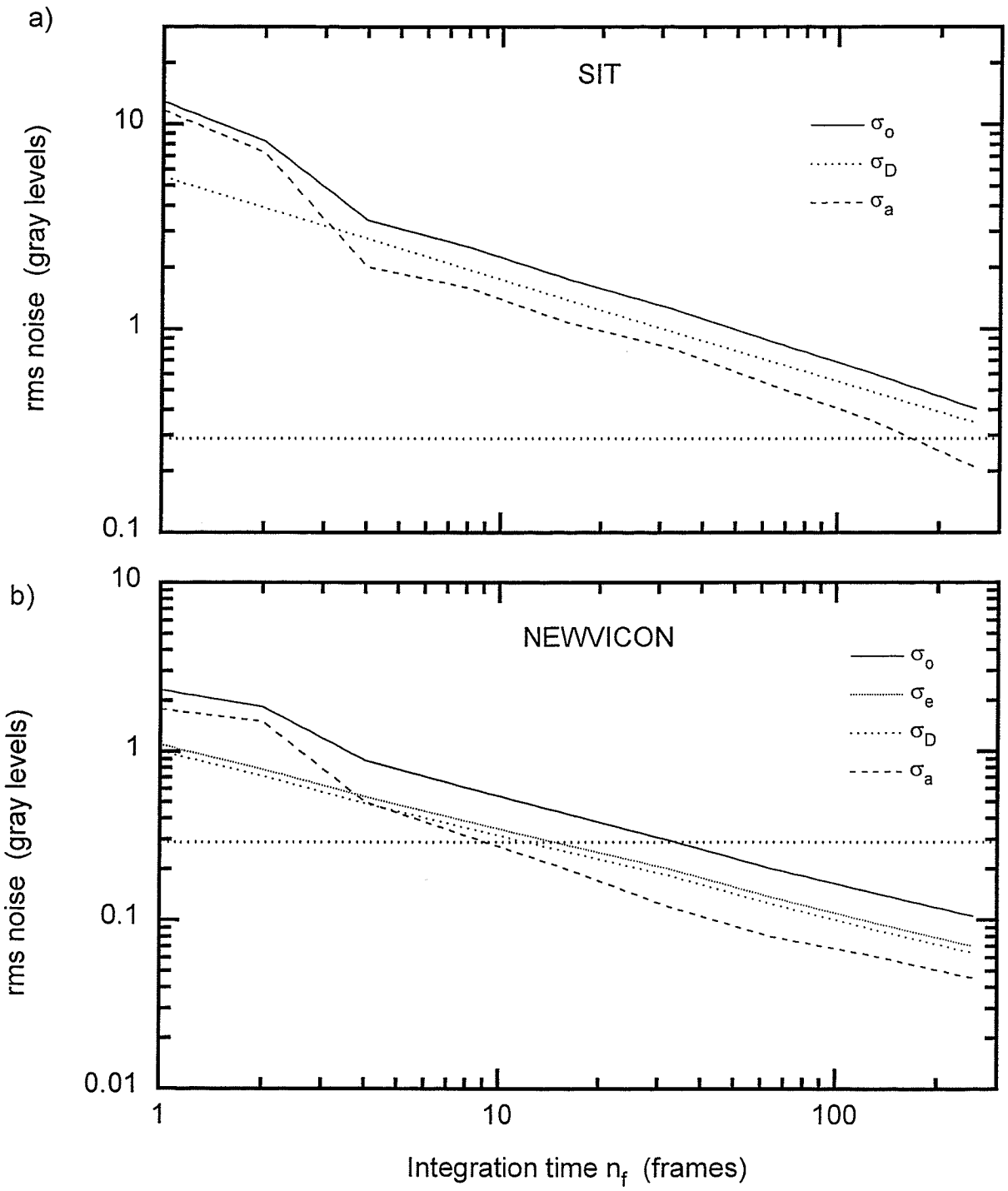

Figure 12-1. a) The change in noise in the images acquired with the SIT camera when frame averaging is performed. b) The corresponding change in noise in the images acquired with the Newvicon camera. The horizontal dotted lines indicate the magnitude of second quantization noise.

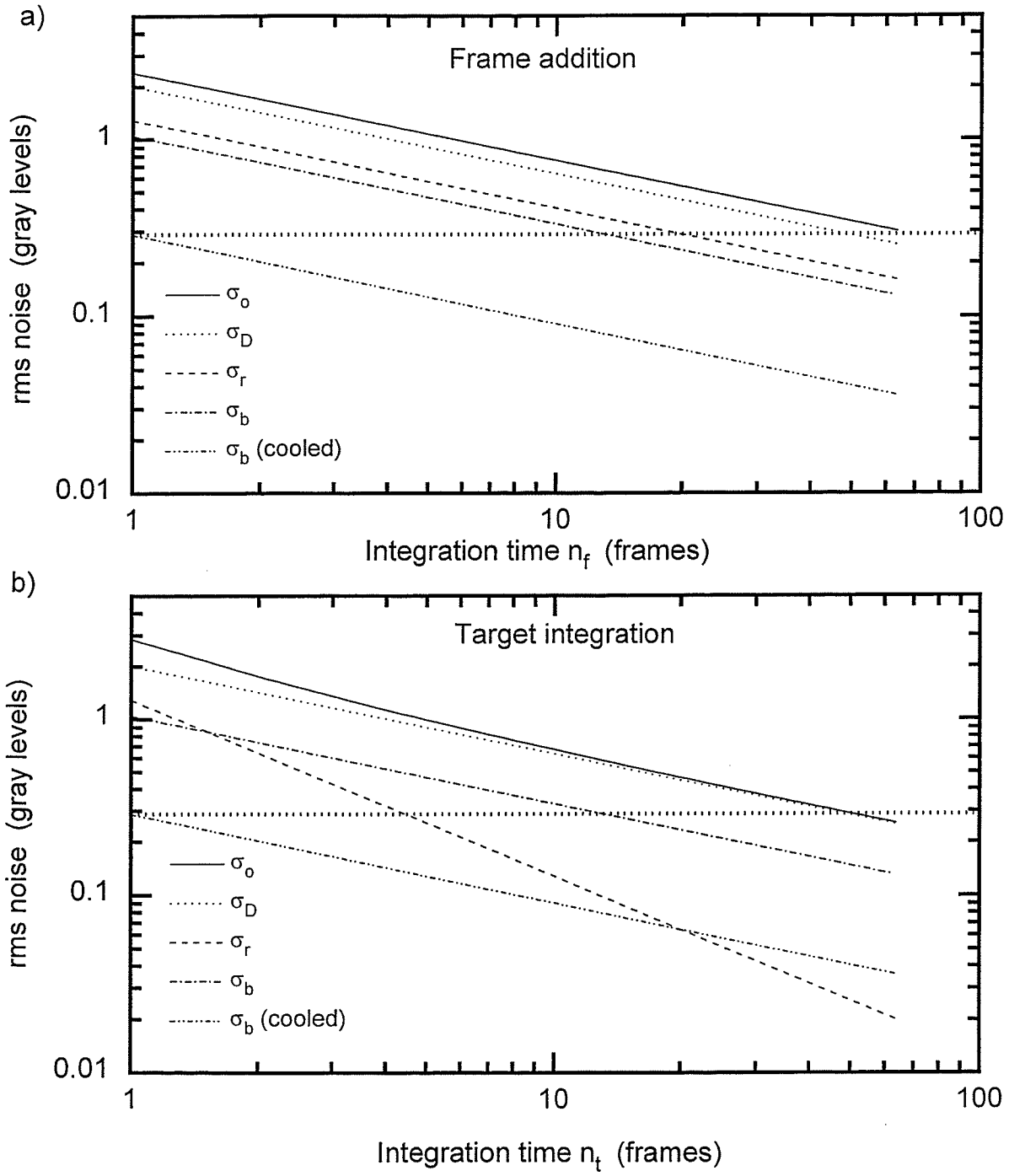

Figure 12-2. The reduction in noise level in the images acquired by the CCD camera. a) The results of frame averaging. b) The results of target integration. The horizontal dotted line indicates the magnitude of second quantization noise.

is reduced by frame averaging, and in the absence of second quantization noise, the images acquired by the Newvicon camera are dominated by the camera electronic noise.

Figure 12-2 shows the reduction in noise level in the images acquired by the CCD camera. The rms noise values were obtained from Table 5-2 (page 99). Figure 12-2a shows the results of frame averaging, and Fig. 12-2b shows the results of target integration. Although the dark current noise with and without cooling is shown, the dark current with cooling was used to obtain the total output noise σ_o. It is seen that the use of target integration instead of frame averaging make the images acquired by the CCD camera quantum noise dominated.

The magnitude of the second quantization noise is shown in Fig. 12-1 and 12-2, but the effect of it is not included in σ_o assuming digital frame addition or floating point frame averaging is utilized. However, if digital (integer) frame averaging is employed, the second quantization noise should be included in σ_o. Under this condition, the second quantization noise will be dominant the images acquired with the Newvicon camera after 32 frame average, whereas it will not be dominant in the images acquired with the SIT camera even at 256 frame average. The images acquired with the CCD camera either by frame averaging or combined use of target integration and frame averaging will be dominated by the second quantization noise when 64 or more frames are utilized.

Although EPIDs are assuming an ever increasing role in the verification of radiation treatments in the clinics today, no standard quality assurance procedures have been established for acceptance, commissioning, and routine quality control. Therefore a quality control test has been developed to test the resolution and contrast-to-noise performances of the VEPID. A QC phantom was also designed for use in the QC procedure. Measurements over a period of two years have shown that the QC test provides a sensitive indication of imaging performance. Inter-institutional trials are now underway in Canada, the US, and Europe for standardizing the quality control procedure.

So far, the electronic portal imaging systems have only been used for verification of photon treatments on linear accelerators. However, the general acceptance of the EPID technology into cancer clinics world wide will be promoted if EPIDs can be used for other clinical applications. Therefore, using phantom studies, it has been shown that the VEPID can be used to verify treatments with electron treatments with linear accelerators. Furthermore, it has been shown that real-time VEPID is capable of monitoring the stability of linear accelerators during the first few seconds of its operation.

It was shown in Chapter 11 that the noise in the optimized system imposes no practical limitation on the ability of the system to measure exit dose. In fact the errors introduced by the use of RS-170 video signal were found to be the most significant source of error which limits the quantitative accuracy of the portal imager. Therefore calibration procedures have been established to overcome some of the errors introduced by the RS-170. The digitization of the video data on the camera head will eliminate the errors associated in using the RS-170 video data. The effect of veiling glare is shown to introduce errors of up to 7%, but this error is easily eliminated by calibrating the portal imager for a given field size.

The preliminary work shown in this thesis clearly indicates that the optimized VEPID is capable of measuring relative exit doses to an accuracy better than 3%; the limit imposed by the non-linearity of the system in detecting light. Although one might calibrate for this non-linearity in order to achieve even better accuracy, aiming for such a high accuracy can not be justified at this point without an established accuracy in the calculations of exit dose.

Finally, it was found that the difference between the exit dose measured with the portal imager and that of an ion chamber can be a as high as 15% due to the energy dependence of the portal imager. Fortunately this imposes no serious problem in portal dosimetry as the objective of measuring exit dose with a portal imager is to compare it with the calculations which can compensate for the energy dependence.